

**Bioinspired Surface for Low Drag, Self-Cleaning, and Antifouling: Shark Skin,
Butterfly and Rice Leaf Effects**

Dissertation

Presented in Partial Fulfillment of the Requirements for the Degree Doctor of Philosophy
in the Graduate School of The Ohio State University

By

Gregory D. Bixler, P.E., M.S.

Graduate Program in Mechanical Engineering

The Ohio State University

2013

Dissertation Committee:

Professor Bharat Bhushan, Adviser

Professor Robert Siston

Professor Ahmet Kahraman

Professor Sandip Mazumder

Gregory D. Bixler

2013

ABSTRACT

Researchers are continually inspired by living nature to solve complex challenges through the field of biomimetics. Nature thrives on effective designs while optimizing the use of precious resources, which is something that inspires engineers worldwide. Gaining a deeper understanding of nature can lead to bioinspired products that save time, money, and lives. Examples include “low drag” boat hulls inspired by shark skin as well as “self-cleaning” windows and “antifouling” medical devices inspired by the superhydrophobic and low adhesion lotus leaf. Common engineering challenges solved in nature but hindering many industries are fluid drag reduction and antifouling. Nature holds clues to these challenges, including the unique surface characteristics of rice leaves and butterfly wings that combine the shark skin (anisotropic flow leading to low drag) and lotus leaf (superhydrophobic and self-cleaning) effects, producing the so-called rice and butterfly wing effect.

In this thesis, first presented is a chapter on biofouling and inorganic-fouling which is generally undesirable for many medical, marine, and industrial applications. A survey of promising flora and fauna are studied in order to discover new antifouling methods that could be mimicked for engineering applications. New antifouling methods will presumably incorporate a combination of physical and chemical controls. Mechanisms and experimental results are presented focusing on my new drag reducing

shark skin inspired surfaces. This includes my new laser etched and microtextured film samples for closed channel drag using water, oil, and air as well as in wind tunnel. Finally mechanisms and experimental results are presented focusing on my newly discovered rice and butterfly wing effect surfaces. I collected and present morphology, drag, antifouling, contact angle, and contact angle hysteresis results to understand the role of sample geometrical dimensions, wettability, viscosity, and velocity. Hierarchical liquid repellent coatings combining nano- and micro-sized features and particles are utilized to recreate or combine various effects. I fabricated such samples with photolithography, soft lithography, hot embossing, and coating techniques. Discussion is provided along with new conceptual models describing the role of surface structures related to low drag and antifouling properties. Modeling provides design guidance when developing novel low drag and antifouling surfaces for medical, marine, and industrial applications.

DEDICATION

Dedicated to my lovely wife and two kiddos.

ACKNOWLEDGMENTS

The accomplishments presented in this dissertation would not have been possible without the support of many people in my life. First I would like to thank my advisor, Professor Bharat Bhushan, who tirelessly provided guidance and feedback throughout the entire process. I will certainly remember all the times that we spent together discussing research and writing papers. I also would like to thank the many lab mates at the Nanoprobe Laboratory for Bio- and Nanotechnology and Biomimetics, especially Dave Maharaj. Many members continually supported my research and offered helpful insight and guidance. I would also like thank my doctoral committee members Professor Robert Siston, Professor Ahmet Kahraman, and Professor Sandip Mazumder at The Ohio State University.

Furthermore, I would like to express my sincere love and appreciation to my entire family who supported my efforts and encouraged me to finish strong. Special thanks to my wife Mary Hannah and two children Brody and Rachel who sacrificed much quality family time while I was working on research.

Finally, I would like to thank The Ohio State University Mechanical Engineering Advising and First Year Engineering staff members who were supportive throughout the masters and doctoral programs. Their support and help truly made this all possible.

VITA

February 1980.....Born – Ohio, USA

2003.....B.S. Mechanical Engineering
The Ohio State University, USA

2007.....M.S. Mechanical Engineering
The Ohio State University, USA

2008 – present.....Graduate Research Associate
The Ohio State University, USA

PUBLICATIONS

Research Publications

1. Bixler, G.D. and Bhushan, B. (2012a), “Biofouling Lessons from Nature,” *Phil. Trans. R. Soc. A* **370**, 2381-2417
2. Bixler, G.D. and Bhushan, B. (2012b), “Bioinspired rice leaf and butterfly wing surface structures combining shark skin and lotus effects,” *Soft Matter* **8**, 11271-11284
3. Bixler, G.D. and Bhushan, B. (2013a), “Bioinspired micro/nanostructured surfaces for oil drag reduction in closed channel flow,” *Soft Matter* **9**, 1620-1635
4. Bixler, G.D. and Bhushan, B. (2013b), “Shark skin inspired low-drag microstructured surfaces in closed channel flow,” *J. Colloid Interf. Sci.* **393**, 384-396
5. Bixler, G.D. and Bhushan, B. (2013c), “Fluid Drag Reduction with Shark-skin Riblet Inspired Microstructured Surfaces,” *Adv. Funct. Mater.* **23**, 4507-4528.
6. Bixler, G.D. and Bhushan, B. (2013d), “Fluid Drag Reduction and Efficient Self-Cleaning with Rice Leaf and Butterfly Wing Bioinspired Surfaces,” *Nanoscale* **5**, 7685-7710.

7. Bixler, G.D. and Bhushan, B. (2013e), “Rice- and Butterfly-Wing Effect Inspired Self-Cleaning and Low Drag Micro/nanopatterned Surfaces in Water, Oil, and Air Flow,” *Nanoscale*, DOI:10.1039/C3NR04755E.
8. Bixler, G.D. and Bhushan, B. (2013f), “Rice- and Butterfly-Wing Effect Inspired Low Drag and Antifouling Surfaces: A Review,” *under review*.
9. Bixler, G.D. and Bhushan, B. (2013g), “Fluid Conveying Apparatus With Low Drag, Anti-Fouling Flow Surface And Methods Of Making Same,” United States Patent Pending.
10. Bixler, G.D., Theiss, A., Bhushan, B., and Lee, S.C. (2013), “Anti-fouling Properties of Microstructured Surfaces Bio-inspired by Rice Leaves and Butterfly Wings,” *under review*.

FIELDS OF STUDY

Major Field: Mechanical Engineering

TABLE OF CONTENTS

ABSTRACT.....	ii
DEDICATION.....	iv
ACKNOWLEDGMENTS.....	v
VITA.....	vi
LIST OF TABLES.....	xiii
LIST OF FIGURES.....	xiv
CHAPTER 1: Introduction.....	1
1.1. Fluid drag and antifouling overview.....	3
1.2. Bioinspired low drag and antifouling.....	8
1.3. The rice and butterfly wing effect.....	10
1.4. Scope of the thesis.....	12
CHAPTER 2: Biofouling: Lessons from Nature.....	14
2.1. Introduction.....	14
2.2. Fields susceptible to biofouling.....	17
2.2.1. Medical.....	17
2.2.1.1. Permanent implants.....	23
2.2.1.2. Temporary implants.....	24
2.2.2. Marine.....	27
2.2.3. Industrial.....	29

2.3.	Biofouling and inorganic fouling formation	31
2.3.1.	Colonization.....	31
2.3.2.	Inorganic fouling.....	34
2.3.3.	Surface factors	36
2.4.	Antifouling examples and methods in practice.....	40
2.4.1.	Lessons from nature	42
2.4.2.	Methods in practice.....	50
2.4.2.1.	Surface property methods	50
2.4.2.2.	Other methods.....	59
2.4.3.	Additional approaches for completeness	60
2.4.3.1.	Cleaning and disinfecting.....	60
2.4.3.2.	Miscellaneous	63
2.5.	Summary and outlook.....	64
CHAPTER 3: Fluid Drag Reduction With Shark-Skin Riblet Inspired Microstructured Surfaces		66
3.1.	Fluid drag reduction with shark skin.....	66
3.2.	Drag mechanisms.....	67
3.2.1.	Shark skin.....	68
3.2.2.	Riblet optimization.....	72
3.3.	Riblets and experimental methods	75
3.3.1.	Riblet geometries and configurations	75
3.3.2.	Riblet fabrication	81
3.3.3.	Drag measurement techniques	83
3.3.3.1.	Open channel	83
3.3.3.2.	Closed channel.....	90
3.4.	Riblet results and discussion	92
3.4.1.	Open channel	93
3.4.2.	Flat plate experiments.....	93
3.4.3.	Flat plate observations	99
3.4.4.	Airfoil experiments	100
3.4.5.	Closed channel.....	106

3.4.5.1.	The role of channel dimensions	106
3.4.5.2.	Micro-sized channel experiments	106
3.4.5.3.	Micro-sized channel observations.....	112
3.4.5.4.	Continuous versus segmented riblets.....	113
3.4.5.5.	Riblets on top or bottom or both sides	113
3.4.5.6.	The role of riblet wettability	118
3.5.	Models of riblets and vortices.....	120
3.5.1.	Riblets for open or macro-sized closed channel flow	120
3.5.2.	Riblets in micro-sized closed channel flow	122
3.5.3.	Thin oil film effect.....	125
3.6.	Conclusions and Outlook.....	127
CHAPTER 4: Rice- and Butterfly-Wing Effect Inspired Low Drag and Antifouling Surfaces		129
4.1.	Fouling formation	129
4.1.1.	Biofouling	129
4.1.2.	Inorganic fouling.....	130
4.1.3.	Self-cleaning mechanisms.....	131
4.2.	Inspiration from living nature	134
4.2.1.	Ambient species	134
4.2.2.	Aquatic species	138
4.2.3.	Rice and butterfly wing effect.....	139
4.3.	Sample fabrication	141
4.3.1.	Fabrication of replicas.....	141
4.3.1.1.	Urethane soft lithography and coating procedure	141
4.3.1.2.	Rice leaf inspired surfaces	142
4.3.1.3.	Silicon master patterns	147
4.3.1.4.	PDMS soft lithography procedure	147
4.3.1.5.	Hot embossing procedure.....	148
4.4.	Experimental procedures	150
4.4.1.	Pressure drop measurements.....	150
4.4.2.	Predicting closed channel pressure drop.....	152

4.4.3.	Antifouling experiments	153
4.4.3.1.	Anti-biofouling	153
4.4.3.2.	Anti-inorganic fouling.....	157
4.4.3.3.	Wettability.....	158
4.5.	Results and discussion	158
4.5.1.	Sample characterization	159
4.5.2.	Actual, replica, and rice leaf inspired	159
4.5.3.	Pressure drop measurements	168
4.5.3.1.	Water flow	168
4.5.3.2.	Oil flow	172
4.5.3.3.	Air flow	176
4.5.3.4.	Nondimensional pressure drop model.....	179
4.5.4.	Antifouling experiments	181
4.5.4.1.	Anti-biofouling	181
4.5.4.2.	Anti-inorganic fouling.....	185
4.5.4.3.	Wettability.....	191
4.5.4.4.	Actual, replica, and rice leaf inspired samples.....	192
4.5.5.	Wettability, drag, and antifouling	198
4.6.	Models for low drag and antifouling.....	202
4.6.1.	Low drag models.....	202
4.6.2.	Antifouling models	206
4.7.	Conclusions.....	208
	CHAPTER 5: CLOSURE.....	211
	BIBLIOGRAPHY	214

LIST OF TABLES

Table 1: Fields susceptible to biofouling including common examples.	18
Table 2: Flora antifouling lessons from nature.	43
Table 3: Fauna antifouling lessons from nature.	44
Table 4: Antifouling coatings.	51
Table 5: Biofouling cleaning/disinfecting techniques.	61
Table 6: Miscellaneous antifouling techniques.	63
Table 7: Open channel riblet experimentation.	78
Table 8: Closed channel riblet experimentation.	79
Table 9: Sawtooth riblet airfoil experimentation.	80
Table 10: Physical characterization of surface structures from actual samples (adapted from Bixler and Bhushan, 2012b).	144
Table 11: Geometric dimensions of rice leaf inspired samples (Bixler and Bhushan, 2013e).	145
Table 12: Replica sample CA predictions (Bixler and Bhushan, 2012b).	199

LIST OF FIGURES

Figure 1: Montage of examples from living nature that have inspired researchers seeking new bioinspired products (adapted from Bhushan, 2009). Shown are (a) water droplet on a self-cleaning lotus leaf and its micropapillae, (b) glands of carnivore plant that trap insects, (c) water strider walking on water and its leg structures, (d) Gecko feet spatula with reversible adhesion, (e) riblet covered low drag and antifouling shark skin, (f) bird wing structure and orientation during landing approach, (g) spider webs made of silk stands, and (h) anti-reflective moth eyes.....	2
Figure 2: Montage of images showing examples of the Golden Ratio, Golden Rectangle, and Fibonacci numbers found in nature and art (adapted from Bixler and Bhushan, 2013d). Examples include galaxies, sunflower heads, flower petals, sea shells, Mona Lisa painting, and pineapple fruit (from top left to bottom right). The Golden Rectangle and Fibonacci or Golden spiral are superimposed on select images. Such proportions and patterns are considered aesthetically pleasing and are believed to enhance performance of systems found throughout nature.	4
Figure 3: Biological and inorganic fouling examples. Biofouling examples are shown with a biofilm covered pacemaker wire (adapted from Marrie and Costerton, 1984) and barnacles on a flat underwater plate (adapted from Edgar, 1997). Inorganic fouling examples are shown with dirt deposits on a stucco building exterior (photo courtesy of www.stocorp.com) and crystallization on the outside of heat exchanger tubing (photo courtesy of H&C Heat Transfer Solutions, Inc).	7
Figure 4: Overview of fields susceptible to biofouling, description of the fouling formation process, and current antifouling strategies (adapted from Bixler and Bhushan, 2012a).....	16
Figure 5: Schematic highlighting areas of the body susceptible to infectious biofilms (adapted from P. Dirckx Center for Biofilm Engineering).	19
Figure 6: Medical device biofilm examples with ventilation tube (adapted from Trinidad et al, 2010), needleless connector (adapted from Janice Carr), and pacemaker wire (adapted from Marrie et al., 1982). Such biofilms may lead to infections that require device removal since antibodies are often ineffective.	22

Figure 7: Biosensor product examples and biofouling (adapted from Bixler and Bhushan, 2012a). Schematic of the implantable glucose biosensor probe illustrates biocompatibility and biofouling issues (bottom). MEMS (adapted from Dana Lipp) and glucose monitors (adapted from Newman and Turner, 2005)..... 25

Figure 8: Marine biofouling examples. Areas susceptible to biofouling on a typical ship (middle) and the common hard shelled barnacle (*Tetraclitella purpurescens*) (top left). Barnacles on underwater plate (adapted from Edgar, 1997). 28

Figure 9: Industrial biofouling examples. Zebra mussels (*Dreissena polymorpha*) clogging power plant intake pipe (top left) (adapted from Peter Yates), biofilm accumulation in a stainless steel tube (top right) (adapted from Cunningham et al., 2008), biofilm (*B. cereus*) on dairy industry stainless steel plate (bottom left) (adapted from Simoes et al., 2010), and biofilm (*P. aeruginosa*) on reverse osmosis (RO) membrane (bottom right) (adapted from Herzberg and Elimelech, 2007). 30

Figure 10: Biofilm development process and cross section example. Schematic illustrates the five stage colonization process (top) (adapted from D. Davis) and SEM of biofilm cross section highlighting the EPS morphology (bottom) (adapted from Andy Blankemeier)..... 32

Figure 11: Inorganic fouling examples. Inside of a clean nuclear power plant heat exchanger tube (top) compared to a fouled tube with corrosion deposits (middle) (adapted from Cunningham et al., 2008). Calcium carbonate crystallization fouling on the outside of a heat exchanger (bottom) (adapted from H&C Heat Transfer Solutions, Inc). 35

Figure 12: Various parameters describing wettability and self-cleaning. (a) Schematic shows droplet contact angles (left) and photos of droplet regimes (right) (adapted from Nosonovsky and Bhushan, 2008). (b) Schematic shows the self-cleaning effect (top) and superhydrophobic examples (bottom) (adapted from Barthlott and Neinhuis, 1997). 38

Figure 13: Schematic shows surface topography antifouling mechanisms demonstrating wettability and texture properties that influence microorganism settlement and colonization (adapted from Bixler and Bhushan, 2012a). Shown are elephant ear (Koch and Barthlott, 2009), shark skin (Reif, 1985), water fern (Koch and Barthlott, 2009), and insect wing (Lee et al., 2004)..... 41

Figure 14: Antifouling examples from nature using wettability properties. Water promotes self-cleaning on low adhesion superhydrophobic surfaces as shown in the lotus (adapted from Bhushan et al, 2009), butterfly (adapted from W. Barthlott), and pigeon (adapted from Bormashenko et al., 2007) examples. Also shown are fish scales (adapted from Liu et al, 2009), which are superoleophobic when submerged. Shark skin is antifouling due to a combination of features including, low drag, riblets, flexion of scales, and mucous layer (adapted from Jung and Bhushan, 2009). 46

Figure 15: Antifouling examples from nature using mechanical cleaning and chemical secretions. Human eye combines wiping with chemical secretions to clean the cornea (top) (adapted from John Nyquist). Red seaweed using a halogenated furanone to manipulate colonizing bacteria “attraction” messages (bottom) (adapted from Yen, 2010). 49

Figure 16: Effectiveness of self-cleaning antifouling coatings. Demonstrated is the improved cleanliness with Lotusan ® hydrophobic self-cleaning paint (top) (adapted from www.stocorp.com) and improved clarity with the SunClean™ hydrophilic self-cleaning glass (bottom) (adapted from www.ppg.com). 54

Figure 17: Medical, marine, and industrial antifouling coating examples. Orthopedic hip implants are covered with a biocompatible coating designed to control biofouling, wear rate, and promote bone growth (top left) (adapted from Ir Jef Vleugels). Marine foul-release organic tin-free hull coating called “Green Ocean Coating Heavy Duty” minimizes manual cleaning (top right) (adapted from Bayer MaterialScience). Polysulfone ultrafiltration membrane treated with silver nanoparticles (nAg) shows antifouling benefit with fewer E. Coli attached (bottom) (adapted from Zodrow et al., 2009). 56

Figure 18: Biomimetic antifouling examples. Inspired by nature’s antifouling Galapagos shark (Carcharhinus Galapagensis) skin (top left) (adapted from Reif, 1985), researchers are developing a Sharklet™ antifouling urinary catheter (top right) (adapted from www.sharklet.com). Experiments demonstrate the Sharklet AFTM antifouling effectiveness with Ulva settlement on various topographies (bottom) (adapted from Carman et al., 2006). 58

Figure 19: Medical, marine, and industrial biofouling cleaning examples. Steam sterilization medical autoclave (top left) (adapted from Life Science Outsourcing), Listerine® effect on bacteria (top right) (adapted from Christoph Schaudinn), water spray on a low-stick ship hull (middle left), automatic brush washing system (middle right) (adapted from Willemsen, 2005), and microfiltration membrane using sonication, chemicals, and water backwash (bottom) (adapted from Lim and Bai, 2003). 62

Figure 20: Biofouling prevention technique (adapted from NASA Ames and Dominic Hart). Biosensor developed by the National Aeronautics and Space Administration detects small amounts of bacteria, viruses, and parasites to prevent the spread of disease. 64

Figure 21: SEM micrographs of shark skin samples from living nature. Actual Mako (top) (adapted from Bixler and Bhushan, 2012b) and replica Spiny Dogfish (bottom) (adapted from Jung and Bhushan, 2010) shark skin micrographs are shown at two magnifications. These highlight the scales (dermal denticles) and riblets which are responsible for low drag and antifouling properties. Arrows indicate fluid flow direction. 69

Figure 22: Flow visualization images using smoke from atomized oil burned in air to study the turbulent vortices behavior with and without riblets at two velocities (adapted from Lee and Lee, 2001). Top images show the vortices on a flat plate with a relatively large amount of surface contact area, which leads to higher drag. Bottom images show the vortices are lifted above the riblet tips, with a relatively small amount of surface contact area, which leads to lower drag. The dimensionless parameters for height (h^+) and spacing (s^+) aid in the understanding of riblet design for any flow condition. Such parameters are based on riblet spacing or height, fluid kinematic viscosity, and wall shear stress velocity..... 71

Figure 23: Typical shark skin inspired riblet geometries and configurations that have been experimentally evaluated (adapted from Bixler and Bhushan, 2013c). Shown are (a) blade, sawtooth, and scalloped geometries as well as (b) continuous, aligned segmented, and staggered segmented configurations. Actual shark skin most closely resembles the scalloped geometry and staggered segmented configuration..... 77

Figure 24: Riblet drag reduction experiments on airplanes and airfoils. In flight tests, total fuel consumption determines the amount of drag reduction. SEM micrograph shows the sawtooth riblet cross section (adapted from Sareen et al., 2011), where riblet grooves are oriented parallel to the fuselage. Section A-A illustrates a typical airfoil. 82

Figure 25: Open channel methods and facilities to measure drag using water, oil, and air (adapted from Bixler and Bhushan, 2013c). (a) In water or oil channel flow, riblets are applied to a force balance plate that is lowered into the moving fluid (top). The deflection of the force balance translates into the total amount of drag. In airfoil experiments (bottom), the wake profile determines the total amount of drag. Drag may also be measured with riblets applied to a flat plate or airfoil using a force balance in the wind tunnel. (b) Open flow channels filled with water or oil are utilized with the force balance (top). Shown is the location of the motor and propellers that produce a constant flow. Wind tunnel schematic (bottom) illustrates set up for the wake traverse method. As air flows through the wind tunnel, the wake traverse lowers at a specified rate to measure the wake profile. Shown also is the infrared camera position utilized to visualize turbulence on the airfoil. 85

Figure 26: Conventional airfoil cross sectional side views. Shown are the thin, thick, curved thin, reflex trailing edge, and symmetrical wind sections (adapted from www.allstart.fiu.edu). Each airfoil is designed for specific applications due to their various attributes such as low drag and high lift..... 88

Figure 27: Closed channel methods and apparatuses to measure drag using water, oil, and air. (a) Split designs are necessary in order to apply riblets inside micro-sized closed channels. Left schematic shows a round split pipe whilst the right shows a rectangular channel sandwich design. The rectangular channel allows for riblets to be fabricated on a flat surface, which may be

desirable (adapted from Bixler and Bhushan, 2013b). (b) Drag is determined via pressure drop reduction using closed channels lined with riblet samples. Flow is regulated with the elevated container (water), pump (water or oil), and laboratory air connected to a rotameter (air). The pressure drop is measured with a manometer connected to both ends of the flow channel. Interface views are shown highlighting the top and bottom halves that are sandwiched together. 91

Figure 28: Open channel experimental results with riblets in water flow (adapted from Walsh, 1990a). Drag reduction is presented as Reynolds numbers compared to negative ΔC_d (%) values, which is the percentage drag coefficient reduction between the smooth and riblet samples. Riblet samples with various h/s values are compared, with the maximum drag reduction near 6%. Riblets are sawtooth geometry and continuous configuration. 94

Figure 29: Open channel experimental results with riblets in oil flow (adapted from Bechert et al., 1997b, 2000a). Drag reduction is presented as Reynolds numbers compared to negative $\Delta\tau/\tau_o$ (%) values, where $\Delta\tau$ is the difference between shear stresses on the riblet sample (τ) and the smooth (τ_o) surfaces. (a) Various experiments with blade, sawtooth, and scalloped riblets were conducted in order to discover the optimal geometry for maximum drag reduction. Varied parameters include the riblet geometry, h/s , t/s , and s^+ , which allows for a better comparison between experiments. Oil channel experiments were conducted using white paraffin oil. (b) Maximum drag reduction results from the various blade, sawtooth, and scalloped experiments are compiled. Results indicate that the blade geometry with $h/s \approx 0.5$ and $t/s \approx 0.02$ produces the maximum drag reduction of 10% near $s^+ \approx 15$. (c) Experimental results comparing continuous and staggered segmented blade riblets, indicating that latter configuration shows less drag reduction. 96

Figure 30: Wind tunnel experimental results with riblets on airfoils. Drag reduction is presented as Reynolds numbers compared to negative ΔC_d (%) values, which is the percentage drag coefficient reduction between the smooth and riblet samples. (a) Drag reduction is shown with wind turbine DU 96-W-180 (adapted from Sareen et al., 2011) and symmetrical NACA 0012 (present work) airfoils with various 3M Corp. sawtooth riblets. The top and bottom Figures show Reynolds numbers in the subsonic and transonic ranges, respectively. Maximum drag reduction is near 7% for the riblets with $h = s = 44 \mu\text{m}$ in transonic flow. (b) Riblet drag reduction is related to angle of attack, as shown with two airfoils with angles of attack up to 12° . The greatest drag reduction of nearly 14% is shown at 6° angle of attack (adapted from Subaschandar et al, 1999). 101

Figure 31: Detecting turbulent air flow using an infrared camera. In order to determine the extent of turbulent flow on an airfoil, an infrared camera may be employed. The friction from turbulent vortices heats the airfoil surface and is detected by the camera. Based on the airfoil geometry and calculated air velocity using pressure taps measurements, a fully turbulent state is shown with Mach 0.6 and $Re = 4,500,000$ 103

Figure 32: Boundary layer thickness related to riblet height. As the Mach number increases, the boundary layer thickness decreases. It is believed for drag reduction that riblets should remain inside the viscous sublayer in order to effectively control the turbulent vortices. Shown is an illustration (not to scale) explaining the relationship. 105

Figure 33: Comparison of open channel flat plate and macro-sized closed channel pipe flow (where neighboring wall effects are assumed negligible). Drag reduction is presented as Reynolds numbers compared to negative $\Delta\tau/\tau_o$ (%) values, where $\Delta\tau$ is the difference between shear stresses on the riblet sample (τ) and the smooth (τ_o) surfaces. Samples consist of sawtooth geometry where the angle $\alpha = 60^\circ$, as defined in Figure 10a. (a) Experimental results are shown with sawtooth riblets on a flat plate (Bechert et al., 1997b) and (b) in round pipe with diameter D (Liu et al., 1990). Maximum drag reduction is similar between the presented flat plate and macro-sized pipe flow. 107

Figure 34: Micro-sized closed channel experimental results with riblets in water and air flow (adapted from Bixler and Bhushan, 2013b). Drag reduction is presented as Reynolds numbers compared to pressure drops between the inlet and outlet of the channel, where lower pressure drop is desirable. Riblets of varying geometries were evaluated in laminar ($Re < 2300$) through turbulent flow ($Re > 4000$) conditions. Experiments evaluated the effect of h/s, t/s, height, hydrophobicity, and smoothness. Riblets were fabricated via laser etching, and a nanostructured coating was applied to achieve the desired hydrophobicity and smoothness. Maximum pressure drop reduction of 34% with water was recorded for hydrophobic riblets in the turbulent regime. Flat milled channel control sample is shown for comparison. Error bars show ± 1 standard deviation. 109

Figure 35: Micro-sized closed channel experimental results with riblets in oil flow (adapted from Bixler and Bhushan, 2013a). Drag reduction is presented as Reynolds numbers compared to pressure drops between the inlet and outlet of the channel, where lower pressure drop is desirable. Riblets of varying geometries were evaluated in laminar ($Re < 375$) flow conditions. Experiments evaluated the effect of h/s, t/s, and oleophilicity. Riblets were fabricated via laser etching, and a nanostructured coating was applied to achieve the desired oleophilicity. Maximum pressure drop reduction of 9% was recorded for the Narrow riblets. Experiments were conducted using white paraffin oil. Flat milled channel control sample is shown for comparison. Error bars show ± 1 standard deviation. 111

Figure 36: Micro-sized closed channel experimental results showing the effect of continuous vs. segmented blade riblets with water, oil, and air flow (adapted from Bixler and Bhushan, 2013b, 2013a). Drag reduction is presented as Reynolds numbers compared to pressure drops between the inlet and outlet of the channel, where lower pressure drop is desirable. Riblets were evaluated in laminar ($Re < 2300$) through turbulent flow ($Re > 4000$) conditions. Results indicate that the continuous riblets increase drag with all fluids, presumably due to the increased wetted surface

area, which leads to higher skin friction. Flat milled channel control sample is shown for comparison. Error bars show ± 1 standard deviation. 114

Figure 37: Micro-sized closed channel experimental results showing the effect of channel height and riblets on the top, bottom, or both sides with water flow (adapted from Bixler and Bhushan, 2013b). Drag reduction is presented as Reynolds numbers compared to pressure drops between the inlet and outlet of the channel, where lower pressure drop is desirable. Riblets were evaluated in laminar ($Re < 2300$) through turbulent flow ($Re > 4000$) conditions. Results indicate that riblets on the bottom reduce drag more than when positioned on the top of the channel. Also, 2x channel height reduces drag, presumably due to vortices from the top and bottom moving apart (i.e. neighboring wall effects are negligible). Flat milled channel control sample is shown for comparison. Error bars show ± 1 standard deviation. 116

Figure 38: Apparent contact angle (CA) measurements for laser etched riblet samples; both with and without the nanostructured coating. Shown on the top and bottom are measurements at the solid-air-water (adapted from Bixler and Bhushan, 2013b) and solid-air-oil (adapted from Bixler and Bhushan, 2013a) interfaces, respectively. Error bars show ± 1 standard deviation. 119

Figure 39: Scale conceptual models of turbulent vortices interacting with various riblet geometries (adapted from Bixler and Bhushan, 2013b). Drag reduction is believed to be possible by lifting and pinning the naturally occurring fluid vortices. This results in less shear stress, momentum transfer, and vortices ejection from the viscous sublayer. A minimum riblet height is necessary to lift and pin the vortices. 121

Figure 40: Scale conceptual models of micro-sized closed channel showing turbulent vortices' behaviors with the flat, Shallow sample, one or two sided, and 2x channel height combinations (adapted from Bixler and Bhushan, 2013b). Vortices are assumed to rotate clockwise on a flat plate and counterclockwise on riblets. When considering the two-sided nature of a closed channel, the rotational direction is believed to account for drag increase or reduction. A 1x channel height is believed to allow vortices from the top and bottom to interact and either increase the rotational speed or cancel each other. Cross stream movement occurs when vortices are not properly pinned, for instance as shown with a flat plate. Increasing the channel height to at least 3x vortex diameter is believed to move the top and bottom side vortices apart so that neighboring wall effects are negligible. 123

Figure 41: Riblet thin oil film model (adapted from Bixler and Bhushan, 2013a). Appropriately sized riblets are believed to reduce drag by increasing the slip length b during laminar oil flow. Higher slip translates into lower drag and increased flow rate. 126

Figure 42: Biofouling in the marine environment (adapted from Bixler and Bhushan, 2012b). Images highlight differences between Humpback whales (adapted from

www.southbank.qm.qld.gov.au) and sharks. Even though whales and sharks live in the same environment, barnacle biofouling growth is evident on the whale but not shark skin. Reportedly such antifouling shark skin properties are due to its riblet microtexture, flexion of scales, and a mucous layer. Bottom image illustrates the lotus-effect with a water droplet removing contaminant particles from the lotus leaf..... 135

Figure 43: Shark skin and lotus effect mechanisms. Flow visualization images using smoke from atomized oil burned in air to study the turbulent vortices behavior with and without riblets at two velocities (adapted from Lee and Lee, 2001). Top left image shows the vortices on a flat plate with a relatively large amount of surface contact area, which leads to higher drag. Top right image show the vortices are lifted above the riblet tips, with a relatively small amount of surface contact area, which leads to lower drag. Bottom left image shows the lotus effect with a water droplet on a lotus leaf and bottom right image shows a mercury droplet collecting contaminants on a Taro leaf (adapted from Bhushan et al., 2009b)..... 137

Figure 44: Rice and butterfly wing effect that combines the shark skin and lotus leaf effects (adapted from Bixler and Bhushan, 2013d). Shown are water droplets resting atop their superhydrophobic and low adhesion surfaces. Rice leaves contain longitudinal grooves with a transverse sinusoidal pattern and butterfly wings contain aligned shingle-like scales that provide anisotropic flow. Hierarchical structures consisting of micropapillae superimposed by waxy nanobumps in rice leaves and microgrooves on shingle-like scales in butterfly wings provide superhydrophobicity and low adhesion. This combination of anisotropic flow, superhydrophobicity, and low adhesion leads to improved drag reduction and antifouling..... 140

Figure 45: Rice leaf inspired geometries for low drag, self-cleaning, and antifouling (adapted from Bixler and Bhushan, 2013e). These surfaces reportedly combine anisotropic flow, liquid repellency, and low adhesion characteristics. Pillars in Samples 1-3 are arranged in a hexagonal array in order to maintain consistent gaps to promote antifouling. Anisotropic flow leading to lower drag is provided by the dual height pillar design of Sample 3 and the dual height pillar and rib combination of Sample 4. Samples 1 and 2 serve as the baseline samples for comparison..... 146

Figure 46: Hot embossing procedure using silicon master patterns and PMMA sheets (adapted from Bixler and Bhushan, 2013e). The sandwich assembly consists of the negative silicon master pattern on the bottom, PMMA sheet in the middle, and flat silicon wafer on the top. The PMMA sheet requires a low surface energy coating for proper de-molding. 149

Figure 47: Apparatuses to measure drag via pressure drop in closed channel flow using water, oil, and air (adapted from Bixler and Bhushan, 2013c). The split rectangular channel design allows for samples to be fabricated inside the channel. Interface views are shown highlighting the top and bottom halves that are sandwiched together. Flow is regulated with the elevated container

(water), pumps (water or oil), and laboratory air connected to a rotameter (air). The pressure drop is measured with a manometer connected to both ends of the flow channel. 151

Figure 48: (a) Antifouling bioassay experimental procedure with *E. coli* cells in the laboratory (adapted from Bixler et al., 2013). (b) Apparatus to uniformly contaminate samples and conduct self-cleaning wash experimentation (adapted from Bixler and Bhushan, 2012b). Water droplets at known velocities and flow rates impact the contaminated sample and particle analysis is conducted to quantify efficiency..... 155

Figure 49: Montage of SEM and optical profiler images depicting actual rice leaf, butterfly wing, fish scale, and shark skin morphologies (adapted from Bixler and Bhushan, 2012b). Shown are (a) SEM images at two magnifications and (b) optical profiler images. Arrows indicate the tendencies of fluid flow in transverse and longitudinal directions. 160

Figure 50: Montage of images depicting ambient and aquatic replicas (adapted from Bixler and Bhushan, 2012b, 2013d). Arrows indicate direction of anisotropic water droplet movement. Shown are (a) SEM images of rice leaf, butterfly wing, fish scale, and shark skin surfaces as well as (b) flat, rice leaf, and shark skin replicas coated in superhydrophobic and superoleophobic solutions. 163

Figure 51: Montage of SEM images for Samples 1-4 and Embossed sample 3 (adapted from Bixler and Bhushan, 2013e). Arrows indicate direction of fluid movement for drag and self-cleaning experiments. Shown are images of Samples 1 and 2 with uniform height pillars arranged in the hexagonal array as well as Sample 3 with dual height pillars and Sample 4 with pillars and ribs. 167

Figure 52: Water pressure drop with replica samples in laminar and turbulent flows (adapted from Bixler and Bhushan, 2012b). Shown are the milled channel and flat channel predicted lines as well as results for replicas of ambient and aquatic species, both with and without nanostructured coatings. Higher pressure drop translates into higher drag; therefore lower pressure drop is desirable. Error bars show ± 1 standard deviation, which is hardly visible in the plots. 169

Figure 53: Water pressure drop with rice leaf inspired samples in laminar and turbulent flows (adapted from Bixler and Bhushan, 2013e). Shown are the flat PDMS and flat channel predicted lines as well as results for Samples 1-4 and Embossed sample 3. Higher pressure drop translates into higher drag; therefore lower pressure drop is desirable. Error bars show ± 1 standard deviation, which is hardly visible in the plots..... 171

Figure 54: Oil pressure drop with replica samples in laminar flow (adapted from Bixler and Bhushan, 2013d). Shown are the milled channel and flat channel predicted lines. Samples include the flat control and replicas of ambient and aquatic species, both with and without the

nanostructured superhydrophobic (superoleophilic) and superoleophobic coatings. Higher pressure drop translates into higher drag; therefore lower pressure drop is desirable. Error bars show ± 1 standard deviation, which is hardly visible in the plots..... 173

Figure 55: Oil pressure drop with rice leaf inspired samples in laminar flow (adapted from Bixler and Bhushan, 2013e). Shown are the flat PDMS and flat channel predicted lines as well as results for Samples 1-4 and Embossed sample 3. Higher pressure drop translates into higher drag; therefore lower pressure drop is desirable. Error bars show ± 1 standard deviation, which is hardly visible in the plots. 175

Figure 56: Air pressure drop with replica and rice leaf inspired samples in laminar and turbulent flow (adapted from Bixler and Bhushan, 2013d, 2013e). Shown are the milled channel, flat PDMS, and flat channel predicted lines. Results are presented for replicas of ambient and aquatic species, both with and without the nanostructured coating, Samples 1-4, and Embossed sample 3. Higher pressure drop translates into higher drag; therefore lower pressure drop is desirable. Error bars show ± 1 standard deviation. 177

Figure 57: Nondimensional pressure drop parameter related to Reynolds number (adapted from Bixler and Bhushan, 2013d). Presented are results from water, oil, and air experiments for flat samples using reported data and the mathematical relationship in Eq. 11. This provides flat channel pressure drop estimations based on fluid properties, flow conditions, and channel dimensions. 180

Figure 58: Images of *E. coli* on flat surfaces after the bioassay procedure (adapted from Bixler et al., 2013) and at a higher magnification (adapted from www.universityofcalifornia.edu). 182

Figure 59: Light microscope images of (a) flat PDMS control samples and (b) tabulated results after *E. coli* bioassay experiments (adapted from Bixler et al., 2013). As indicated, *E. coli* covers the majority of the surface after 4 hours in ideal growing conditions. This baseline serves to compare the various Samples 1-4 and Embossed sample 3 when calculating percentage reduced coverage. 183

Figure 60: Light microscope images of rice leaf inspired samples after bioassay experiments using *E. coli* (adapted from Bixler et al., 2013). Presented are images of flat PDMS, Samples 1-4, and Embossed sample 3 with two *E. coli* concentrations and two incubation times. Long and narrow cylindrically shaped objects are the *E. coli*. 184

Figure 61: Anti-biofouling results from with rice leaf inspired samples after *E. coli* bioassay experiments (adapted from Bixler et al., 2013). Results are presented for flat PDMS, Samples 1-4, and Embossed sample 3. The percentage reduced coverage is calculated from the flat PDMS

control samples. It is believed that antifouling efficiency improves with high CA and low CAH. Error bars show ± 1 standard deviation.	186
Figure 62: Scanning electron microscope (SEM) images of silicon carbide (SiC) contamination particles on rice leaf and shark skin replicas before anti-inorganic fouling self-cleaning wash experimentation (adapted from Bixler and Bhushan, 2012b).	187
Figure 63: Anti-inorganic self-cleaning results from particle wash experiments (adapted from Bixler and Bhushan, 2013d, 2013e). (a) Results are presented for flat urethane and replica samples as well as select samples coated in superhydrophobic and superoleophobic coatings. (b) Results are presented for replica rice leaf, flat PDMS, and rice leaf inspired samples. Self-cleaning efficiency improves with high CA and low CAH. Error bars show ± 1 standard deviation.....	188
Figure 64: Water droplet images indicating that actual rice leaves and butterfly wings are superhydrophobic, whereas fish scales and shark skin are hydrophilic (adapted from Bixler and Bhushan, 2012b).	193
Figure 65: Wettability results with water and oil droplets (both in air and underwater) using actual, replica, and rice leaf inspired samples (adapted from Bixler and Bhushan, 2012b, 2013a, 2013d, 2013e). Shown are values for apparent CA for (a) actual, replica, and coated samples and (b) rice leaf inspired samples. Also shown are values for CAH (c) actual, replica, and coated samples and (d) rice leaf inspired samples. Self-cleaning efficiency improves with high CA and low CAH. Error bars show ± 1 standard deviation.	194
Figure 66: Water droplet control conceptual models of rice leaves, butterfly wings, fish scales, and shark skin (adapted from Bixler and Bhushan, 2012b, 2013d, 2013e). Each example contains mechanisms that are believed to promote low drag, self-cleaning, and antifouling. Arrows indicate the tendencies of fluid flow in transverse and longitudinal directions.	201
Figure 67: Drag reducing mechanisms with rice leaf inspired samples (adapted from Bixler and Bhushan, 2013d, 2013e). Velocity profiles show that slip length (b) is believed to increase with the rice leaf inspired surfaces. This leads to lower drag, increased flow rate, and improved antifouling. Sample 3 is shown based on the rice and butterfly wing effect with dual height pillars to promote anisotropic flow. It is believed that drag reduction leading to self-cleaning may be achieved by either superhydrophobic/oleophobic or superoleophilic (thin film effect) surfaces.	204
Figure 68: Anti-inorganic fouling mechanisms with rice leaf inspired samples (adapted from Bixler and Bhushan, 2012b, 2013d, 2013e). Model shown utilizes uniformly spaced micro-sized single height pillars in a hexagonal array. Inorganic fouling may be washed away in fluid flow via self-cleaning when coupled with high CA and low CAH.	205

Figure 69: Anti-biofouling mechanisms with rice leaf inspired samples (adapted from Bixler et al., 2013). Shown are conceptual models based on anti-biofouling experiments using *E. coli* with low and high concentrations and short and long incubation times. Microorganisms prefer to cluster in groups and around the base of pillars. Microstructured discontinuities and sharp edges are believed to discourage *E. coli* colonization – where they may expire in the process of searching for an ideal landing site. Similar anti-biofouling mechanisms are expected with microorganisms of various shapes and sizes..... 207

CHAPTER 1: Introduction

Optimized designs to conserve precious resources are key attributes found throughout living nature – therefore researchers are constantly seeking nature for inspiration. Various flora and fauna have been studied with much attention given to nature’s structures, materials, and surfaces. Copying nature’s designs is called biomimicry, or biological mimicking, but often engineers are simply inspired by nature to create bioinspired solutions. Nature efficiently uses resources and incorporates novel methods to solve problems. Shown in Figure 1 are various examples in nature that have led to bioinspired designs. These include wall-climbing robots inspired by Gecko feet, low drag and antifouling surfaces inspired by shark skin, high strength rope inspired by spider webs, flying machines inspired by birds, anti-reflective surfaces inspired by moth eyes, and “self-cleaning” windows inspired by the superhydrophobic lotus leaf (*Nelumbo nucifera*) (Collins and Brebbia, 2004; Reis and Weiner, 2004; Bhushan, 2009, 2010; Bhushan et al., 2009b; Allen, 2010; Armstrong et al., 2010; Bar-Cohen, 2011). Furthermore, unlocking the secrets behind these examples and many more has lead researchers to study the Golden Ratio and Fibonacci numbers – which describe unique patterns found throughout the universe (Vajda, 1989; Livio, 2002; Posamentier and Lehmann, 2007).

Montage of living nature examples inspiring field of biomimetics

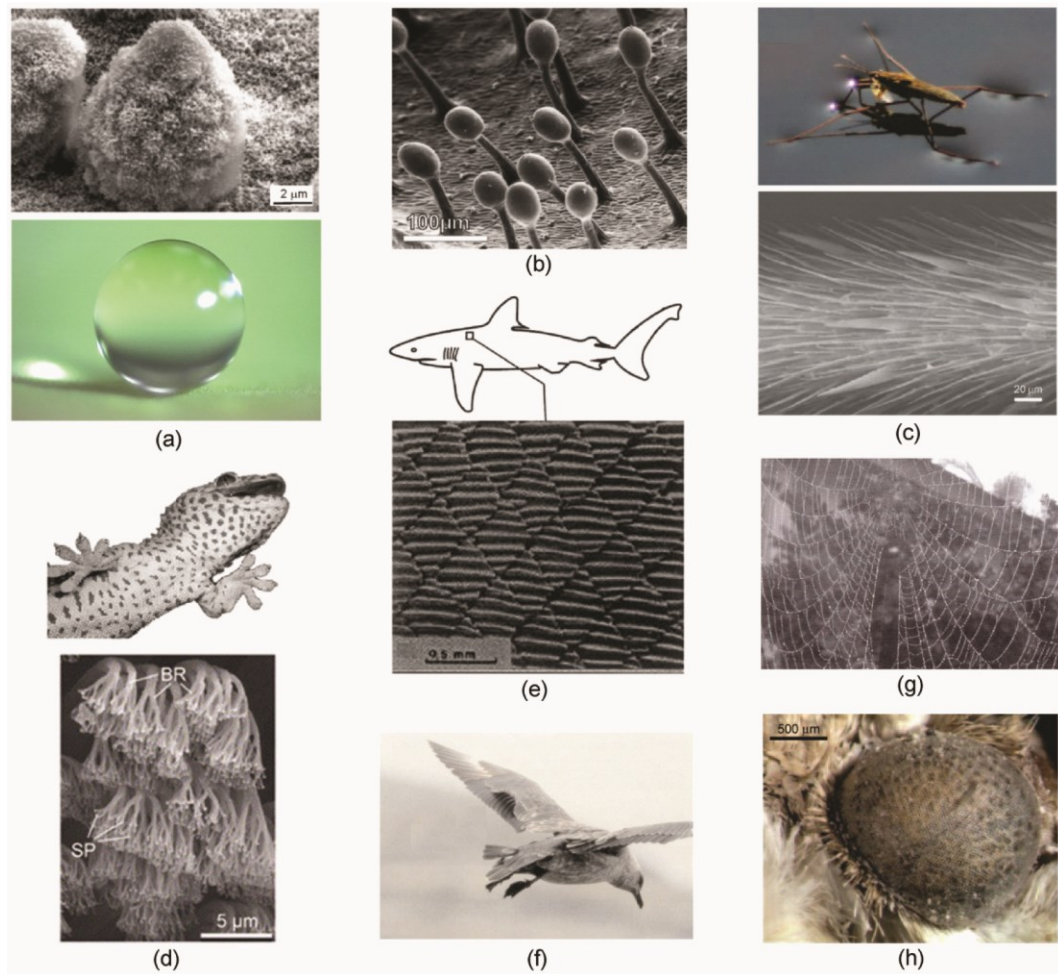


Figure 1: Montage of examples from living nature that have inspired researchers seeking new bioinspired products (adapted from Bhushan, 2009). Shown are (a) water droplet on a self-cleaning lotus leaf and its micropapillae, (b) glands of carnivore plant that trap insects, (c) water strider walking on water and its leg structures, (d) Gecko feet spatula with reversible adhesion, (e) riblet covered low drag and antifouling shark skin, (f) bird wing structure and orientation during landing approach, (g) spider webs made of silk stands, and (h) anti-reflective moth eyes.

The Golden Ratio is considered ideal from functionality/aesthetics standpoint and is defined as $\frac{height}{width} \approx 1.618$ where the values *height* and *width* are non-dimensional lengths of a rectangle. A rectangle produced using the Golden Ratio is called the Golden Rectangle, and for example describes the shape of the Milky Way galaxy. Famous artists have included the Golden Ratio in their own works, such as Leonardo da Vinci's "Mona Lisa" as shown in Figure 2. Furthermore, Fibonacci numbers and the Fibonacci spiral describe geometries of various structures found in nature. For example, this includes the number and sequence of patterns on pineapples and sunflower heads as well as the number of petals on flowers. The Fibonacci numbers are described with the mathematical expression $F_n = F_{n-1} + F_{n-2}$ starting with $F_0 = 0$ and $F_1 = 1$ that provides the sequence of values 0, 1, 1, 2, 3, 5, 8, 13, 21, 34, ... and so on (Vajda, 1989; Posamentier and Lehmann, 2007).

1.1. Fluid drag and antifouling overview

Two common engineering challenges plaguing industry but solved in living nature are fluid drag reduction (Batchelor, 1970; Blevins, 1984; Davies, 2002; White, 2006; Brostow, 2008) and antifouling (Melo et al., 1988; Fingerman et al., 1999; Walker et al., 2000; Railkin, 2004; Bhushan et al., 2009a, 2009b; Hellio and Yebra, 2009; Bhushan and Jung, 2011; Bhushan, 2012; Bixler and Bhushan, 2012a). Drag is the resistant force against an object moving through the fluid, and is generally higher in turbulent versus laminar fluid flow (Kline et al., 1967). Biofouling is the accumulation of undesired

Examples of Golden Ratio ($h/w = 1.618$), Fibonacci numbers, and Fibonacci or Golden spirals found in nature and art

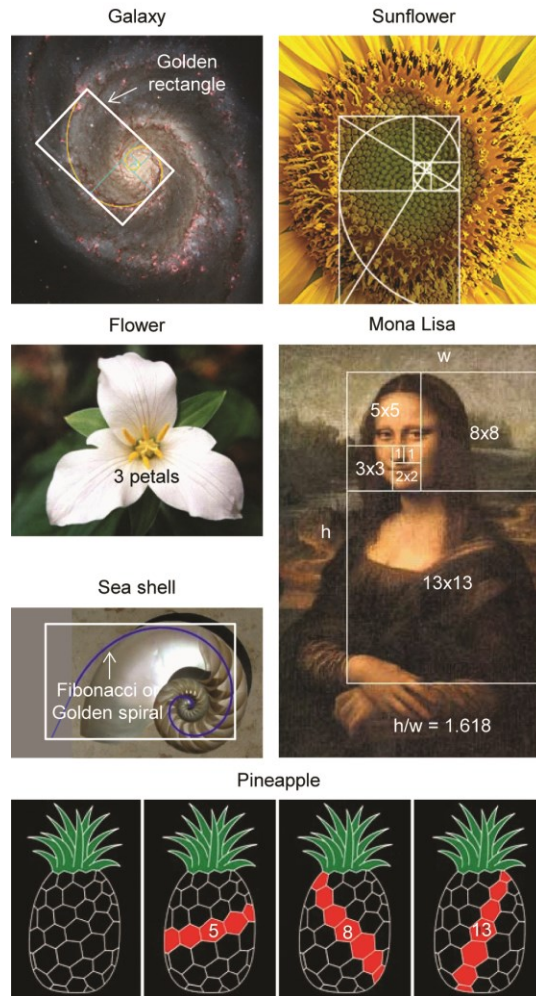


Figure 2: Montage of images showing examples of the Golden Ratio, Golden Rectangle, and Fibonacci numbers found in nature and art (adapted from Bixler and Bhushan, 2013d). Examples include galaxies, sunflower heads, flower petals, sea shells, Mona Lisa painting, and pineapple fruit (from top left to bottom right). The Golden Rectangle and Fibonacci or Golden spiral are superimposed on select images. Such proportions and patterns are considered aesthetically pleasing and are believed to enhance performance of systems found throughout nature.

organisms on hard surfaces, with biofilms created by microorganisms and macroscale biofouling (macrofouling) created by organisms (for instance, barnacles). Inorganic fouling includes deposits of dirt, corrosion, crystals, suspended particles, oil, and ice. The type and extent of fouling depends on the environment, inorganic deposits, and organisms present (Bixler and Bhushan, 2012a). The term fouling describes both biofouling and inorganic fouling, where antifouling is the prevention of any biological or inorganic fouling. Conversely, self-cleaning is the removal of fouling already deposited on a surface.

Numerous engineering applications can benefit from low drag and antifouling surfaces. Examples include airplanes (Viswanath, 2002), wind turbines (Sareen et al., 2011), ship hulls (Anon, 1952), implanted medical devices (Shirtliff and Leid, 2009), heat exchangers (Cunningham et al., 2008), touch screen electronic devices (Bixler and Bhushan, 2013a), and pipelines (Walker et al., 2000). Low drag surfaces often equate to less fouling by washing away any contaminants present, which often leads to energy conservation (Bhushan et al., 2009b; Bhushan and Jung, 2011; Bixler and Bhushan, 2012a, 2012b). Furthermore, anti-ice fouling may be accomplished with water repellent surfaces, which is beneficial for airplane wings, helicopter blades, oil platforms, power lines, locks and dams, and wind turbines (Cao et al., 2009; Meuler et al., 2010).

In addition to lowering drag, antifouling surfaces have various functions in medical, marine, and industrial applications. For instance in the medical industry, such surfaces can reduce the spread of infectious diseases by limiting biofilms. Medical biofouling occurs in areas such as prosthetic implants, biosensors, catheters, dental

implants, and medical equipment. Problems include implant rejection, malfunction of biosensors, and spread of infectious diseases (Vo-Dinh, 2007; Schulz et al., 2009; Shirtliff and Leid, 2009; Chan and Wong, 2010). Biofouling is commonly associated with marine environments where noticeable aquatic growth appears on ships and underwater structures. This increases ship hull drag, corrosion, fuel consumption, and engine stress (Copisarow, 1945; Anon, 1952; Ray, 1959; Melo et al., 1988; Railkin, 2004). Industrial fouling occurs in areas such as power plants, water treatment systems, and food/beverage industries. Problems include pipe blockage, decreased membrane flux, contaminated water, and reduced heat exchanger efficiency (Somerscales and Knudsen, 1981; Walker et al., 2000; Chan and Wong, 2010).

Medical, marine, and industrial fouling often exhibits different characteristics. For instance, medical fouling typically takes the form of biofilms (Stoodley et al., 2002; Vo-Dinh, 2007; Schulz et al., 2009; Shirtliff and Leid, 2009; Chan and Wong, 2010), whereas marine and industrial biofouling typically includes macrofouling (Fingerman et al., 1999; Walker et al., 2000; Railkin, 2004; Hellio and Yebra, 2009) and inorganic fouling (Somerscales and Knudsen, 1981; Bott, 1988a, 1988b; Pritchard, 1988; Melo et al., 1988). Shown in Figure 3 is a biofilm on a pacemaker wire removed from a patient and barnacles on a flat plate representing macrofouling on underwater structures. Inorganic fouling examples are shown with dirt deposits on stucco and crystallization fouling on a heat exchanger. Antifouling may also be accomplished through self-cleaning, where undesired liquids or contaminants are removed from a surface in a fluid flow.

Biological and inorganic fouling examples

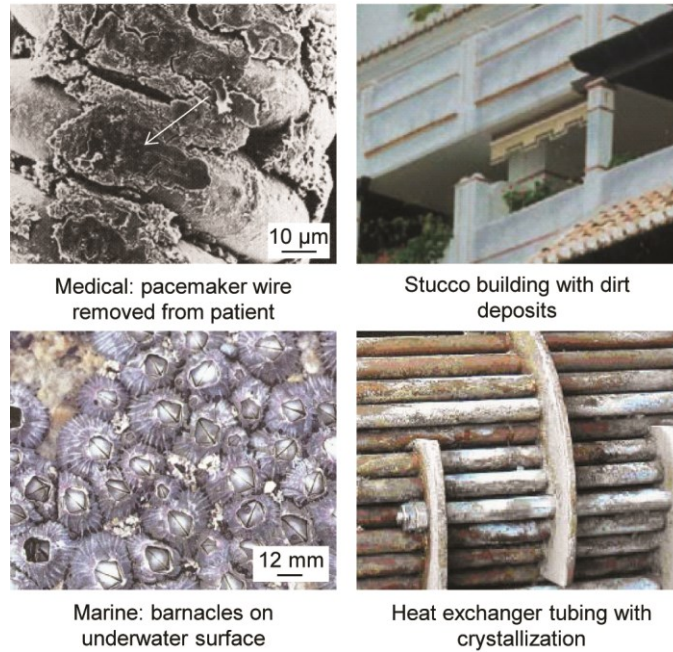


Figure 3: Biological and inorganic fouling examples. Biofouling examples are shown with a biofilm covered pacemaker wire (adapted from Marrie and Costerton, 1984) and barnacles on a flat underwater plate (adapted from Edgar, 1997). Inorganic fouling examples are shown with dirt deposits on a stucco building exterior (photo courtesy of www.stocorp.com) and crystallization on the outside of heat exchanger tubing (photo courtesy of H&C Heat Transfer Solutions, Inc).

Multiple coatings and anti-fouling techniques have been reported for engineering applications. In the medical industry these often include hydrophobic polymers with antimicrobial properties (LoVetri et al., 2010; Bixler and Bhushan, 2012a). Example applications include catheters, endotracheal tubes (Dror et al., 2009), and orthopedic hip implants (Shirtliff and Leid, 2009). In the marine environment, common tributyltin

coatings were banned by the International Maritime Organization, adding urgency to the development of more environmentally friendly antifouling and foul-release coatings. As a result, researchers have been exploring environmentally friendly methods such as new nontoxic antifouling paints and foul-release coatings (Callow, 1999; Fingerman et al., 1999; Railkin, 2004; Hellio and Yebra, 2009). As for industrial antifouling, applications such as food processing require different approaches. For example, antifouling success is reported with titanium dioxide nanoparticles on reverse osmosis membranes (Kim et al., 2003) and antimicrobial silver nanoparticles on ultrafiltration membranes (Zodrow et al., 2009). Even though fouling prevention is the goal, often fouling must be cleaned using various methods such as scrubbing, chemical disinfection, high-pressure water spray, and membrane back washing (Cologer, 1984; Walker et al., 2000; Sharma et al., 2004; Hellio and Yebra, 2009; Chan and Wong, 2010; Bixler and Bhushan, 2012a).

1.2. Bioinspired low drag and antifouling

Many flora and fauna flourish due to their low drag and antifouling properties, with commonly studied examples including shark skin and lotus leaves. The skin of fast swimming sharks is both low drag and antifouling; and lotus leaves are antifouling via self-cleaning (Barthlott and Neinhuis, 1997; Kesel and Liedert, 2007; Ralston and Swain, 2009; Bhushan, 2012). Sharks remain clean due to their microstructured riblets, flexion of dermal denticles, and a mucous layer (Bechert et al., 1985, 1997a, 2000b; Collins and Brebbia, 2004; Dean and Bhushan, 2010; Bixler and Bhushan, 2013c). Lower drag is necessary for shark survival, since it allows sharks to swim faster in order to catch prey (Reif, 1985; Bechert et al., 1997a, 2000b; Bixler and Bhushan, 2013c). Increased fluid

flow velocity at the skin reduces microorganism settlement time and promotes antifouling (Kesel and Liedert, 2007; Ralston and Swain, 2009; Dean and Bhushan, 2010), along with riblet spacing smaller than microorganisms (Schumacher et al., 2007a, 2007b; Scardino, 2009; Brennan et al., 2010; Bhushan, 2012). Conversely, lotus leaf surfaces are comprised of hierarchical micro papillae with a waxy nanostructure that repel water droplets and provide self-cleaning (via superhydrophobicity and low adhesion) by removing unwanted contaminants (Barthlott and Neinhuis, 1997; Bhushan et al., 2009a).

Living nature has inspired the development of drag reducing and antifouling products. An ideal low drag and antifouling surface would withstand harsh environments, adhere to a variety of substrates, and be relatively inexpensive. Low drag surfaces have been the subject of much experimentation using shark skin riblet-inspired microtextured surfaces. Previous experiments have utilized a variety of riblet geometries, configurations, materials, fluids, and flow conditions (laminar and turbulent flow). Geometries include blade, sawtooth, scalloped, and bullnose geometries with continuous and segmented (aligned and staggered) configurations in water, oil, and air (Bechert et al., 1997a; Jung and Bhushan, 2010; Bixler and Bhushan, 2012b; Bixler and Bhushan, 2013b). Larger scale drag reducing efforts have included the experimental 3M Corp. (Minneapolis, MN) vinyl riblets (Marentic and Morris, 1992) as well as the commercially available Speedo brand FastSkin[®] fabric racing swimsuit. Such riblet technology has captured the attention of the National Aeronautics and Space Administration (NASA), U.S. Department of Energy, U.S. Navy, Airbus, Boeing, as well as Olympic competitors. In the 1984 Los Angeles Olympics and 1987 America's Cup, 3M riblets were applied to

U.S. boats, which presumably helped to secure victories. The 2008 Beijing Olympics witnessed the benefit of the Speedo FastSkin[®] swimsuit when American Michael Phelps set Olympic records and won several gold medals (Bixler and Bhushan, 2013c). Reportedly, the swimsuits reduce drag up to 4% for men and 3% for women (Krieger, 2004).

In addition to drag reducing products, antifouling product examples include the microorganism repellent shark skin inspired Sharklet[™] microtextured pattern (Carman et al., 2006; Schumacher et al., 2007a; Scardino, 2009; Brennan et al., 2010). Furthermore, lotus leaf inspired self-cleaning products effective against inorganic fouling include water repellent hydrophobic paints, roof tiles, and fabrics as well as hydrophilic windows and membranes. Examples include Lotusan[®] paints by Sto (www.stocorp.com), Erlus Lotus[®] roof tiles (www.erlus.com), NanoSphere[®] fabrics by Schoeller Technologies (www.schoeller-textiles.com), and SunClean[®] glass by PPG Industries (www.ppg.com). Self-cleaning hydrophilic SunClean[®] glass with titanium dioxide uses the sheeting action of water to efficiently gather and remove contaminants (www.ppg.com) (Bixler and Bhushan, 2012b).

1.3. The rice and butterfly wing effect

Inspired by shark skin and lotus leaves, Bixler and Bhushan (2012b, 2013a, 2013d, 2013e) found rice leaves and butterfly wings combine the shark skin and lotus effects. It is reported that sinusoidal grooves in rice leaves and aligned shingle-like scales in butterfly wings provide the anisotropic flow. Hierarchical structures consisting of micropapillae superimposed by waxy nanobumps in rice leaves and microgrooves on top

of shingle like scales in butterfly wings provide the superhydrophobicity and low adhesion. Various studies suggest that this combination of anisotropic flow, superhydrophobicity, and low adhesion leads to improved drag reduction and antifouling (Bixler and Bhushan, 2012b, 2013d, 2013e; Bixler et al., 2013).

Both shark skin (Carman et al., 2006; Schumacher et al., 2007a, 2007b; Bixler and Bhushan, 2013b, 2013c) and rice leaf inspired (Bixler and Bhushan, 2012b, 2013a, 2013d, 2013e; Bixler et al., 2013) antifouling topographical features include micro-sized pillars, ribs, and a combination thereof using various dimensions. Surfaces with appropriately sized topographies prevent colonization by various microorganisms including *Ulva* spores, *Balanus Amphitrite* cyprids (Carman et al., 2006; Schumacher et al., 2007a, 2007b), and *E. coli* (*Escherichia coli*) (Bixler et al., 2013). Up to 85% spore settlement reduction is reported with micro-sized ribs when compared to flat control samples (Carman et al., 2006; Schumacher et al., 2007b) (*E. coli* antifouling is reported in detail later). Antifouling is attributed to the micro-sized feature spacing that is slightly smaller than the microorganisms under investigation (Carman et al., 2006; Schumacher et al., 2007a, 2007b) as well as presence of sharp edged discontinuities (Bixler et al., 2013). The so-called engineered antifouling micro-topographies are designed to target specific microorganisms based on their shape and size (Schumacher et al., 2007b).

Fabricating inexpensive, drag reducing, and antifouling surfaces may be possible with hot embossing patterns onto adhesive backed flexible films. Such films could be applied to flat or curved substrates such as pipeline interiors, airplane wings, and ship hulls. Fabricating embossed surfaces has been the subject of several studies (Lin et al.,

1996, 1998; Bixler and Bhushan, 2013e) and techniques depend on the type of master mold and molding materials. Commonly the master mold is silicon (Lin et al., 1996; Velten et al., 2010) and the molding material is polymethylmethacrylate (PMMA) (Lin et al., 1996; Kricka et al., 2002; Mappes et al., 2008; Amaya et al., 2009; Mathur et al., 2009; Bixler and Bhushan, 2013e). Embossing can be used to fabricate various structures including, for example, microfluidic flow channels (Mizuno et al., 2004; Narasimhan and Papautsky, 2004; Mathur et al., 2009), plastic microchips (Kricka et al., 2002), and moveable microstructures (Amaya et al., 2009). Such components are reported to yield sub-micron scale features (Roos et al., 2001; Mappes et al., 2008).

1.4. Scope of the thesis

In this thesis, I first present shark skin riblet research that has been conducted in both open channel (external) and closed channel (internal) flow experiments. I fabricated new samples using laser etching and soft lithography techniques. Experimental parameters include riblet geometry, continuous and segmented configurations, fluid velocity (laminar and turbulent flow), fluid viscosity (water, oil, and air), closed channel height dimensions, wettability, and scalability. Results are discussed and new conceptual models are shown suggesting the effect of viscosity, coatings, and the interaction between vortices and riblet surfaces. Results provide design guidance when developing novel low drag and antifouling surfaces for applications in the medical, marine, and industrial fields.

Also presented in this thesis are results from my fluid drag and antifouling research using rice and butterfly wing effect samples. Reported are results from

experiments investigating actual and replica rice leaves, butterfly wings, and fish scales as well as rice leaf inspired samples – combined with various coatings that provide superhydrophobicity, superoleophilicity, and superoleophobicity. I fabricated samples via photolithography, soft lithography, and hot embossing techniques. A series of investigations highlighting the rice leaf inspired samples are presented describing drag reduction and antifouling effectiveness. Experimental parameters include sample morphology, fluid velocity (laminar and turbulent flow), fluid viscosity (water, oil, and air), and wettability. New antifouling experiments are reported from my anti-biofouling and anti-inorganic fouling experiments using bioassay and self-cleaning techniques, respectively. My new rice leaf inspired embossed sheets are evaluated and their characteristics compared to samples fabricated by traditional methods, in order to demonstrate the potential of scaled up production. Results are discussed and new conceptual models are provided suggesting the effectiveness of rice and butterfly wing effect surfaces on drag reduction and antifouling.

CHAPTER 2: Biofouling: Lessons from Nature

2.1. Introduction

Biofouling morphology is characterized by the thickness, density, structure, composition, bioadhesive strength, and weight of fouling organisms. Since biofouling ranges from microorganisms to macroorganisms, a variety of measurement techniques are necessary to record the properties. Such properties are measured with weight scales as well as light, transmission electron, scanning electron, atomic force, and fluorescence microscopy techniques (Marrie and Costerton, 1984; Keevil et al., 1999; Flemming et al., 2000; Hellio and Yebra, 2009; Chan and Wong, 2010; Trinidad et al., 2010).

For humans, biofouling poses significant health risks and financial losses in the medical, marine, and industrial fields. Medical biofouling occurs in areas such as prosthetic implants, biosensors, catheters, dental implants, and medical equipment. Problems include implant rejection, malfunction of biosensors, and spread of infectious diseases (Vo-Dinh, 2007; Schulz et al., 2009; Shirtliff and Leid, 2009; Chan and Wong, 2010). Biofouling is commonly associated with marine environments where noticeable aquatic growth appears on ships and underwater structures. This increases ship hull drag, corrosion, fuel consumption, and engine stress (Copisarow, 1945; Anon, 1952; Ray, 1959; Melo et al., 1988; Railkin, 2004). Industrial fouling occurs in areas such as power plants, water treatment systems, and food/beverage industries. Problems include pipe

blockage, decreased membrane flux, contaminated water, and reduced heat exchanger efficiency (Somerscales and Knudsen, 1981; Walker et al., 2000; Chan and Wong, 2010).

Looking to nature for antifouling lessons reveals several examples of both physical and chemical control methods, and a combination thereof (Bhushan, 2009; Bar-Cohen, 2011). Physical controls include low drag, low adhesion, wettability, microtexture, grooming, sloughing, and various miscellaneous behaviors; and chemical controls include various secretions. Fouling is both prevented and removed with the aforementioned physical and chemical controls. In the ambient environment plants and insects employ these controls; and in the marine environment plants, corals, and fish employ them. Specific antifouling examples range from the lotus leaf (Barthlott and Neinhuis, 1997; Neinhuis and Barthlott, 1997; Nosonovsky and Bhushan, 2008, 2009; Bhushan and Jung, 2011) to shark skin (Carman et al., 2006; Genzer and Efimenko, 2006; Kesel and Liedert, 2007; Ralston and Swain, 2009; Dean and Bhushan, 2010).

Controlling biofouling is accomplished through a variety of ways in medical, marine, and industrial applications. Common controls exist, such as low drag and low adhesion surfaces that reduce biofouling. In fluid flow, a low drag surface will promote removal (washing away) of microorganisms, whilst low adhesion surfaces prevent microorganism colonization through reduced adhesive strength. Furthermore, improving biocompatibility will reduce medical biofouling, since foulers will not target the implanted device (Lee et al., 2005; Bhushan et al., 2006a, b). Figure 4 shows an overview of this paper focusing on antifouling lessons from nature. To understand the importance of fouling, a review of fields susceptible to biofouling is included, with

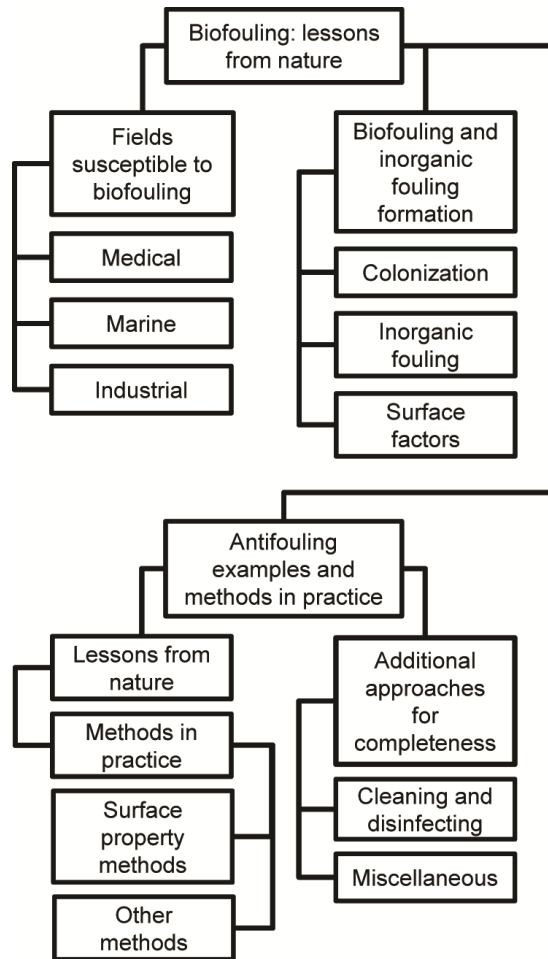


Figure 4: Overview of fields susceptible to biofouling, description of the fouling formation process, and current antifouling strategies (adapted from Bixler and Bhushan, 2012a).

medical, marine, and industrial examples. The relevant types of fouling are addressed with a description of biofouling and inorganic fouling. Biomimetics addresses the importance of surface textures and chemistries that influence the antifouling properties. A description of flora and fauna that exhibit antifouling properties are mentioned along with the mechanisms at work. Current antifouling methods in practice are described including surface textures, coatings, cleaning methods, and experimental techniques. An outlook on new research of bio-inspired antifouling surfaces is also presented.

2.2. Fields susceptible to biofouling

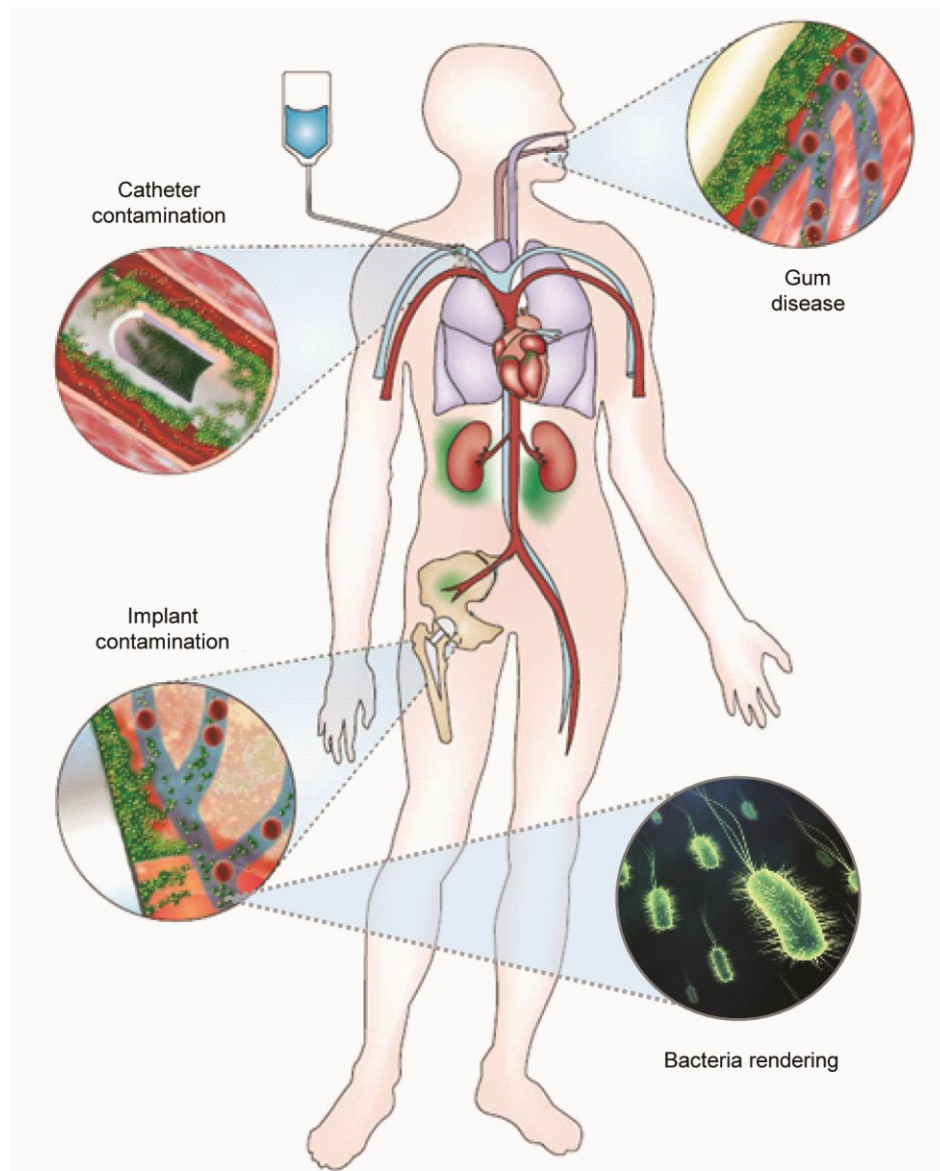
Fouling is prevalent in medical, marine, and industrial fields causing significant problems related to health risks, environmental impact, and financial losses (Walker et al., 2000; Railkin, 2004; Vo-Dinh, 2007; Hellio and Yebra, 2009). Table 1 outlines many examples in susceptible fields. Specific examples of biofouling hazards are described along with the need for improved control methods.

2.2.1. Medical

Areas susceptible to biofilm infection are shown in Figure 5, highlighting catheter contamination, implant contamination, and gum disease (Hall-Stoodley et al., 2004; Vo-Dinh, 2007; Schulz et al., 2009; Shirtliff and Leid, 2009; Chan and Wong, 2010). As far as biofouling on artificial surfaces is concerned, more than 45% of hospital-contracted infections are traced to biofilm infected medical devices. For instance, catheters are the most commonly used medical device and second highest cause of infection (Chan and Wong, 2010; LoVetri et al., 2010). Estimates show that 10% of

Table 1: Fields susceptible to biofouling including common examples.

<i>Type</i>	<i>Problems</i>	<i>Source</i>
Medical		
Orthopedic implant	Removal due to infection	Smeltzer et al. (2009)
Respirator	Ventilator associate pneumonia	Thomas et al. (2009)
Contact lens	Eye infection	Banerjee et al. (2011)
Catheter	Urinary tract infections	O'May et al. (2009)
Hemodialysis	Infectious break-outs	Pasmore and Marion
Teeth/dental implant	Periodontal disease, gingivitis	Armellini et al. (2009)
Biosensor	Failure from fibrous encapsulation	Yeh et al. (2007)
Marine		
Ship hull	Increased fuel consumption	Dobretsov (2009)
Ship engine	Increased stress from extra drag	Jones (2009)
Marine platform	Increased marine structure	Jones (2009)
Metal	Increased biocorrosion	Lebret et al. (2009)
Industrial		
Membrane	Reduced flux	Pangarkar et al. (2011)
Heat exchanger	Reduced convection efficiency	Lebret et al. (2009)
Fluid flow	Frictional loss in pipes	Nebot et al. (2010)
Drinking water	Pathogens in potable water	Lebret et al. (2009)
Fuel	Diesel fuel contamination	Morton (2000)
Food, paper, and	Food spoilage and worker health	Jass and Walker (2000)
Metal cutting fluid	Filter blockage and worker health	Morton (2000)



Infectious biofilms possible entrances

Figure 5: Schematic highlighting areas of the body susceptible to infectious biofilms (adapted from P. Dirckx Center for Biofilm Engineering).

hospital patients will contract an infection from a clinical implant such as a urethral catheter, tracheal tube, or vascular catheter with more than 5000 annual deaths due to infections. Research shows that 9% of 9000 patients using a ventilator in 1998 acquired ventilator associated pneumonia which increased the average hospital stay costs by \$40,000 (Millar, 2005; Shirtliff and Leid, 2009; Chan and Wong, 2010), making ventilator associated pneumonia the most expensive nosocomial infection in United States (U.S.) hospitals (Thomas et al., 2009). Furthermore, approximately 8% of orthopedic implants develop complications due to biofilm or biocompatibility issues and often require surgery (Smeltzer et al., 2009).

Biofouling and biocompatibility are generally detrimental and often lead to medical device failure. Biocompatibility describes the compatibility of the device to the body, since foreign objects are naturally rejected (for example causing fibrous encapsulation). Biofouling describes the adhesion of proteins or microorganisms to the device (biofilm) and begins soon after implantation. In certain applications, however, the fibrous encapsulation is not harmful and can even be beneficial. For instance, encapsulation of devices such as pacemaker power wires help prevent unwanted movement within the body. Conversely, undesired encapsulation of devices such as biosensors and orthopedics may cause sensor malfunction and prevent bone growth, respectively (Saliterman, 2006; Vo-Dinh, 2007; Schulz et al., 2009).

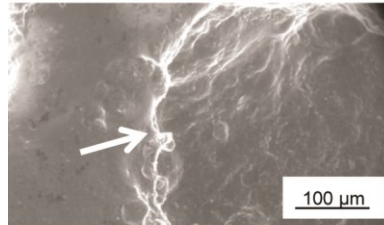
Treating biofilms on infected medical devices often requires surgical replacement, which increases the risk of mortality and antibody-resistance. Infections caused by pathogenic *Staphylococcus aureus* (MRSA) bacteria are the worst due to its methicillin

resistance (Vo-Dinh, 2007; Shirtliff and Leid, 2009). Antibiotics are usually ineffective against biofilms, which leads to difficulties treating biofilm-induced medical conditions such as cystic fibrosis (Monroe, 2007). Furthermore, protein fouling on biological implants reduces efficiency and may lead to thrombosis (blood clots) (Banerjee et al., 2011).

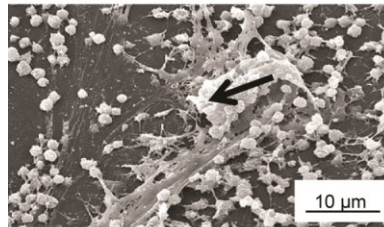
Biofilms contain a diverse variety of microorganisms such as gram-positive or gram-negative bacteria. Gram-positive include *E. faecalis*, *S. aureus*, *S. epidermidis*, and *S. viridans* and the gram-negative include *E. coli*, *K. pneumoniae*, *P. mirabilis*, and *P. aeruginosa*. Prevalent infection-causing microorganisms include *P. aeruginosa*, *E. coli*, *S. aureus*, and *S. epidermidis* (Donlan, 2001; Saliterman, 2006; Vo-Dinh, 2007; Schulz et al., 2009).

Infectious biofilms in medical equipment such as hemodialysis machines can form even with advanced purification systems. This microbial presence is especially detrimental to sick patients, and cleaning, descaling, and disinfecting are difficult (Pasmore and Marion, 2009). Examples of medical biofilms are shown in Figure 6 with scanning electron microscope (SEM) images of a titanium ventilation tube, needleless connector, and pacemaker wire. The ventilation tube was removed from a patient after three months due to a foul smelling odor (Trinidad *et al.*, 2010). The needleless connector biofilm, found on the inner surface of the connector, increases risk of bloodstream infections (Donlan, 2001). The pacemaker wire was removed from a patient who suffered from *S. aureus* bacteremia (presence of bacteria in the blood) (Marrie et al., 1982; Marrie and Costerton, 1984).

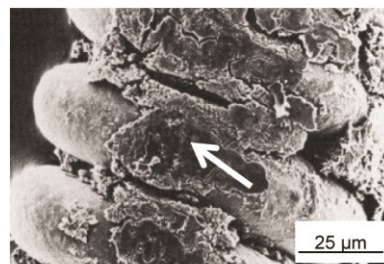
Medical biofouling SEM examples



Ventilation tube removed from patient



Needleless connector



Pacemaker wire removed from patient

Figure 6: Medical device biofilm examples with ventilation tube (adapted from Trinidad et al, 2010), needleless connector (adapted from Janice Carr), and pacemaker wire (adapted from Marrie et al., 1982). Such biofilms may lead to infections that require device removal since antibodies are often ineffective.

Medical devices affected by biofouling can be classified into two major categories, including permanent and temporary devices. In general, a permanent device is implanted and intended for “long-term” (non-disposable) use, whereas a temporary device is intended for “short-term” (disposable) use.

2.2.1.1. Permanent implants

Permanent implant devices include biosensors, heart valves, bone plates, fasteners, orthopedic implants, dental implants, pacemakers, drug delivery devices, and ventilation tubes (Millar, 2005; Vo-Dinh, 2007; Schulz *et al.*, 2009). Immediately after surgery, the permanent implant is flooded with blood followed by adsorption of proteins onto the surface (Vadgama, 2005; Reis and Weiner, 2004). Such adsorption on a biosensor may lead to sensor “blindness” (Yeh *et al.*, 2007), reduced lifespan, and increased power consumption. Furthermore, biofouling causes problems with sensor stability and calibration (Newman and Turner, 2005). Mechanical heart valve biofilms can lead to prosthetic valve endocarditis (tissue inflammation) from *S. epidermidis* and *S. aureus*. During implant surgery such microorganisms can enter the bloodstream by the surrounding skin or other devices (Donlan, 2001). Patients suffering severe trauma often require bone plate and fastener implants (osteosynthesis) after a catastrophic injury. These medical implants are susceptible to biofilm formation due to the high concentration of microorganisms such as *S. aureus* in the contaminated wound area, and an overall weakened immune system. When the plates or fasteners become infected by biofilm, they are generally untreatable by antibiotics and require removal to control the infection (Donlan, 2001; Montali, 2006; Khan *et al.*, 2008).

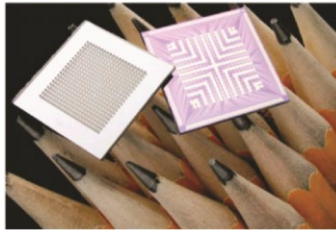
Dental implants are a source of infection, especially when the socket is exposed during surgery. Dental plaque biofilm is a diverse collection of microorganisms in the oral cavity, containing many species of bacteria such as *S. mutans*. Plaque grows on teeth, gums, tongue, and cheeks leading to dental decay and periodontal disease. The microorganisms living in saliva colonize tooth enamel, dental implants, and cementum. Plaque can form inside teeth sockets where microorganisms are protected from cleaning mechanisms such as chewing, saliva, mouth rinses, and brushing. Problems occur when microorganisms are not eliminated by the host defenses (Wilkins, 2005; Parini and Pitt, 2006; Armellini *et al.*, 2009).

2.2.1.2. Temporary implants

Temporary implant devices include biosensors, catheters, drug delivery devices, bone plates, fasteners, ventilation tubes, needleless connectors, and ventilator tubes (Millar, 2005; Vo-Dinh, 2007; Schulz *et al.*, 2009). Perhaps the most common biosensor is the single use blood glucose monitoring device for diabetic patients. Such blood glucose sensors are relatively imprecise, inaccurate, but also inexpensive (Kissinger, 2005). Glucose diffuses from capillaries through the sensor membrane, which is semi-permeable, and acts as the interface between the enzymes and electrode. Failures occur from biocompatibility issues such as membrane biofouling, fibrous encapsulation, electrode passivation, and biodegradation (Newman and Turner, 2005). Membrane biofouling starts upon bodily contact when microorganisms, proteins, and other components adhere to the surface, impeding the sensor's diffusion ability. See Figure 7 example of the OneTouch[®] blood glucose monitoring device and an implantable

Biosensor examples and biofouling

Products examples



MEMS drug delivery device



OneTouch® glucose monitor

Implanted biosensor biofouling problem

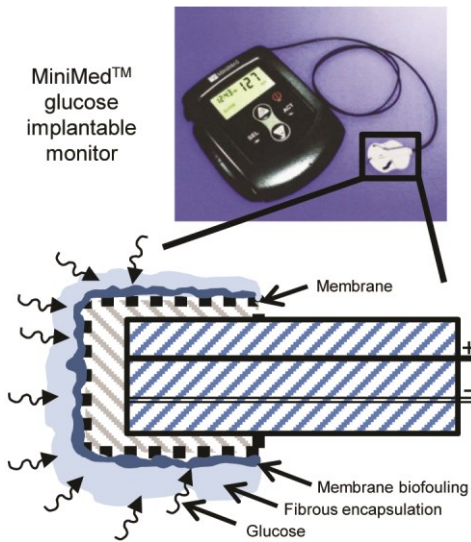


Figure 7: Biosensor product examples and biofouling (adapted from Bixler and Bhushan, 2012a). Schematic of the implantable glucose biosensor probe illustrates biocompatibility and biofouling issues (bottom). MEMS (adapted from Dana Lipp) and glucose monitors (adapted from Newman and Turner, 2005).

biosensor probe with a schematic of biofouling-induced failure points. Membrane biofouling and fibrous encapsulation prevent glucose from contacting the probe for accurate measurements (Wisniewski *et al.*, 2000; Adiga *et al.*, 2008).

Urinary catheter calcification from bacterial colonization may cause bladder stone formation and urinary tract infections (O'May *et al.*, 2009). Urinary catheter biofilms contain *S. epidermidis*, *E. faecalis*, *E. coli*, *P. mirabilis*, *P. aeruginosa*, *K. pneumoniae*, and other gram-negative microorganisms. Central venous catheter biofilms contain *S. epidermidis*, *S. aureus*, *C. albicans*, *P. aeruginosa*, *K. pneumoniae*, and *E. faecalis* that originate from the patient's skin, device, or healthcare worker (Donlan, 2001; Saliterman, 2006; Vo-Dinh, 2007; Schulz *et al.*, 2009).

Pulmonary, transdermal, intravenous, and subcutaneous drug delivery through implanted devices are available for treating conditions such as brain tumors and prostate cancer. A Micro Electromechanical Systems (MEMS) drug delivery device example is shown in Figure 7. Drug delivery devices are divided into passive and active categories, where drugs diffuse or degrade in the body at a constant rate. Micro- and nano-electromechanical devices help where long term treatments with complex dosages are required. Advanced devices gather, use, and communicate biological data to the healthcare worker (Maloney *et al.*, 2005; Saliterman, 2006; Staples *et al.*, 2006; Vo-Dinh, 2007). Such devices often require biosensors, which limit the long-term operation due to biofouling of electrode surfaces or membranes. An ideal implantable drug delivery device is small, resists biofouling (for example by protective reservoirs), allows liquid or solid

drug delivery, and is controllable by healthcare workers (Maloney *et al.*, 2005; Staples *et al.*, 2006).

2.2.2. Marine

Perhaps the most recognized form of biofouling is found in the marine environment. Biofouling colonizes ships, buoys, sonar devices, pontoons, offshore structures, oil installations, platforms, underwater cables, underwater acoustic instruments, seawater cooling systems, and marinas. Issues include increased costs, reduced speed, environmental concerns, corrosion, and safety hazards (Copisarow, 1945; Anon, 1952; Ray, 1959; Melo *et al.*, 1988; Fingerman *et al.*, 1999; Callow and Callow, 2002; Railkin, 2004; Hellio and Yebra, 2009). Areas with the best aeration, such as a ship's waterline, propeller, and rudder blade experience the highest amount of fouling (Lebret *et al.*, 2009). Common marine foulers are green algae *Ulva australis* and brown algae *Ectocarpus* (Callow, 1986). Figure 8 illustrates the areas susceptible to biofouling on a typical petroleum ship and common hard-shelled barnacles (*Tetraclitella purpurescens*) (Edgar, 1997).

Biofouling reduces ship speed due to the extra drag, which increases fuel consumption and engine stress. In 1981 the U.S. Navy consumed 18 million barrels of fuel with 3.3 million attributed to biofouling losses (Railkin, 2004; Jones, 2009). A biofilm 1mm thick can increase ship hull friction by 80%, which translates into a 15% loss in speed (Gordon and Mawatari, 1992). Furthermore, a 5% increase in biofouling increases ship fuel consumption by 17% with a 14% increase in greenhouse gases CO₂, NO_x and SO₂ emissions (Dobretsov, 2009).

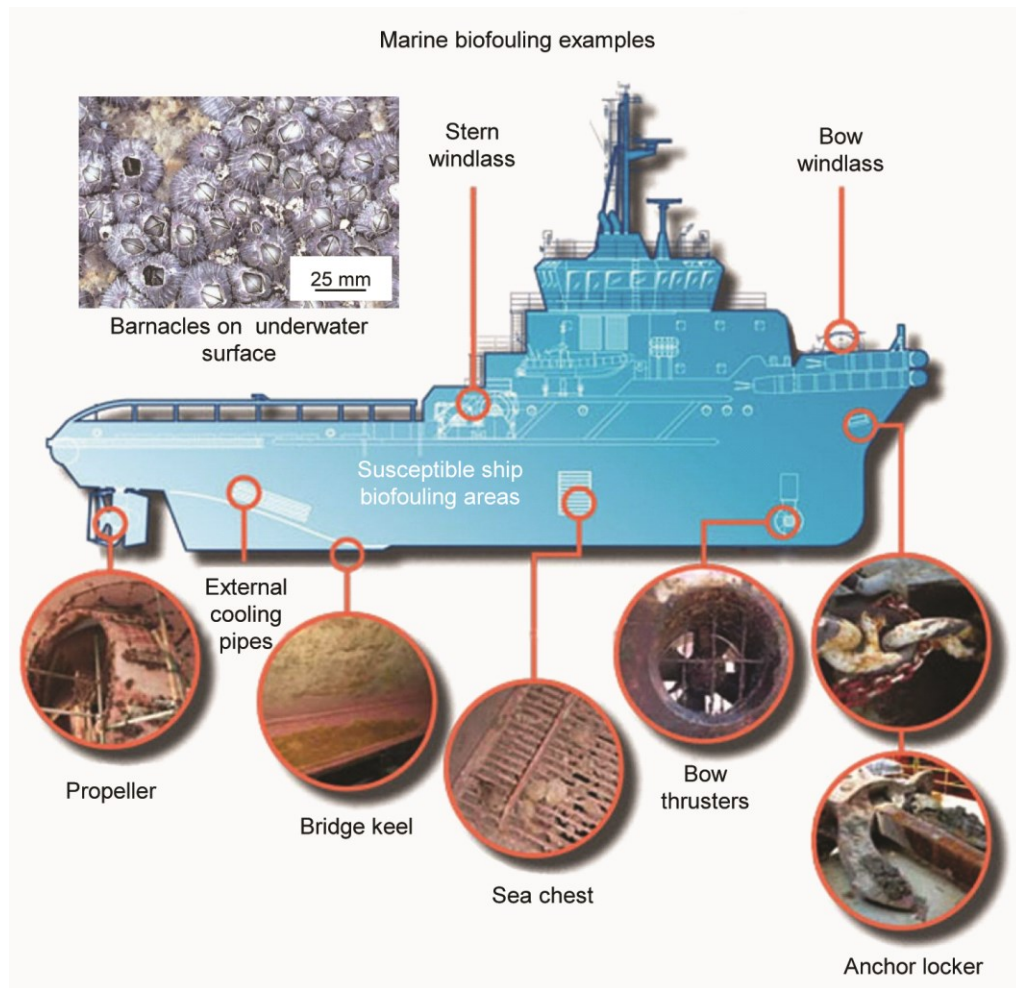


Figure 8: Marine biofouling examples (adapted from Bixler and Bhushan, 2012a). Areas susceptible to biofouling on a typical ship (middle) and the common hard shelled barnacle (*Tetraclitella purpurescens*) (top left). Barnacles on underwater plate (adapted from Edgar, 1997).

2.2.3. Industrial

Industrial fouling affects applications ranging from nuclear power plants to food production (Somerscales and Knudsen, 1981; Walker *et al.*, 2000; Chan and Wong, 2010). Biofilms increase friction, energy needs, and pipe pressure drops as well as decrease heat transfer efficiency (Richardson, 1984). Often nuclear power plant condenser cooling tubes suffer from biofouling induced corrosion and blockage (Nebot *et al.*, 2010). Biofilms can also harbor dangerous pathogenic microorganisms in potable water supplies (Lebret *et al.*, 2009).

Most water supplies, even stainless steel pipes with ultrapure water, are susceptible to biofilms. Fungi initiated by biofilms can grow causing poor taste and odor problems (Camper and McFeters, 2000). Figure 9 shows such biofouling examples with Zebra mussels (*D. polymorpha*) clogging a power plant intake pipe (www.marinebiotech.org), biofilm accumulation in a stainless steel tube (Cunningham *et al.*, 2008), biofilm (*B. cereus*) on a dairy industry stainless steel plate (Simoes *et al.*, 2010), and biofilm (*P. aeruginosa*) on a reverse osmosis membrane (Herzberg and Elimelech, 2007).

Membranes are used for various purposes including desalination and water purification. Membrane biofouling occurs in applications such as reverse osmosis, nano/microfiltration, clarification, virus removal, and bioreactors. Removal of salt from brackish water or seawater is effectively accomplished with reverse osmosis and nanofiltration, but fouling decreases flux and efficiency. Such fouling originates from deposits of organic material, iron, phosphorus, and microorganisms that lead to

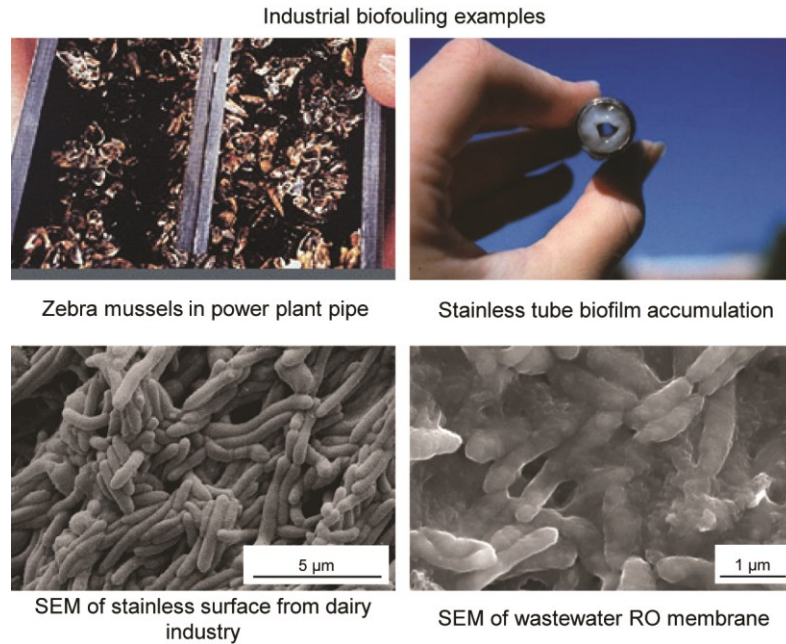


Figure 9: Industrial biofouling examples. Zebra mussels (*Dreissena polymorpha*) clogging power plant intake pipe (top left) (adapted from Peter Yates), biofilm accumulation in a stainless steel tube (top right) (adapted from Cunningham et al., 2008), biofilm (*B. cereus*) on dairy industry stainless steel plate (bottom left) (adapted from Simoes et al., 2010), and biofilm (*P. aeruginosa*) on reverse osmosis (RO) membrane (bottom right) (adapted from Herzberg and Elimelech, 2007).

detrimental increases in osmotic pressure and hydraulic resistance (Ridgway *et al.*, 1982; Cui and Wan, 2005; Herzberg and Elimelech, 2007; Pangarkar *et al.*, 2011).

2.3. Biofouling and inorganic fouling formation

The genesis of biofouling formation occurs when microorganisms transition from free floating planktonic to stationary sessile lifestyles, thus forming a biofilm. They adhere to one another and a hard surface with an adhesive called the extracellular polymeric substance (EPS). The biofilm continues to grow and become more diverse by attracting more microorganisms through chemical “messages”. The general principles of biofilm formation and factors leading to the settlement on hard surfaces are similar in medical, marine, and industrial applications (Melo *et al.*, 1988; Walker *et al.*, 2000; Stoodley *et al.*, 2002; Railkin, 2004; Monroe, 2007; Costerton, 2008; Chan and Wong, 2010). Described in the following section are biofouling colonization, bioadhesion, inorganic fouling, and hard substrate surface factors affecting settlement. Due to similarities of biofouling applications, marine fouling is detailed to illustrate various attributes affecting formation.

2.3.1. Colonization

Colonization is the process of biofouling organisms collecting and growing on a surface. In the marine environment, this usually starts with the formation of a biofilm that attracts larger macrofoulers (Stoodley *et al.*, 2002; Railkin, 2004; Costerton, 2008; Hellio and Yebra, 2009). For instance, tubeworms prefer settling on biofilms, but bryozoans and barnacles do not require a biofilm (Ralston and Swain, 2009). Figure 10 illustrates the five-stage colonization process, which includes initial attachment, irreversible

attachment, initial growth, final growth, and dispersion. Initial attachment starts the colonization process, which begins within days to a few weeks. The biofilm covered surface then attracts other organisms that may have been previously deterred. Initial attachment of microorganisms is reversible, but once they secrete the EPS, the bond becomes irreversible. This permanent attachment allows initial growth, final growth, and dispersion (Stoodley et al., 2002; Railkin, 2004; Monroe, 2007; Costerton, 2008). Figure 10 also shows a biofilm cross section highlighting the EPS morphology.

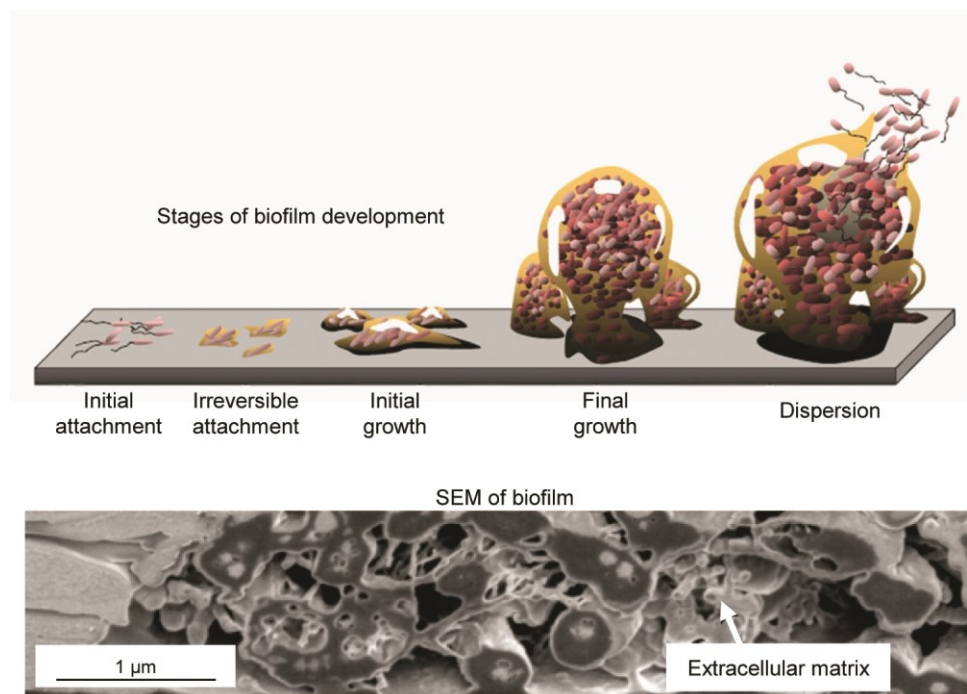


Figure 10: Biofilm development process and cross section example. Schematic illustrates the five stage colonization process (top) (adapted from D. Davis) and SEM of biofilm cross section highlighting the EPS morphology (bottom) (adapted from Andy Blankemeier).

Underwater environments are ideal for biofouling since currents deliver nutrients and carry away wastes, promoting colonization by planktonic and sessile organisms. Biofouling growth rates depend on the organism, substrate, flow velocity, shear stress, and temperature (Griebe and Flemming, 2000; Railkin, 2004; Jones, 2009). Organism transportation to a surface is either passive from the current or active from the propagule, juvenile, or adult organism. Active mechanisms include electrostatic repulsion, Brownian motion, turbulent pulsations, and cell outgrowths (Railkin, 2004; Ralston and Swain, 2009).

As far as the tenacity of the biofouling is concerned, bioadhesion plays an important role (Stoodley et al., 2002; Railkin, 2004; Monroe, 2007; Costerton, 2008). Bioadhesion is the adhesion strength of biofouling on a hard surface. This depends on the organism type, substrate, and separating fluid (Callow et al., 1986), due to influences of electrostatic forces and surface wettability (Bhushan, 2003; Feng and Jiang, 2006; Koch and Barthlott, 2009; Scardino, 2009; Sheng et al., 2010). Biofilm bioadhesion is a two-stage process, starting with the initial attachment and then the irreversible attachment.

Initial attachment is controlled by a physical adhesion between the microorganism and the substrate. Also known as adsorption, the initial colonists attach to a surface through weak, reversible van der Waals bonds, which are slightly stronger than electrostatic repulsive force. Irreversible attachment is accomplished with secretion of the EPS, which exhibits a sponge-like matrix. This adhesive permanently bonds the microorganisms to one another and collectively to the surface (Flemming *et al.*, 1999; Stoodley *et al.*, 2002; Railkin, 2004).

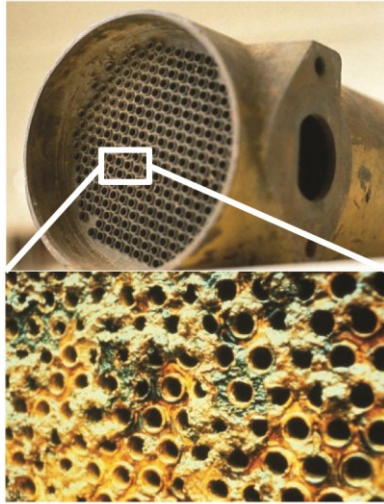
2.3.2. Inorganic fouling

Inorganic fouling composed of non-living particles may form in addition to or independently from biofouling. Particles originate from corrosion, crystallization, suspended particles, oil, and ice. For instance, salts from aqueous solutions crystallize and deposit on surfaces. Other deposits may result from minerals found in water such as magnesium, calcium, and barium (Somerscales and Knudsen, 1981; Walker *et al.*, 2000; Chan and Wong, 2010).

Types of inorganic fouling include particulate, freeze, and gas stream particulate. Particulate fouling occurs when suspended solid particles deposit onto a heat transfer surface (Epstein, 1988). Deposition of crystals from freeze fouling occurs in locations such as cold region oil pipelines when waxy hydrocarbons contact cold pipe walls. Gas stream particulate fouling occurs in gas lines, reactors, combustion chambers, and heat exchangers. This includes mineral, organic, and inorganic particles, which are common in oil or gas combustion systems (Bott, 1988b).

Biofouling may initiate inorganic fouling, where biocorrosion causes the formation of corrosion particles. Such fouling is prevalent in boilers, cooling condensers, desalination plants, food processing equipment, geothermal plants, and oil production equipment (Pritchard, 1988). Heat exchangers can develop hard deposits called “scale” or more porous deposits such as “sludge” (Bott, 1988a). Figure 11 shows inorganic fouling by comparing the inside of a clean nuclear power plant heat exchanger tube to a similar tube covered in corrosion deposits (Cunningham *et al.*, 2008). Also shown is calcium carbonate crystallization fouling on the outside of a heat exchanger (www.hcheattransfer.com).

Inorganic fouling examples



Clean (top) fouled (bottom) power plant heat exchanger



Heat exchanger tubing with crystallization

Figure 11: Inorganic fouling examples. Inside of a clean nuclear power plant heat exchanger tube (top) compared to a fouled tube with corrosion deposits (middle) (adapted from Cunningham et al., 2008). Calcium carbonate crystallization fouling on the outside of a heat exchanger (bottom) (adapted from H&C Heat Transfer Solutions, Inc).

2.3.3. Surface factors

Biofouling and inorganic fouling depend on the surface factors such as wettability, microtexture, color, and contours (Fingerman *et al.*, 1999; Railkin, 2004; Vadgama, 2005; Costerton, 2008; Hellio and Yebra, 2009). For instance, bryozoan and mussel larvae prefer hydrophobic surfaces (Gordon and Mawatari, 1992); hydroids, bryozoans, and ascidians prefer microtextured surfaces; larvae, sponges, barnacles, ascidians, and mollusks prefer light colored surfaces; barnacles prefer convex contours; and calcareous sponges prefer concave contours (Railkin, 2004).

Surface wettability influences fouler colonization, which ranges from water-fearing superhydrophobic to water-loving superhydrophilic surfaces (Fingerman *et al.*, 1999; Railkin, 2004; Vadgama, 2005; Costerton, 2008; Hellio and Yebra, 2009; Jung and Bhushan, 2009). A hydrophobic surface exhibits low wettability and low surface energy, whereas a hydrophilic surface exhibits high wettability and high surface energy. Water droplets on a hydrophobic surface will “bead up”, whilst droplets on a hydrophilic surface will spread out evenly. The prefix “super” indicates higher tendencies in either direction, such as superhydrophobic and superhydrophilic. The degree of wettability is determined by contact angle measurements, where contact angles less than 10° are superhydrophilic and over 150° are superhydrophobic. Figure 12a shows the contact angles for superhydrophilic, hydrophilic, hydrophobic, and superhydrophobic surfaces as well as photos of water droplets in the Cassie and Baxter, and Wenzel regimes, highlighting the air pocket effect.

Close examination of the liquid-solid-air interface reveals that the Wenzel regime does not contain an air pocket unlike the Cassie-Baxter regime. This difference, due to

surface roughness, influences the surface wettability since the air pocket affords a larger contact angle θ , which relates to wettability (Nosonovsky and Bhushan, 2008). Equations (1), (2), and (3) describe the Wenzel equation (no air pockets) where θ = contact angle, θ_f = contact angle of the droplet on the solid surface, R_f = roughness factor, A_F = flat solid-liquid contact area, and A_{SL} = projection of the solid-liquid area. Equation (3) describes the Cassie –Baxter equation (with air pockets) where f_{SL} = fractional solid-liquid contact area (Jung and Bhushan, 2009). Furthermore the Contact Angle Hysteresis (CAH) is the difference between the advancing (downhill side) and receding (uphill side) contact angles, which is low for Cassie-Baxter and high for Wenzel regimes. As the CAH increases, so does the adhesion strength, which explains the deformed shape of a water droplet adhered to a vertical window (Nosonovsky and Bhushan, 2008).

$$\text{Wenzel: } \cos \theta = R_f \cos \theta_f \quad (1)$$

$$\text{where } R_f = \frac{A_{SL}}{A_F} \quad (2)$$

$$\text{Cassie – Baxter: } \cos \theta = R_f f_{SL} \cos \theta_f - 1 + f_{SL} \quad (3)$$

Low adhesive, superhydrophobic surfaces promote contaminant removal with the application of liquid, through an action simply called “self-cleaning”. The schematic in Figure 12b illustrates the self-cleaning action of a water droplet on a low adhesive, superhydrophobic surface. On an incline, the water droplet slides past the particles on the hydrophilic surface, whilst the water droplet rolls and collects particles on the superhydrophobic surface (www.hk-phy.org). Also shown are droplets of water and mercury, each collecting contaminants on lotus (*Nelumbo nucifera*) and taro (*Colocasia*

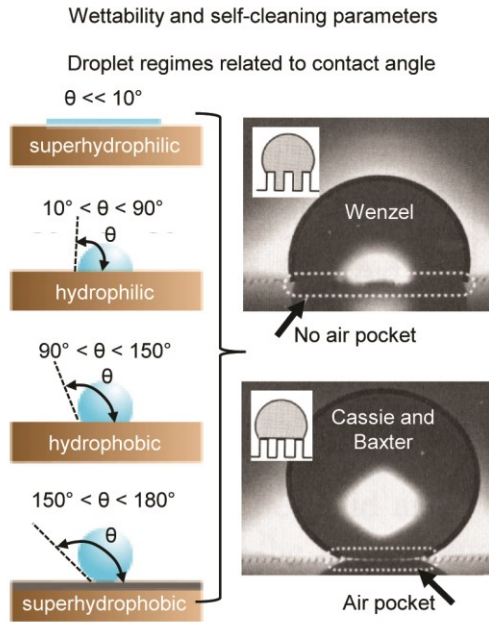


Figure 12: Various parameters describing wettability and self-cleaning. (a) Schematic shows droplet contact angles (left) and photos of droplet regimes (right) (adapted from Nosonovsky and Bhushan, 2008). (b) Schematic shows the self-cleaning effect (top) and superhydrophobic examples (bottom) (adapted from Barthlott and Neinhuis, 1997).

esculenta) leaves, respectively (Barthlott and Neinhuis, 1997; Nosonovsky and Bhushan, 2008).

Antifouling, superhydrophilic surfaces attract water to form an evenly distributed water layer, which can confuse and disrupt microorganism settlement (Harder and Yee, 2009). In general though, microorganisms prefer to colonize hydrophilic surfaces, although some actually prefer hydrophobic surfaces. For example *Ulva linza* prefer hydrophobic surfaces, whereas *Balanus Amphitrite* prefer hydrophilic surfaces. Furthermore, microorganisms such as *Ulva linza* attach more easily to hydrophobic surfaces, but experience decreased adhesive strength (Scardino, 2009). Additionally, sheeting action of sliding liquid on a superhydrophilic surface can promote self-cleaning, where the liquid helps collect and remove fouling (www.ppg.com).

Surface microtexture influences organisms such as hydroids, bryozoans, and ascidians that seek shelter against strong currents by settling in grooves, pits, cracks, and crevices (Fingerman *et al.*, 1999; Railkin, 2004). Microorganisms prefer to settle in areas slightly larger than themselves for maximum protection and surface area contact with the substrate. Fewer attachment points between the microorganism and substrate translate into lower bioadhesive strength (Scardino *et al.*, 2008). Bioadhesion is also affected by the effectiveness of EPS flowing into crevices formed by surface roughness, which depends on the adhesive viscosity. Furthermore, when adhesive only contacts the surface asperity peaks or tops of microtexture ridges, applied force to break bonds is significantly reduced (Vladkova, 2008).

Figure 13 demonstrates physical control antifouling mechanisms affecting microorganism settlement and colonization. Microorganisms search for an ideal site to settle, which can depend on parameters such as wettability and texture (Scardino, 2009; Feng and Jiang, 2006). During the search process, microorganisms will settle, move on, or expire in the process. In general, biofouling on superhydrophobic surfaces wash off more easily (self-cleaning) as compared to superhydrophilic surfaces. Images show a variety of examples found in nature, including the hydrophilic elephant ear (*Alocasia odora*) (Koch and Barthlott, 2009), microtextured shark skin (*Carcharhinus Galapagensis*) (Reif, 1985), hydrophobic water fern (*Regnellidium diphyllum*) (Koch and Barthlott, 2009), and superhydrophobic nanocolumns on an insect wing (*Cicada orni*) (Lee *et al.*, 2004).

2.4. Antifouling examples and methods in practice

When considering antifouling methods, many strategies exist in nature and industry, including physical and chemical controls. Due to the complex nature of fouling organisms, nature often uses a combination of physical and chemical controls. Industry mimics this approach through various antifouling technologies (Melo *et al.*, 1988; Fingerman *et al.*, 1999; Walker *et al.*, 2000; Railkin, 2004; Willemsen, 2005; Saliterman, 2006; Vo-Dinh, 2007; Hellio and Yebra, 2009; Ralston and Swain, 2009). Described in detail are antifouling lessons from nature, antifouling mechanisms, and current industry antifouling methods.

Surface topography antifouling mechanisms

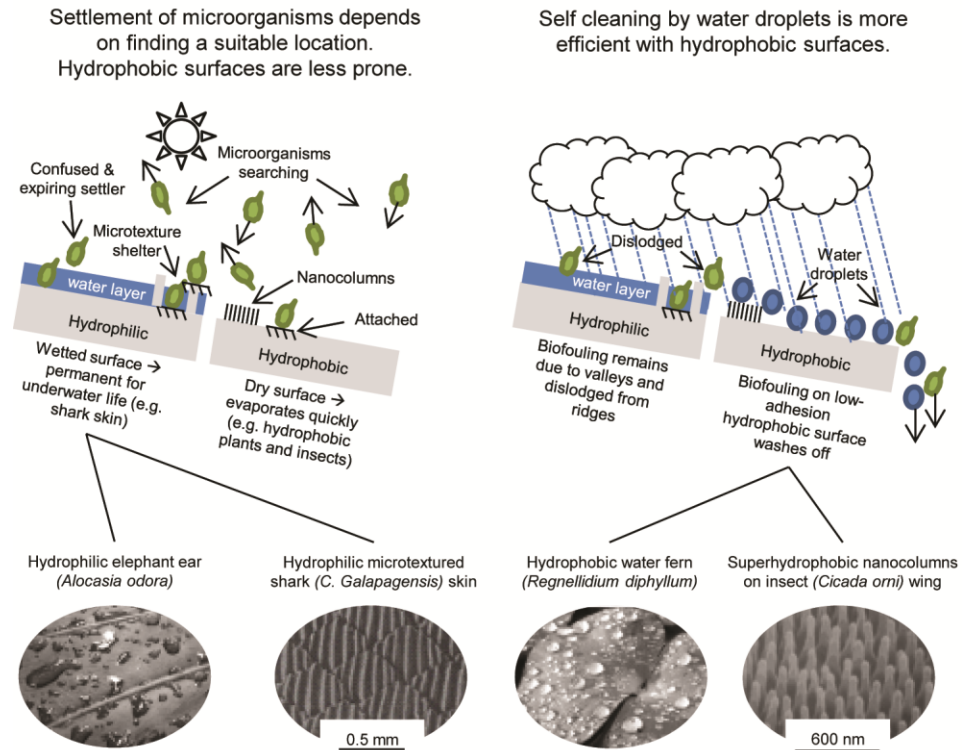


Figure 13: Schematic shows surface topography antifouling mechanisms demonstrating wettability and texture properties that influence microorganism settlement and colonization (adapted from Bixler and Bhushan, 2012a). Shown are elephant ear (Koch and Barthlott, 2009), shark skin (Reif, 1985), water fern (Koch and Barthlott, 2009), and insect wing (Lee et al., 2004).

2.4.1. Lessons from nature

Biofouling occurs throughout nature, but many examples of antifouling flora and fauna exist, as shown in Table 2 (flora) and Table 3 (fauna). These Tables include a variety of both land-based and underwater examples. Antifouling mechanisms for each are included to demonstrate the wide variety of techniques that could be mimicked. Common mechanisms include low drag, low adhesion, wettability, microtexture, grooming, sloughing, various miscellaneous behaviors, and chemical secretions (Fingerman *et al.*, 1999; Neinhuis and Barthlott, 1997; Bormashenko *et al.*, 2007; Costerton, 2008; Hellio and Yebra, 2009; Ralston and Swain, 2009; Bhushan, 2009; Bar-Cohen, 2011).

Low drag, fast swimming shark skin is antifouling due to its riblet microtexture, flexion of scales, and a mucous layer. The skin contains scales called dermal denticles, which are covered by specially sized and spaced riblets oriented parallel to the swimming direction (see Figure 11). Low drag is achieved by the riblets lifting and constraining the naturally occurring fluid vortices, which reduces the transfer of momentum and total shear stress. When the vortices are pinned just above the riblet tips, the cross-stream movement and entanglement of stream wise vortices is limited, thus reducing the transfer of momentum. The total shear stress is reduced since the vortices only contact the small riblet tips, as compared to the total surface area. Lower drag also allows the water layer next to the skin to move faster, which reduces microorganism settlement time and helps wash them away (Reif, 1985; Lee and Lee 2001; Bechert *et al.*, 1997a; Dean and Bhushan, 2010; Deyuan *et al.*, 2011b).

Table 2: Flora antifouling lessons from nature.

<i>Type</i>	<i>Mechanism</i>	<i>Source</i>
Lotus (<i>Nelumbo nucifera</i>), Taro (<i>Colocasia esculenta</i>)	Superhydrophobic self-cleaning surface	Barthlott and Neinhuis (1997); Nosonovsky and Bhushan (2008)
Jewelweed (<i>Impatiens capensis</i>)	Hydrophobic surface	Valdes (2010)
Water fern (<i>Salvinia</i>)	Superhydrophobic surface	Koch et al. (2009)
Eelgrass (<i>Zostera marina</i>)	Zosteric acid secretions	Callow and Callow (2002)
Lady mantle (<i>Alchemilla mollis</i>)	Hydrophobic surface	Lee et al. (2011)
Broccoli (<i>Brassica oleracea</i>)	Superhydrophobic surface	Lee et al. (2011)
Red seaweed (<i>Delisea pulchra</i>)	Bacteria message manipulation	de Nys and Steinberg (2002)
Coralline algae (<i>Porphyridium purpureum</i>)	Shading, chemical secretion, and shedding/sloughing	Scardino (2009)
Seaweed (<i>Ulva lactuca</i>)	Chemical secretions	Rao et al. (2005)
Indian cress (<i>Tropaeolum majus</i>)	Hydrophobic surface	Barthlott and Neinhuis (1997)

Table 3: Fauna antifouling lessons from nature.

<i>Type</i>	<i>Mechanism</i>	<i>Source</i>
Human		
Red blood cell	Phospholipid bilayer	Cui and Wan (2005)
Cornea	Eyelid wiper and chemical	Menton (2008)
Birds		
Dove (<i>Zenaida</i>), Pigeon (<i>Columba</i>), Duck (<i>Anas</i>)	Superhydrophobic feathers	Bhushan (2009)
Insects		
Dragonfly (<i>Libellula</i>), Damselfly (<i>Ischnura</i>), Mayfly (<i>Hexagenia</i>), Lacewing (<i>Notiobiella</i>)	Hydrophobic wax covered wings	Bar-Cohen (2011)
Soybean aphid (<i>Aphis glycines</i>)	Hydrophobic mushroom like spines	Bar-Cohen (2011)
Butterfly (<i>Polyommatus Icarus</i>), Cicadae (<i>Cicada orni</i>)	Superhydrophobic wings	Feng and Jiang (2006)
Mollusks and Crustaceans		
Blue mussel (<i>Mytilus edulis</i>), <i>Mytilus galloprovincialis</i> , <i>Perna perna</i> , <i>Pteria penguin</i>	Microtexture and filter feeding	Ralston and Swain (2009); Scardino (2009)
Crab (<i>Cancer pagurus</i>), Crawfish (<i>Orconectes</i>), Lobster (<i>Homarus</i>)	Microtexture and self-grooming	Bers and Wahl (2004); Yen (2010)
Corals		
Gorgonian sea fans (<i>Pseudopteragorgia america</i> & <i>Pseudopteragorgia acerosa</i>)	Microtexture, surface energy, sloughing, and mucous	Guenther and de Nys (2007); Scardino (2009)
Marine Mammals		
Pilot whale (<i>Globicephala melas</i>), Common dolphin (<i>Delphinus delphis</i>)	Microtexture, surface energy, and enzymes	Baum et al. (2003); Meyer and Seegers (2004)
Echinoderms		
Brittle star (<i>Ophiura texturata</i>), Sea urchin (<i>Diadema</i>)	Sloughing and mucous	Scardino (2009)
Fish		
Shark (<i>Squalus acanthias</i>)	Low drag, riblets, flexion of scales, and mucous	Kesel and Liedert (2007); Scardino (2009)
Dogfish (<i>Scyliorhinus canicula</i>) egg case	Parallel ridge microtexture surface	Davenport (1999)
Fish (<i>Micropterus</i>) scales	Hierarchical scale structure	Lui et al. (2009)
Stonefish (<i>Synanceja horribilis</i>)	Skin sloughing	Ralston and Swain (2009)

In addition to low drag, shark skin microtexture deters certain microorganisms, since they prefer particular groove widths and depths for settlement. As a result of these mechanisms, microorganisms have difficulty adhering to and colonizing shark skin (Carman *et al.*, 2006; Genzer and Efimenko, 2006; Kesel and Liedert, 2007; Ralston and Swain, 2009; Dean and Bhushan, 2010).

Desirable wettability properties include low adhesive superhydrophobic and superoleophobic self-cleaning surfaces that resist fouling since water washes away the contaminating particles (Neinhuis and Barthlott, 1997; Jung and Bhushan, 2009). Figure 14 shows superhydrophobic examples with the lotus leaf, butterfly wings, and pigeon feathers; as well as a superoleophobic example with fish scales. Submerged fish scales are oil resistant due to their hierarchical structure, which consists of 4-5mm diameter scales covered by papillae 100-300 μm long and 30-40 μm wide (Liu *et al.*, 2009). Other superhydrophobic examples include broccoli, lady mantle, and the insect cicada (Lee *et al.*, 2004, 2011).

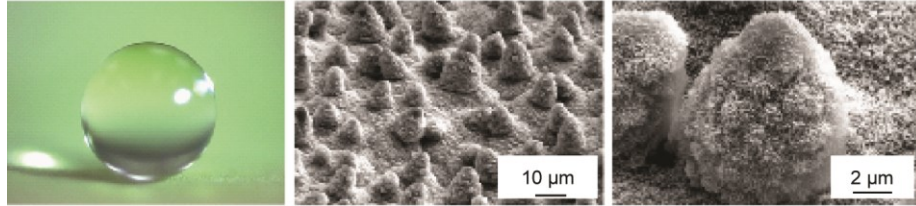
Certain microtextured surfaces resist biofouling since organisms seek ideal surface features for settlement, and may be deterred if no suitable surface is found. The barnacle *Cypris* larvae are deterred by microtextured surfaces if the features are the same size or slightly smaller than juveniles. The mussel *Mytilus* deters foulers with a micro-hair covered surface, and the dogfish shark egg case deters foulers with a microtextured surface (Davenport, 1999; Bers and Wahl, 2004; Ralston and Swain, 2009). Also the

Figure 14: Antifouling examples from nature using wettability properties. Water promotes self-cleaning on low adhesion superhydrophobic surfaces as shown in the lotus (adapted from Bhushan et al, 2009), butterfly (adapted from W. Barthlott), and pigeon (adapted from Bormashenko et al., 2007) examples. Also shown are fish scales (adapted from Liu et al, 2009), which are superoleophobic when submerged. Shark skin is antifouling due to a combination of features including, low drag, riblets, flexion of scales, and mucous layer (adapted from Jung and Bhushan, 2009).

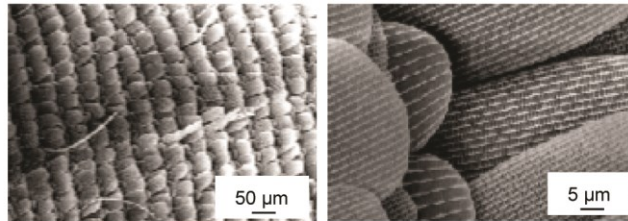
Figure 14

Antifouling surface examples from nature

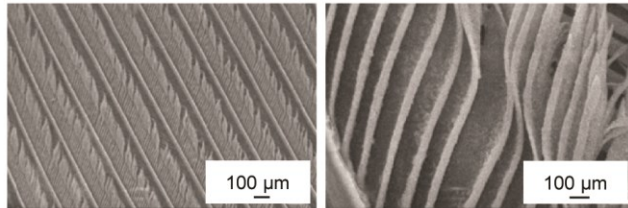
Examples of self-cleaning surfaces



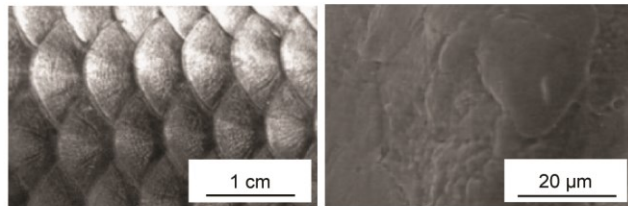
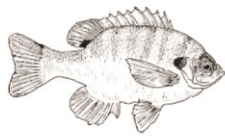
Superhydrophobic lotus (*N. nucifera*) leaf



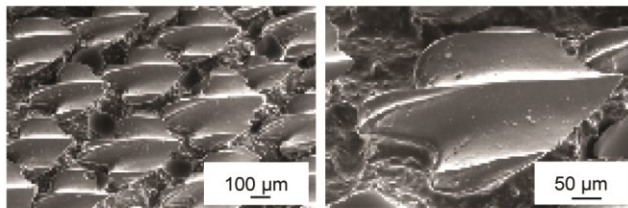
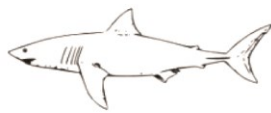
Superhydrophobic butterfly (*P. icarus*) wings



Superhydrophobic pigeon (*Columba*) feathers



Superoleophobic fish (*Micropterus*) scales



Low drag shark (*S. acanthias*) skin

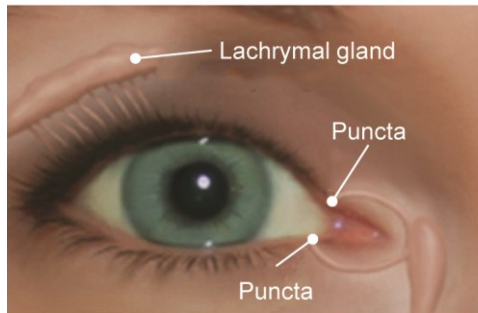
pilot whale (*Globicephala melas*) and the common dolphin (*Delphinus delphis*) deter biofouling with microtextured skin (Baum *et al.*, 2003; Meyer and Seegers, 2004).

Grooming is the physical removal of biofouling from the host, which effectively controls slow and fast growing biofouling. Decapods and crustaceans groom other creatures with special brush structures for removing foulers from gills and appendages. Echinoderms and bryozoans use special structures called pedicellaria to groom macroepibionts while crayfish depend on *Branchiobdellid annelids* to feed on foulers in their gills. Sloughing is the slow shedding of the outermost layer of an organism, which effectively controls slow growing biofouling. This method is employed by organisms such as crustaceans, stonefish *S. horribilis*, and seaweed (Ralston and Swain, 2009).

Miscellaneous antifouling behaviors include any physical action that prevents or removes fouling. Such behaviors include activities such as burrowing, hiding in the dark, flexing, and mechanical cleaning. These may be used in conjunction with antifouling mechanisms such as low drag, low adhesion, wettability, microtexture, grooming, sloughing, and chemical secretions. Burrowing scrapes off foulers, and hiding in the dark inhibits algae formation (Becker and Wahl, 1996). Algae prevent biofouling by flexing and bending, unlike rigid foulers such as barnacles and tubeworms (Walters *et al*, 2003). Figure 15 illustrates a mechanical cleaning example combining wiping with chemical secretion as demonstrated in the human eye via the lachrymal gland secreting tears, puncta collecting tears, and eyelid wiping the cornea (Menton, 2008).

Antifouling examples from nature

Mechanical cleaning



Self-cleaning human eye

Chemical secretions



Red seaweed (*Delisea pulchra*)

Figure 15: Antifouling examples from nature using mechanical cleaning and chemical secretions. Human eye combines wiping with chemical secretions to clean the cornea (top) (adapted from John Nyquist). Red seaweed using a halogenated furanone to manipulate colonizing bacteria “attraction” messages (bottom) (adapted from Yen, 2010).

Chemical secretion methods range from preventing to removing biofouling. Figure 15 shows the red seaweed (*Delisea pulchra*), which uses a halogenated furanone to manipulate colonizing bacteria “attraction” messages (Yen, 2010). Other chemical examples include snails that leave a predatory mucous trail, antimicrobial coral egg shells (Ramasamy and Murugan, 2007), mucous on shark skin (Ralston and Swain, 2009), and antifouling chemicals produced by the bacteria *Roseobacter gallaeciensis* (Rao *et al.*, 2006). Furthermore, blood cell protein adsorption and cell adhesion is inhibited with phosphorylcholine (Saliterman, 2006).

2.4.2. Methods in practice

Several bioinspired antifouling methods in practice benefit or could potentially benefit medical, marine, and industrial applications. These include mimicking nature’s physical and chemical control methods such as low drag, low adhesion, wettability, and microtextured surface properties as well as grooming, sloughing, various miscellaneous behaviors, and chemical secretions (Reis and Weiner, 2004; Nosonovsky and Bhushan, 2008; Ralston and Swain, 2009; Bar-Cohen, 2011). Coatings are perhaps the most common method of biofouling control (Hellio and Yebra, 2009; Schulz *et al.*, 2009) and examples are shown in Table 4.

2.4.2.1. Surface property methods

Low drag surfaces provide antifouling benefits, and drag reduction is demonstrated by saw tooth, scalloped, and bullnose shark skin-inspired riblets. Laboratory experiments show such microtextures can reduce drag up to 9.9 percent, with an optimized relationship between the blade thickness and spacing (Walsh and

Table 4: Antifouling coatings.

<i>Type</i>	<i>Mechanism</i>	<i>Source</i>
Medical		
Metal	Toxic silver or zinc coated surface	Dror et al. (2009)
Hydroxyapatite	Toxic coating for osteosynthesis applications	Montali (2006)
Antiseptic	Toxic coating with chlorhexidine and/or	Montali (2006)
Antibodies	Toxic coating with antibiotics	Montali (2006)
Polyethylene glycol (PEG)	SAMS hydrophilic surface deters protein adsorption and adhesion	Emmenegger <i>et al.</i> (2009)
Oligoethylene glycol	SAMS hydrophilic surface deters fibrinogen adsorption	Emmenegger <i>et al.</i> (2009)
Zwitterionic polymers	Hydrophilic surface deters protein adsorption and reduces bioadhesion	Emmenegger <i>et al.</i> (2009)
Fluoropolymer & fluorosilane	Films increase biocompatibility for implantable devices to reduce protein	Lee <i>et al.</i> (2004)
Marine/Industrial		
Metal coating	Toxic copper or silver coated surfaces	Railkin (2004); Zodrow <i>et al.</i>
Silicone elastomer	Low surface energy promotes low bioadhesion	Callow and Callow (2002)
Self-polishing	Self-polishing paint with copper, tin, zinc, or	Abarzua <i>et al.</i>
Hydrogels	Hydrophilic surface confuses settlers	Lewis (2009)
Biological	Deterrents include bacteria, algae, and	Abarzua <i>et al.</i>
Enzymes	Lowers bioadhesion and lyses bacteria	Olsen <i>et al.</i> (2007)
Hormones	Promotes premature metamorphosis of larva	Fischer <i>et al.</i>
Short fibers	Fibers or spikes confuse settlers	Lewis (2009)
Conductive paint	Electrochemical disinfection process	Matsunaga <i>et al.</i>
Organo-metallic	Toxic flexible metal surface	Willemsen (2005)
Plastic film	Disposable film removed with attached	Fischer <i>et al.</i>
Photoactive film	Self-cleaning film uses UV or visible	Banerjee <i>et al.</i>
Cayenne pepper	Deterrent pepper with silicone grease	Manov <i>et al.</i>

Lindermann, 1984; Bechert *et al.*, 1997b). Both two dimensional (2D) and three dimensional (3D) riblets have been studied for their drag reduction effectiveness, but no significant improvement is observed with 3D versus 2D (Wilkinson *et al.*, 1988). Styles of riblets include aligned segmented blade (Wilkinson and Lazos, 1988), offset segmented blade, offset 3D blade (Bechert *et al.*, 2000a), and 3D shark skin replicas (Bechert *et al.*, 2000b; Lang *et al.*, 2008; Deyuan *et al.*, 2011b; Jung and Bhushan, 2010). A riblet optimization review paper suggests that a blade riblet height divided by spacing equaling 0.5 is optimal for drag reduction, regardless of riblet length (Dean and Bhushan, 2010).

Riblet-inspired drag-reducing products include the experimental 3M™ saw tooth riblets as well as the Speedo FastSkin® fabric racing swimsuit. The 3M™ riblets are manufactured in polymer films and have been tested in various aerospace, marine, and industrial applications (Gaudet, 1989; Rohr *et al.*, 1992; Deyuan *et al.*, 2011a). Riblet technology has captured the attention of the National Aeronautics and Space Administration (NASA), U.S. Navy, Airbus, Boeing, as well as Olympic competitors. In the 1984 Los Angeles Olympics and 1987 America's Cup, riblets were applied to U.S. boats, which presumably helped to secure victories. The 2008 Beijing Olympics witnessed the benefit of the Speedo FastSkin® swimsuit when American Michael Phelps set Olympic records and won several gold medals. Reducing fluid drag can also benefit wind turbine, microfluidics, and oil pipeline industries (Marentic and Morris, 1992; Kennedy, 1993; Davies, 2002; Krieger, 2004).

Low adhesive products include a variety of self-cleaning hydrophobic paints, roof tiles, and fabrics as well as self-cleaning hydrophilic windows and membranes. Examples are Lotusan[®] paints by Sto (www.stocorp.com), Tegotop[®] paints by Degussa (www.goldschmidt.com), Erlus Lotus[®] roof tiles (www.erlus.com), NanoSphere[®] fabrics by Schoeller Technologies (www.schoeller-textiles.com), and SunClean[®] glass by PPG Industries (www.ppg.com). Self-cleaning is achieved with the hydrophobic Lotusan[®] roll on and Tegotop[®] spray paints that create a microstructure surface (www.stocorp.com; www.goldschmidt.com), hydrophobic Erlus Lotus[®] roof tiles with an etched surface finish (www.erlus.com), and hydrophobic NanoSphere[®] fabrics with integrated nano particles (www.schoeller-textiles.com). Self-cleaning hydrophilic SunClean[®] glass with titanium dioxide uses the sheeting action of water to efficiently gather and remove contaminants (www.ppg.com). Figure 16 shows the improved cleanliness with Lotusan[®] hydrophobic self-cleaning paints on concrete and stucco (www.stocorp.com), and better clarity with the SunClean[™] hydrophilic self-cleaning glass (www.ppg.com).

Hydrophobic polymers and antimicrobials such as Nitrofurazone or silver-based hydrogel are examples of medical device coatings (LoVetri *et al.*, 2010). Select applications include catheters, endotracheal tubes (Dror *et al.*, 2009), and orthopedic hip implants. Hydrophobic surfaces reduce protein bioadhesion, and antimicrobial surfaces reduce ambient microorganisms (Monroe, 2007). Surfaces with superhydrophilic polyethylene glycol or polyethylene oxide show less protein adsorption and bioadhesion (Sharma *et al.*, 2007; Vladkova, 2008). Other coating examples include Self-Assembled Monolayers (SAMs), which are desirable since they coat the surface with a molecularly



Figure 16: Effectiveness of self-cleaning antifouling coatings. Demonstrated is the improved cleanliness with Lotusan ® hydrophobic self-cleaning paint (top) (adapted from www.stocorp.com) and improved clarity with the SunClean™ hydrophilic self-cleaning glass (bottom) (adapted from www.ppg.com).

thick biocompatible film. This is especially important for applications such as Biomedical Micro/Nano Electromechanical Systems (BioMEMS/NEMS) (Lee *et al.*, 2005; Bhushan *et al.*, 2006a, b; Kwon *et al.*, 2011). Figure 17 shows an orthopedic hip implant covered with a biocompatible coating designed to control biofouling, wear rate, and promote bone growth (Anonymous, 1999; Vleugels, 2006).

In 2008 the International Maritime Organization banned tributyltin coatings, due to harmful effects to the surrounding marine environment. As a result, efforts are

underway exploring environmentally friendly methods such as new nontoxic antifouling paints and foul-release coatings (Callow, 1999; Fingerman *et al.*, 1999; Railkin, 2004; Hellio and Yebra, 2009). Marine foul-release coatings are nontoxic hydrophobic surfaces that promote self-cleaning. Nano/microtextured surfaces control surface energy, charge, conductivity, porosity, roughness, wettability, and friction (Clare and Aldred, 2009). Hydrophobic materials such as fluoropolymers and silicone elastomers are nontoxic, adhesion resistant, environmentally friendly, and easy to clean (Clarkson, 1999). Siloxane elastomers provide a combination of lower elastic modulus and lower surface energy, creating a hydrophobic, low-stick surface. Silicone foul-release coatings are used for some quick moving boats, but degrade over time (Vladkova, 2007, 2008). Figure 17 shows a foul-release organic tin-free hull coating called “Green Ocean Coating Heavy Duty” by Advanced Marine Coatings, whose smoothness and hardness reduces cleaning cycles (www.bayermaterialscience.com).

Industrial heat exchanger applications utilize SAMs to reduce bioadhesive strength between foulers and a heated surface, using low surface energy hydrophobic properties. Materials such as silicon can withstand temperatures up to 200°C whilst materials such as hexadecyl disulfide can withstand up to 225°C. SAMs furthermore offer corrosion protection by limiting the oxygen and water diffusion at the substrate surface. This technique could be widely used for heat exchangers but needs long term durability testing (Venkatesan and Murthy, 2008).

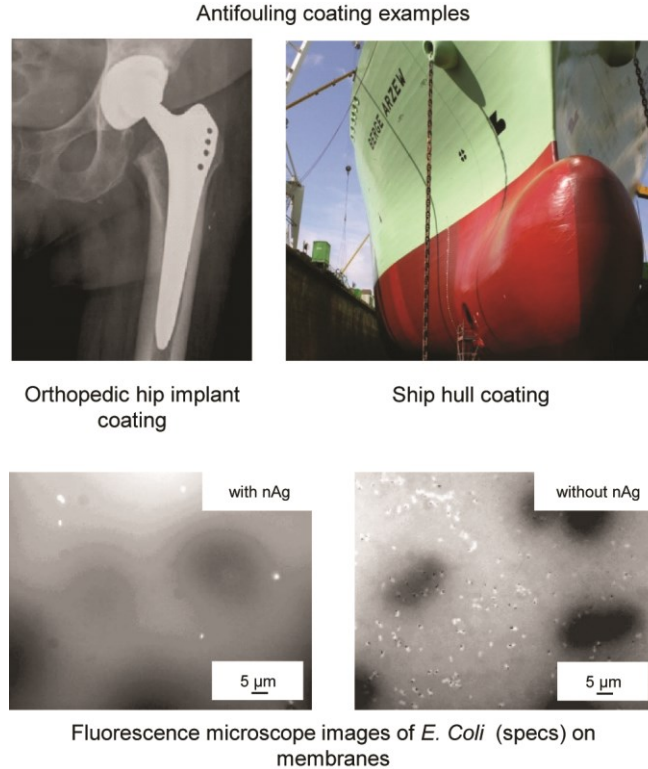


Figure 17: Medical, marine, and industrial antifouling coating examples. Orthopedic hip implants are covered with a biocompatible coating designed to control biofouling, wear rate, and promote bone growth (top left) (adapted from Ir Jef Vleugels). Marine foul-release organic tin-free hull coating called “Green Ocean Coating Heavy Duty” minimizes manual cleaning (top right) (adapted from Bayer MaterialScience). Polysulfone ultrafiltration membrane treated with silver nanoparticles (nAg) shows antifouling benefit with fewer *E. Coli* attached (bottom) (adapted from Zodrow et al., 2009).

Hydrophilic red blood cell plasma membranes are inspiring research to improve medical device and other synthetic membranes (Cui and Wan, 2005). For instance, Advanced Hydro[®] applies hydrophilic polymer coatings to water purification and filtration membranes, and results show a 30-50% reduction in fouling (www.advancedhydro.net). Clean Membranes[®] utilize a “smart-comb” copolymer in ultrafiltration membranes to provide antifouling and increased permeability (www.cleanmembranes.com). Researchers at University of California Los Angeles combine superhydrophilic and antimicrobial nanoparticles in a polyamide thin film coating for antifouling of reverse osmosis membranes (www1.cnsi.ucla.edu). Furthermore, studies show success using titanium dioxide (TiO₂) nanoparticles as a thin film on reverse osmosis membranes to control biofouling due to the photocatalytic effects that eliminate bacteria (Kim *et al.*, 2003). Similarly, ultrafiltration membranes impregnated with antimicrobial and hydrophilic silver nanoparticles (nAg) show antifouling benefit. Figure 17 compares nAg treated and untreated polysulfone ultrafiltration membranes, showing fewer *E. Coli* attached to the nAg membrane (Zodrow *et al.*, 2009).

A microtexture film with riblet-inspired antifouling properties includes the Sharklet AF[™], which operates on the principle that microorganisms are deterred from hydrophobic surfaces and crevices slightly smaller than themselves. Research suggests that appropriately sized topographies prevent colonization by various microorganisms including *Ulva* spores and *Balanus Amphitrite* cyprids (Carman *et al.*, 2006; Schumacher *et al.*, 2007). Figure 18 demonstrates the experimental Sharklet[™] urinary catheter

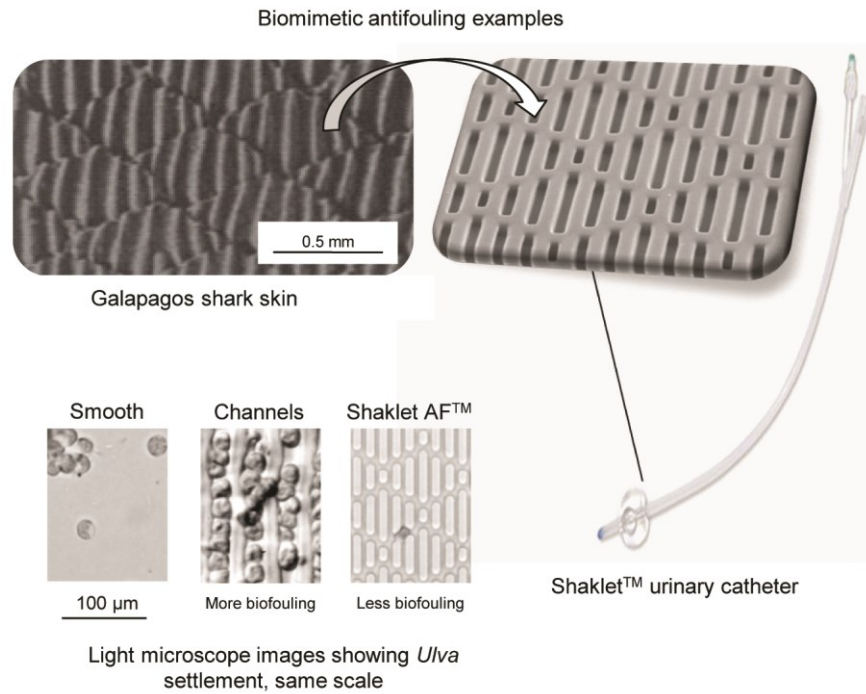


Figure 18: Biomimetic antifouling examples. Inspired by nature’s antifouling Galapagos shark (*Carcharhinus Galapagensis*) skin (top left) (adapted from Reif, 1985), researchers are developing a Sharklet™ antifouling urinary catheter (top right) (adapted from www.sharklet.com). Experiments demonstrate the Sharklet AFTM antifouling effectiveness with *Ulva* settlement on various topographies (bottom) (adapted from Carman et al., 2006).

compared to Galapagos shark (*Carcharhinus Galapagensis*) skin and the antifouling effectiveness of Sharklet AF™ with *Ulva* settlement on various surface topographies (Carman *et al.*, 2006).

2.4.2.2. Other methods

Grooming and sloughing methods to control biofouling are used in many applications. For instance, the U.S. Navy sponsored the development of a ship hull cleaning tool called the Bio-inspired Underwater Grooming (BUG) robot (www.onr.navy.mil). This robot cleans a ship hull similar to a groomer on a host organism. Surface renewal in self-polishing paints mimics the actions of sloughing prevalent in nature. Current commercially available biocidal self-polishing paints are considered low maintenance, effective, and repairable. Such paints types include biocidal free association (released from resinous matrix) and ablative (bonded in soluble matrix that eventually peels-off) (Abarzua *et al.*, 1999). Self-polishing copolymer paints contain antifouling toxins that erode over time, shedding the attached biofouling, and continually exposing fresh toxins. However, biofouling is the most difficult to control in ports due to the lack of movement and higher concentration of bacteria from pollution and stagnant water (Ketchum, 1952; Railkin, 2004). Self-polishing paints without biocides are not as effective since the rate of removal is too slow to control fouler growth.

Behavior antifouling methods include freshwater rinsing for ships. Researchers found that a fouled ship in saltwater moved into freshwater (such as the Panama Canal) for nine days and then back to saltwater removed 90% of biofouling (Ralston and Swain, 2009). Chemical control antifouling examples include low adhesive surfaces using

zosteric acid extracted from eelgrass (*Zostera marina*) and polymers from sea urchin and killer whales (Callow and Callow, 2002). Antifouling coatings include bio-inspired dopamine from mussels (Yen, 2010) and natural enzyme (Olsen *et al.*, 2007) additives. Additionally researchers have studied antifouling coatings with metabolites from microorganisms, living bacteria, and dopamine (Ralston and Swain, 2009). So-called living paints contain inhibitory bacteria to reduce biofouling, as demonstrated by incorporation of *Pseudoalteromonas Tunicate* into hydrogels (de Nys and Steinberg, 2002).

2.4.3. Additional approaches for completeness

2.4.3.1. Cleaning and disinfecting

Physical cleaning and chemical disinfecting are often considered effective methods to remove biofouling, albeit most tedious (Cologer, 1984; Walker *et al.*, 2000; Sharma *et al.*, 2004; Hellio and Yebra, 2009; Anonymous, 2010; Chan and Wong, 2010). Table 5 lists many examples of methods in practice from medical, marine, and industrial fields. Most employ mechanical methods such as manual scrubbing to disrupt and remove the biofouling. Disinfecting is commonly employed in dental applications with antiseptic mouth rinses such as Listerine[®]. For example, the active ingredient chlorhexidine attacks and reduces dental biofilm to control plaque and gingivitis in the oral cavity (Charles *et al.*, 2004). The biofilm is reduced when the individual bacteria walls rupture, as illustrated in Figure 19 (www.jjdentalprofessional.com). Mouth rinses combined with brushing and flossing increase the effectiveness, since such “mechanical methods” disrupt the biofilm (Sharma *et al.*, 2004).

Table 5: Biofouling cleaning/disinfecting techniques.

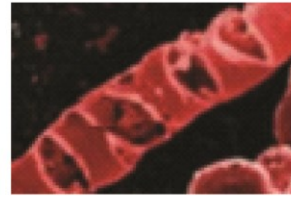
<i>Type</i>	<i>Mechanism</i>	<i>Source</i>
Medical		
Chemicals	Toxic disinfectants (ex: chlorine, alcohol)	Okochi et al. (2005)
Wet heat	Steam autoclave sterilization	Anonymous (2010)
Dry heat	Hot dry air sterilization	Anonymous (2010)
Vibrations	Ultrasonic alcohol bath sterilization	Railkin (2004)
Plasma	Cool plasma targets biofilms inside teeth	Dunham (2009)
Gamma rays	Radiation exposure sterilization	Anonymous (2010)
Ethylene oxide	Toxic gas sterilizes plastics, optics,	Anonymous (2010)
Marine/Industrial		
Air bubbles	Toxic air bubbles with dissolved kerosene	Railkin (2004)
Mechanical	Manual scraping or with rotary tool removal	Cristiani (2010)
Jet spray	Pressurized water blasting removal	Cristiani (2010)
Air drying	Toxic dry-docking or air-drying	Cristiani (2010)
Explosives	Explosion induced removal	Fischer et al. (1984)
pH level	Toxic acidic/alkaline solutions	Cui and Wan
Phages	Viruses target and infect bacteria	Simoës et al. (2010)

Biofouling cleaning examples

Disinfecting



Sterilization



Listerine® bacteria rupture

Mechanical cleaning

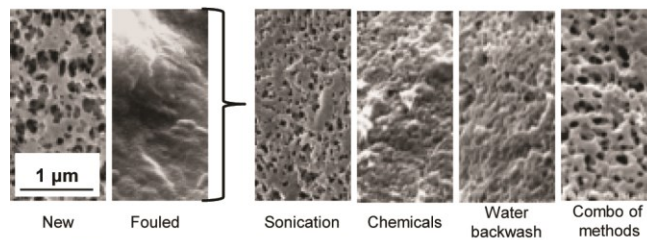


Water spray



Automatic brush

Combination of methods



SEM images comparing membrane cleaning techniques, same scale

Figure 19: Medical, marine, and industrial biofouling cleaning examples. Steam sterilization medical autoclave (top left) (adapted from Life Science Outsourcing), Listerine® effect on bacteria (top right) (adapted from Christoph Schaudinn), water spray on a low-stick ship hull (middle left), automatic brush washing system (middle right) (adapted from Willemsen, 2005), and microfiltration membrane using sonication, chemicals, and water backwash (bottom) (adapted from Lim and Bai, 2003).

2.4.3.2. Miscellaneous

Table 6 shows a variety of antifouling prevention methods. For instance, as shown in Figure 20, a biosensor developed by NASA detects small amounts of bacteria, viruses, and parasites to prevent the spread of disease. It can prevent biohazards in applications ranging from Earth to the International Space Station. The sensor operates by implementing ultra-sensitive carbon nanotubes, which sends an electrical signal to determine the level of microorganisms in a sample. Detecting the presence of pathogens can prevent an infectious outbreak before people become sick (www.earlywarninginc.com).

Table 6: Miscellaneous antifouling techniques.

<i>Type</i>	<i>Mechanism</i>	<i>Source</i>
Miscellaneous		
Biosensor	Detects presence of bacteria	www.earlywarninginc.com
UV-C	Organism DNA manipulation inhibits	Lebret et al. (2009)
Filters	Removal of micro/macroorganisms	Lebret et al. (2009)
Active surface	Cyclic parameters (ex: varying	Harder and Yee (2009)
Electricity	Electric field/shear stress prevents	Yeh et al. (2007)
Surface charge	Positive/negative charges deters	Greer et al. (2003)
Responsive	Changes in wettability (due to light,	Genzer and Efimenko

Biofouling prevention technique



Biosensor detects bacteria

Figure 20: Biofouling prevention technique (adapted from NASA Ames and Dominic Hart). Biosensor developed by the National Aeronautics and Space Administration detects small amounts of bacteria, viruses, and parasites to prevent the spread of disease.

2.5. Summary and outlook

Biofouling is the accumulation of unwanted biological material on surfaces, as found in medical, marine, and industrial applications. Biofouling can pose substantial health risks and financial losses, such as disease-spreading biofilms in hospitals and increased drag on ships. Biofouling composition includes organisms ranging from bacteria to barnacles, whereas inorganic fouling composition includes particles ranging from salt crystals to corrosion. Generally microorganisms initially colonize a surface and form a biofilm. In marine and industrial applications, macrofouling and inorganic fouling usually accompany biofilms.

Nature's flora and fauna demonstrate a multitude of antifouling lessons that can be mimicked for engineering purposes. Many of nature's antifouling mechanisms have

been studied to unlock their secrets, including examples such as self-cleaning lotus leaf and shark skin. Antifouling mechanisms include physical and chemical controls such as low drag, low adhesion, wettability, microtexture, grooming, sloughing, various miscellaneous behaviors, and chemical secretions. Nature frequently uses a combination of methods in order to successfully prevent fouling. Examples of biomimetic methods in practice include shark skin inspired surface microtextures as well as sloughing-inspired self-polishing paints.

Other antifouling approaches range from biocidal and self-cleaning coatings to various disinfecting techniques. For instance, medical devices utilize antimicrobial coatings to inhibit biofilm formation, ships utilize low adhesion paints, and power plants utilize chemical treatments. Medical cleaning is accomplished with sterilization and disinfecting chemicals, whilst marine and industrial cleaning primarily relies on high pressure water jets or brush scrubbing.

Developing physical control nontoxic foul-release surfaces for medical, marine, and industrial applications is particularly appealing. Approaches include creating antifouling surfaces with microtextured topographies as well as with superhydrophobic or superhydrophilic wettability properties. Variables to consider and test include the antifouling physical and chemical control mechanisms found in nature. Research could focus on gleaning the best properties from each example and combining them to produce an effective antifouling surface resistant to a variety of foulers.

CHAPTER 3: Fluid Drag Reduction With Shark-Skin Riblet Inspired Microstructured Surfaces

3.1. Fluid drag reduction with shark skin

In this chapter, presented are mechanisms behind fluid drag, current methods of drag reduction, drag reduction research, and conceptual models using shark skin inspired riblet surfaces. Determining the optimal riblet surface morphology for maximum drag reduction has been the focus of many efforts. Experimental results indicate that shark skin inspired surfaces effectively reduce drag in open and closed channel flow, although limited data is available with closed channel. Furthermore, my closed channel experiments are reported to study the neighboring wall effects by using micro-sized closed channels.

In open channel, drag has been measured using water (Reidy and Anderson, 1988; Gillcrist and Reidy, 1989; Walsh, 1990a; Neumann and Dinkelacker, 1991; Rohr et al., 1992), oil (Bechert et al., 1997a, 2000a; Buttner and Schulz, 2011; Gruneberger and Hage, 2011), and air (Walsh, 1982; Walsh and Lindermann, 1984; Bechert et al., 1985, 2000a; Wilkinson and Lazos, 1988; Coustols, 1989; Subaschandar et al., 1999; Viswanath, 1999, 2002; Han et al., 2003; Sareen et al., 2011). Similarly, in closed channel flow, drag has been measured using water (Reidy and Anderson, 1988; Lui et al., 1990; Rohr et al., 1992; Jung and Bhushan, 2010; Bixler and Bhushan, 2013b), oil (Bixler and Bhushan, 2013a), and air (Nitschke, 1983; Enyutin et al., 1995; Bixler and

Bhushan, 2013b). Both drag (for open channel) and the pressure drop (for closed channel) measurements characterize the riblet drag reduction efficiency.

3.2. Drag mechanisms

Drag is commonly categorized into pressure and skin friction drag, where the shark skin riblet microstructures generally reduce the skin friction drag. Describing pressure drag is best accomplished by imagining walking through a pool of water, where the resistance is primarily due to the pressure or form drag. The pressure drag is the drag that occurs due to the required energy necessary to move the fluid from the front to the back of the object, such as water moving around the one's legs. This drag may be reduced with streamlined shapes, such as airfoil designs common to aircrafts. Conversely, skin friction or viscous drag is the drag that occurs due to the interaction of the closest fluid layer to the object's surface, such as the skin of the one's legs in the water. This drag is due to the attraction of fluid molecules to the surface, which creates friction and thus resistance. Away from the surface the velocity of the molecules increases until the fluid achieves the mean fluid flow velocity. Higher viscosity fluids exhibit higher drag due to the higher attraction between fluid layers, which then leads to increased skin friction (Batchelor, 1970; Blevins, 1984; Davies, 2002; White, 2006; Fox and McDonald, 2011).

Laminar and turbulent boundary layers help describe fluid flow, where turbulent boundary layers lead to higher skin friction drag. The boundary layer is the fluid layer adjacent to the surface, with the innermost layer called the viscous sublayer. In this layer, laminar flow appears smooth and orderly whilst turbulent flow appears random and chaotic. Additionally, laminar flow is controlled by viscous forces between the fluid

molecules whereas turbulent flow is controlled by inertial forces. Turbulent vortices in the viscous sublayer naturally translate in the cross flow and streamwise directions, which leads to vortices intermingling and ejecting from the viscous sublayer. This movement increases momentum transfer and shear stress, which results in higher drag (Kline et al., 1967; Munson et al., 2005). Therefore, laminar flow is preferred for low drag; however in many real-world fluid flow applications, the boundary layers naturally transition from laminar to turbulent. This transition can be described with the dimensionless Reynolds number (Re), which is the ratio of inertial forces to viscous forces, or (White, 2006):

$$Re = \frac{VD}{\nu} \quad (4)$$

where V is the fluid mean flow velocity, ν the fluid kinematic viscosity, and D is the characteristic length which is the hydraulic diameter (for closed channel) or a distance downstream from the leading edge (for open channel). For a rectangular closed channel, $D = 4A/c$, where A is the cross sectional area and c is the wetted perimeter. Transition from laminar to turbulent flow depends on parameters in Eq. 4 as well as surface roughness and freestream disturbances, where such features may “trip” the boundary layer to become turbulent. Such transition occurs around $Re = 2300$ for closed channel and $Re = 500,000$ for open channel flow (White, 2006; Fox and McDonald, 2011).

3.2.1. Shark skin

Shark skin is designed with microstructured features that effectively control naturally occurring turbulent vortices, which leads to less momentum transfer and shear stress, and thus reduces drag. Therefore much attention has been given to actual shark

skin and the mechanisms at work. The skin of fast swimming sharks (such as Mako, *Isurus oxyrinchus*) is covered with scales called dermal denticles, which contain specially sized and spaced riblets oriented parallel to the swimming direction. Dermal denticles from both the Mako and Spiny Dogfish shark species are shown in Figure 21, with the flow direction indicated by the arrows.

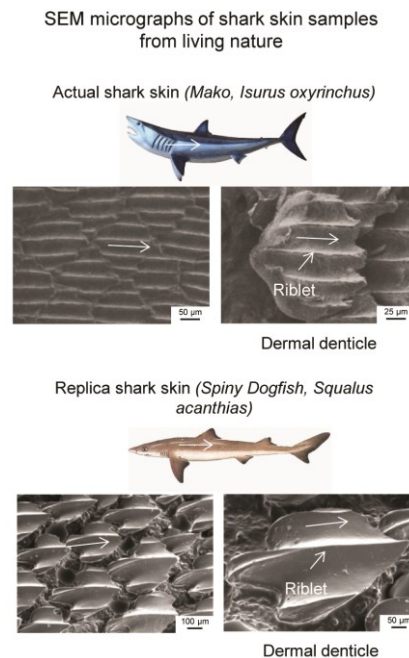


Figure 21: SEM micrographs of shark skin samples from living nature. Actual Mako (top) (adapted from Bixler and Bhushan, 2012b) and replica Spiny Dogfish (bottom) (adapted from Jung and Bhushan, 2010) shark skin micrographs are shown at two magnifications. These highlight the scales (dermal denticles) and riblets which are responsible for low drag and antifouling properties. Arrows indicate fluid flow direction.

The shape and size of the dermal denticles as well as the number of riblets varies between shark species. Riblets can also vary between different locations on the same shark (Reif, 1985; Bechert et al., 2000a, 2000b; Bhushan, 2012). However riblets operate on similar principles, where low drag is achieved by efficiently directing water at the solid-liquid interface.

The microstructured riblets encourage anisotropic flow as well as control vortices on the skin naturally present in turbulent flow. The riblets lift and presumably pin any vortices generated in the viscous sublayer, which leads to lower drag. Images in Figure 22 show flow visualization experimental results using smoke from atomized oil burned in air, both with and without riblets, and at two different velocities (V). Shown are the dimensionless riblet lateral spacing (s^+) and height (h^+) parameters, which provide helpful guidance to riblet optimization, as described in the following section. The images suggest that with appropriately sized riblets, vortices are lifted above the surface and presumably pinned at the riblet tips. Lifting reduces the total shear stress since vortices contact just the small riblet tips (as opposed to the total surface area). Pinning is believed to reduce the cross-stream motion of fluid (i.e. provides anisotropic flow) and ejection of vortices from the viscous sublayer, which reduces momentum transfer (Bechert et al., 1985, 1997a, 1997b, 2000a, 2000b; Lowrey and Harasha, 1991; Luchini et al., 1991; Lee and Lee, 2001; Dean and Bhushan, 2010; Deyuan et al., 2011b; Oeffner and Lauder, 2012). Turbulent vortices are also present in fluids besides water; therefore the shark skin inspired riblets are expected to provide a similar drag-reducing benefit with any fluid such as air and oil.

Flow visualization of vortices interacting with flat and riblet surfaces using smoke in air from atomized oil (flow into the page)

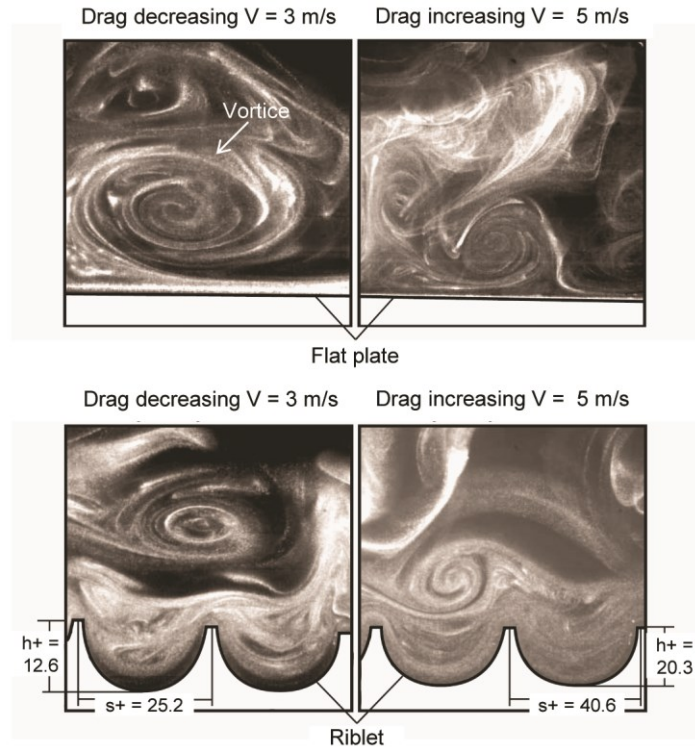


Figure 22: Flow visualization images using smoke from atomized oil burned in air to study the turbulent vortices behavior with and without riblets at two velocities (adapted from Lee and Lee, 2001). Top images show the vortices on a flat plate with a relatively large amount of surface contact area, which leads to higher drag. Bottom images show the vortices are lifted above the riblet tips, with a relatively small amount of surface contact area, which leads to lower drag. The dimensionless parameters for height (h^+) and spacing (s^+) aid in the understanding of riblet design for any flow condition. Such parameters are based on riblet spacing or height, fluid kinematic viscosity, and wall shear stress velocity.

3.2.2. Riblet optimization

In addition to experimenting with actual shark skin or replicas, research has been conducted by fabricating shark skin inspired artificial riblets. Such riblets represent those found on actual shark skin; however their shape and size differ in order to optimize the tradeoff between drag reduction and feasible manufacturing techniques. Optimizing riblet geometries is twofold; one is to lift and pin vortices, and the other is to minimize drag (skin friction) due to the riblets themselves. Since riblets protrude into the flow channel, the increased surface area equates to increased drag. In order to optimize drag reduction, the riblets should lift and pin the vortices as well as encourage anisotropic flow along the surface. Such efficient flow is found by considering each valley between riblets and minimizing the wetted perimeter, since increased wetted perimeter leads to increased drag.

Another consideration for riblet optimization includes utilizing dimensionless parameters (measured in wall units). These are denoted by the $^+$ symbol, which allow for better comparison of experiments with various riblet geometries and flow conditions. Minimizing energy losses can be accomplished with riblets that effectively lift and presumably pin the turbulent vortices. In general, skin friction or viscous drag increases with higher Reynolds numbers, which is related to energy dissipated through heat loss. As shown in Eq. 4, length multiplied by mean flow velocity and divided by kinematic viscosity provides the Reynolds number. Similarly, Reynolds numbers based on riblet parameters can also be calculated, which are useful for riblet optimization. Important riblet parameters include spacing (s), height (h), and thickness (t), which are described below.

The Reynolds numbers based on spacing and height of the riblets are defined as (Kline et al., 1967; Wilkinson 1983; Bechert et al., 1997a, 2000a):

$$s^+ = \frac{sV_\tau}{\nu} \quad (5)$$

$$h^+ = \frac{hV_\tau}{\nu} \quad (6)$$

The Reynolds numbers based on thickness is being defined here as:

$$t^+ = \frac{tV_\tau}{\nu} \quad (7)$$

where V_τ is the wall shear stress velocity.

Considering kinetic energy, the wall shear stress expression $\tau_o = \rho V_\tau^2$ provides the wall shear stress velocity as (Kline et al., 1967; Wilkinson 1983; Bechert et al., 1997a, 2000a):

$$V_\tau = \left(\frac{\tau_o}{\rho}\right)^{1/2} \quad (8)$$

where ρ is the fluid mass density.

For pipe flow, the approximate wall shear stress (τ_o) can be found by combining the Blasius and Fanning friction factor formulas (Kline et al., 1967; Wilkinson 1983; Bechert et al., 1997a, 2000a). The Blasius formula describes the coefficient of friction for turbulent flow as (White, 2006):

$$c_f = 0.0791(Re)^{-1/4} \quad (9)$$

The Fanning friction factor formula describes the coefficient of friction for laminar flow as (White, 2006):

$$c_f = \frac{2\tau_o}{\rho V^2} \quad (10)$$

Combining the two above equations and solving for wall shear stress yields:

$$\tau_o = 0.03955v^{1/4}\rho V^{7/4}D^{-1/4} \quad (11)$$

Determining optimal riblet dimensions for various flow conditions is possible by considering dimensionless parameters. For instance, the optimized riblet spacing for a given fluid can be determined by rewriting Eq. 5 where $s = s^+ v/V_\tau$. This equation indicates that for a constant s^+ value, the required riblet spacing for maximum drag reduction increases as kinematic viscosity (ν) increases (Bechert et al., 1992, 1997a, 2000a). Appropriate s^+ values may be determined by varying the riblet spacing with a constant flow velocity or vice versa, where varying velocity is generally more feasible. Experimental results will be presented later indicating that an s^+ near 15 is optimal for maximum drag reduction with various riblet geometries (Walsh, 1990b; Bechert et al., 1997a). Furthermore, it will be shown later that a correlation exists between riblet spacing, vortex diameter, and vortex lateral spacing.

Visualizing the interaction between riblets and vortices provides insight in order to optimize riblets. Turbulent flow visualization experiments indicate that vortices equal approximately 35-50 wall units in diameter (shown in Figure 22). Additionally, these measurements are verified with experiments using dye in water (Kline et al., 1967) and analysis of the turbulent boundary layer (Jang et al., 1986). Such dimensions are important in order to optimize riblet spacing. For experiments shown in Figure 22, velocities $V = 3$ m/s and 5 m/s produce s^+ values equaling 25.2 and 40.6, respectively. As presented, the $V = 3$ m/s case shows drag decreasing, whereas the $V = 5$ m/s case shows drag increasing. In the $V = 3$ m/s case, vortex diameter is larger than s^+ which leads to lifting the vortex, thus lowering drag. However for the $V = 5$ m/s case, the vortex

diameter is about the same as s^+ , therefore providing less vortex lifting, thus leading to higher drag. Furthermore, velocities $V = 3$ m/s and 5 m/s produce h^+ values equaling 12.6 and 20.3, respectively. For constant h/s , h^+ increases with s^+ , which then further increases the contact area between vortices and riblets; thus leading to higher drag.

Therefore an s^+ near 15 with $h/s = 0.5$ corresponds to approximately three riblets per vortex, where vortices are believed to remain lifted and presumably pinned about the riblet tips. Both s^+ and h^+ information is useful in order to determine relationships between drag, fluid viscosity, and riblet dimensions. Such information allows for scaling riblets for turbulent drag reduction and comparing experimental results.

3.3. Riblets and experimental methods

In this section, we first provide an overview of the various riblet designs and configurations. Next we present various fabrication techniques utilized to create riblets as well as their advantages and disadvantages. Finally we describe the experimental procedures for open and closed channel experimentation using water, oil, and air.

3.3.1. Riblet geometries and configurations

Shark skin dermal denticles and riblets exhibit rather complex three dimensional geometries and configurations, therefore fabrication of such microstructured features is challenging. Additionally, in order to study the dimensional effects of riblets in fluid flow, experiments with varying sizes of relatively durable fluid-tolerant riblets are necessary. However due to the micro-sized nature of the riblets, this poses difficulty in producing cost effective riblet samples, especially for larger sample sets. In response, the

assumably most important characteristics of the riblets have been identified, and then samples have been fabricated for experimentation.

Riblet sizes range from species to species and from location to location on sharks. For reference, the Spiny Dogfish shark *Squalus acanthias* has triangular shaped riblets with a base width of 100 to 300 μm , summit radius of about 15 μm , height of 200 to 500 μm , and spacing of 100 to 300 μm (Jung and Bhushan, 2010). Using actual riblets for inspiration, simplified artificial riblet samples include various combinations of blade, sawtooth, scalloped, and bullnose geometries with continuous and segmented (aligned and staggered) configurations. It is believed that actual shark skin most closely resembles scalloped riblets with a staggered segmented configuration. Schematics of simplified riblets fabricated for experimentation are illustrated in Figure 23, with typical geometries and configurations. Dimensions of interest include riblet height (h), spacing (s), thickness (t), and valley width (vw); and their importance will be discussed in the results section. Open and closed channel experiments and their subsequent geometries and configurations are summarized in Tables 7-9.

Shark skin inspired riblet geometries and configurations

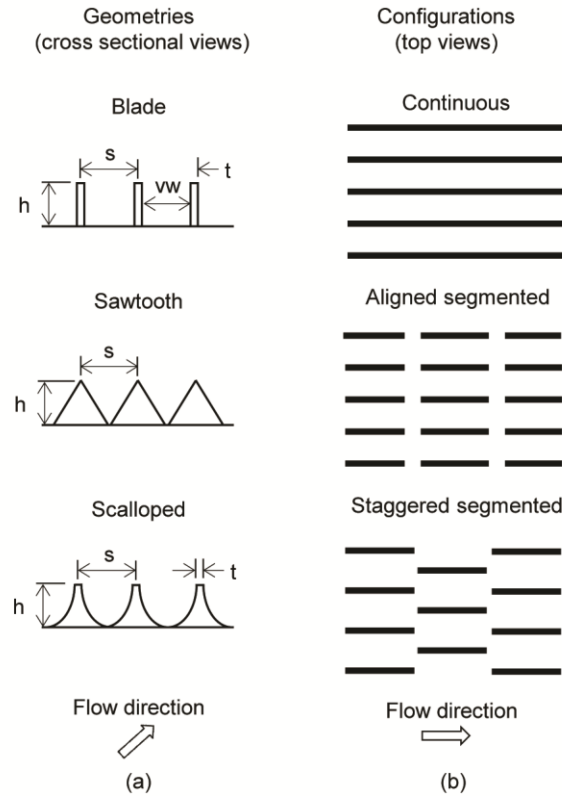


Figure 23: Typical shark skin inspired riblet geometries and configurations that have been experimentally evaluated (adapted from Bixler and Bhushan, 2013c). Shown are (a) blade, sawtooth, and scalloped geometries as well as (b) continuous, aligned segmented, and staggered segmented configurations. Actual shark skin most closely resembles the scalloped geometry and staggered segmented configuration.

Table 7: Open channel riblet experimentation.

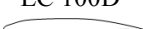
Fluid	Riblet design	Riblet configuration	Riblet material	Max turbulent drag reduction	Reference
Water	Sawtooth	Continuous	Polymer	8%	Reidy and Anderson (1988)
	Sawtooth	Continuous	Vinyl	9%	Rohr et al. (1992)
	Sawtooth	Continuous	Vinyl	6%	Walsh (1990a)
	Sawtooth	Continuous	Vinyl	13%	Neumann and Dinkelacker (1991)
	Sawtooth	Continuous	Polymer	7%	Gillcrist and Reidy (1989)
Oil	Blade, sawtooth & scalloped	Continuous	Brass & Plexiglas	9.9%	Bechert et al. (1997b)
	Blade	Staggered segmented	Brass	7%	Bechert et al. (2000a)
	Blade	Continuous	Titanium & nickel	4.9%	Buttner and Schulz (2011)
	Sawtooth	Continuous	Polyurethane	7.6%	Gruneberger and Hage (2011)
Air	Blade	Continuous	Metal & polymer	8.5%	Wilkinson and Lazos (1988)
	Blade	Staggered segmented	Epoxy	7%	Bechert et al. (2000a)
	Sawtooth, scalloped & bullnose	Continuous	Aluminum & vinyl	8%	Walsh (1982)
	Sawtooth, scalloped & bullnose	Continuous	Aluminum & vinyl	8%	Walsh and Lindermann (1984)

Table 8: Closed channel riblet experimentation.

Fluid	Riblet design	Riblet configuration	Riblet material	Max turbulent pressure drop/drag reduction	Reference
Water	Blade	Aligned segmented	Acrylic	23%*	Jung and Bhushan (2010)
	Blade & sawtooth	Aligned segmented & continuous	Vinyl & acrylic	22%*	Bixler and Bhushan (2013b)
	Sawtooth	Continuous	Vinyl	9%	Rohr et al. (1992)
	Sawtooth	Continuous	Polymer	28%	Reidy and Anderson (1988)
	Sawtooth	Continuous	Vinyl	7%	Lui et al. (1990)
Oil	Blade	Aligned segmented & continuous	Acrylic	7%*	Bixler and Bhushan (2013a)
Air	Blade	Continuous	Polymer	3%	Nitschke (1983)
	Blade & sawtooth	Aligned segmented & continuous	Vinyl & acrylic	11%*	Bixler and Bhushan (2013b)
	Sawtooth	Continuous	Epoxy	7%	Enyutin et al (1995)

*micro-sized channel

Table 9: Sawtooth riblet airfoil experimentation.

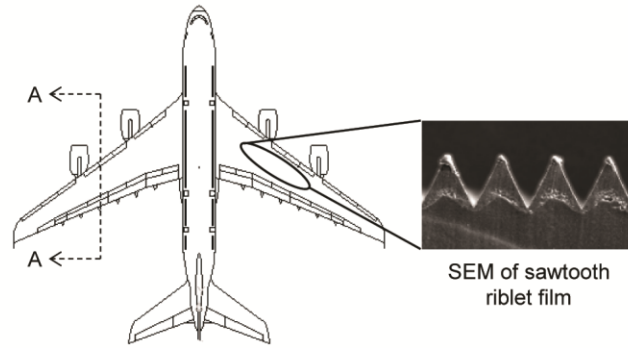
Reynolds number	Airfoil cross section description	Airfoil type	Sawtooth riblet size with $h=s$ (μm)	Riblets applied to longitudinal location /chord length	Trip applied to longitudinal location /chord length	Angle of attack	Max drag reduction	Reference
17,000	Symmetrical	NACA 0012 	180	0-100%	n/a	0°	4.3%	Han et al. (2003)
250,000	Symmetrical	NACA 0012 	23, 76, 152	10-100%	n/a	0°	13.3%	Caram and Ahmed (1991)
530,000 - 790,000	Thin	LC 100D 	76, 152	20-95%	2.5%	0°	2.7%	Coustols (1989)
750,000	Thin	GAW-2 	114	12-96%	10%	0-6°	6%	Sundaram et al. (1999)
1,000,000	Symmetrical	NACA 0012 	76, 152	12-96%	10%	0-6°	13%	Sundaram et al. (1996)
1,000,000	Thin	GAW-2 	76	12-96%	10%	0-12°	10%	Subaschandar et al. (1999)
1,000,000	Thin	NACA 0012 	76	12-96%	10%	0-12°	14%	Subaschandar et al. (1999)
1,000,000	Thick	NREL S807 	114	5-100%	5%	0°	5%	Wetzel and Farokhi (1996)
1,000,000 - 1,850,000	Thick	DU 96-W-180 	44, 62, 100, 152	40-100%	n/a	0°	5%	Sareen et al. (2011)
3,000,000	Thick	ADA-S1 	18	15-100%	6%	-0.5-1°	10%	Viswanath and Mukund (1995)
3,300,000	Thin	CAST 7 	17, 23, 33, 51	15-100%	n/a	0°	3.3%	Coustols and Schmitt (1990)
2,000,000 - 6,000,000	Symmetrical	NACA 0012 	44, 100, 152	0-100%	5%	0°	7%	Present work
4,900,000 - 22,300,000	n/a	Conical nose with cylindrical body 	33, 51, 76	87% coverage	n/a	0°	4%	Coustols and Cousteix (1994)

3.3.2. Riblet fabrication

Riblets have been fabricated with a variety of polymers and metals using various fabrication and assembly processes. The actual process depends on many factors, such as costs, geometry/configuration, durability, precision, accuracy, base material, experimental set-up, chemical compatibility, and sample set size. Feasible riblet fabrication techniques include using metal shims (Bechert et al., 1997a), machined acrylic (Bechert et al., 1997a; Dean and Bhushan, 2012), machined aluminum (Walsh and Lindemann., 1984), extruded/coextruded polymer (Marentic and Morris, 1992), embossed polymer (Marentic and Morris, 1992), soft lithography (Jung and Bhushan, 2010; Bixler and Bhushan, 2012b), photolithography (Brennan et al., 2010), wet and dry etching (Brennan et al., 2010), grinding (Denkena et al., 2010), rolling (Hirt and Thome, 2007), and laser etching (Dickinson and Proudley, 1991; Bixler and Bhushan, 2013b, 2013a). In general, blade and scalloped riblets are less durable than sawtooth riblets, and continuous riblets are easier to fabricate than segmented. Furthermore, photolithography is preferred for producing the most accurate two-dimensional riblet geometries, but can be cost prohibitive.

The 3M Corp (Minneapolis, MN) produces an experimental vinyl adhesive backed riblet sheet, which has been used in many fluid drag studies. The riblet cross sectional shape consists of equilateral triangles (sawtooth geometry) where the height (h) equals the spacing (s), as illustrated in Figure 23 and Figure 24. Sizes range from 44 to 150 μm . These sawtooth riblets have many advantages such as ease of installation onto large flat or curved surfaces and high durability. The sheets are reported to be either

Riblet drag reduction experiments



Airfoil with riblet film covering upper and lower surfaces

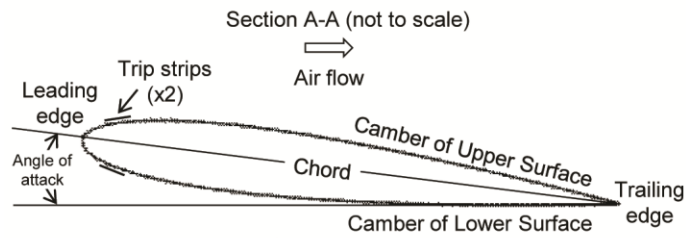


Figure 24: Riblet drag reduction experiments on airplanes and airfoils. In flight tests, total fuel consumption determines the amount of drag reduction. SEM micrograph shows the sawtooth riblet cross section (adapted from Sareen et al., 2011), where riblet grooves are oriented parallel to the fuselage. Section A-A illustrates a typical airfoil.

coextruded through a die capable of a patterned surface or more likely embossed with a negative master mold using heat and/or pressure (Marentic and Morris, 1992).

In addition to riblet geometries and configurations, researchers have examined the effect of applying coatings to alter wettability properties. For instance, studies suggest that superhydrophobic surfaces exhibit lower water drag (Ou et al., 2004; Jung and Bhushan, 2010; Daniello et al., 2009; Martell et al., 2009, 2010; Bhushan and Jung, 2011; Bhushan, 2012; Bixler and Bhushan, 2012b, 2013b) and self-cleaning (Genzer and Efimenko, 2006; Bhushan and Jung, 2011; Bhushan, 2012; Bixler and Bhushan, 2012b) properties, which are believed to promote antifouling. Furthermore, another study suggests that superoleophilic and possibly superoleophobic surfaces can also reduce oil drag (Bixler and Bhushan, 2013a). In a recent study, a nanostructured coating was created with silica particles and applied to laser etched polymer riblets (Bixler and Bhushan, 2013b) using a specified dip-coating method with nano particles suspended in a resin binder (Ebert and Bhushan, 2012a, 2012b). This coating is believed to actually improve the smoothness of milled or laser etched riblets, which may be desirable for air flow.

3.3.3. Drag measurement techniques

In this section, we present the various methods to evaluate riblets in water, oil, and air in both open and closed channel experiments. Within each of these experimental set ups includes descriptions of the various drag measurement techniques.

3.3.3.1. Open channel

Measuring drag in open channel is conducted with water and oil channels as well as in wind tunnels. Various methods include using force balances and wake traverses,

depending on the fluid and application. For instance, force balances measure water, oil, and air drag; whereas wake traverses measure wind tunnel airfoil drag (Caram and Ahmed, 1992; Viswanath, 1999). Riblets have also been evaluated on airplanes during flight tests, with riblets covering a portion of the wing and fuselage sections, as shown in Figure 24. Total fuel consumption is measured during the riblet flight tests in order to evaluate the total amount of drag reduction (Viswanath, 1999).

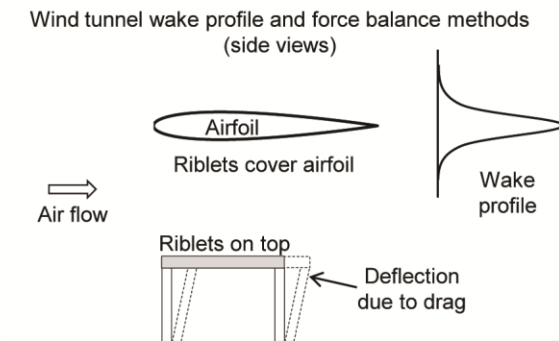
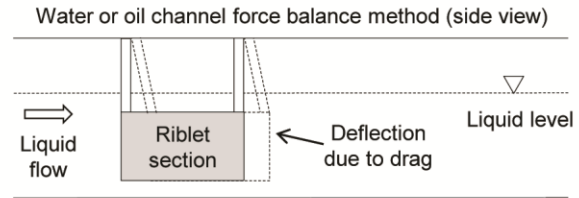
A typical force balance method for open channel experimentation is illustrated in Figure 25a, where flat sample plates mounted on a force balance are lowered into the moving liquid (typically water or oil). The flow rate is maintained with a flow channel set-up as illustrated in Figure 25b, with much research conducted using the so-called Berlin oil channel (Bechert et al., 1992). Propeller driven flow provides a constant current in order to measure the drag resistance force on the sample plates. The percentage drag reduction is calculated using the dimensionless expression $\Delta\tau/\tau_o$ (%), where $\Delta\tau$ is the difference between measured shear stresses on the riblet sample (τ) and the smooth (τ_o) surfaces.

Typical wake traverse and force balance methods for wind tunnel experimentation are also illustrated in Figure 25a. Many experiments have been conducted with subsonic tunnels, whereas fewer with the transonic or supersonic tunnels. A transonic wind tunnel design is illustrated in Figure 25b, which highlights the transverse wake probe and infrared camera locations. High pressure air in holding tanks is suddenly released into the settling chamber, which then flows across the airfoil sample at a known constant speed. Drag is measured using a traversing wake probe, which measures

Figure 25: Open channel methods and facilities to measure drag using water, oil, and air (adapted from Bixler and Bhushan, 2013c). (a) In water or oil channel flow, riblets are applied to a force balance plate that is lowered into the moving fluid (top). The deflection of the force balance translates into the total amount of drag. In airfoil experiments (bottom), the wake profile determines the total amount of drag. Drag may also be measured with riblets applied to a flat plate or airfoil using a force balance in the wind tunnel. (b) Open flow channels filled with water or oil are utilized with the force balance (top). Shown is the location of the motor and propellers that produce a constant flow. Wind tunnel schematic (bottom) illustrates set up for the wake traverse method. As air flows through the wind tunnel, the wake traverse lowers at a specified rate to measure the wake profile. Shown also is the infrared camera position utilized to visualize turbulence on the airfoil.

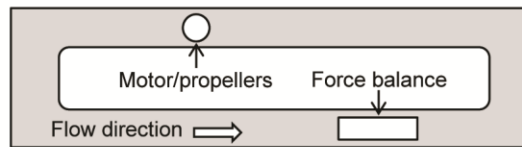
Figure 25.

Methods (a) and facilities (b) to measure open channel drag with water, oil, and air

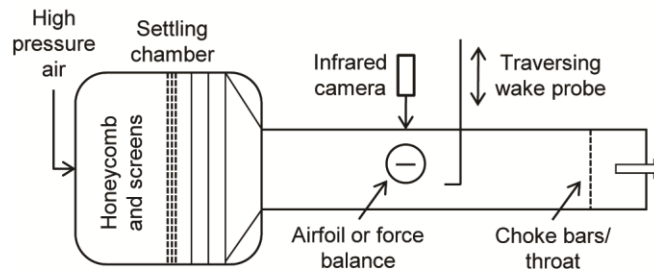


(a)

Water or oil channel facility (top view)



Wind tunnel facility (side view)



(b)

pressure by traversing downwind from the airfoil during experimentation. The probe measures the pressure in the airfoil wake, and when compared with a smooth airfoil is used to calculate the percentage drag reduction. The drag coefficient (C_d) is calculated with the wake integral expression using velocity calculated from the wake pressure profile (Lee et al., 1978; Barlow et al., 1999; Anderson, 2010). The percentage drag reduction is calculated using the dimensionless expression $\Delta C_d(\%)$, which is the difference between drag coefficient on the riblet sample and the smooth surfaces. For completeness, C_d is expressed as (White, 2006):

$$C_d = \frac{F_d}{0.5\rho V^2 A_w} \quad (12)$$

where F_d is the drag force and A_w is the total surface area in contact with the fluid (or wetted area).

A symmetric airfoil cross section is shown in Figure 24 with riblets applied to the upper and lower camber from the leading to trailing edges. Flow in a boundary layer over an airfoil may begin laminar, and then transition to turbulent depending on surface roughness or freestream disturbances. Trip strips help ensure the transition of laminar to turbulent flow at a particular location, which allows for a more direct comparison of experiments when the turbulent coverage is known (Barlow et al., 1999; Anderson, 2010). Airfoil geometries vary in design, as shown in Figure 26 with thin, thick, curved thin, reflex trailing edge, and symmetrical wing section options. Such geometries allow for low drag, high speed, low lift, and high drag when necessary. A summary of wind tunnel experiments is shown in Table 9, which presents airfoil designs with

Conventional airfoil side views and characteristics

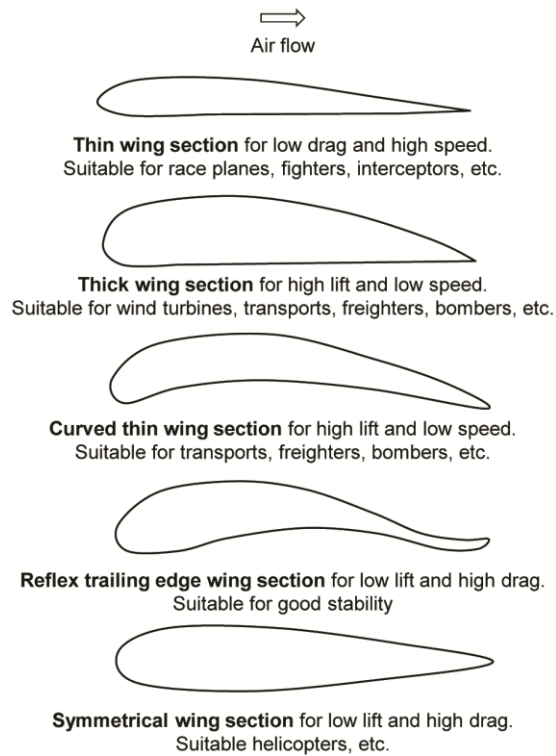


Figure 26: Conventional airfoil cross sectional side views. Shown are the thin, thick, curved thin, reflex trailing edge, and symmetrical wing sections (adapted from www.allstart.fiu.edu). Each airfoil is designed for specific applications due to their various attributes such as low drag and high lift.

designations such as NACA 0012 and GAW-2 for applications such as aircraft wings and wind turbines, respectively.

In wind tunnel experiments, riblet covered airfoils have been evaluated on over a wide range of speeds and angle of attacks. Accounting for compressibility effects, speed is defined as the Mach number (Ma), with subsonic ($Ma < 0.75$), transonic ($0.75 < Ma < 1.2$), and supersonic ($1.2 < Ma < 5$) designations. Military aircraft commonly experience transonic and supersonic flight, however commercial aircraft usually cruise between Mach 0.78 and 0.9 (Barlow et al., 1999; Unknown, 2007; Anderson, 2010). In the lab, achieving transonic or supersonic flow requires specialized wind tunnels that are relatively expensive to operate. The airfoil angle of attack is shown in Figure 24, which is the angle between the level horizontal and the chord lines. This angle varies during flight in order to maintain lift, where at lower and higher speeds, a higher and lower angle of attack are required, respectively. Experiments have been conducted between 0° and 12° angle of attack in order to cover the majority of cruise conditions (Unknown, 2007; Anderson, 2010).

Evaluating each of the airfoil designs over a wide range of Reynolds numbers covers a variety of applications of interest. For example, the wind turbine blades rotate much slower than the helicopter blade, so therefore lower Mach numbers and Reynolds numbers are applicable. Furthermore, various studies have examined complete or partial coverings of riblets on airfoils. Knowing that riblets may increase drag in laminar flow, riblets are only applied in the turbulent region of an airfoil, therefore leading to improved drag reduction. Trip strips are installed in many experiments in order to force transition to

turbulence at a particular location (Barlow et al., 1999; Anderson, 2010). A summary of conditions for open channel flat plate experiments is shown in Table 7 outlining the various riblet geometries, configurations, and materials that have been evaluated. Also Table 9 shows wind tunnel experiments that have been conducted with various airfoils, conditions, riblet coverage, and trip strip locations.

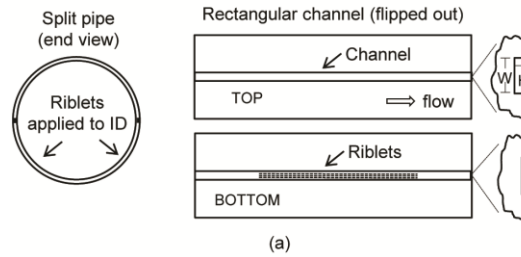
3.3.3.2. Closed channel

Measuring drag in closed channel flow is conducted with water, oil, and air experiments using both circular and rectangular cross section pipes and channels. Various closed channel experiments have been conducted using riblets applied to their interiors. In such cases, the fluid flows through the sample test area and the pressure difference between two points is measured with a pressure manometer, where lower pressure drop is desired. Apparatuses for both split round pipe and rectangular channel designs are illustrated in Figure 27a. Drag reduction is presented as negative $\Delta\tau/\tau_o$ (%) as well as pressure drop versus Reynolds numbers. Drag reduction is also described with negative $\Delta P/P_o$ (%) values, where ΔP is the difference in pressure drop between the riblet sample (P) and the smooth (P_o) surfaces.

Generally the greatest challenge is applying riblets inside of the closed channel. For larger pipes (or macro-sized closed channels), flexible sheets such as the 3M vinyl adhesive backed riblets can be applied to the interiors. Smaller pipes (or micro-sized closed channels) must be split in order to apply the flexible 3M riblet sheets. However, when riblets are not in the form of flexible sheets, they need to be fabricated via processes such as milling, soft lithography, or laser etching. Such fabrication generally

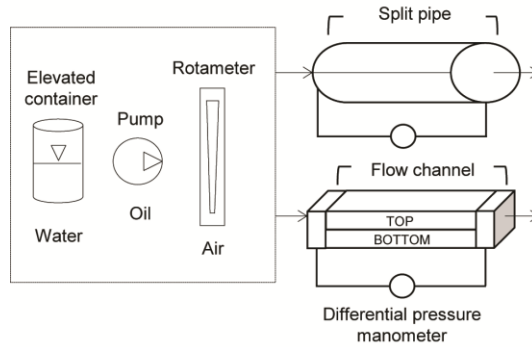
Methods (a) and apparatuses (b) to measure closed channel drag with water, oil, and air

Split pipe and rectangular channel methods



(a)

Closed channel drag measurement apparatuses using air, water, and oil



(b)

Figure 27: Closed channel methods and apparatuses to measure drag using water, oil, and air. (a) Split designs are necessary in order to apply riblets inside micro-sized closed channels. Left schematic shows a round split pipe whilst the right shows a rectangular channel sandwich design. The rectangular channel allows for riblets to be fabricated on a flat surface, which may be desirable (adapted from Bixler and Bhushan, 2013b). (b) Drag is determined via pressure drop reduction using closed channels lined with riblet samples. Flow is regulated with the elevated container (water), pump (water or oil), and laboratory air connected to a rotameter (air). The pressure drop is measured with a manometer connected to both ends of the flow channel. Interface views are shown highlighting the top and bottom halves that are sandwiched together.

requires flat and not curved surfaces. In these cases, the split rectangular channel design is more feasible by allowing riblets to be applied inside the channel prior to final assembly.

During experiments, fluid is introduced a variety of different methods depending on its viscosity and desired flow rates, as shown in Figure 27b. For instance, experiments with water have been conducted with both elevated bottle apparatuses (Jung and Bhushan, 2010; Bixler and Bhushan, 2013b) as well as syringe and gear pumps (Jung and Bhushan, 2010; Dean and Bhushan, 2012; Bixler and Bhushan, 2013b, 2013a). Experiments have been conducted with air flow by connecting a rotometer to a laboratory air supply (Jung and Bhushan, 2010; Bixler and Bhushan, 2013b), in order to achieve particular flow velocities. In the case of water and oil experiments, flow velocity can be calculated from the volumetric flow rate and channel cross sectional area. A summary of experimental closed channel conditions is shown in Table 8 outlining the various riblet geometries, configurations, and materials that have been evaluated.

3.4. Riblet results and discussion

In this section, we present open followed by closed channel drag measurement results using water, oil, and air flow. Results are discussed and compared between the various measurement techniques, riblet geometries, riblet configurations, and flow regimes. This comparison helps to provide an overview understanding of the past and present work on riblet drag reduction.

Open and closed channel results can be presented similarly, including drag compared to riblet dimensions and aspect ratios. Comparing and studying such

parameters allows for the development of lessons learned in order to optimize riblets. Micro-sized closed channel results are presented with pressure drop reduction compared to Reynolds number based on the channel dimensions. This differs from open channel results in order to account for hydraulic diameter, due to the interaction of vortices from neighboring walls, as described in Section 4.3. Therefore both open and closed channel results are presented in forms that best represent their findings.

3.4.1. Open channel

In open channel flow using water, oil, and air, results indicate that properly designed riblets can reduce drag. A summary of experimental results are presented in Table 7 for flat plate and Table 9 for wind tunnel airfoil flow. Several studies have included varying geometries and configurations, which have been conducted with laminar through turbulent flow. Drag reduction is presented as negative $\Delta\tau/\tau_o$ (%) and ΔC_d (%) values compared to Reynolds numbers.

3.4.2. Flat plate experiments

Water channel experiments indicate maximum drag reduction of nearly 6% using continuous sawtooth riblets on a flat plate, as shown in Figure 28. Results also show that the greatest drag reduction is around s^+ equaling 10-15 (Walsh, 1990b), which correlates well with oil channel findings (Bechert et al., 1997a). Extensive research has been conducted with oil channel flow, since oil allows for larger scale riblets, which drastically eases the challenge of riblet fabrication. Such experiments include blade, sawtooth, and scalloped riblet geometries with continuous and staggered segmented

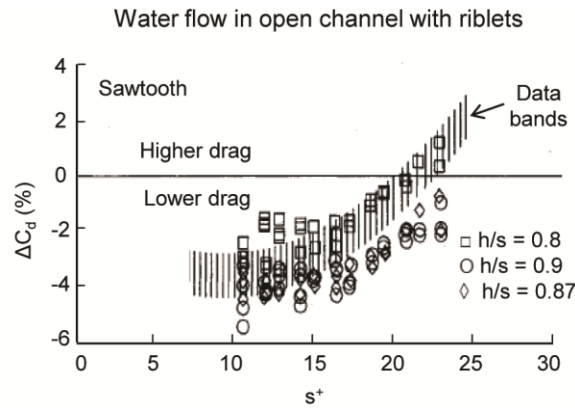


Figure 28: Open channel experimental results with riblets in water flow (adapted from Walsh, 1990a). Drag reduction is presented as Reynolds numbers compared to negative ΔC_d (%) values, which is the percentage drag coefficient reduction between the smooth and riblet samples. Riblet samples with various h/s values are compared, with the maximum drag reduction near 6%. Riblets are sawtooth geometry and continuous configuration.

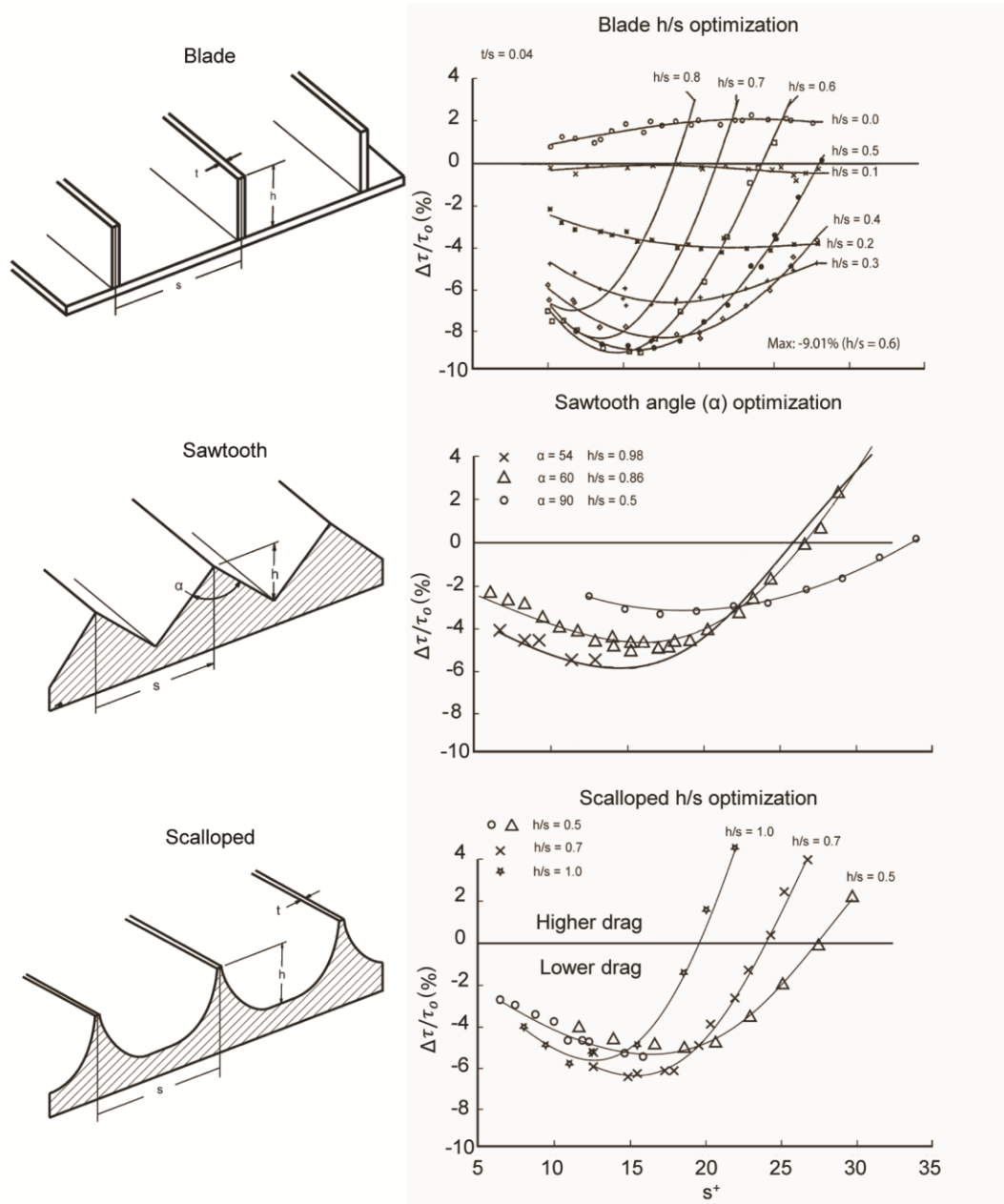
configuration, all using white paraffin oil ($\nu = 1.2 \times 10^5 \text{ m}^2/\text{s}$). This research is highlighted in Figure 29a, showing a wide range of h/s values, which are deemed important in determining the optimal drag reducing geometry. A summary of oil channel experiments is provided in Figure 29b, showing the greatest drag reduction from each of the geometries (Bechert et al., 1997a). Furthermore Figure 29c shows the effect of continuous and staggered segmented configurations (Bechert et al., 1997a, 2000a).

Results indicate maximum drag reduction of nearly 9% is possible with blade riblets where $h/s = 0.5$, $t/s = 0.04$, and $s^+ \approx 15$. This drag reduction further improves with a lower t/s value of 0.02, where maximum drag reduction is nearly 10% (Bechert et al., 1997a). Furthermore, sawtooth riblets with $h/s = 0.98$ and $\alpha = 54^\circ$ provides the greatest drag reduction of nearly 6%, indicating that the smaller α is beneficial. Also scalloped riblets with $h/s = 0.7$ provides the greatest drag reduction of nearly 7%. Results also indicate that staggered segmented trapezoidal shaped riblets provided less drag reduction compared to continuous blade riblets (about 6% versus 10%) (Bechert et al., 1997a, 2000a). However, the staggered segmented provides drag reduction (albeit less magnitude) for a larger s^+ range, as compared to the continuous riblets.

Figure 29: Open channel experimental results with riblets in oil flow (adapted from Bechert et al., 1997b, 2000a). Drag reduction is presented as Reynolds numbers compared to negative $\Delta\tau/\tau_o$ (%) values, where $\Delta\tau$ is the difference between shear stresses on the riblet sample (τ) and the smooth (τ_o) surfaces. (a) Various experiments with blade, sawtooth, and scalloped riblets were conducted in order to discover the optimal geometry for maximum drag reduction. Varied parameters include the riblet geometry, h/s , t/s , and s^+ , which allows for a better comparison between experiments. Oil channel experiments were conducted using white paraffin oil. (b) Maximum drag reduction results from the various blade, sawtooth, and scalloped experiments are compiled. Results indicate that the blade geometry with $h/s \approx 0.5$ and $t/s \approx 0.02$ produces the maximum drag reduction of 10% near $s^+ \approx 15$. (c) Experimental results comparing continuous and staggered segmented blade riblets, indicating that latter configuration shows less drag reduction.

Figure 29a

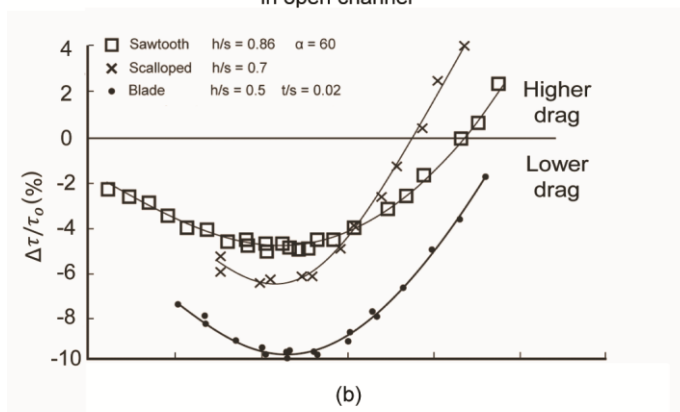
Oil flow in open channel with riblets



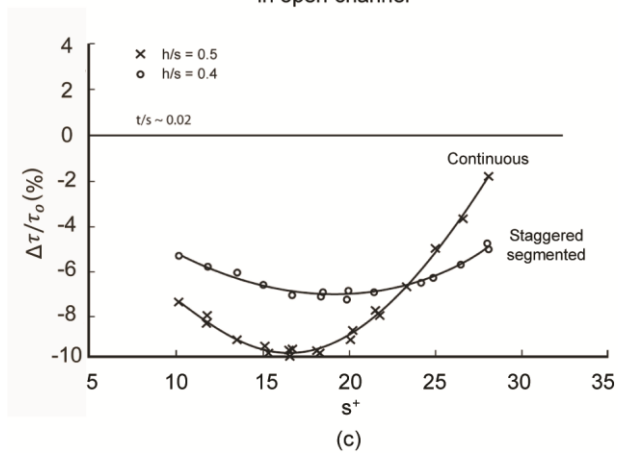
(a)

Figure 29b

Optimized riblet geometries with oil flow
in open channel



Blade riblet configurations with oil flow
in open channel



3.4.3. Flat plate observations

Many observations can be made from studying the presented water and oil channel experimental results. For instance, riblets with lower h/s values show less maximum drag reduction but over a wider range of s^+ values (e.g. blade riblets where $h/s = 0.2-0.3$ versus $h/s = 0.5$). This is presumably due to the vortices interacting with larger area on the riblets and with each other. Previously presented flow visualization indicates for the higher flow velocity (where s^+ and h^+ increase and $h/s = 0.5$) the vortices appear to lower in vertical elevation, and shear stresses at the riblet tips are believed to increase. With constant h and increasing s values (thus lowering h/s), it is believed that the vortices lower in between the riblets (for instance at $h/s = 0.2-0.3$ versus $h/s = 0.5$). Furthermore, increasing h/s increases wetted surface area between riblets, which leads to increased friction and thus drag.

Choosing an optimal h/s based on the aforementioned experimental results depends on particular applications, specifically whether or not the flow velocities are known or constant. For instance, riblets may be optimized for drag reduction over a wider range of s^+ values, where flow velocity conditions are varying. Conversely, riblets may be optimized for maximum drag reduction over a smaller s^+ range, where flow velocity is relatively constant, such as aircraft at cruising speed. In addition to h/s , the t/s ratio affects drag, where the smaller ratio is desirable. Furthermore research suggests that drag reduction is possible with sawtooth and scalloped riblets, but such geometries require differing h/s values. It should be noted that the blade riblets are the most fragile, followed by scalloped and sawtooth, so therefore clear tradeoffs are necessary when designing riblets for commercial applications.

3.4.4. Airfoil experiments

With the advent of the 3M vinyl riblet sheets, many experiments have been conducted with airfoils in wind tunnels. Such experimental results are shown in Figure 30a for riblets applied to the wind turbine DU 96-W-180 airfoil as well as the aircraft wing NACA 0012 airfoil. Results indicate that the smaller height riblets provide the greatest drag reduction, around 2% for the DU 96-W-180 airfoil (Sareen et al., 2011) and 7% for the NACA 0012 airfoil. Larger sized riblets and higher Reynolds numbers provide less drag reduction, and in some cases the drag increases compared to the smooth airfoil. The Reynolds numbers for experiments provide a wide spectrum of subsonic ($Ma < .75$ with $Re = 1,000,000$) to transonic ($0.75 < Ma < 1.2$ with $Re = 6,000,000$) velocities. This allows for comparison airfoils, Reynolds numbers, and riblet sizes. An additional variable of interest includes the angle of attack, as shown in Figure 30b using sawtooth riblets. The greatest drag reduction nearly 14% occurs at 6° angle of attack for the NACA 0012 airfoil (Subaschandar et al., 1999).

Since riblets are more effective in turbulent versus laminar regimes, and in order to better compare experiments, it is important to understand which areas of the airfoil are experiencing turbulence. Images in Figure 31 (present work) were taken during transonic wind tunnel NACA 0012 airfoil experimentation with a total covering from leading to trailing edges of vinyl sawtooth riblets provided by 3M Corp. The infrared camera detects heat generated by skin friction on the airfoil surface due to the turbulent boundary layer, where lighter colors indicate higher temperatures.

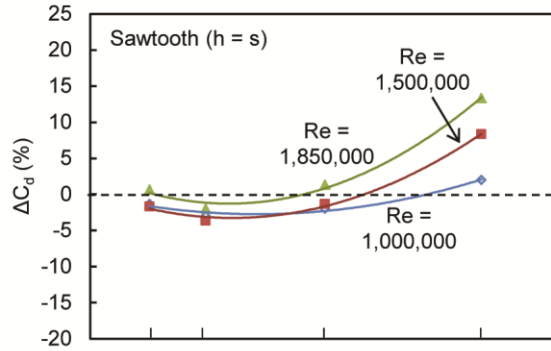
As illustrated, a turbulent trip strip is installed on the leading edge in order to ensure turbulent flow. Detecting the increased heat with an infrared camera is normally

Figure 30: Wind tunnel experimental results with riblets on airfoils. Drag reduction is presented as Reynolds numbers compared to negative ΔC_d (%) values, which is the percentage drag coefficient reduction between the smooth and riblet samples. (a) Drag reduction is shown with wind turbine DU 96-W-180 (adapted from Sareen et al., 2011) and symmetrical NACA 0012 (present work) airfoils with various 3M Corp. sawtooth riblets. The top and bottom Figures show Reynolds numbers in the subsonic and transonic ranges, respectively. Maximum drag reduction is near 7% for the riblets with $h = s = 44 \mu\text{m}$ in transonic flow. (b) Riblet drag reduction is related to angle of attack, as shown with two airfoils with angles of attack up to 12° . The greatest drag reduction of nearly 14% is shown at 6° angle of attack (adapted from Subaschandar et al, 1999).

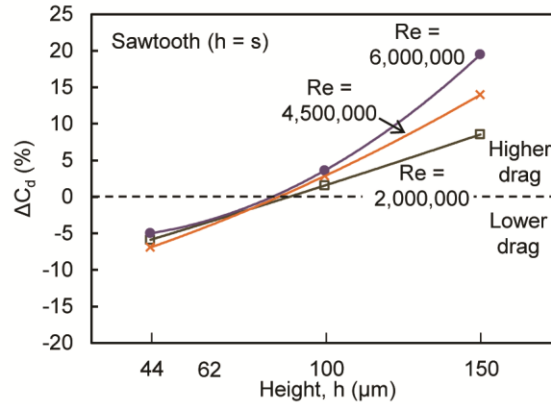
Figure 30

Air flow in wind tunnel with riblets

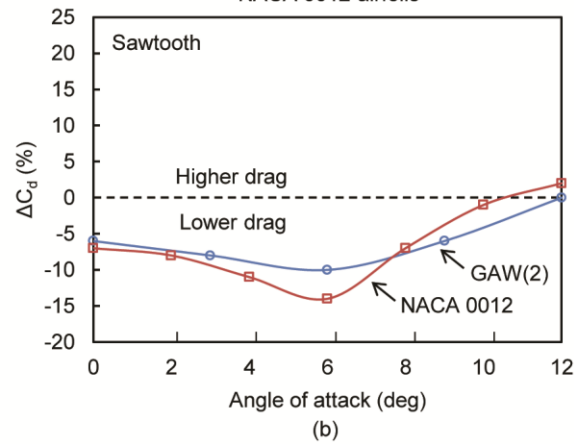
Subsonic speeds using DU 96-W-180 airfoil



Transonic speeds using NACA 0012 airfoil



Angle of attack using GAW(2) and NACA 0012 airfoils



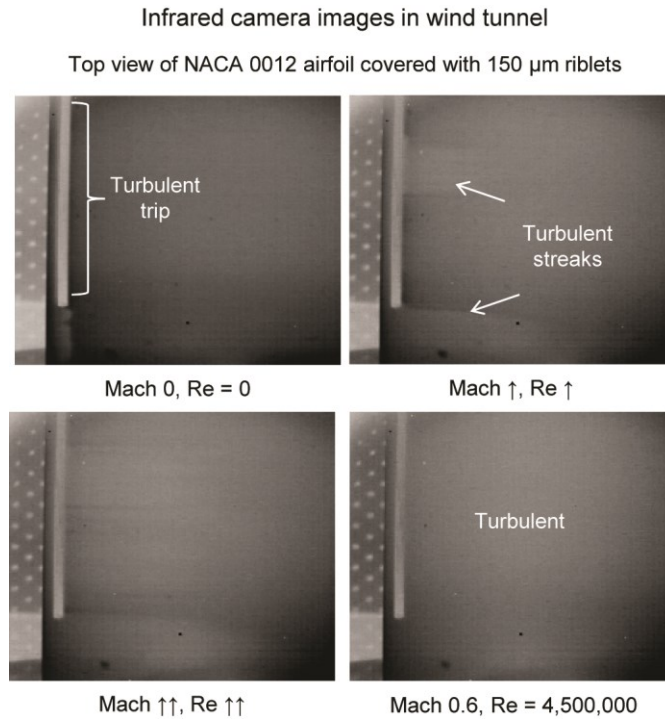


Figure 31: Detecting turbulent air flow using an infrared camera. In order to determine the extent of turbulent flow on an airfoil, an infrared camera may be employed. The friction from turbulent vortices heats the airfoil surface and is detected by the camera. Based on the airfoil geometry and calculated air velocity using pressure taps measurements, a fully turbulent state is shown with Mach 0.6 and $Re = 4,500,000$.

conducted with polymer airfoils, since the heat generated remains on the surface. However the airfoil utilized in the experiments was metallic, which acted as a heat sink, thus having the potential of lowering the surface temperature. Nevertheless, it was found that the vinyl sawtooth riblets applied to the metallic airfoil provided sufficient insulation from the heat sink effect thus providing usable images. Reynolds number is calculated from airfoil geometry and the wind speed found from pressure tap measurements (Gompertz et al., 2012).

The images in Figure 31 are shown from the start to the end of experimentation ($0 < \text{Mach} < 0.6$ and $0 < \text{Re} < 4,500,000$), with the white streaks representing turbulence. The upper left image shows the beginning state before experiments, indicating the baseline airfoil surface temperature based on ambient air temperature conditions. The upper right image shows that with increasing Mach and Reynolds numbers that turbulent white streaks begin to appear. The bottom left image shows that with higher Mach and Reynolds numbers that the white streaks cover more of the airfoil surface. Finally, the bottom right image shows what is believed to be a fully turbulent state with white streaks covering nearly the entire airfoil surface. As indicated earlier a Reynolds number over 500,000 for open channel flat plate flow is considered turbulent, and the Reynolds number here is calculated at 4,500,000.

Boundary layers shown in Figure 32 illustrate a conceptual model of flow over an airfoil and flat plate. As shown with increasing Mach number (and thus Reynolds number), the turbulent boundary layer thickness decreases. Riblets are effective by remaining inside the turbulent viscous sublayer, in order to properly lift and presumably

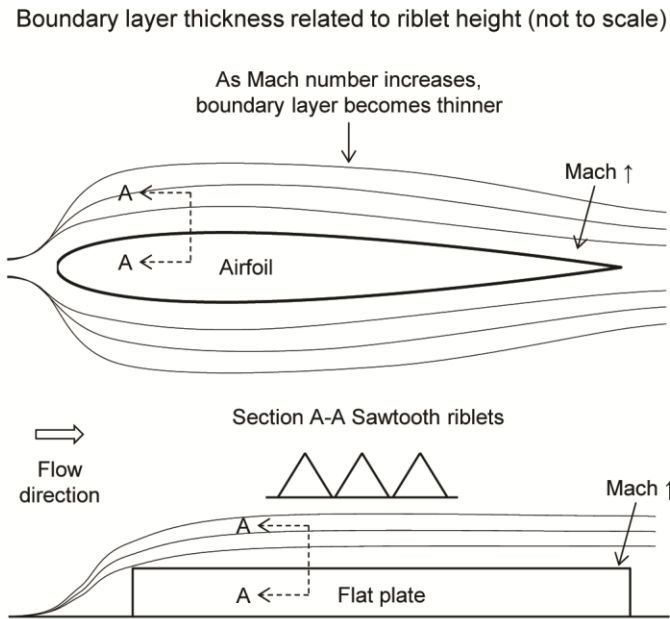


Figure 32: Boundary layer thickness related to riblet height. As the Mach number increases, the boundary layer thickness decreases. It is believed for drag reduction that riblets should remain inside the viscous sublayer in order to effectively control the turbulent vortices. Shown is an illustration (not to scale) explaining the relationship.

pin any vortices. However, if the riblet protrudes outside of the viscous sublayer, the increased surface area of the riblets will increase skin friction and thus drag. Therefore, it is believed that riblets must remain within the viscous sublayer in order to provide benefit.

3.4.5. Closed channel

In closed channel flow using water, oil, and air, results indicate that properly designed riblets can reduce drag. A summary of micro-sized closed channel experimental results are presented in Table 8. Several studies have included varying geometries and configurations, which have been conducted with laminar through turbulent flow. Drag reduction is presented as negative $\Delta\tau/\tau_o$ (%) and pressure drop values compared to Reynolds numbers.

3.4.5.1. The role of channel dimensions

A comparison of open and macro-sized closed channel results show that drag reduction is similar when neighboring wall effects are negligible, as indicated in Figure 33. These results represent cases when neighboring walls are sufficiently far apart, as shown with pipe diameters approximately 25 mm or greater. However when channel dimensions are relatively small (as shown in Figure 27a with micro-sized closed channel where $H = 0.7$ mm and $W = 3.2$ mm), neighboring wall effects are believed to play an important role in riblet drag reduction. A set of experiments were conducted with such micro-sized closed channels, with results presented in the following section.

3.4.5.2. Micro-sized channel experiments

Micro-sized closed channel experiments have included varying geometries, configurations, hydrophobicity, oleophilicity, and channel dimensions with laminar

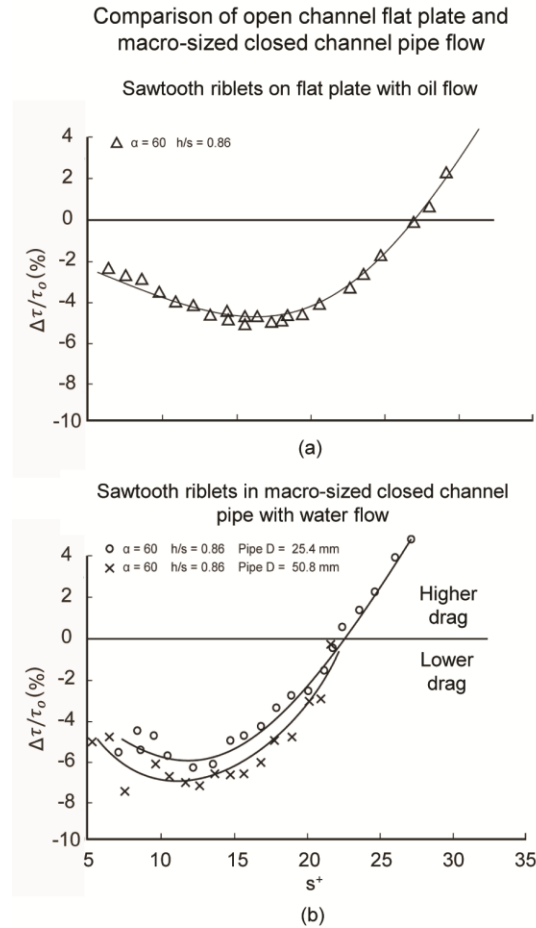


Figure 33: Comparison of open channel flat plate and macro-sized closed channel pipe flow (where neighboring wall effects are assumed negligible). Drag reduction is presented as Reynolds numbers compared to negative $\Delta\tau/\tau_0$ (%) values, where $\Delta\tau$ is the difference between shear stresses on the riblet sample (τ) and the smooth (τ_0) surfaces. Samples consist of sawtooth geometry where the angle $\alpha = 60^\circ$, as defined in Figure 10a. (a) Experimental results are shown with sawtooth riblets on a flat plate (Bechert et al., 1997b) and (b) in round pipe with diameter D (Liu et al., 1990). Maximum drag reduction is similar between the presented flat plate and macro-sized pipe flow.

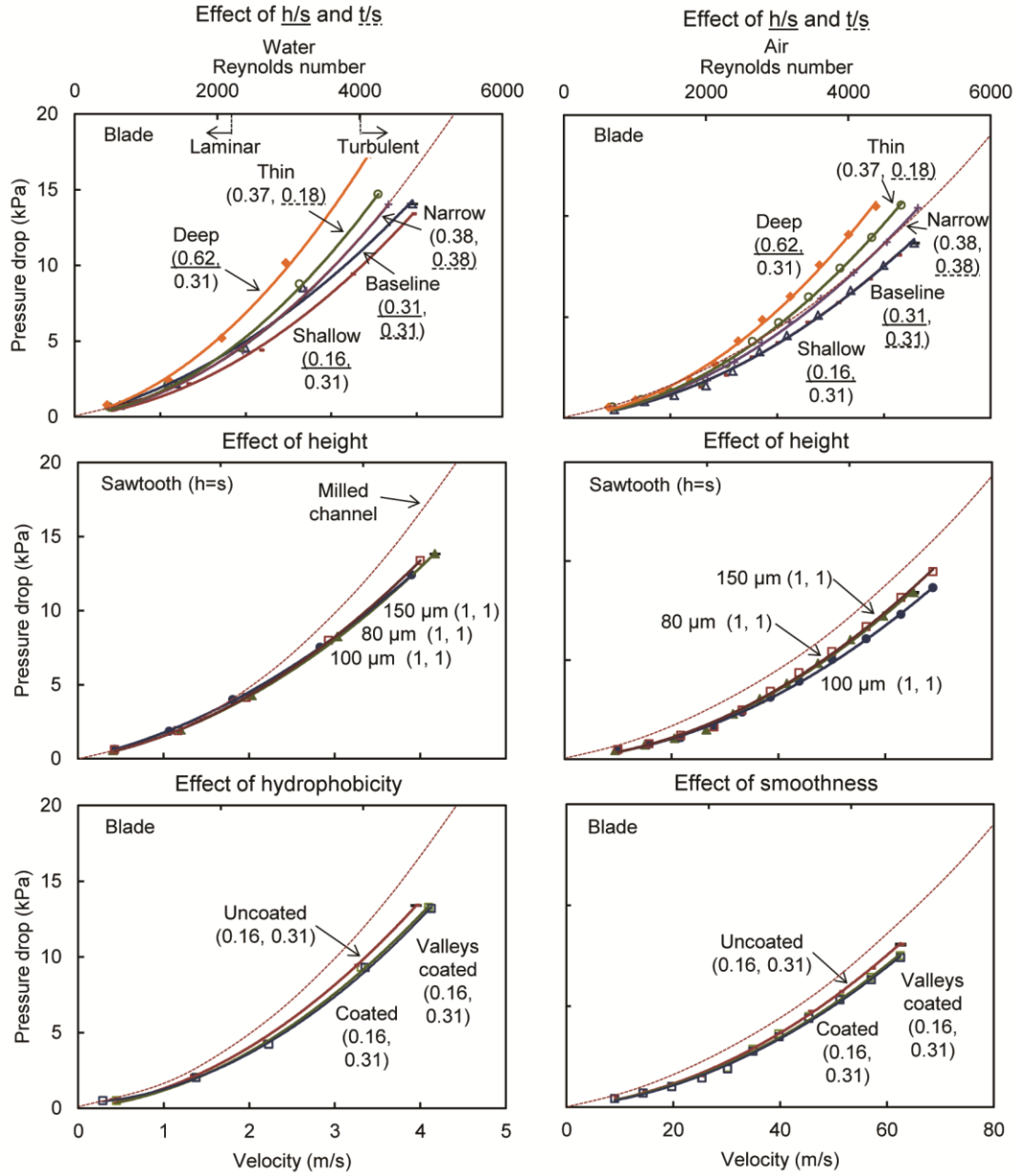
through turbulent flow (Bixler and Bhushan, 2013b, 2013a). The presented results include samples reported with riblets designated as “sample description (h/s, t/s)” value. For example, the 3M riblet sample with height and spacing equaling 44 μm is written as “44 μm (1, 1)” or more simply “44 μm sample”. The baseline blade dimensions were $h = 127 \mu\text{m}$, $vw = 280 \mu\text{m}$, and $t = 127 \mu\text{m}$, with variations presented later in the modeling section. All samples exhibit blade geometry with the aligned segmented configuration, except the 3M riblets which exhibit sawtooth geometry and continuous configuration. Also select riblet samples received a nanostructured coating (e.g. “coated” samples). Such coated samples are either superhydrophobic or superoleophilic, and are believed to improve riblet smoothness. Furthermore, the same nanostructured coating applied to replica shark skin samples indicates that the coating lowers adhesion forces (Bixler and Bhushan, 2012b).

Presented are micro-sized closed channel water and air results in Figure 34 and oil (white paraffin oil with CAS 8012-95-1) in Figure 35, which are compared to the flat milled sample. Various riblet geometries and dimensions were evaluated in flows ranging from laminar to turbulent regimes. The effect of h/s and t/s, h, hydrophobicity/oleophilicity, and smoothness are shown. The Shallow sample shows the most pressure drop reduction at 19% in water and 13% in air (Bixler and Bhushan, 2013b). Due to their initial performance, these riblets received the nanostructured coating, which then produced an improved pressure drop reduction of 34% in water and 24% in air (Bixler and Bhushan, 2013b). The 100 μm sample also reduced pressure drop

Figure 34: Micro-sized closed channel experimental results with riblets in water and air flow (adapted from Bixler and Bhushan, 2013b). Drag reduction is presented as Reynolds numbers compared to pressure drops between the inlet and outlet of the channel, where lower pressure drop is desirable. Riblets of varying geometries were evaluated in laminar ($Re < 2300$) through turbulent flow ($Re > 4000$) conditions. Experiments evaluated the effect of h/s , t/s , height, hydrophobicity, and smoothness. Riblets were fabricated via laser etching, and a nanostructured coating was applied to achieve the desired hydrophobicity and smoothness. Maximum pressure drop reduction of 34% with water was recorded for hydrophobic riblets in the turbulent regime. Flat milled channel control sample is shown for comparison. Error bars show ± 1 standard deviation.

Figure 34

Water and air flow in micro-sized closed channel with riblets



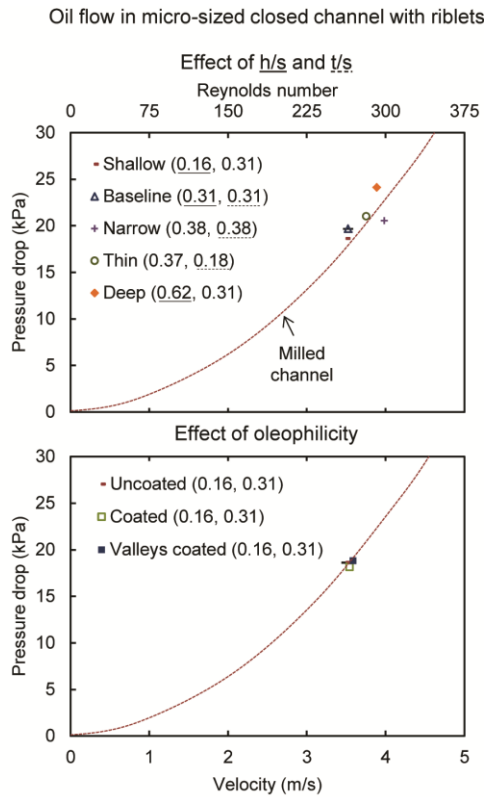


Figure 35: Micro-sized closed channel experimental results with riblets in oil flow (adapted from Bixler and Bhushan, 2013a). Drag reduction is presented as Reynolds numbers compared to pressure drops between the inlet and outlet of the channel, where lower pressure drop is desirable. Riblets of varying geometries were evaluated in laminar ($Re < 375$) flow conditions. Experiments evaluated the effect of h/s , t/s , and oleophilicity. Riblets were fabricated via laser etching, and a nanostructured coating was applied to achieve the desired oleophilicity. Maximum pressure drop reduction of 9% was recorded for the Narrow riblets. Experiments were conducted using white paraffin oil. Flat milled channel control sample is shown for comparison. Error bars show ± 1 standard deviation.

by 30% in water. In oil flow, the Narrow sample shows the most pressure drop reduction at 9% (Bixler and Bhushan, 2013a).

3.4.5.3. Micro-sized channel observations

Many observations can be made from studying the presented water, oil, and air micro-sized closed channel experimental results. For instance, lower h/s values appear to provide the greatest drag reduction, although this differs from the open channel results. However with rectangular micro-sized closed channel experiments, the neighboring wall effects are believed to play a role in the drag reduction. In the closed channel experiments, samples with the lowest h/s performed the best presumably due to less interaction between the vortices on the top and the bottom. This effect is described later in more detail.

Understanding the differences in performance between riblet samples in water, oil, and air flow can be explained by considering the Reynolds numbers as well as the drag reducing mechanisms. It is believed that different mechanisms are at work, mainly due to the effect of viscosity, as well as Reynolds number. For instance, water and air flow was turbulent, where the riblets are believed to lift and pin the vortices, and thus reduce drag. However, oil was laminar, which benefited from the so-called thin oil film, which reduces skin friction at the solid-liquid interface and thus reduces drag (Bixler and Bhushan, 2013a). The thin oil film effect will be shown and discussed later in more detail. Additionally, it is believed that turbulent oil flow would benefit from the shark skin effect.

3.4.5.4. Continuous versus segmented riblets

To understand the effects of riblet configurations, namely continuous and aligned segmented, a series of water, oil, and air flow experiments were conducted (Bixler and Bhushan, 2013b, 2013a). Results are presented in Figure 36, which shows the blade samples Continuous and Baseline, representing the continuous and aligned segmented configurations respectively. Intuitively, the Continuous sample should provide higher drag due to the increased wetted surface area. Each experiment with the Continuous sample exhibits a higher drag as compared to the Segmented sample. However, this drag increase is less with air as compared to water, for similar Reynolds numbers. The continuous blades may reduce cross stream movement with air more efficiently than with segmented blades. As the lower viscosity air vortices rotate in the channel, the gap area between segmented blades perhaps disrupts and unpins the vortices.

3.4.5.5. Riblets on top or bottom or both sides

To understand the effects of riblets on one versus two sides and with differing micro-sized channel heights, a series of water flow experiments were conducted (Bixler and Bhushan, 2013b). Such combinations included experiments with 1x channel height, 2x channel height, riblets on bottom, riblets on top, and riblets on top and bottom; all with Shallow samples. The top row of Figure 37 shows results from riblets on the top only and bottom only. Results indicate that riblets located on the bottom side perform differently from the same riblets located on the top side. The pressure drop increases by 20% when the riblets are transferred from the bottom to the top (Bixler and Bhushan, 2013b).

Figure 36: Micro-sized closed channel experimental results showing the effect of continuous vs. segmented blade riblets with water, oil, and air flow (adapted from Bixler and Bhushan, 2013b, 2013a). Drag reduction is presented as Reynolds numbers compared to pressure drops between the inlet and outlet of the channel, where lower pressure drop is desirable. Riblets were evaluated in laminar ($Re < 2300$) through turbulent flow ($Re > 4000$) conditions. Results indicate that the continuous riblets increase drag with all fluids, presumably due to the increased wetted surface area, which leads to higher skin friction. Flat milled channel control sample is shown for comparison. Error bars show ± 1 standard deviation.

Figure 36

Effect of continuous vs. segmented riblets with micro-sized closed channel flow

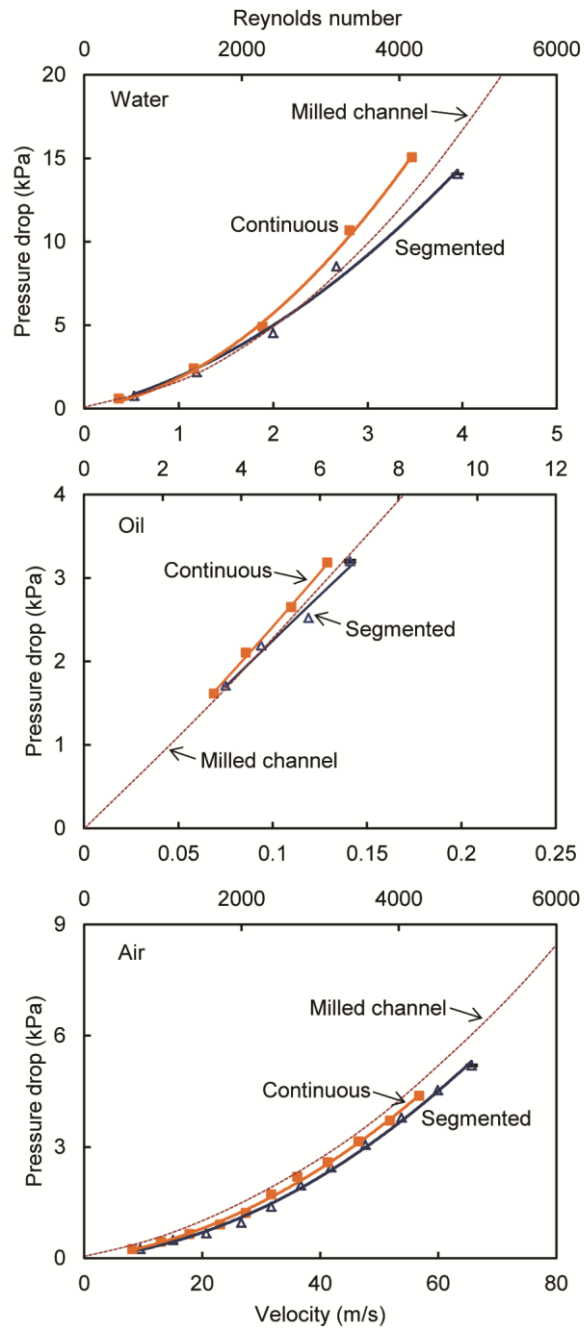
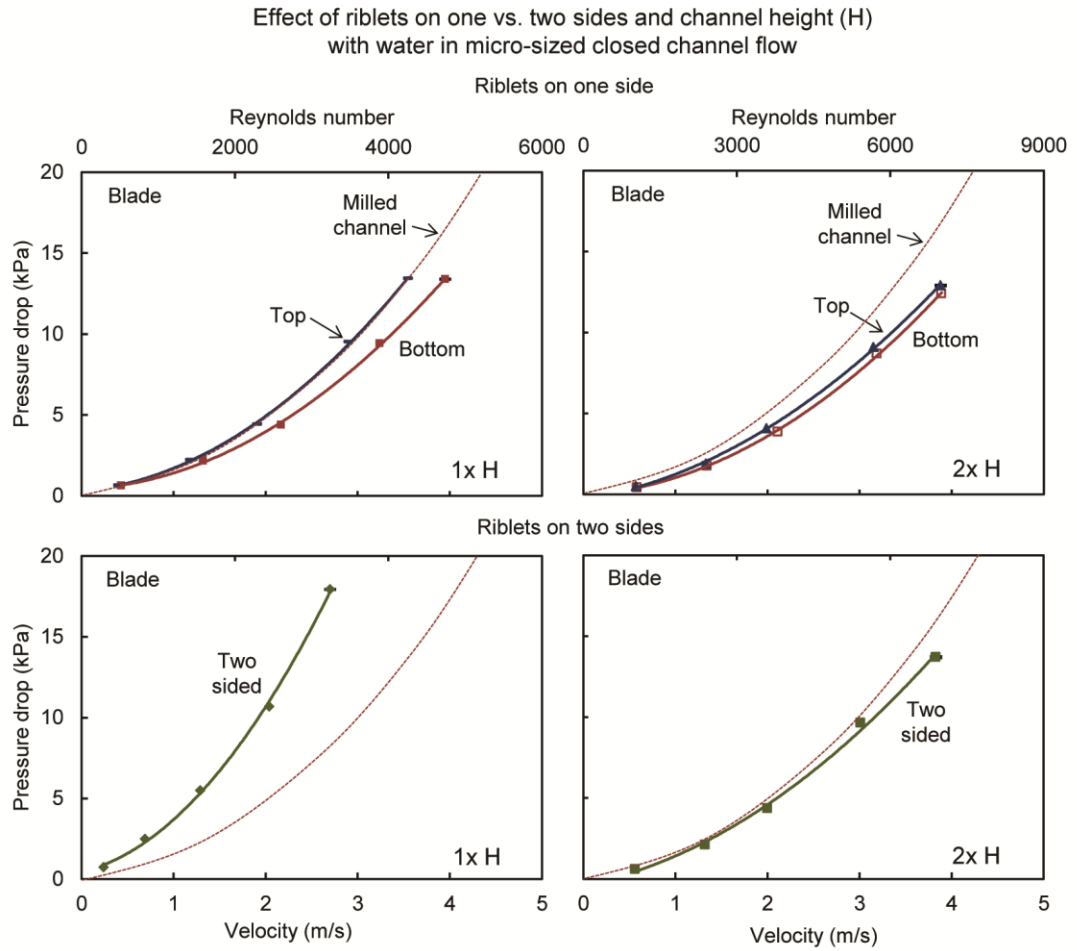


Figure 37: Micro-sized closed channel experimental results showing the effect of channel height and riblets on the top, bottom, or both sides with water flow (adapted from Bixler and Bhushan, 2013b). Drag reduction is presented as Reynolds numbers compared to pressure drops between the inlet and outlet of the channel, where lower pressure drop is desirable. Riblets were evaluated in laminar ($Re < 2300$) through turbulent flow ($Re > 4000$) conditions. Results indicate that riblets on the bottom reduce drag more than when positioned on the top of the channel. Also, 2x channel height reduces drag, presumably due to vortices from the top and bottom moving apart (i.e. neighboring wall effects are negligible). Flat milled channel control sample is shown for comparison. Error bars show ± 1 standard deviation.

Figure 37



Similar experiments were conducted to study the effect of channel height with riblets on the top or bottom. Results indicate that pressure drop with the riblets on the

bottom are unaffected by channel height, but pressure drop improves with topside riblets and 2x channel height. The bottom row of Figure 37 shows results from riblets on both the top and bottom sides of the channel. Neighboring wall effects are assumed by observing the percentage pressure drop with the 1x channel height and decrease with the 2x channel height. It is believed that the vortices from neighboring walls with the 1x channel height interact and increase the drag, but the larger gap distance in the 2x channel height reduces this effect. The aforementioned effects are believed to have a connection with the vortices interaction, as described later when presenting the conceptual models.

3.4.5.6. The role of riblet wettability

A correlation exists when comparing riblet sample pressure drop results with and without the nanostructured coating. It was discovered that only appropriately sized riblets coupled with the nanostructured coating provide drag reducing benefit. Contact angle measurements in air using water and white paraffin oil droplets (5 μ L) for the various samples are shown in Figure 38 (Bixler and Bhushan, 2013b, 2013a). In water flow, drag reduction improves with superhydrophobicity and low adhesion (Bixler and Bhushan, 2012b, 2013b), in air flow with smoothness (Bixler and Bhushan, 2013b), and in oil flow with superoleophilicity (Bixler and Bhushan, 2013a). Results indicate that the coupling of appropriately sized riblets with the nanostructured coating is necessary. For instance, shark skin replicas were examined in another study with the nanostructured

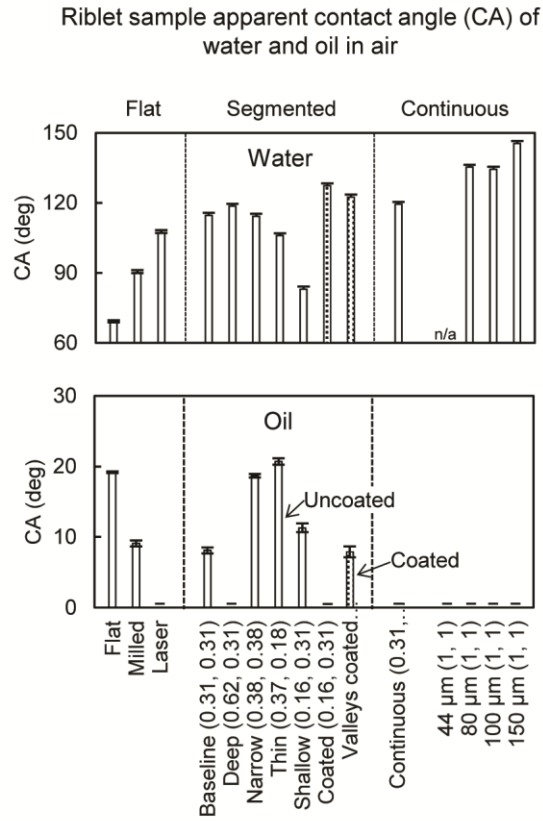


Figure 38: Apparent contact angle (CA) measurements for laser etched riblet samples; both with and without the nanostructured coating. Shown on the top and bottom are measurements at the solid-air-water (adapted from Bixler and Bhushan, 2013b) and solid-air-oil (adapted from Bixler and Bhushan, 2013a) interfaces, respectively. Error bars show ± 1 standard deviation.

coating, and the oil drag increased. This was likely due to the absence of the thin oil film effect (Bixler and Bhushan, 2013a).

3.5. Models of riblets and vortices

Experimental results with open and closed channel flow indicate drag reduction for a variety of riblets in water, oil, and air flow. However design principles differ depending on micro-sized closed channel dimensions, due to neighboring wall interactions. For instance, results indicate h/s for maximum drag reduction should be 0.5 for open channel and 0.16 for micro-sized closed channel flow. In order to fully understand the mechanisms behind the drag reduction, careful consideration is given to the boundary layer and riblet interaction. With experimental data from both water and air, there are several theories to imagine when describing the behaviors of vortices in turbulent conditions. Also presented is the drag reduction theory for laminar oil flow, which is called the thin oil film effect.

3.5.1. Riblets for open or macro-sized closed channel flow

Illustrations shown in Figure 39 provide one explanation of turbulent flow behavior and the effects of riblets of varying geometries, when neighboring wall effects are negligible (Bixler and Bhushan, 2013b). Shown are the effects on drag with regards to riblet tip to vortices contact area, riblet valley wetted surface area, vortices entanglement, and vortices pinning. Dimensions of interest include h , s , t , and v_w . The riblets and vortices are believed to be scalable; with the dominate features being lateral spacing (s^+), where s^+ equaling one third the vortex diameter is believed to provide maximum drag reduction with a variety of fluids and flow conditions. The s^+ value is an important

Turbulent vortices interaction with riblets
(flow into page, to relative scale)

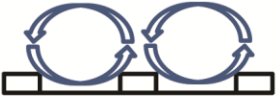
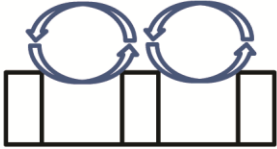
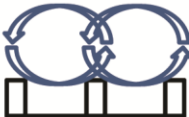
<p>Flat plate</p> 	<p>Vortices contact Surface area Entanglement Pinning Drag</p>
<p>Baseline (h, s, vw, t)</p> 	<p>Vortices contact ↓ Surface area ↑↑ Pinning ↑ Drag ↓</p>
<p>Shallow ($\frac{1}{2}h, s, vw, t$)</p> 	<p>Vortices contact ↓ Surface area ↑ Pinning ↑ Drag ↓↓</p>
<p>Deep ($2h, s, vw, t$)</p> 	<p>Vortices contact ↓ Surface area ↑↑↑ Pinning ↑ Drag ↑↑</p>
<p>Narrow ($h, \frac{7}{8}s, \frac{3}{4}vw, t$)</p> 	<p>Vortices contact ↓ Surface area ↑↑ Entanglement ↑ Pinning ↓ Drag ↑</p>
<p>Thin ($h, \frac{3}{4}s, vw, \frac{1}{2}t$)</p> 	<p>Vortices contact ↓ Surface area ↑↑ Entanglement ↑ Pinning ↓↓ Drag ↑</p>

Figure 39: Scale conceptual models of turbulent vortices interacting with various riblet geometries (adapted from Bixler and Bhushan, 2013b). Drag reduction is believed to be possible by lifting and pinning the naturally occurring fluid vortices. This results in less shear stress, momentum transfer, and vortices ejection from the viscous sublayer. A minimum riblet height is necessary to lift and pin the vortices.

parameter to study, since an s^+ too large allows vortices to drop between riblets, and an s^+ too small increases riblet tip to vortices contact area, both of which increase drag. In general, minimizing the higher velocity vortices' contact is desired, along with minimizing wetted perimeter for the lower velocity flow between riblets (Bixler and Bhushan, 2013b).

Entanglement is perhaps worse with the flat plate, and is believed to occur when riblets are too closely spaced. As thickness increases, so does drag, which is due to higher contact area between riblet tips and vortices. Therefore a minimal thickness is desired, although thickness is determined by fabrication techniques and material properties to maintain structural integrity during flow. The height effect is evident when comparing the three riblet heights, since the Deep sample shows the highest drag likely due to its increased riblet valley wetted perimeter. The h/s ratios were varied with increasing or decreasing height, which also affects the wetted perimeter of the sample. The best performer is the Shallow sample, since it is believed that the vortices are still lifted and pinned, but the entanglement and wetted perimeter are minimized. Furthermore, the values of t and t/s should be minimized in order to reduce the contact with the higher speed vortices, which are believed to interact with riblet tips (Bixler and Bhushan, 2013b).

3.5.2. Riblets in micro-sized closed channel flow

Micro-sized closed channel flow operates differently than macro-sized closed channel or open channel flow, so therefore an applicable conceptual model was developed as shown in Figure 40 (Bixler and Bhushan, 2013b). During such flow when

Vortices interaction with riblets in micro-sized closed channel (flow into page, to relative scale)

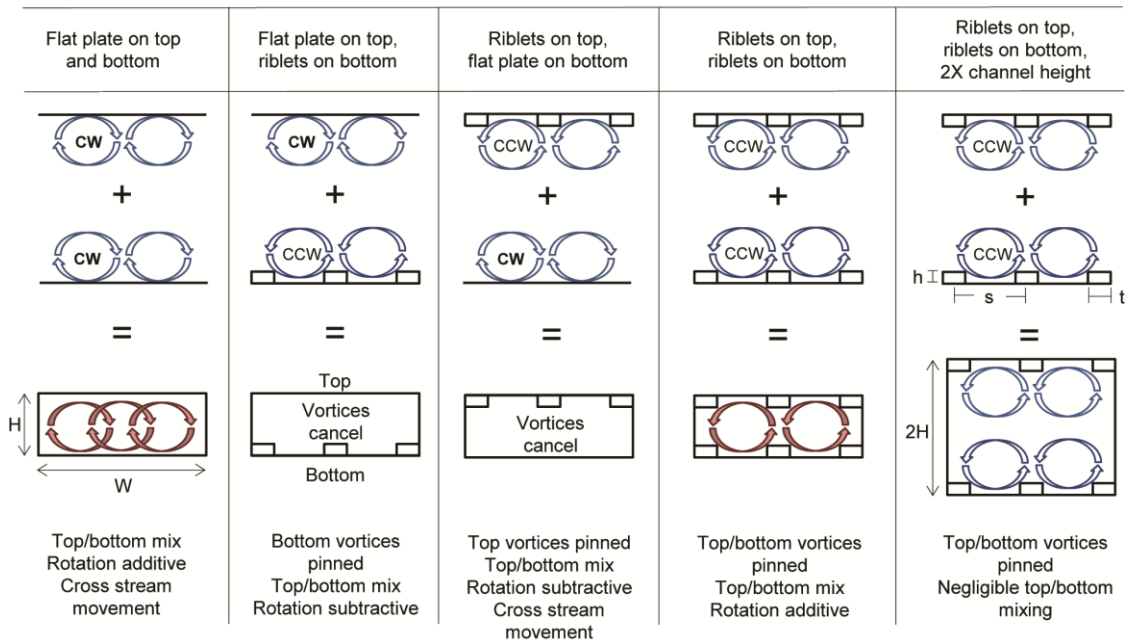


Figure 40: Scale conceptual models of micro-sized closed channel showing turbulent vortices' behaviors with the flat, Shallow sample, one or two sided, and 2x channel height combinations (adapted from Bixler and Bhushan, 2013b). Vortices are assumed to rotate clockwise on a flat plate and counterclockwise on riblets. When considering the two-sided nature of a closed channel, the rotational direction is believed to account for drag increase or reduction. A 1x channel height is believed to allow vortices from the top and bottom to interact and either increase the rotational speed or cancel each other. Cross stream movement occurs when vortices are not properly pinned, for instance as shown with a flat plate. Increasing the channel height to at least 3x vortex diameter is believed to move the top and bottom side vortices apart so that neighboring wall effects are negligible.

neighboring wall effects play a role, vortices from the top and bottom perhaps mix and their rotation is either additive or subtractive. The illustration highlights the assumed interaction between the vortices in micro-sized closed channel flow with and without riblets. This model shows how the top and bottom vortices may interact, which was developed from micro-sized channel and flow visualization experimental data presented earlier. Illustrated are channels with flat surfaces, riblets only on the bottom, riblets only on the top, riblets on both sides, and riblets on both sides with a doubled height. Understanding these interactions will aid in the design of efficient micro-sized closed channel flow systems.

In these models, vortices seem to rotate clockwise on flat plates and counterclockwise on riblet surfaces. This difference in direction affects how the vortices mix by determining if they reduce or increase total drag. Vortices that rotate in opposite directions may cancel each other and reduce total drag, as shown with riblets on one side (top or bottom). When no riblets are present, the vortices are believed to mix from the top and bottom, as well as translate in the cross stream direction, thus leading to high drag. Conversely, vortices that rotate in the same direction may add to one another, and increase total drag. When considering riblets on both sides (2x channel height), the vortices are believed to be lifted and pinned as expected. Furthermore since the channel height is ample, the top and bottom do not mix, thus reducing drag. Therefore a channel height of at least 3x the diameter of vortices (or ~ 150 wall units) is believed necessary to reduce drag (Bixler and Bhushan, 2013b).

3.5.3. Thin oil film effect

As previously mentioned, it is believed that the oil drag reduction mechanism differs from the water and air, mainly due to the viscosity effect as well as boundary layer condition. Experimental results indicate that drag reduction is possible with laminar flow, as shown with the micro-sized closed channel results presented earlier. This may be explained by the thin oil film concept, as illustrated in Figure 41. This model indicates that during flow, oil becomes trapped and holds stationary between the narrow riblets, and essentially lubricates the solid-liquid interface. The lubricating effect is believed to increase slip length (b), so therefore the flow velocity increases at the channel wall. A similar effect has been observed with the Pitcher plant (*Nepenthes genus*) peristome (Koch and Barthlott, 2009; Bhushan, 2009). This was later demonstrated with the so-called biomimetic SLIPS (Wong et al., 2011) as well as rice leaf and butterfly wing effect surfaces (Bixler and Bhushan, 2012b). Such an effect shows promise for drag reduction even with laminar flow.

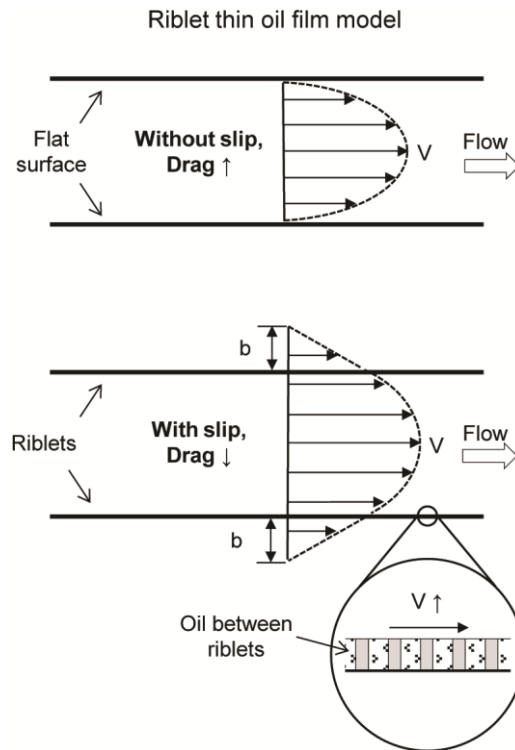


Figure 41: Riblet thin oil film model (adapted from Bixler and Bhushan, 2013a).

Appropriately sized riblets are believed to reduce drag by increasing the slip length b during laminar oil flow. Higher slip translates into lower drag and increased flow rate.

3.6. Conclusions and Outlook

Experiments attempting to unlock the secrets behind shark skin have included both open and closed channel flow, using a variety of blade, sawtooth, scalloped, and bullnose riblet geometries in continuous and segmented configurations. These have been studied with water, oil, and air in laminar through turbulent regimes. The majority of experimentation has been conducted with open channel flow. Such experiments measure drag with flat plates on force balances placed into water, oil, and air flows. Other experiments include airfoils in wind tunnels with drag measured by using wake traverses. More recently experiments have been conducted to measure drag via pressure drop reduction using riblet lined micro-sized closed channels. These experiments have provided greater insight to the role of neighboring wall effects and riblet drag reduction.

Riblets show an improved drag reduction in turbulent versus laminar flow, presumably due to the lifting and pinning of vortices. Results also indicate drag reduction improves in most cases with increasing Reynolds number (until expected plateauing). In open channel experiments, the maximum drag reduction up of 10% has been reported (Bechert et al., 1997a). In closed channel experiments, maximum pressure drop reduction up to 34% has been reported (Bixler and Bhushan, 2013b). Experiments using water, oil, and air also indicate that properly sized riblets combined with an appropriate nanostructured coating further enhances drag reduction. Mechanisms include superhydrophobicity for water, improved smoothness for air, and superoleophilicity for oil flow.

Producing optimal and scalable drag reducing riblets for any fluid is believed to require the following design principles: low h , t/s , t , and vw ; with $h/s = 0.5$, $s^+ \approx 15$, $H \approx$

150 wall units, blade geometry, and continuous configuration. In open and closed channel flow, riblets may be scaled up according to the fluid viscosity, where higher viscosity allows for larger riblets. Furthermore, micro sized closed channel flow requires additional considerations, such as the vortices interaction between the neighboring walls. Such design principles are applicable for open and closed channel flow; thus providing new insight for various medical, marine, and industrial applications.

The outlook of riblet technology is promising for a variety of applications; however a few areas could be further explored to provide greater insight into riblet optimization. These include more research to fully understand the role of riblets with oil flow. I suspect that oleophobicity will enhance drag reduction, but this needs to be verified. Furthermore, additional computer analysis would be helpful to verify and possibly discover new optimal riblet geometries for a variety of fluids and flow conditions. Such analysis should include visualizing vortices interaction with riblets and one another. Finally, bioassay experiments would be useful to quantify the antifouling effects of low drag riblets.

CHAPTER 4: Rice- and Butterfly-Wing Effect Inspired Low Drag and Antifouling Surfaces

4.1. Fouling formation

In this chapter, presented are fouling formation mechanisms, current antifouling methods, my new drag reduction/antifouling research, and conceptual models using rice and butterfly wing effect surfaces (in closed and open channel flow with air, oil, and water).

4.1.1. Biofouling

The general principles of biofouling formation and factors leading to the settlement on surfaces are similar in medical, marine, and industrial applications (Melo et al., 1988; Walker et al., 2000; Stoodley et al., 2002; Railkin, 2004; Monroe, 2007; Costerton, 2008; Chan and Wong, 2010; Bixler and Bhushan, 2012a). Biofouling morphology is characterized by the thickness, density, structure, composition, bioadhesive strength, and weight of fouling organisms (Marrie and Costerton, 1984; Keevil et al., 1999; Flemming et al., 2000; Hellio and Yebra, 2009; Chan and Wong, 2010; Simoes et al., 2010; Trinidad et al., 2010). During the biofouling process, microorganisms colonize a surface and then attract macrofoulers (Railkin, 2004; Costerton, 2008). In biofilms, microorganisms adhere to one another and the substrate with an adhesive called the extracellular polymeric substance (EPS). The biofilm continues to grow and become more diverse by attracting microorganisms. Shown in

Figure 10 is the five-stage colonization process, which includes initial attachment, irreversible attachment, initial growth, final growth, and dispersion. Initial attachment starts the colonization process, which begins within days to a few weeks. Initial attachment of microorganisms is reversible, but once they secrete the EPS, the bond becomes irreversible. This permanent attachment allows initial growth, final growth, and dispersion (Stoodley et al., 2002; Railkin, 2004; Monroe, 2007; Costerton, 2008).

Bioadhesion is important to consider for antifouling as it describes the adhesion strength to a surface (Stoodley et al., 2002; Railkin, 2004; Monroe, 2007; Costerton, 2008). This strength depends on the organism type, substrate, and separating fluid (Callow et al., 1986), due to influences of electrostatic forces and surface wettability (Feng and Jiang, 2006; Koch and Barthlott, 2009; Scardino, 2009; Sheng et al., 2010). The two-stage process starts with the initial attachment and then the irreversible attachment. Initial attachment is controlled by a physical adhesion between the microorganism and the substrate. Also known as adsorption, the initial colonists attach to a surface through weak, reversible van der Waals bonds, which are slightly stronger than electrostatic repulsive force. Irreversible attachment is accomplished with secretion of the EPS, which exhibits a sponge-like matrix. This adhesive permanently bonds the microorganisms to one another and to the surface (Flemming et al., 1999; Stoodley et al., 2002; Railkin, 2004).

4.1.2. Inorganic fouling

Inorganic fouling is composed of non-biological particles that may form in addition to or independently from biofouling (Somerscales and Knudsen, 1981; Walker et

al., 2000; Chan and Wong, 2010; Bixler and Bhushan, 2012a). Types of inorganic fouling include particulate, freeze, and gas stream particulate. Particulate fouling occurs when suspended solid particles deposit onto a surface, such as heat transfer tubing (Epstein, 1988). Deposition of crystals from freeze fouling occurs in locations such as cold region oil pipelines when waxy hydrocarbons contact cold pipe interior walls. Gas stream particulate fouling occurs in gas pipes, reactors, combustion chambers, and heat exchangers. This includes mineral, organic, and inorganic particles, which are common in oil or gas combustion systems (Bott, 1988a).

Biofouling may initiate inorganic fouling, where biocorrosion causes the formation of corrosion particles. Such fouling is prevalent in boilers, cooling condensers, desalination plants, food processing equipment, geothermal plants, and oil production equipment (Pritchard, 1988). Heat exchangers can develop hard deposits called “scale” or more porous deposits such as “sludge” (Bott, 1988b). Inorganic fouling particles may also originate from corrosion, crystallization, suspended particles, oil, and ice. For instance, salts from aqueous solutions crystallize and deposit on surfaces. Other deposits may result from minerals found in water such as magnesium, calcium, and barium (Somerscales and Knudsen, 1981; Walker et al., 2000; Chan and Wong, 2010).

4.1.3. Self-cleaning mechanisms

Wettability plays an important role in antifouling via self-cleaning, for instance as found in nature with the water repellent lotus leaf or water attracting pitcher plant surfaces (Koch and Barthlott, 2009; Bhushan, 2009, 2012; Wong et al., 2011; Nishimoto and Bhushan, 2013). In general for liquid repelling surfaces, it is necessary for the

surface tension of the repelling surface to be lower than the liquid being repelled. Contact angle (CA) is the angle between the liquid and surface whilst contact angle hysteresis (CAH) is the difference between the advancing (downhill side) and receding (uphill side) contact angles. Furthermore, common wetting regimes include Cassie-Baxter (droplet sitting on top of asperities with air pocket) and Wenzel (droplet penetrating gaps between asperities). High CAH and adhesion strength explains the deformed shape of a water droplet adhered to a vertical window (Nosonovsky and Bhushan, 2008).

With lotus effect, a high CA ($> 150^\circ$) coupled with low CAH ($< 10^\circ$) repels many liquids and may remove contaminant particles (Koch and Barthlott, 2009; Bhushan, 2009, 2012). With pitcher plant effect, a thin surface water film encourages the sheeting or shearing effect which may also remove contaminant particles (Nishimoto and Bhushan, 2013). This effect occurs when water uniformly spreads and traverses the surface removing any contaminants, as compared to droplets beading up and rolling off with contaminants (i.e. lotus effect). Similar self-cleaning mechanisms are possible with a variety of liquids, depending on the surface's ability to repel or attract the liquids. In either case, self-cleaning is most effective when the contaminant particles are sufficiently larger than the surface microstructures. For instance, the droplets would be unable to contact and gather contaminant particles that rest within the Cassie-Baxter regime air pockets (Bixler and Bhushan, 2013d, 2013e).

To further understand mechanisms behind liquid repellent surfaces, Young's equations are useful to examine the roles of solid-air, solid-liquid, and liquid-air surface tensions (Bixler and Bhushan, 2013a). To start, a water droplet placed on a surface in air

forms the solid-air-water interface and the droplet contact angle can be measured. The equation for the contact angle of a water droplet θ_W in air is predicted by Young's equation (Israelachvili, 1992):

$$\cos\theta_W = \frac{\gamma_{SA} - \gamma_{SW}}{\gamma_{WA}} \quad (13)$$

where γ_{SA} , γ_{SW} , and γ_{WA} are the surface tensions of the solid-air, solid-water, and water-air interfaces, respectively. Eq. 13 predicts that hydrophilicity is possible when $\gamma_{SA} > \gamma_{SW}$.

However, the equation for the contact angle of an oil droplet θ_O in air is predicted by Young's equation:

$$\cos\theta_O = \frac{\gamma_{SA} - \gamma_{SO}}{\gamma_{OA}} \quad (14)$$

where γ_{SA} , γ_{SO} , and γ_{OA} are the surface tensions of the solid-air, solid-oil, and oil-air interfaces, respectively. Eq. 14 predicts that oleophilicity in air is possible when $\gamma_{SA} > \gamma_{SO}$ where the surface energy of a solid surface must be higher than the surface tension of the oil (Jung and Bhushan, 2009; Liu et al., 2009).

Furthermore, the equation for contact angle of an oil droplet θ_{OW} in water is predicted by Young's equation:

$$\cos\theta_{OW} = \frac{\gamma_{SW} - \gamma_{SO}}{\gamma_{OW}} \quad (15)$$

where γ_{SW} , γ_{SO} , and γ_{OW} are the surface tensions of the solid-water, solid-oil, and oil-water interfaces, respectively. Eq. 15 predicts that oleophobicity underwater (at the solid-water-oil interface) is possible when $\gamma_{SO} > \gamma_{SW}$.

As previously mentioned, Wenzel regime does not contain an air pocket at the liquid-solid interface unlike the Cassie-Baxter regime. This difference influences the surface wettability since the air pockets encourage a larger contact angle θ and smaller CAH. Eq. 1 describes the Wenzel regime where θ = contact angle, θ_0 = contact angle of the droplet on the flat surface, R_f = roughness factor (Eq. 2), A_F = flat projected area, and A_{SL} = solid-liquid surface area; whereas Eq. 3 describes the Cassie-Baxter regime with f_{LA} = fractional flat liquid-air contact area (Nosonovsky and Bhushan, 2008; Bhushan, 2012). The contact angle of replica rice leaf, butterfly wing, fish scales, and shark skin samples is possible by using roughness factor and fractional liquid-air contact area values (Bixler and Bhushan, 2012b).

4.2. Inspiration from living nature

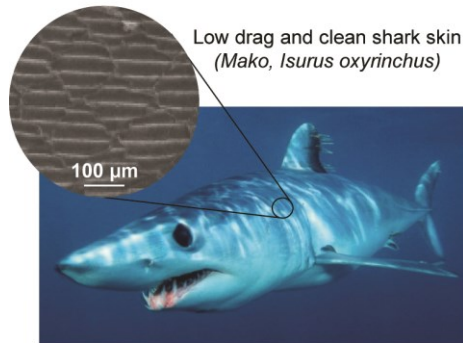
In this section, we explain characteristics and mechanisms of rice leaf, butterfly wing, fish scale, shark skin, lotus leaf surfaces.

4.2.1. Ambient species

In the ambient environment, many surfaces including lotus leaves (Barthlott and Neinhuis, 1997; Nosonovsky and Bhushan, 2008; Bhushan, 2009, 2010, 2012), rice leaves, and butterfly wings (Bixler and Bhushan, 2012b) exhibit self-cleaning superhydrophobic and low adhesion characteristics. Shown in Figure 42 is a water droplet cleaning inorganic fouling from a

Low drag and antifouling lessons from nature: shark skin and lotus effects

Barnacle biofouling on Humpback Whale



Water droplet cleaning lotus leaf
(*Nelumbo nucifera*)



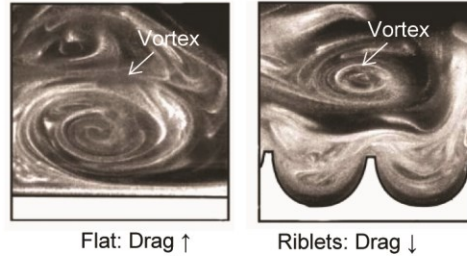
Figure 42: Biofouling in the marine environment (adapted from Bixler and Bhushan, 2012b). Images highlight differences between Humpback whales (adapted from www.southbank.qm.qld.gov.au) and sharks. Even though whales and sharks live in the same environment, barnacle biofouling growth is evident on the whale but not shark skin. Reportedly such antifouling shark skin properties are due to its riblet microtexture, flexion of scales, and a mucous layer. Bottom image illustrates the lotus-effect with a water droplet removing contaminant particles from the lotus leaf.

lotus leaf surface. The lotus leaf relies on hierarchical micropapillae, which are described as microbumps superimposed with low surface energy waxy nanostructures (Barthlott and Neinhuis, 1997; Bhushan et al., 2009a), which provide antifouling via self-cleaning properties. It should be noted that several other plant species also exhibit antifouling properties due to superhydrophobic and low adhesion characteristics, with the air pocket at the solid-liquid interface (Barthlott and Neinhuis, 1997; Nosonovsky and Bhushan, 2008; Bhushan, 2009, 2010, 2012).

In nature, rain droplets impact the lotus leaf surface and effectively roll off due to the water repellency. This leads to self-cleaning, where droplets collect and remove any contaminant particles, as illustrated in Figure 43 with the mercury droplet on a Taro leaf (which exhibits lotus effect characteristics). The lotus effect relies on roughness induced superhydrophobicity and low adhesion, where air pockets are present at the solid-liquid interface (Barthlott and Neinhuis, 1997; Nosonovsky and Bhushan, 2008; Bhushan, 2009, 2010, 2012). Experiments with lotus effect surfaces show drag reduction in laminar (Ou et al., 2004; Jung and Bhushan, 2010; Bixler and Bhushan, 2013d) and turbulent flows (Daniello et al., 2009; Jung and Bhushan, 2010; Martell et al., 2009, 2010; Bixler and Bhushan, 2013d). Additionally, self-cleaning experiments show maximum contaminant removal of 99% for the lotus leaf replica (Bhushan et al., 2009a).

Shark skin and lotus effect mechanisms

Shark skin effect: flow visualization with smoke from atomized oil (flow into the page)



Lotus effect: superhydrophobicity and low adhesion

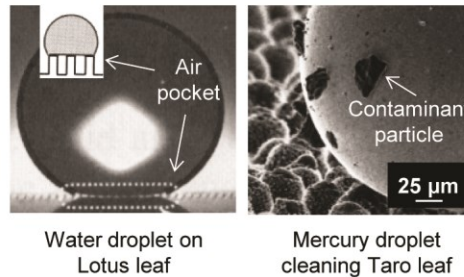


Figure 43: Shark skin and lotus effect mechanisms. Flow visualization images using smoke from atomized oil burned in air to study the turbulent vortices behavior with and without riblets at two velocities (adapted from Lee and Lee, 2001). Top left image shows the vortices on a flat plate with a relatively large amount of surface contact area, which leads to higher drag. Top right image show the vortices are lifted above the riblet tips, with a relatively small amount of surface contact area, which leads to lower drag. Bottom left image shows the lotus effect with a water droplet on a lotus leaf and bottom right image shows a mercury droplet collecting contaminants on a Taro leaf (adapted from Bhushan et al., 2009b).

4.2.2. Aquatic species

In the aquatic environment, surfaces including shark skin (Bechert et al., 1985, 1997a, 1997b, 2000a, 2000b; Lee and Lee 2001; Dean and Bhushan, 2010; Deyuan et al., 2011b; Bixler and Bhushan, 2013b, 2013c) and fish scales (Bixler and Bhushan, 2012b, 2013a) exhibit low drag and antifouling characteristics. Shown in Figure 42 is a comparison between barnacle covered whale skin and clean shark skin, even though both live in the same environment (Bixler and Bhushan, 2013c). Shark skin is designed with microstructured features (dermal denticles covered by riblets) that effectively control naturally occurring turbulent vortices. Anisotropic flow characteristics of shark skin are due to riblet microstructures aligned in the swimming direction. The riblets reportedly lift and pin any vortices generated in the viscous sublayer – where lifting reduces the total shear stress and pinning reduces the cross-stream motion of fluid and ejection of vortices from the viscous sublayer (Bechert et al., 1985, 1997a, 1997b, 2000a, 2000b; Lee and Lee 2001; Dean and Bhushan, 2010; Deyuan et al., 2011a, 2011b; Oeffner and Lauder, 2012; Bixler and Bhushan, 2013b, 2013c). Shark skin effect flow visualization is shown in Figure 43, where smoke from atomized oil visually demonstrates the lifting and presumably pinning of the turbulent vortices (Lee and Lee 2001), which leads to lower drag and antifouling.

In addition to shark skin in the aquatic environment, certain fish (for example rainbow trout), exhibit low drag in order to presumably better navigate fast moving streams (Bixler and Bhushan, 2012b). Fish are covered with oriented scales that promote anisotropic flow from head to tail. Furthermore, scales are hinged preventing motion in the opposite direction further facilitating movement (Bixler and Bhushan, 2012b).

Experiments with shark skin inspired riblet and fish scale samples suggest reduced drag in laminar and turbulent flows (Bechert et al., 1997b; Jung and Bhushan, 2010; Bixler and Bhushan, 2012b, 2013c). Shark skin and fish scales are also reportedly oil-repellent at the solid-water-oil interface (Liu et al., 2009; Liu and Jiang, 2011; Bixler and Bhushan, 2013a).

4.2.3. Rice and butterfly wing effect

Bixler and Bhushan (2012b, 2013a, 2013d, 2013e, 2013f) reported that rice leaves and butterfly wings combine the shark skin (anisotropic flow leading to low drag) and lotus (superhydrophobic and self-cleaning) effects. The combination of anisotropic flow, superhydrophobicity, and low adhesion is reported to reduce drag and facilitate antifouling (Bixler and Bhushan, 2012b, 2013d). It is believed that since rice plants thrive in humid, marshy environments, self-cleaning prevents unwanted fouling, which may inhibit photosynthesis (Bixler and Bhushan, 2012b). Since butterflies are fragile and unable to clean their wings, these properties are critical to maintain structural coloration and flight control (Wagner et al., 1996). Shown in Figure 44 are actual rice leaves and butterfly wings that exhibit unique water repellency and anisotropic flow characteristics, where droplets roll down the blade of the rice leaf and axially away from the butterfly body (Bixler and Bhushan, 2012b).

Reportedly hierarchical structures are found on rice leaves and butterfly wings that provide the anisotropic flow, superhydrophobicity, and low adhesion properties (Bixler and Bhushan, 2012b). The “shark skin effect” anisotropic flow is facilitated by the longitudinal grooves with a transverse sinusoidal pattern in rice leaves and aligned

Rice and butterfly wing effect:
combining shark skin and lotus leaf effects

Rice leaf (*Oryza sativa*)



Butterfly wing (*Blue Morpho didius*)



Figure 44: Rice and butterfly wing effect that combines the shark skin and lotus leaf effects (adapted from Bixler and Bhushan, 2013d). Shown are water droplets resting atop their superhydrophobic and low adhesion surfaces. Rice leaves contain longitudinal grooves with a transverse sinusoidal pattern and butterfly wings contain aligned shingle-like scales that provide anisotropic flow. Hierarchical structures consisting of micropapillae superimposed by waxy nanobumps in rice leaves and microgrooves on shingle-like scales in butterfly wings provide superhydrophobicity and low adhesion. This combination of anisotropic flow, superhydrophobicity, and low adhesion leads to improved drag reduction and antifouling.

shingle-like scales in butterfly wings. The “lotus effect” superhydrophobicity and low adhesion is facilitated by micropapillae superimposed by self-assembled epicuticular waxy nanobumps in rice leaves (O’Toole et al., 1979; Feng et al., 2002; Sun et al., 2005; Guo and Liu, 2007; Liu and Jiang, 2011) and hierarchical scales with microgrooves on butterfly wings (for example Blue Morpho didius) (Wagner et al., 1996; Zheng et al., 2007; Goodwyn et al., 2009; Sato et al., 2009; Liu and Jiang, 2011; Bixler and Bhushan, 2012b).

4.3. Sample fabrication

In this section, we explain sample fabrication processes of rice leaf, butterfly wing, fish scale, and shark skin replicas as well as rice leaf inspired samples for fluid drag and antifouling experimentation by Bixler and Bhushan (2012b, 2013a, 2013d, 2013e, 2013f).

4.3.1. Fabrication of replicas

Actual samples of the rice leaf (*Oryza sativa*), butterfly wing (*Blue Morpho didius*), rainbow trout fish scale (*Oncorhynchus mykiss*), and Mako shark skin (*Isurus oxyrinchus*) were collected to fabricate various samples (Bixler and Bhushan, 2012b).

4.3.1.1. Urethane soft lithography and coating procedure

Urethane replicas from actual samples were created using a two-step soft-lithography molding procedure (Bixler and Bhushan, 2012b). Using liquid silicone, negative molds were taken after cleaning the actual samples. With the silicone molds complete, liquid urethane polymer was applied and cured, yielding precise positive replicas. To combine shark skin and lotus effects, the rice leaf and shark skin replicas received nanostructured coatings. Such lotus effect coatings are known to exhibit both

low drag and self-cleaning properties (Ou et al., 2004; Genzer and Efimenko, 2006; Bhushan et al., 2009a, 2009b; Jung and Bhushan, 2010; Daniello et al., 2009; Martell et al., 2009, 2010; Bhushan and Jung, 2011; Bhushan, 2012).

Superhydrophobic (superoleophilic) and superoleophobic coatings were selected for various drag and antifouling experiments. For the nanostructured superhydrophobic (superoleophilic) coating, a solution consisting of 50 nm (\pm 15 nm) hydrophobized silica nanoparticles combined with methylphenyl silicone resin dissolved in tetrahydrofuran and isopropyl alcohol was utilized (Ebert and Bhushan, 2012a, 2012b). For the nanostructured superoleophobic coating, a two-step coating system was selected (Ultra-Dry[®] SE 7.6.110, Glenwood Springs, Colorado). The base and top coats were individually applied with an airbrush (Bixler and Bhushan 2012b, 2013a, 2013d). As for naming conventions, the uncoated urethane rice leaf sample that received the superhydrophobic nanostructured coating is called the rice leaf replica, since it replicates actual rice leaves. Conversely, the superhydrophobic shark skin sample is the uncoated urethane shark skin sample that received the superhydrophobic nanostructured coating. Furthermore, the samples that received the superoleophobic coating are described as superoleophobic (flat), superoleophobic rice leaf, or superoleophobic shark skin.

4.3.1.2. Rice leaf inspired surfaces

Rice and butterfly wing effect samples were created using rice leaves as inspiration – due to desirable low drag, antifouling, and relatively simple morphology (Bixler and Bhushan 2012b, 2013a, 2013d). The so-called rice leaf inspired surfaces were designed and fabricated from silicon master patterns (Bixler and Bhushan, 2013d).

Sample geometrical dimensions are based on actual rice leaf morphology shown in Table 10. Actual rice leaf surfaces are covered by a sinusoidal pattern of micropapillae with height 2-4 μm , diameter 2-4 μm , pitch 5-10 μm , and peak radius 0.5-1 μm (Bixler and Bhushan, 2012b). Rice leaf inspired topographies shown in Figure 45 were designed to include anisotropic flow and superhydrophobicity. The arrow indicates flow direction for maximum drag reduction and antifouling benefit. Geometrical dimensions are shown in Table 11 with pillar height, pillar diameter or rib width, and pitch. Samples 1 and 2 represent pillars found in actual rice leaf patterns whereas dual height features are present in Sample 3 (only pillars) and Sample 4 (pillars and ribs). Such dual height features create a hierarchical structure designed to facilitate the anisotropic flow similar to the sinusoidal grooves in actual rice leaves (Bixler and Bhushan, 2013d).

Pitch length of the microstructured features found in Samples 1-4 resembles that of actual rice leaves, in order to promote the so-called thin film effect (Bixler and Bhushan, 2013a, 2013d). The thin film effect is believed to occur when a thin layer of oil is held stationary at the solid-liquid interface, which is believed to lower drag during oil flow (Bixler and Bhushan, 2012b, 2013d). Pillars just tall and close enough to develop the thin film are necessary; however pillars too tall or far apart will impede fluid flow and thus increase the drag. Averaging the actual rice leaf micropapillae pitch length yields the pitch length of 7 μm for Samples 1-4. It is believed that antifouling is most effective when the gap between features is less than the approximate diameter of fouling microorganisms (Carman et al., 2006; Schumacher et al., 2007a; Scardino, 2009; Brennan et al., 2010). For Samples 1-4, the pitch is 7 μm and thus the gap is 2 μm , which is

Table 10: Physical characterization of surface structures from actual samples (adapted from Bixler and Bhushan, 2012b).

Sample	Actual						
	Description		z-dim (μm)	x-dim/diameter (μm)	y-dim (μm)	x-spacing (μm)	Peak radius (μm)
Rice leaf (<i>Oryza sativa</i>)	Sinusoidal grooves array covered with micropapilla and nanobumps	Grooves	125-150	150-175	Full length	150-175	5-10
		Micropapillae	2-4	2-4 dia	n/a	5-10	0.5-1
Butterfly wing (<i>Blue Morpho didius</i>)	Shingle-like scales with aligned microgrooves	Scales	30-50	50-75	100-125	50-75	n/a
		Microgrooves	1-2	1-2	100-125	1-2	0.5-1
Fish scales (<i>Oncorhynchus mykiss</i>)	Overlapping hinged scales with concentric rings	Scales	175-200	2-2.5 mm dia	n/a	1-1.25 mm	n/a
		Rings	5-8	0.1-2.5 mm dia	n/a	20-25	1-2
Shark skin (<i>Isurus oxyrinchus</i>)	Overlapping dermal denticles with triangular cross sectional riblets	Dermal denticles	75-100	150-175	135-150	150-175	n/a
		Riblets	10-15	15-25	100-150	30-50	1-2

Table 11: Geometric dimensions of rice leaf inspired samples (Bixler and Bhushan, 2013e).

	Description	Height (H ₁ or H ₂) (μm)	Pillar diameter (D) or rib width (W) (μm)	Pitch (P) (μm)
Sample 1	Hexagonal array of single height pillars	2	5	7
Sample 2		4		
Sample 3	Alternating rows of dual height pillars	2 & 4		
Sample 4	Alternating rows of single height pillars & ribs	2 (pillars) 4 (ribs)		

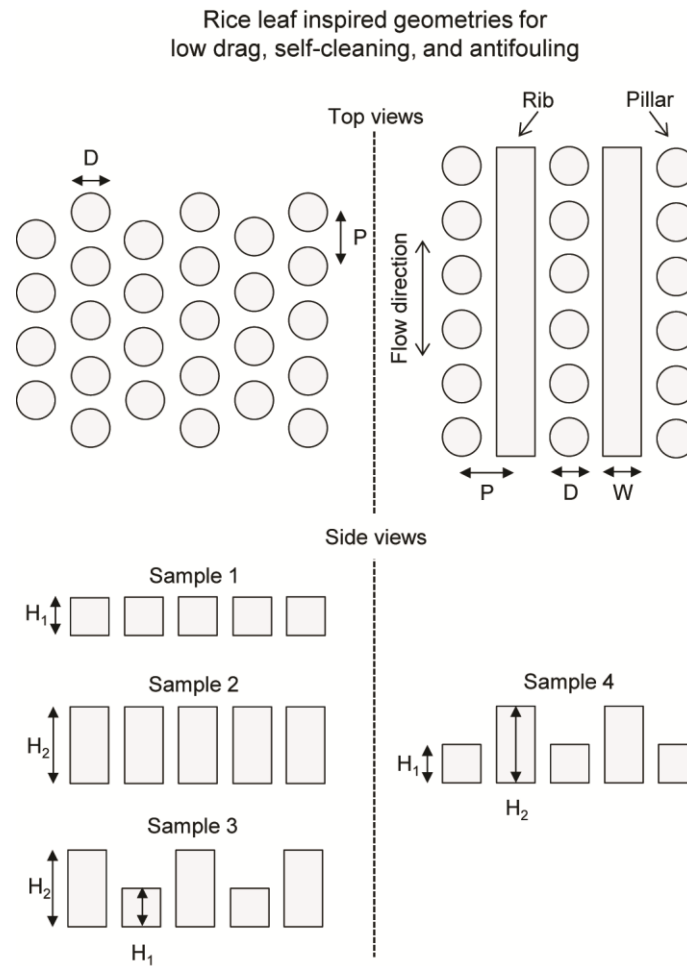


Figure 45: Rice leaf inspired geometries for low drag, self-cleaning, and antifouling (adapted from Bixler and Bhushan, 2013e). These surfaces reportedly combine anisotropic flow, liquid repellency, and low adhesion characteristics. Pillars in Samples 1-3 are arranged in a hexagonal array in order to maintain consistent gaps to promote antifouling. Anisotropic flow leading to lower drag is provided by the dual height pillar design of Sample 3 and the dual height pillar and rib combination of Sample 4. Samples 1 and 2 serve as the baseline samples for comparison.

expected to provide antifouling of microorganisms that measure approximately 2-5 μm in diameter (Bixler and Bhushan, 2013e).

4.3.1.3. Silicon master patterns

Creating rice leaf inspired samples with micro-sized features required microfabrication techniques to achieve the desired dimensions and tolerances. As such, Samples 1-4 were fabricated using silicon master patterns and soft-lithography techniques (Bixler and Bhushan, 2013d). To create the silicon master patterns, a single square photomask (130 mm x 130 mm x 2.3 mm thick with the critical dimensional tolerance of ± 0.025 microns) was produced containing each pattern for Samples 1-4. Silicon master patterns for Samples 1-4 were created on separate 4" (10.16 cm) round silicon wafers with sample areas measuring 6 mm by 100 mm. The etching procedure included standard wafer dehydration, wafer prime, resist coating, wafer exposure, post exposure bake, wafer development, and hard bake. Silicon master patterns with pits (negative vs. positive features) were fabricated in order to emboss polymer films and to accurately produce master patterns. Embossing protrusions onto polymer films using master patterns is possible when the master pattern contains pits. In addition, pits are less challenging to fabricate as compared to protrusions for the dual height features (Bixler and Bhushan, 2013d).

4.3.1.4. PDMS soft lithography procedure

Rice leaf inspired Samples 1-4 were fabricated in polydimethylsiloxane (PDMS) with a three-step soft lithography technique using silicon master patterns (Bixler and Bhushan, 2013d). PDMS was chosen due to its low surface energy which leads to high

contact angle, which is believed to lower drag and increase antifouling efficiency. However, PDMS bonds well to bare silicon wafers and to itself, so therefore it was necessary to consider de-molding options for the soft lithography procedure. A hydrophilic vinyl polysiloxane dental impression material was selected to create positive master molds from the negative silicon master patterns. The positive master molds in the dental impression material were used to create negative molds in urethane material. Liquid urethane polymer was chosen due to its dimensional stability, ease of casting, ability to de-mold easily from the dental impression material, and ability to de-mold from PDMS. The negative urethane molds were used to create final positive samples in PDMS by pouring liquid PDMS and curing. Final samples were easily de-molded from the urethane negative master molds.

4.3.1.5. Hot embossing procedure

To demonstrate the feasibility of scaled-up manufacturing using rice leaf inspired topographies, Bixler and Bhushan (2013d) fabricated samples using a hot embossing procedure. Embossing polymer films was conducted using a commercial hot embossing machine in a clean room environment. Sample 3 was selected to be embossed due to its superior drag and antifouling properties in PDMS. The hot embosser produces single-sided embossed polymer films (optically clear PMMA 175 μm thick) from silicon master patterns using a combination of heat and pressure. The sandwich assembly shown in Figure 46 consists of a 4" (10.16 cm) round silicon master pattern on the bottom, 4" (10.16 cm) round PMMA sheet in the middle, and 4" (10.16 cm) round flat silicon wafer on the top. The PMMA film required a low surface energy coating on both sides for

Hot embossing with silicon master pattern and PMMA sheet

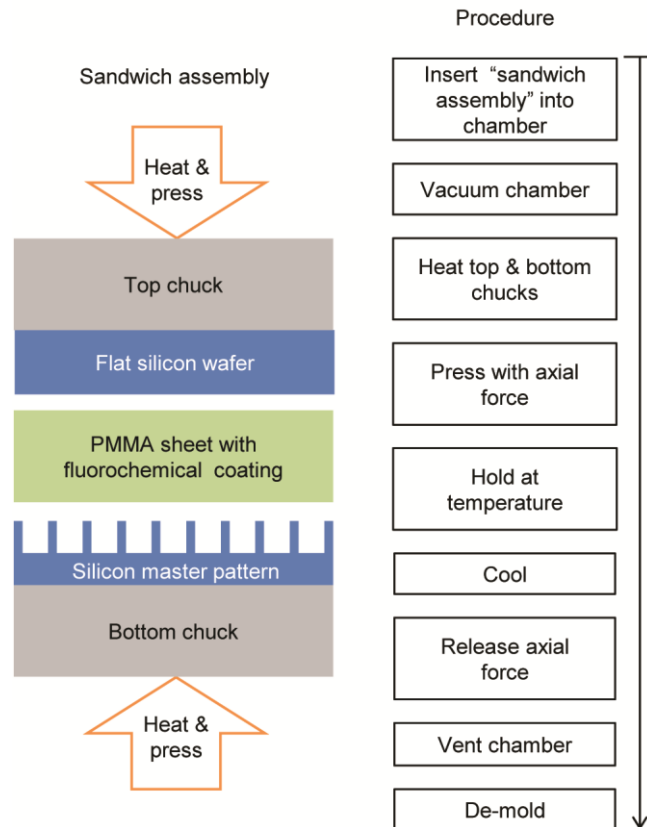


Figure 46: Hot embossing procedure using silicon master patterns and PMMA sheets (adapted from Bixler and Bhushan, 2013e). The sandwich assembly consists of the negative silicon master pattern on the bottom, PMMA sheet in the middle, and flat silicon wafer on the top. The PMMA sheet requires a low surface energy coating for proper de-molding.

proper de-molding from the silicon wafers. The aqueous fluorochemical CapstoneTM ST-100 was selected and diluted with deionized water.

The hot embossing protocol was developed from previous studies (Lin et al., 1996) as well as trial and error (investigating pressures, temperatures, hold times, release coatings, PMMA thickness) to ensure desired outcomes. Once assembled, the hot embosser chamber was vacuumed and the top and bottom chucks heated to ensure proper polymer softening. Once heated, an axial clamping force was applied and increased in increments of 2,000 N to 10,000 N with a minimum hold time at each step. Upon completion, the sandwich assembly was cooled, clamping force was released, and the chamber was vented. De-molding was possible using a razor blade around the edges without damaging the silicon (Bixler and Bhushan, 2013d).

4.4. Experimental procedures

In this section, we explain apparatuses which provided drag, antifouling, contact angle, and contact angle hysteresis measurements for experiments by Bixler and Bhushan (2012b, 2013a, 2013d, 2013e).

4.4.1. Pressure drop measurements

For the various drag experiments by Bixler and Bhushan (2012b, 2013a, 2013d, 2013e) using replica and rice leaf inspired samples, the channel dimensions were based on hospital catheter tubes (3-5 mm diameter). A rectangular channel sandwich design was selected so that samples could be applied to one side and then sandwiched together. In order to measure fluid drag via pressure drop, an experimental apparatus was fabricated according to the schematic in Figure 47 (Bixler and Bhushan, 2013c).

Fluid drag experimental apparatus
water, oil, and air flow

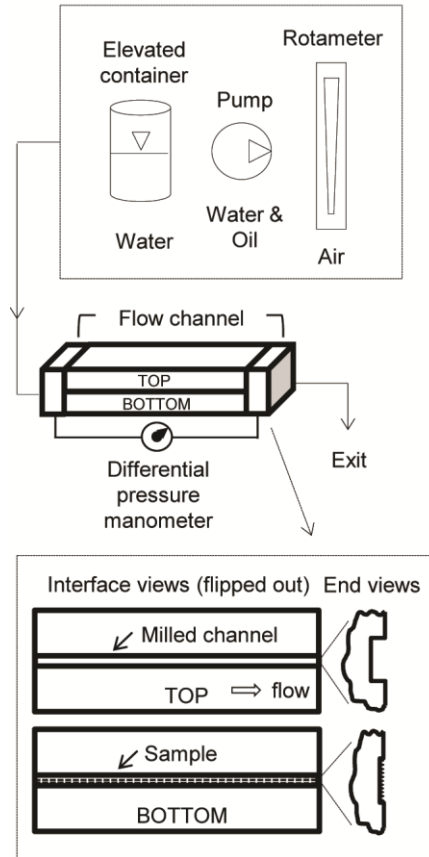


Figure 47: Apparatuses to measure drag via pressure drop in closed channel flow using water, oil, and air (adapted from Bixler and Bhushan, 2013c). The split rectangular channel design allows for samples to be fabricated inside the channel. Interface views are shown highlighting the top and bottom halves that are sandwiched together. Flow is regulated with the elevated container (water), pumps (water or oil), and laboratory air connected to a rotameter (air). The pressure drop is measured with a manometer connected to both ends of the flow channel.

Experimental results are reported for water, oil, and air (Bixler and Bhushan, 2012b, 2013a, 2013d, 2013e) – using the elevated bottle, gear pump, syringe pump, and rotameter for controlled flow rates. For oil experiments, white paraffin oil was selected due to its low surface tension, chemical compatibility with samples, and low health hazard (Bechert et al., 1992).

4.4.2. Predicting closed channel pressure drop

Comparing the predicted pressure drop to experimental data allows one to detect anomalies such as leaks and misalignments. Predicting pressure drop of a flat rectangular duct requires use of the incompressible flow equations for straight uniform pipes. Since the Mach number is less than 0.3 for all experiments, incompressible flow equations may be used (Blevins, 1984). The predicted pressure drop was calculated using the total channel cross-sectional area.

Pressure drop (Δp) between two points in a flat hydrophilic straight uniform closed channel with incompressible and fully developed flow is found with the Darcy-Weisbach formula (Blevins, 1984):

$$\Delta p = \frac{\rho V^2 f L}{2D} \quad (16)$$

where ρ is the fluid density, V is the flow velocity, f is the friction factor, L is the length between two points on a channel, and D is the hydraulic diameter. Flow velocity (V) is determined by dividing the volumetric flow rate by the channel cross sectional area. In air experiments, the rotameter values were used with manufacturer provided charts to determine the flow velocity.

The friction factor for rectangular duct flow is:

$$f = \frac{k}{\text{Re}} \quad (17)$$

where for laminar flow: $k = 64$ (18a)

and for turbulent flow:

$$k = 64 / \left[\frac{2}{3} + \frac{11b}{24a} \left(2 - \frac{b}{a} \right) \right] \quad (18b)$$

$$\text{with } \frac{b}{a} \leq 1$$

The rectangular closed channel hydraulic diameter is:

$$D = \frac{2ab}{a+b} \quad (19)$$

where a is the width and b is the height.

Eqs. 16-19 are used to predict the pressure drop for the rectangular closed channels, as presented later for experiments with water, oil, and air (where $b/a = 1.5 \text{ mm}/3.3 \text{ mm} = 0.45$) (Bixler and Bhushan, 2012b, 2013a, 2013d, 2013e). Eq. 18b shows the friction factor is dependent on channel geometry and independent of the surface roughness. In order to account for roughness, friction factor values for pipes can be estimated with the Moody chart (Fox and McDonald, 1998).

4.4.3. Antifouling experiments

In this section, we explain antifouling experimental procedures and measurement techniques using biological and inorganic fouling contaminants.

4.4.3.1. Anti-biofouling

Several anti-biofouling bioassay experiments have been conducted with various microorganisms such as zoospores (*Enteromorpha*) (Callow et al., 2002), (*Ulva linza*) (Finlay et al., 2002), proteins (Banerjee et al., 2011), *E. coli* (Ma et al., 2000; Bixler et al.,

2013), and MRSA (*Methicillin-resistant Staphylococcus aureus*) (Fletcher et al., 2007). Bixler et al. (2013) selected the microorganism *E. coli* to study the antifouling effect of rice leaf inspired samples due to its prevalence, availability, and access to facilities. Reported are procedures for the antifouling experiments using rice leaf inspired samples with *E. coli* (Bixler et al., 2013).

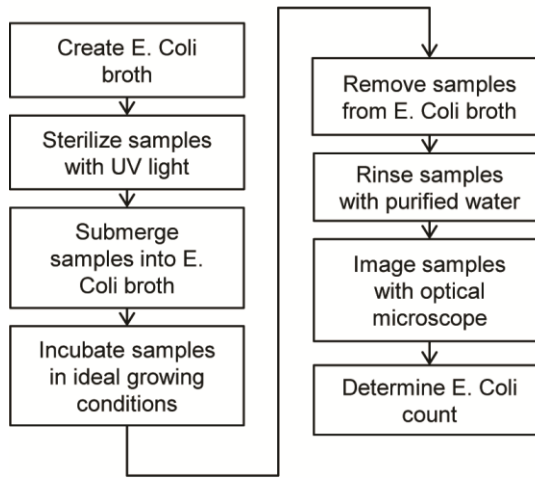
The bioassay procedure in Figure 48a shows *E. coli* streaked onto tryptone and yeast extract dehydrated agar plates and then incubated overnight (Bixler et al., 2013). To prepare *E. coli* broth, a single colony was picked from streak plates, inoculated into sterile lysogeny broth in a beveled flask, and grown while shaking. After incubation, *E. coli* solution was diluted to 1/100 and 1/10 into sterile lysogeny broth and stored on ice. Samples 1-4 and Embossed sample 3 were placed in the bottom of a sterile polystyrene culture dish and sterilized via ultraviolet exposure. *E. coli* broth was added to the culture dish until all samples were covered before final incubation. The aforementioned concentrations and incubation times were determined from trial and error to achieve appropriate *E. coli* growth (i.e. to determine a difference at 1000x magnification between flat control and rice leaf inspired samples under investigation) (Bixler et al., 2013).

After incubation, samples were removed from *E. coli* broth and rinsed. Rinsing removed any unattached *E. coli* from the surface prior to imaging. An auto-pipette with sterile PBS was clamped and held stationary to rinse samples, and then samples were immediately placed onto a glass microscope slide with cover slip. Using a light microscope and CCD camera, each sample was imaged and processed. Images were collected with a 100x oil immersion objective lens for a total magnification of 1000x.

Figure 48: (a) Antifouling bioassay experimental procedure with *E. coli* cells in the laboratory (adapted from Bixler et al., 2013). (b) Apparatus to uniformly contaminate samples and conduct self-cleaning wash experimentation (adapted from Bixler and Bhushan, 2012b). Water droplets at known velocities and flow rates impact the contaminated sample and particle analysis is conducted to quantify efficiency.

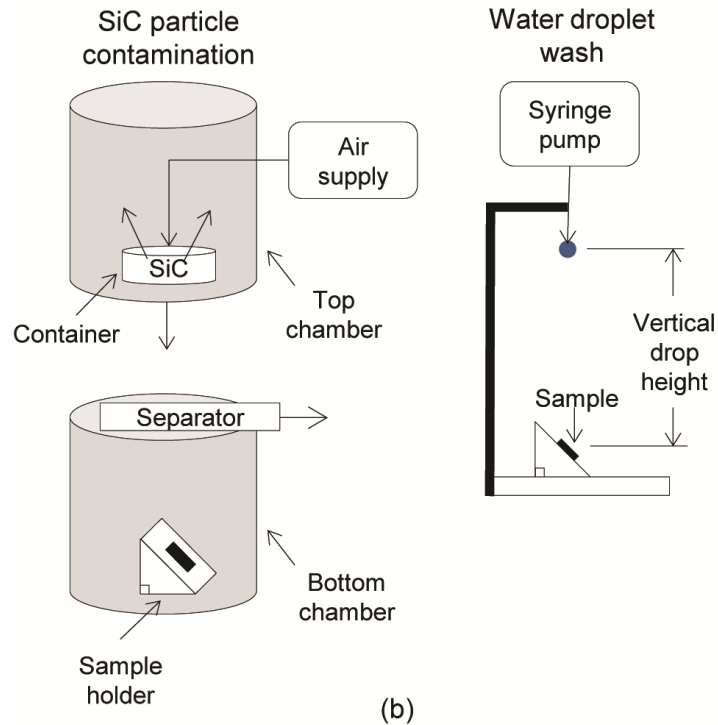
Figure 48

Anti-biofouling experimental procedure



(a)

Anti-inorganic fouling experimental procedure



(b)

Image analysis software recognizes contaminating *E. coli* as dark areas and counts the total number (Bixler et al., 2013).

4.4.3.2. Anti-inorganic fouling

Anti-inorganic effectiveness of replica and rice leaf inspired samples via self-cleaning experiments was conducted by Bixler and Bhushan (2013d, 2013e). Experiments entailed contaminating samples, employing a wash technique, and determining the percentage of inorganic particles removed. Shown in Figure 48b are the apparatuses to deposit contaminate particles on the samples and facilitate self-cleaning. A tray containing hydrophilic silicon carbide (SiC) contaminants (400 mesh size ranging from 10-15 μm) was placed in the top chamber with an air hose directed in the center. These particles were chosen because of their similar properties to natural dirt (shape, size, and hydrophilicity). Contaminants were blown with laboratory air and then allowed to settle before the separator panel was removed.

After a wait period, samples were removed and subjected to a pre-wash experiment particle analysis. Using a light microscope and CCD camera each sample was imaged and analyzed with image processing software. This process was performed before and after each wash experiment. Wash experiments consisted of exposing the tilted replicas to water droplets falling from a specified heights and drip rates. Droplet velocities were approximately 1 and 5.6 m/s at heights of 0.02 and 0.4 m, respectively. This translates into pressures of 200 and 4000 Pa, respectively (Bixler and Bhushan 2013d, 2013e).

4.4.3.3. Wettability

To understand the role of wettability on drag reduction and antifouling, CA and CAH measurements were collected for actual, replica, and rice leaf inspired samples (Bixler and Bhushan, 2013d, 2013e; Bixler et al., 2013). Water in air, oil in air, and oil underwater are reported – to understand the self-cleaning efficiency of ambient as well as underwater surfaces. Since fish scales and shark skin are naturally covered by mucous, the actual samples were cleaned and dehydrated prior to contact angle measurements. Purified water droplets approximately 1 mm in diameter (5 μL) were deposited and measured with an automated goniometer. White paraffin oil droplets of similar dimensions were deposited using a microliter syringe. For oil CA measurements underwater, the oil droplet was deposited with the sample inverted since the density of white paraffin oil (880 kg m^{-3}) is lower than water (1000 kg m^{-3}) (Lide, 2009). CAH was determined by tilting the sample until the droplet began to move (up to 90°), and subtracting the advancing and receding contact angles. Measurements were taken and images captured with an automated goniometer.

4.5. Results and discussion

In this section, we present images and measurements characterizing actual, replica, and rice leaf inspired samples. Reported are measurements of various features from actual and replica samples describing surface morphology and replication success. Also included are results from drag, wettability, and antifouling experiments. Finally, conceptual models are provided to further understand nature's mechanisms for drag reduction and antifouling.

4.5.1. Sample characterization

To characterize the actual and replica samples, Bixler and Bhushan (2012b, 2013e) examined actual, replica, and rice leaf inspired samples. Reported are scanning electron microscope (SEM) and optical profiler images for a qualitative and quantitative comparison and understanding of the relevant mechanisms. The SEM provides high resolution in the x/y direction whereas optical profiler provides high resolution height map information in the z direction (Bixler and Bhushan, 2012b). A summary of the various features of interest from each sample are reported in Table 10.

4.5.2. Actual, replica, and rice leaf inspired

SEM images in Figure 49a by Bixler and Bhushan (2012b) show surface structures of actual rice leaf, butterfly wing, fish scale, and shark skin. Highlighted are cylindrically tapered micropapillae on rice leaves and microgrooves on butterfly wing scales (Bixler and Bhushan, 2012b). Fish skin is covered by oriented scales with concentric rings overlapping and hinged such that water flow is from head to tail. Shark skin is covered by diamond-shaped dermal denticles overlapping and hinged such that the riblets are aligned in the water flow direction from head to tail (Bixler and Bhushan, 2012b). Optical profiler images in Figure 49b provide three dimensional renderings and height maps of each actual sample showing features not clearly observed in the SEM images (Bixler and Bhushan, 2012b).

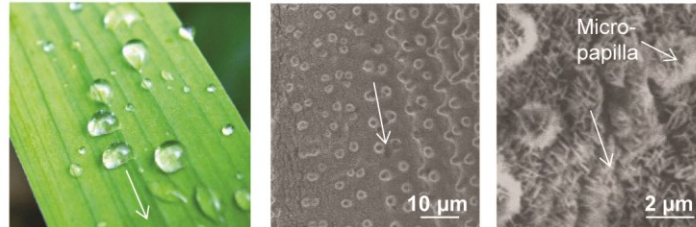
Replica samples by Bixler and Bhushan (2013d) include both the uncoated and coated samples. Shown in Figure 50a are SEM images of the replica samples and in Figure 50b the flat, rice leaf, and shark skin samples that received the superhydrophobic and superoleophobic nanostructured coatings. As expected the rice leaf

Figure 49: Montage of SEM and optical profiler images depicting actual rice leaf, butterfly wing, fish scale, and shark skin morphologies (adapted from Bixler and Bhushan, 2012b). Shown are (a) SEM images at two magnifications and (b) optical profiler images. Arrows indicate the tendencies of fluid flow in transverse and longitudinal directions.

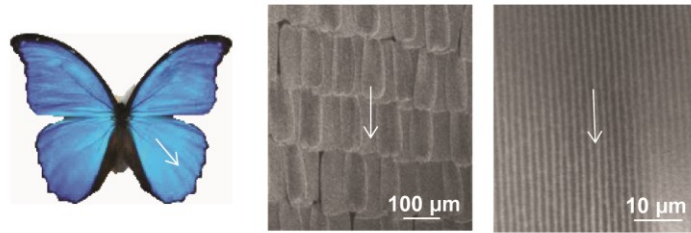
Figure 49a

Ambient superhydrophobic, self-cleaning, antifouling examples in nature (actual samples)

Rice leaf (*Oryza sativa*)



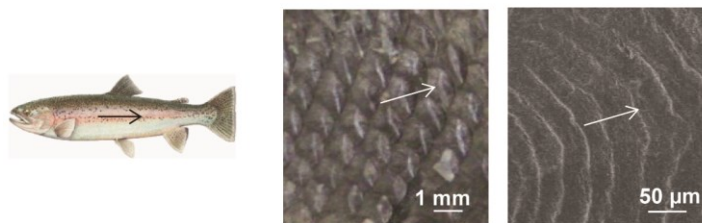
Butterfly wing (*Blue Morpho didius*)



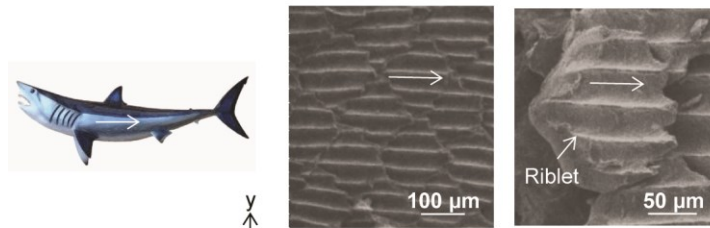
Microgrooves

Aquatic hydrophilic, self-cleaning, low drag, antifouling examples in nature (actual samples)

Fish scales (*Rainbow trout, Oncorhynchus mykiss*)



Shark skin (*Mako, Isurus oxyrinchus*)

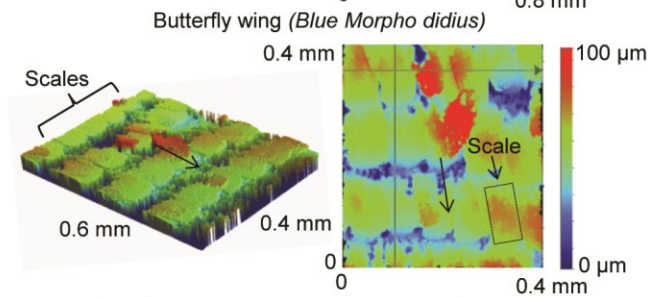
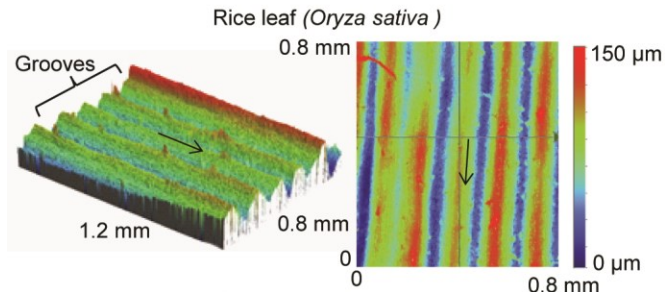


Dermal denticle

(a)

Figure 49b

Ambient superhydrophobic, self-cleaning, antifouling examples in nature (actual samples)



Aquatic hydrophilic, self-cleaning, low drag, antifouling examples in nature (actual samples)

Fish scales (*Rainbow trout, Oncorhynchus mykiss*)

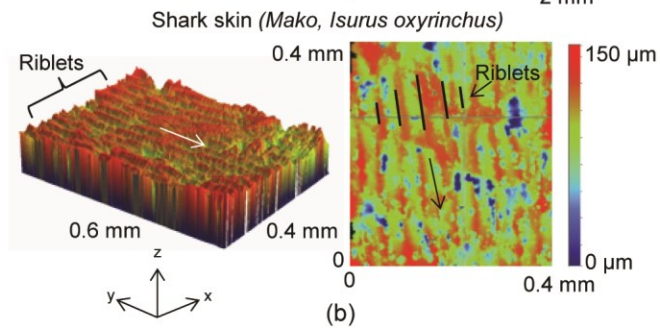
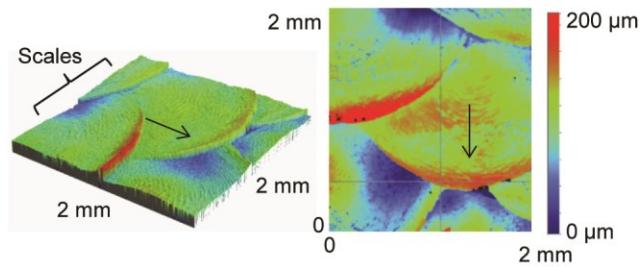
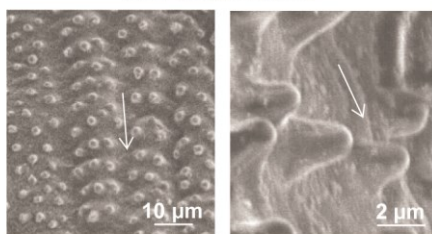


Figure 50: Montage of images depicting ambient and aquatic replicas (adapted from Bixler and Bhushan, 2012b, 2013d). Arrows indicate direction of anisotropic water droplet movement. Shown are (a) SEM images of rice leaf, butterfly wing, fish scale, and shark skin surfaces as well as (b) flat, rice leaf, and shark skin replicas coated in superhydrophobic and superoleophobic solutions.

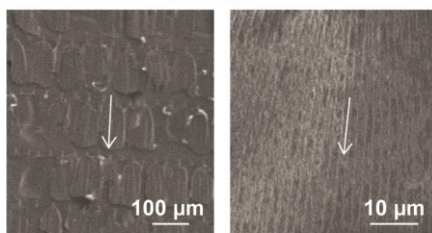
Figure 50a

SEM images of ambient and aquatic
replica samples

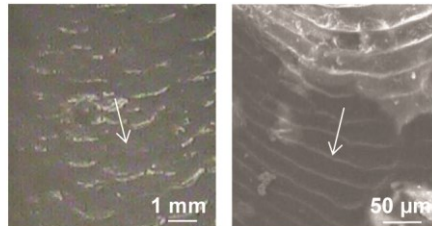
Rice leaf (urethane)



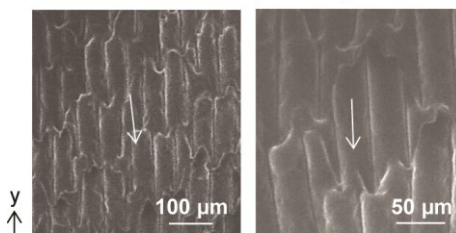
Butterfly wing (urethane)



Fish scales (urethane)



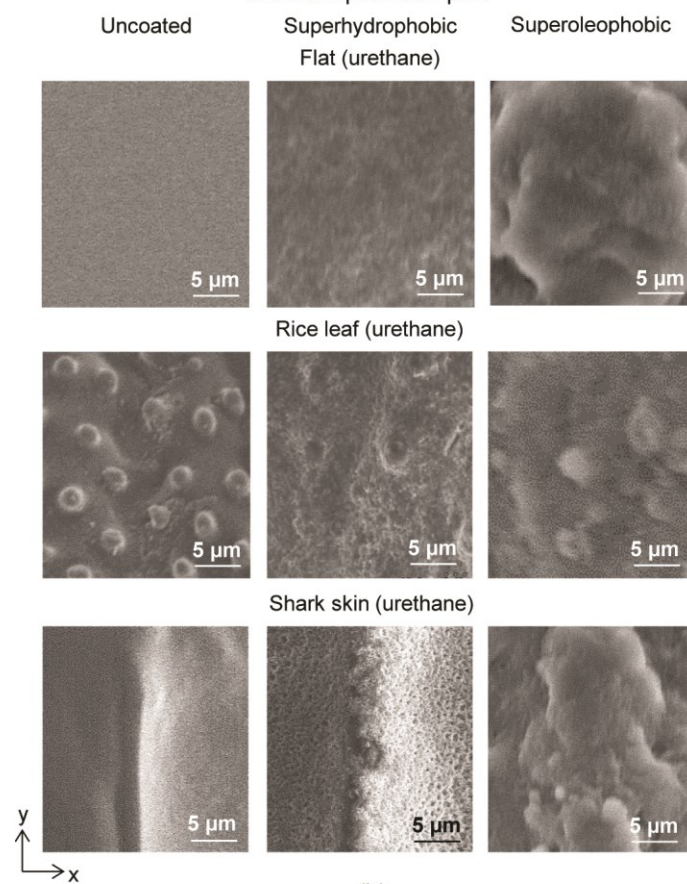
Shark skin (urethane)



(a)

Figure 50b

SEM images of ambient and aquatic coated replica samples



micropapillae hierarchical structure detail was not reproduced in the replica. Furthermore, the coatings increases surface nano roughness as compared to the uncoated replicas (Bixler and Bhushan, 2012b). A summary of R_f and f_{LA} values along with predicted and measured CA values are shown later in detail.

Using optical profiler height map images, the values of R_f and f_{LA} were reported by Bixler and Bhushan (2012b) to calculate CA of samples. Data suggests that the measured and predicted values correlate with the Cassie-Baxter regime for rice leaf and butterfly wing replicas; and Wenzel regime for fish scales and shark skin. This coincides with living nature, since rice leaves and butterfly wings are found in the ambient environment (with air pockets), whereas fish scales and shark skin are found in the aquatic environment (no air pockets) (Bixler and Bhushan, 2012b).

SEM images in Figure 51 by Bixler and Bhushan (2012e) show the surface structures of rice leaf inspired samples. Dual-height pillars are evident in images of Sample 3 along with the dual height pillars/ribs of Sample 4. Each of the sample features appears smooth and with minimal defects from the soft-lithographic process. Images of Embossed sample 3 show features have similar characteristics as with the PDMS molded Sample 3. There appears to be fine strands of presumably PMMA material on select pillars, which are believed to be remnants of the hot embossing procedure created during the de-molding step (Bixler and Bhushan, 2013e). As shown, the features are accurately produced for each sample with geometric dimensions as indicated in Table 10.

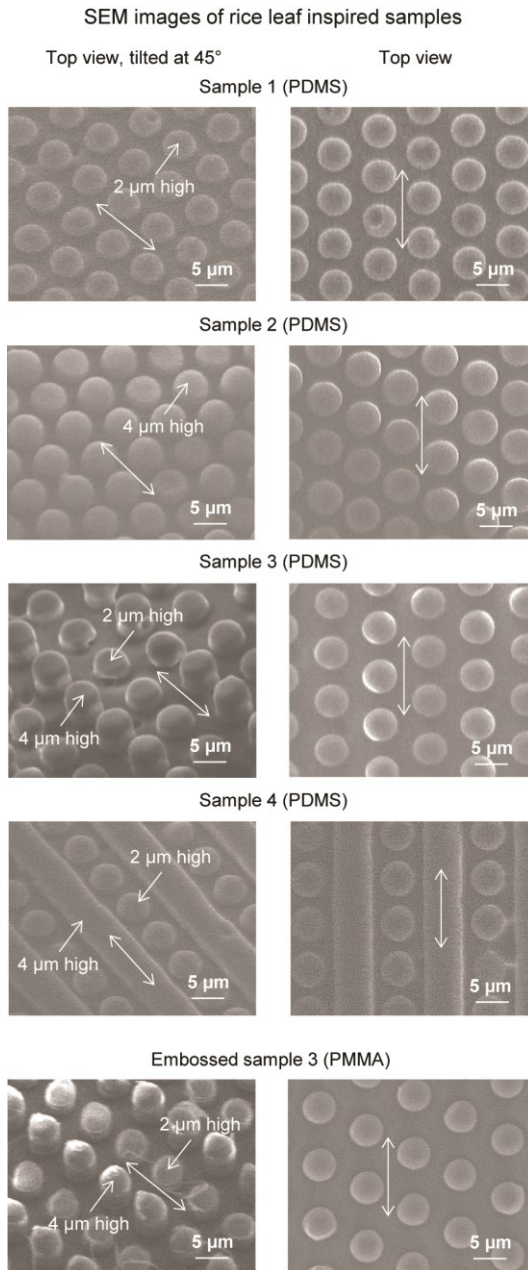


Figure 51: Montage of SEM images for Samples 1-4 and Embossed sample 3 (adapted from Bixler and Bhushan, 2013e). Arrows indicate direction of fluid movement for drag and self-cleaning experiments. Shown are images of Samples 1 and 2 with uniform height pillars arranged in the hexagonal array as well as Sample 3 with dual height pillars and Sample 4 with pillars and ribs.

4.5.3. Pressure drop measurements

Pressure drop measurements are reported for replicas (Bixler and Bhushan, 2012b, 2013a, 2013d, 2013f) and rice leaf inspired samples (Bixler and Bhushan, 2013e) using water, oil, and air flow. As appropriate for each fluid, shown are flat channel predicted (using Eq. 16) and measured flat channel (milled or PDMS) lines. In order to account for milled channel surface roughness, friction factor values estimated from the Moody chart were selected based on the roughness value of $\varepsilon = 0.0025$ mm. Trend lines are connected through the origin in each plot.

4.5.3.1. Water flow

Water flow results by Bixler and Bhushan (2013d, 2013e) are presented comparing the replicas, coated samples, and rice leaf inspired samples. Results are shown from experiments with low velocity laminar flow ($0 < Re < 200$) and high velocity turbulent flow ($0 < Re < 12,500$). Calculations use the values for mass density (ρ) equaling 1000 kg m^{-3} and kinematic viscosity (ν) equaling $1.034 \times 10^{-6} \text{ m}^2 \text{ s}^{-1}$ (Lide, 2009). Samples that received the superhydrophobic and low adhesion nanostructured coating were selected based on their initial drag performance. In general, a higher pressure drop reduction is reported for the higher flow velocity conditions, where turbulent vortices are believed to be present.

Provided in Figure 52 are pressure drop measurements for replica, control, and coated samples (Bixler and Bhushan, 2013d). When considering error bars, the rice leaf and butterfly wing sample pressure drops appear similar in both laminar and turbulent flow. The fish scale and shark skin sample pressure drops appear similar in laminar flow

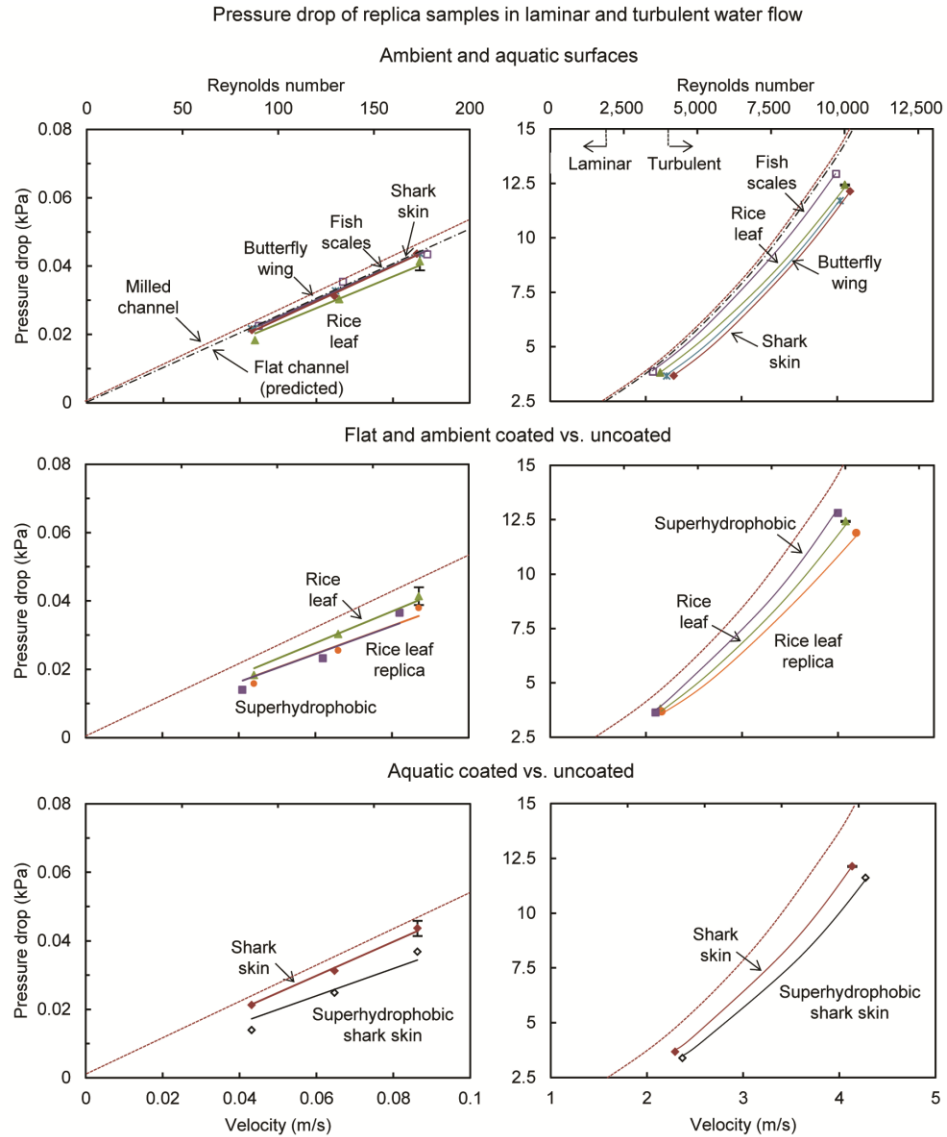


Figure 52: Water pressure drop with replica samples in laminar and turbulent flows (adapted from Bixler and Bhushan, 2012b). Shown are the milled channel and flat channel predicted lines as well as results for replicas of ambient and aquatic species, both with and without nanostructured coatings. Higher pressure drop translates into higher drag; therefore lower pressure drop is desirable. Error bars show ± 1 standard deviation, which is hardly visible in the plots.

but differ in turbulent flow, with shark skin superior. In laminar water flow, the maximum pressure drop reduction of 26% is shown with the superhydrophobic flat sample (Bixler and Bhushan, 2012b). In turbulent water flow, maximum pressure drop reduction is shown with rice leaf replica and superhydrophobic shark skin at 26% and 29%; and uncoated at 17% and 19%, respectively (Bixler and Bhushan, 2012b). It is reported that the rice leaf replica benefits from anisotropic flow and low adhesion, which leads to lower drag (Bixler and Bhushan, 2013e). In addition, the superhydrophobic shark skin replica benefits from the shark skin effect combined with low adhesion, which also leads to lower drag.

Shown in Figure 53 are pressure drop measurements reported for rice leaf inspired samples (Bixler and Bhushan 2013e). Results from the turbulent conditions indicate that Samples 1 and 2 increase the drag, and Samples 3 and 4 reduce the drag, which is believed due to anisotropic flow characteristics. In laminar flow, Sample 3 provides the greatest pressure drop reduction at 15% (Bixler and Bhushan, 2013e) while in turbulent flow Embossed sample 3 provides the greatest pressure drop reduction at 23% (Bixler and Bhushan, 2012b). Sample 2 shows the greatest pressure drop increase at 13%, presumably due to the taller pillars impeding the fluid flow and vortices translating on the pillars. Furthermore in turbulent flow, Embossed sample 3 yields more pressure drop reduction than Sample 3, with values of 23% and 12%, respectively (Bixler and Bhushan, 2013e).

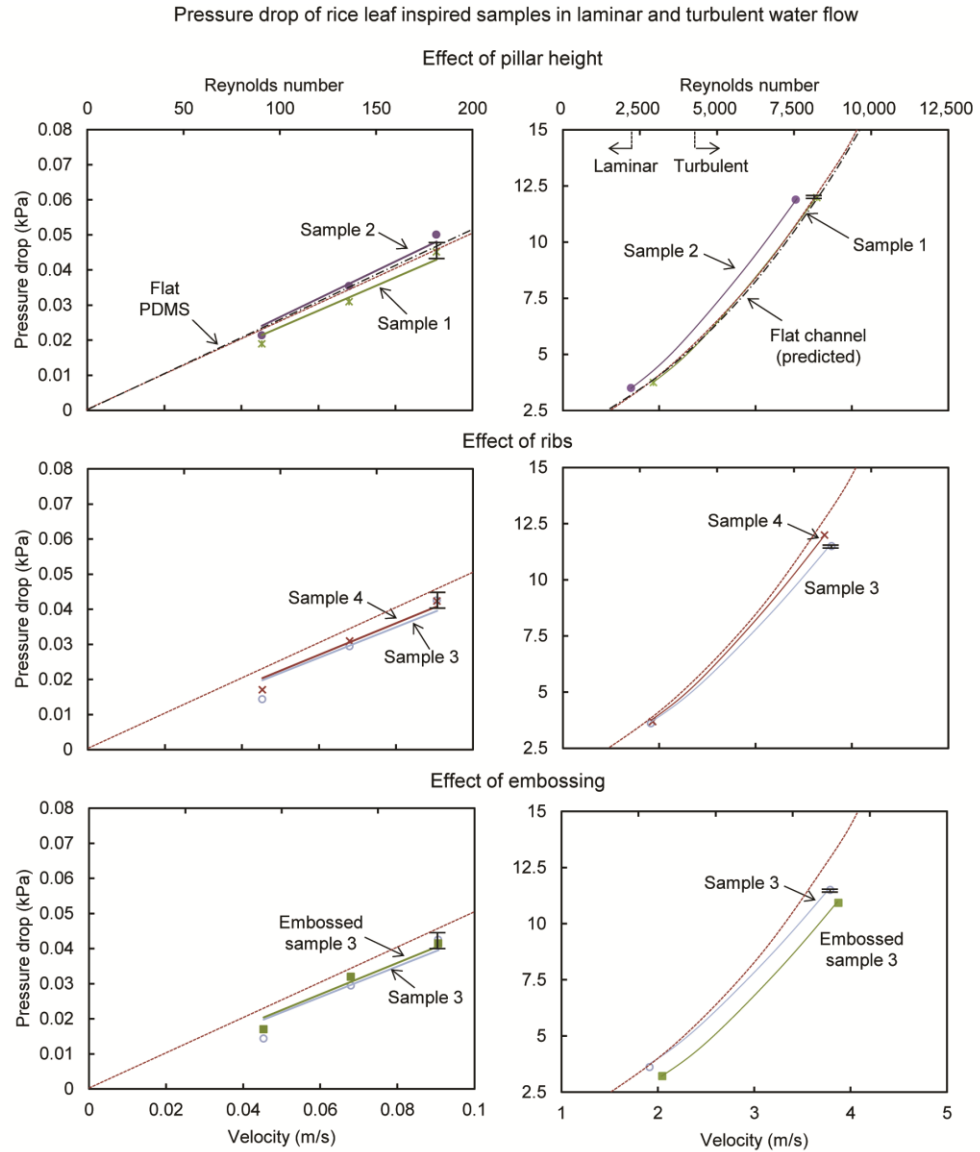


Figure 53: Water pressure drop with rice leaf inspired samples in laminar and turbulent flows (adapted from Bixler and Bhushan, 2013e). Shown are the flat PDMS and flat channel predicted lines as well as results for Samples 1-4 and Embossed sample 3. Higher pressure drop translates into higher drag; therefore lower pressure drop is desirable. Error bars show ± 1 standard deviation, which is hardly visible in the plots.

4.5.3.2. Oil flow

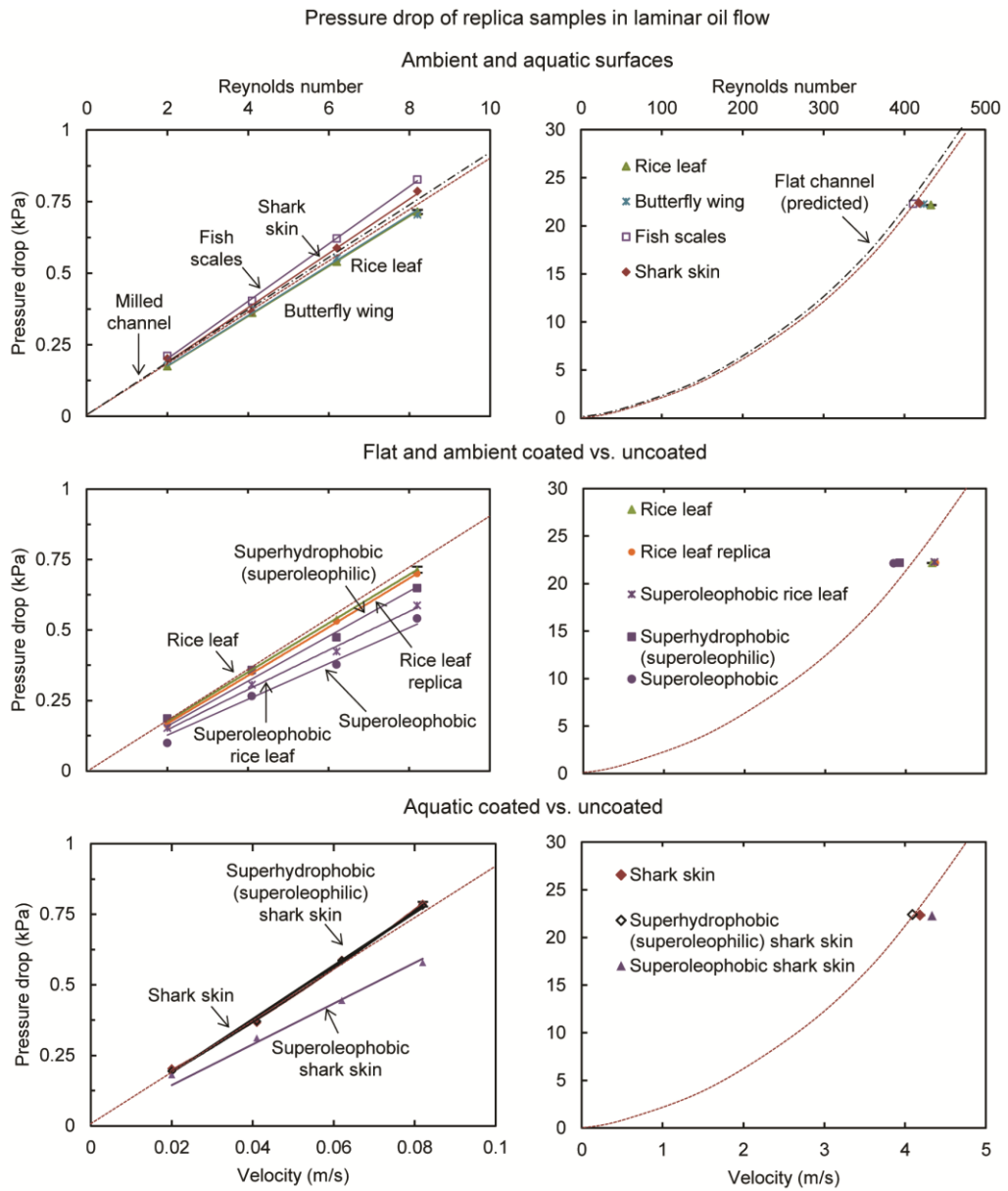
Oil flow results by Bixler and Bhushan (2013d, 2013e) are presented comparing the replicas, coated samples, and rice leaf inspired samples. Results are shown from experiments with low velocity laminar flow ($0 < Re < 10$) high velocity laminar flow ($0 < Re < 500$). To investigate the role of superoleophobicity on rice leaf and shark skin replicas in oil flow, a superoleophobic coating was applied in addition to a superhydrophobic (superoleophilic) coating. Calculations use the values for mass density (ρ) equaling 880 kg m^{-3} and kinematic viscosity (ν) estimated at $2.2 \times 10^{-5} \text{ m}^2 \text{ s}^{-1}$ (Lide, 2009).

Shown in Figure 54 are pressure drop measurements for replica, control, and coated samples (Bixler and Bhushan 2013d). The superoleophilic and superoleophobic flat samples at high velocity show drag increases, which is presumably due to the lack of anisotropic flow control and increased surface roughness. Pressure drop reduction is detected at the high velocities for the rice leaf and butterfly wing samples. At the low and high velocities, the superoleophobic rice leaf and shark skin samples reduce drag, due to anisotropic flow and low adhesion. In addition, the superhydrophobic (superoleophilic) rice leaf replica also provides drag reduction due to the so-called thin film effect (Bixler and Bhushan, 2013a). In high velocity, maximum pressure drop reduction is shown with superhydrophobic (superoleophilic) and superoleophobic coated rice leaf and the uncoated butterfly wing replicas at 10% and 6%, respectively (Bixler and Bhushan, 2013a).

Shown in Figure 55 are pressure drop measurements reported for rice leaf inspired samples (Bixler and Bhushan 2013e). A pressure drop difference is observed at

Figure 54: Oil pressure drop with replica samples in laminar flow (adapted from Bixler and Bhushan, 2013d). Shown are the milled channel and flat channel predicted lines. Samples include the flat control and replicas of ambient and aquatic species, both with and without the nanostructured superhydrophobic (superoleophilic) and superoleophobic coatings. Higher pressure drop translates into higher drag; therefore lower pressure drop is desirable. Error bars show ± 1 standard deviation, which is hardly visible in the plots.

Figure 54



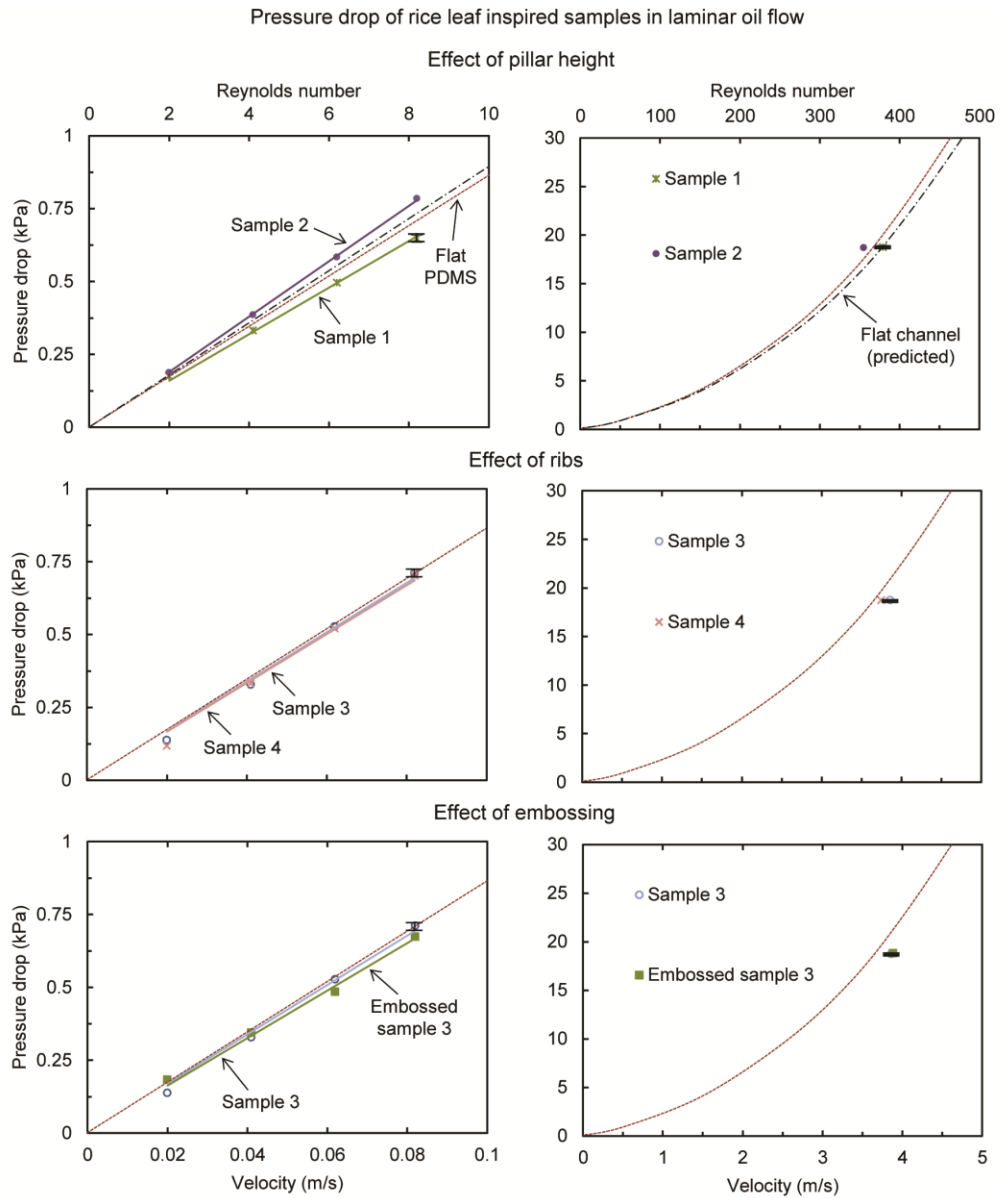


Figure 55: Oil pressure drop with rice leaf inspired samples in laminar flow (adapted from Bixler and Bhushan, 2013e). Shown are the flat PDMS and flat channel predicted lines as well as results for Samples 1-4 and Embossed sample 3. Higher pressure drop translates into higher drag; therefore lower pressure drop is desirable. Error bars show ± 1 standard deviation, which is hardly visible in the plots.

high velocities when examining the effect of ribs and embossing for Samples 3 and 4. Furthermore, Samples 1,3,4, and Embossed sample 3 show drag reduction reportedly due to anisotropic flow (all but Sample 1) and the thin film effect. Embossed sample 3 provides the greatest drag reduction in low and high velocity laminar flow, at 5% and 6% pressure drop reduction, respectively (Bixler and Bhushan, 2013a). Sample 2 shows the greatest pressure drop increase at 11%, presumably due to the taller pillars impeding the fluid flow (leading to increased surface area and friction). The so-called thin film effect is believed to be present in all samples except Sample 2 (Bixler and Bhushan, 2013e).

4.5.3.3. Air flow

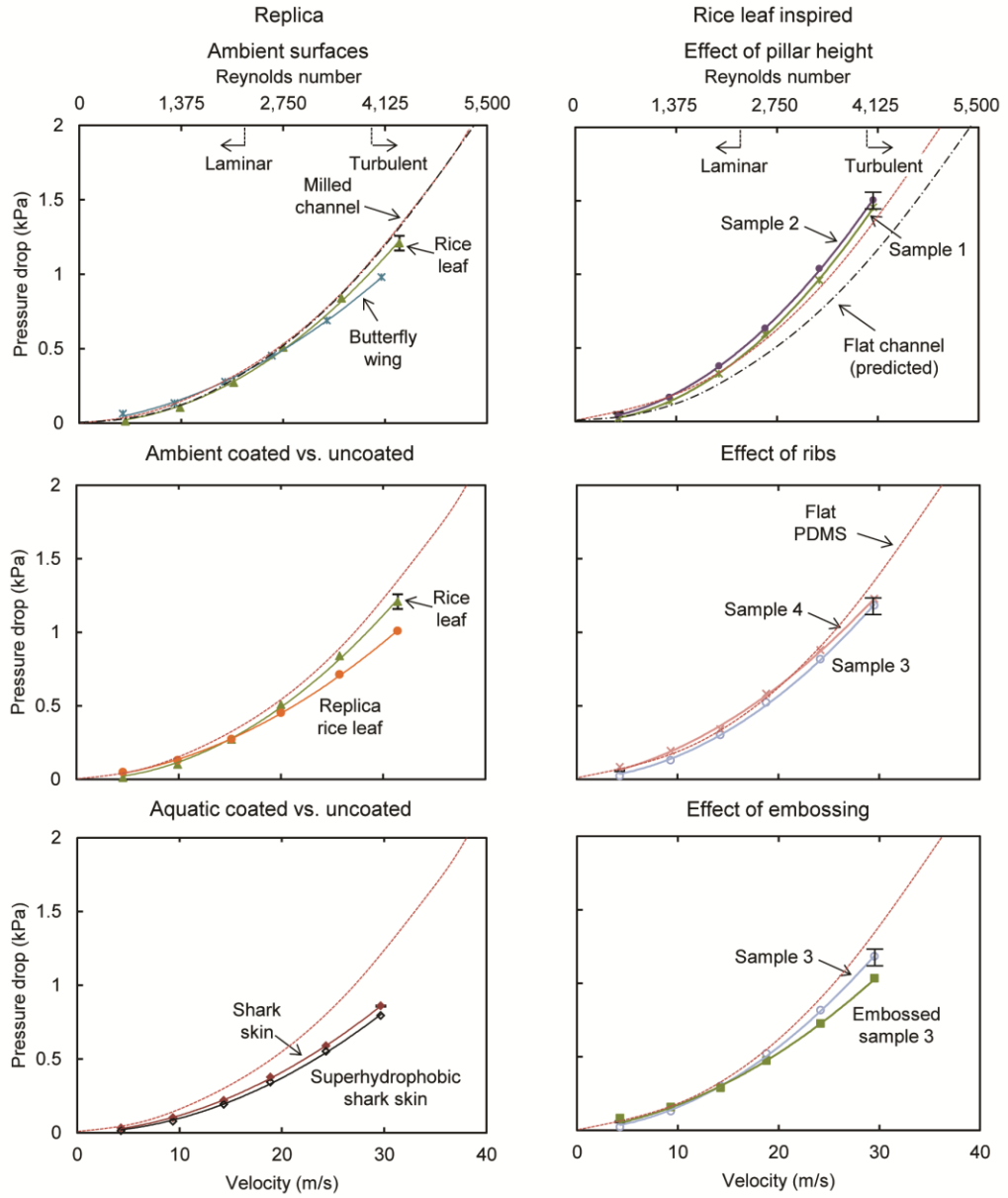
Air flow results are presented comparing the replicas, coated samples, and rice leaf inspired samples (Bixler and Bhushan, 2013d, 2013e), as shown in Figure 56. With air, the achievable velocity range was higher as compared to the water or oil, and the higher Reynolds numbers show continued pressure drop reduction (until expected plateauing). Results are shown from experiments with laminar through high velocity turbulent air flow ($0 < Re < 5,500$). Calculations use the values for mass density (ρ) equaling 1.2 kg m^{-3} and kinematic viscosity (ν) equaling $1.51 \times 10^{-5} \text{ m}^2 \text{ s}^{-1}$ (Lide, 2009).

When comparing fish scales and shark skin replicas, a smaller difference is observed in air versus water. The superhydrophobic coated rice and shark skin replicas show an improved pressure drop reduction compared to the uncoated, but this is independent of the superhydrophobicity. When comparing the various samples in turbulent flow, in water the superhydrophobic shark skin sample reduces pressure by

Figure 56: Air pressure drop with replica and rice leaf inspired samples in laminar and turbulent flow (adapted from Bixler and Bhushan, 2013d, 2013e). Shown are the milled channel, flat PDMS, and flat channel predicted lines. Results are presented for replicas of ambient and aquatic species, both with and without the nanostructured coating, Samples 1-4, and Embossed sample 3. Higher pressure drop translates into higher drag; therefore lower pressure drop is desirable. Error bars show ± 1 standard deviation.

Figure 56

Pressure drop of replica and rice leaf inspired samples in laminar and turbulent air flow



29% ($Re = 10,000$) and in air reduces pressure by 27% ($Re = 4200$) (Bixler and Bhushan, 2012b). It is believed that the coated shark skin benefits from the shark skin effect combined with reduced surface roughness between riblets, which leads to lower drag (Bixler and Bhushan, 2013c, 2013d). Furthermore, Samples 3 and 4, and Embossed sample 3 show pressure drop reduction, which is believed due to anisotropic flow and vortices pinned (Bixler and Bhushan, 2013e). Embossed sample 3 provides the greatest drag reduction in laminar and turbulent flow, at 10% and 12% pressure drop reduction, respectively (Bixler and Bhushan, 2013a). Sample 2 shows the greatest pressure drop increase at 7%, presumably due to the taller pillars impeding the fluid flow and vortices translating on the pillars (Bixler and Bhushan, 2013e).

4.5.3.4. Nondimensional pressure drop model

A nondimensional pressure drop expression was developed to estimate pressure drop for various fluids and conditions (Bixler and Bhushan, 2013d). This was accomplished by combining Eqs. 16-19 and the Reynolds number for a flat sample. Solving for the nondimensional pressure drop as a function of Reynolds number yields (Bixler and Bhushan, 2013d):

$$\overline{\Delta p} = \frac{\Delta p}{G} = Re \quad (20)$$

$$\text{with } G = \frac{\rho L k v^2}{2D^3}$$

where G is the fluid property and channel dimension parameter. Eq. 16 shows that pressure drop is directly proportional to velocity and Eq. 20 shows that nondimensional pressure drop is proportional to the Reynolds number. Shown in Figure 57 is the nondimensional pressure drop versus Reynolds numbers for a flat milled channel

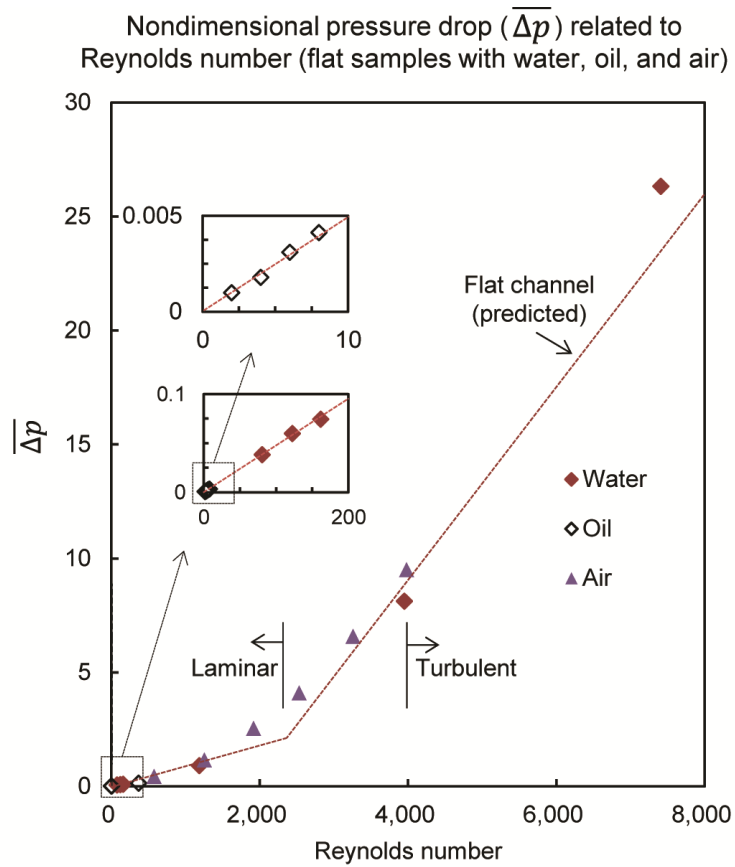


Figure 57: Nondimensional pressure drop parameter related to Reynolds number (adapted from Bixler and Bhushan, 2013d). Presented are results from water, oil, and air experiments for flat samples using reported data and the mathematical relationship in Eq. 11. This provides flat channel pressure drop estimations based on fluid properties, flow conditions, and channel dimensions.

in water, oil, and air experiments (Bixler and Bhushan, 2013d). These fluids represent a wide range of densities and viscosities found in medical, marine, and industrial applications. As shown, the nondimensional pressure drop values follow similar calculated linear trend lines based on water flow, with a slope change between laminar and turbulent flow. In order to account for milled channel surface roughness, friction factor values estimated from the Moody chart were selected based on the relative roughness value of $\epsilon = 0.0025$ mm. The Moody chart plots the Darcy-Weisbach friction factor, Reynolds number, and the relative roughness value for fully developed pipe flow. The relative roughness factor is calculated by dividing the pipe roughness by its internal diameter (Fox and McDonald, 2011).

4.5.4. Antifouling experiments

In this section, we present images and measurements characterizing replica and rice leaf inspired samples from anti-biofouling and anti-inorganic fouling experiments.

4.5.4.1. Anti-biofouling

To understand the antifouling effectiveness of the rice leaf inspired samples, Bixler et al. (2013) conducted a series of bioassay experiments with *E. coli* microorganisms. Shown in Figure 58 are microscopic images the *E. coli* colonized on a flat sample. As shown, the *E. coli* are long cylindrically shaped microorganisms that tend to cluster in groups and align themselves from head to tail. *E. coli* cells are approximately 1 μm in diameter and 2-4 μm long. When actively growing and dividing, the cells stretch to ~ 4 μm before dividing into two cells (Bixler et al., 2013).

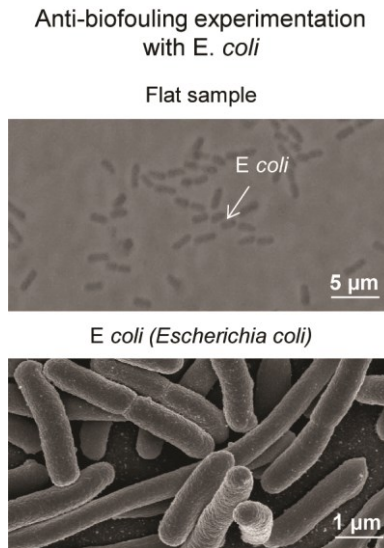
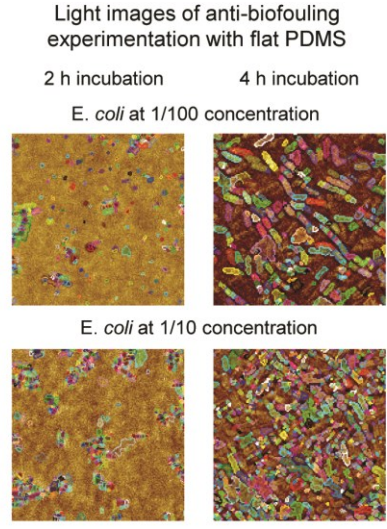


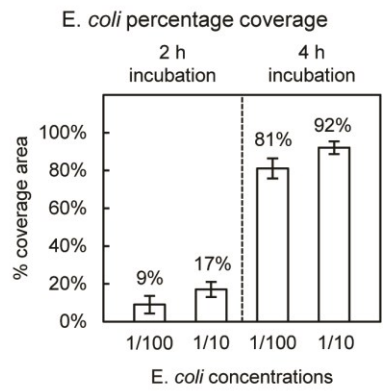
Figure 58: Images of *E. coli* on flat surfaces after the bioassay procedure (adapted from Bixler et al., 2013) and at a higher magnification (adapted from www.universityofcalifornia.edu)

Presented for flat PDMS samples at the two concentrations and incubation times are light microscope images shown in Figure 59a (with *E. coli* highlighted by the software). As indicated, a higher *E. coli* cell count is present as concentration and incubation time increases. Shown in Figure 59b are the tabulated results of percentage coverage area of *E. coli* on the surfaces for 1/100 and 1/10 concentrations at 2 and 4 hour incubation times. Furthermore, as expected, the lower concentration does not provide as much coverage area, however the differences are within 10% for both incubation times (Bixler et al., 2013).

Shown in Figure 60 are light microscopic images of the flat PDMS control sample, Samples 1-4, and the Embossed sample 3. Tabulated data of percentage reduced



(a)



(b)

Figure 59: Light microscope images of (a) flat PDMS control samples and (b) tabulated results after *E. coli* bioassay experiments (adapted from Bixler et al., 2013). As indicated, *E. coli* covers the majority of the surface after 4 hours in ideal growing conditions. This baseline serves to compare the various Samples 1-4 and Embossed sample 3 when calculating percentage reduced coverage.

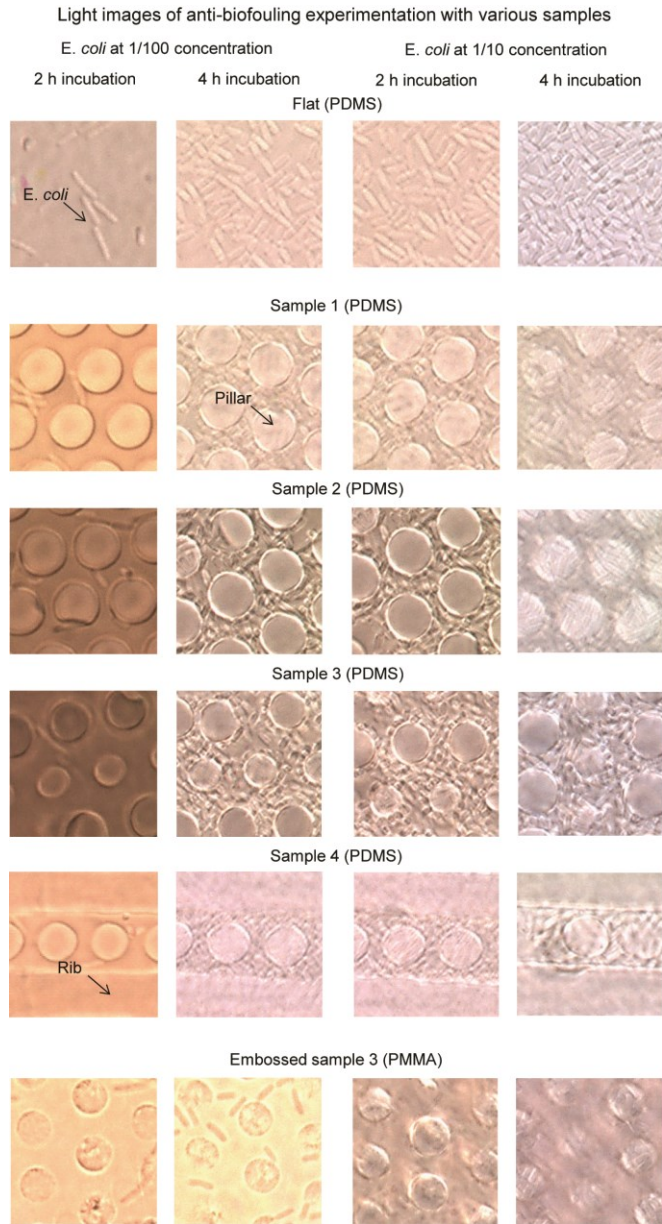


Figure 60: Light microscope images of rice leaf inspired samples after bioassay experiments using *E. coli* (adapted from Bixler et al., 2013). Presented are images of flat PDMS, Samples 1-4, and Embossed sample 3 with two *E. coli* concentrations and two incubation times. Long and narrow cylindrically shaped objects are the *E. coli*.

coverage compared to the flat control samples are shown in Figure 61 with error bars. Bixler et al. (2013) determined antifouling effectiveness by comparing various samples to the total number of *E. coli* cells on flat control samples. Results reported in percentage *E. coli* reduced coverage, where a high percent reduced coverage is desired. Reportedly due to the discontinuities, Samples 1-4 and the Embossed sample 3 provided antifouling benefit (Bixler et al., 2013). The greatest antifouling benefit is demonstrated with Sample 4 at 1/100 and 1/10 concentrations at 33% and 29% reduced coverage, respectively. Interestingly, all samples are shown to provide antifouling benefit and are within about 10% of each other's value. It is reported that *E. coli* are less likely to settle on and colonize the pillar or rib tops, and most often settled in between the features (Bixler et al., 2013). Furthermore, it is believed that high CA and low CAH will amplify the antifouling abilities of the samples, as it is believed that microorganisms will have more difficulty adhering to the surface (Bixler et al., 2013).

4.5.4.2. Anti-inorganic fouling

To understand the anti-inorganic fouling effectiveness of the various samples, Bixler and Bhushan (2013d, 2013e) conducted a series of self-cleaning wash experiments. Contaminant particles on rice leaf and shark skin replica surfaces are shown in Figure 62, highlighting the shape of the particles as well as their relative size to replica surface features. Tabulated data are shown in Figure 63a for replica samples and Figure 63b for rice leaf inspired samples from both low and high velocity droplet wash experiments.

Percentage biofouling reduced
coverage compared to flat samples

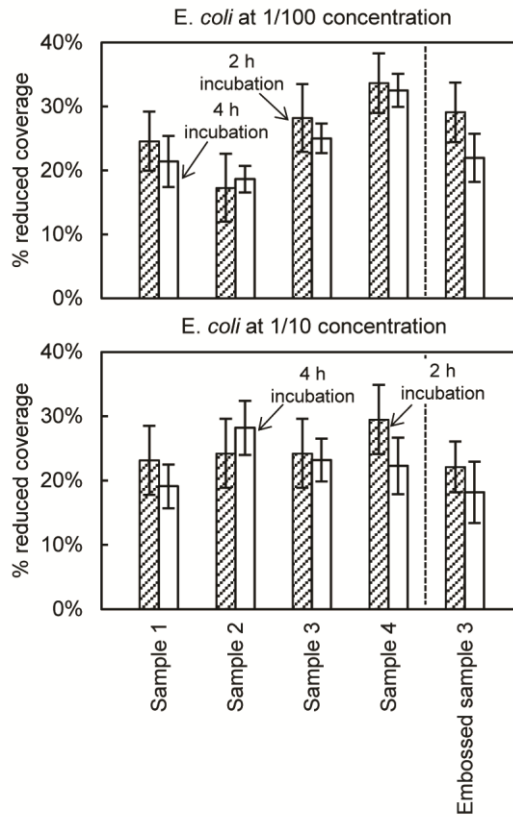


Figure 61: Anti-biofouling results from with rice leaf inspired samples after *E. coli* bioassay experiments (adapted from Bixler et al., 2013). Results are presented for flat PDMS, Samples 1-4, and Embossed sample 3. The percentage reduced coverage is calculated from the flat PDMS control samples. It is believed that antifouling efficiency improves with high CA and low CAH. Error bars show ± 1 standard deviation.

SEM images of anti-inorganic fouling experimentation with SiC particles

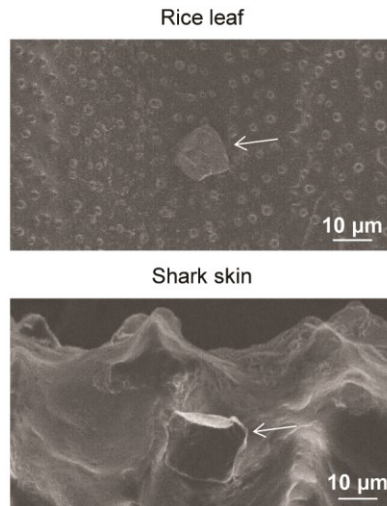
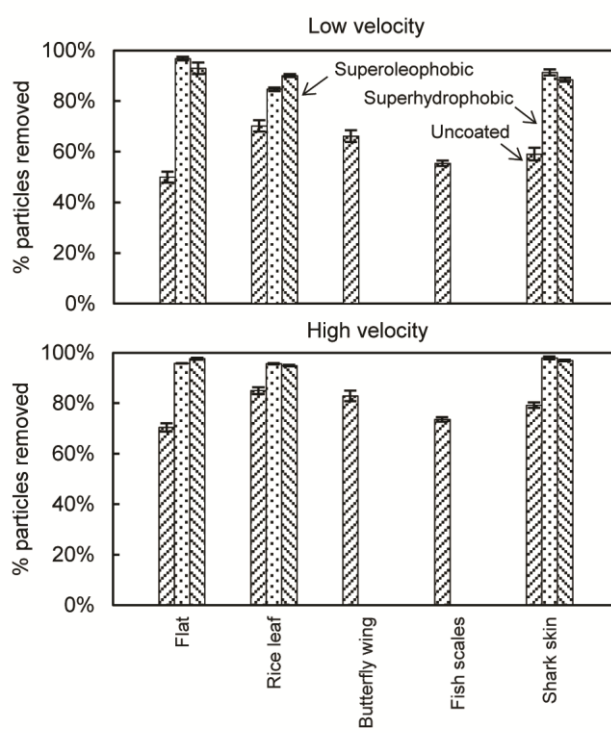


Figure 62: Scanning electron microscope (SEM) images of silicon carbide (SiC) contamination particles on rice leaf and shark skin replicas before anti-inorganic fouling self-cleaning wash experimentation (adapted from Bixler and Bhushan, 2012b).

Figure 63: Anti-inorganic self-cleaning results from particle wash experiments (adapted from Bixler and Bhushan, 2013d, 2013e). (a) Results are presented for flat urethane and replica samples as well as select samples coated in superhydrophobic and superoleophobic coatings. (b) Results are presented for replica rice leaf, flat PDMS, and rice leaf inspired samples. Self-cleaning efficiency improves with high CA and low CAH. Error bars show ± 1 standard deviation.

Figure 63a

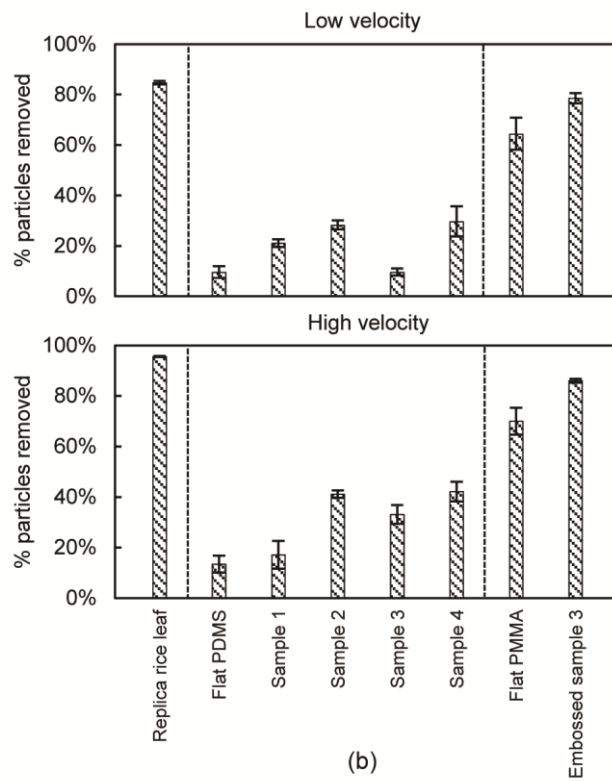
Anti-inorganic fouling experimental results using replica samples



(a)

Figure 63b

Anti-inorganic fouling experimental results using rice leaf inspired samples



(b)

As expected, the superhydrophobic rice leaf replica outperformed the other samples, and more particles were removed at higher versus lower velocities. Self-cleaning is demonstrated with rice leaf replica and Embossed sample 3 at 95% and 86% contaminant removal, respectively; as compared to uncoated samples at 85% and 70%, respectively (Bixler and Bhushan, 2013d, 2013e). Interestingly, the Embossed sample 3 provides nearly the same self-cleaning ability as the rice leaf replica, even though Embossed sample 3 is not superhydrophobic. Nevertheless, high CA and low CAH is believed to amplify the self-cleaning abilities of the samples, as it is believed that the droplets are able to roll and collect the particles after impact. Furthermore, the nanostructure-coated samples exhibit lower adhesion forces, suggesting that the particles are easier to remove versus uncoated (Bixler and Bhushan, 2012b).

4.5.4.3. Wettability

To understand the role of CA and CAH on drag and antifouling, Bixler and Bhushan (2013d, 2013e) conducted a series of experiments with actual, replica, flat control, and rice leaf inspired samples. Measurements are reported for both the stream-wise and transverse flow directions, with the maximum values reported. For instance, rice leaf samples show a lower water contact angle when viewed in the stream-wise compared to the cross-stream direction, since the droplets are pinned between the longitudinal grooves. Measurements are reported for solid-air-water, solid-air-oil, and solid-water-oil interfaces.

4.5.4.4. Actual, replica, and rice leaf inspired samples

In air, Bixler and Bhushan (2012b) report that actual rice leaf and butterfly wing samples exhibit superhydrophobic characteristics due to Cassie-Baxter wetting. Conversely, the fish scales and shark skin show lower contact angles, presumably due to the Wenzel wetting, see images in Figure 64 (Bixler and Bhushan, 2012b). With oil droplets in air, each of the actual samples exhibits superoleophilicity (Bixler and Bhushan, 2013a). Furthermore with oil droplets underwater, actual rice leaf and butterfly wing samples exhibit superoleophilicity, however fish scale and shark skin samples exhibit superoleophobicity. It is reported that the rice leaf hierarchical morphology leads to the low contact angle, and that oil penetrates into the butterfly wing open lattice microstructure. With fish scales, it is reported that a thin water layer forms between the oil droplet and the impenetrable scale surface to encourage superoleophobicity. With shark skin, water soaks into the skin and combined with the impenetrable dermal denticle microstructures produces superoleophobicity (Bixler and Bhushan, 2012b, 2013a).

Experimental results from CA and CAH experiments by Bixler and Bhushan (2013d, 2013e) are tabulated. For actual, replica, and coated samples, Figure 65a and Figure 65b show CA and CAH, respectively; for rice leaf inspired samples, Figure 65c and Figure 65d show CA and CAH, respectively. For actual samples at the solid-air-water interface, the rice leaf shows the highest CA = 164° and lowest CAH = 3° . For comparison, maximum water contact angle of actual lotus leaves is 164° (Koch et al., 2009b). Also as expected, the coated rice leaf and shark skin replica samples exhibit a

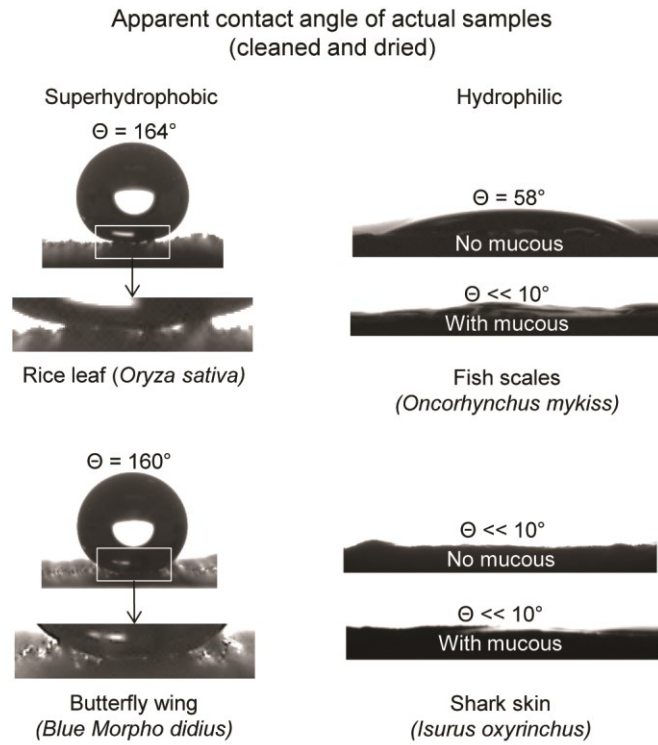
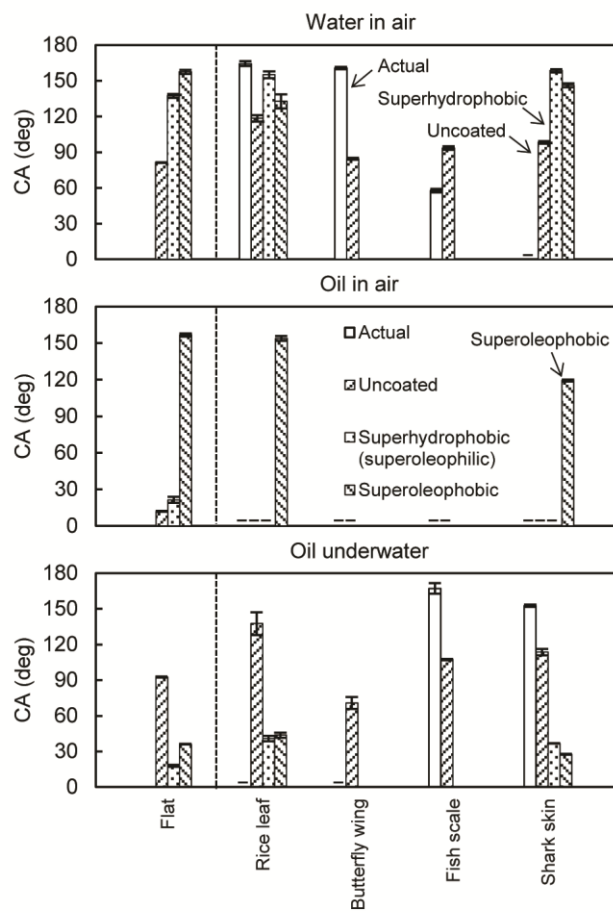


Figure 64: Water droplet images indicating that actual rice leaves and butterfly wings are superhydrophobic, whereas fish scales and shark skin are hydrophilic (adapted from Bixler and Bhushan, 2012b).

Figure 65: Wettability results with water and oil droplets (both in air and underwater) using actual, replica, and rice leaf inspired samples (adapted from Bixler and Bhushan, 2012b, 2013a, 2013d, 2013e). Shown are values for apparent CA for (a) actual, replica, and coated samples and (b) rice leaf inspired samples. Also shown are values for CAH (c) actual, replica, and coated samples and (d) rice leaf inspired samples. Self-cleaning efficiency improves with high CA and low CAH. Error bars show ± 1 standard deviation.

Figure 65a

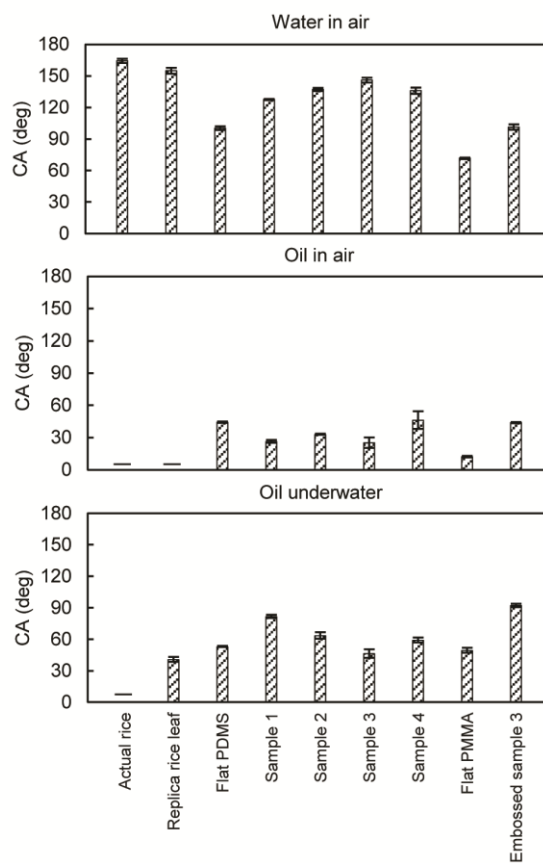
Apparent contact angle (CA)
(actual, replica, and coated samples)



(a)

Figure 65b

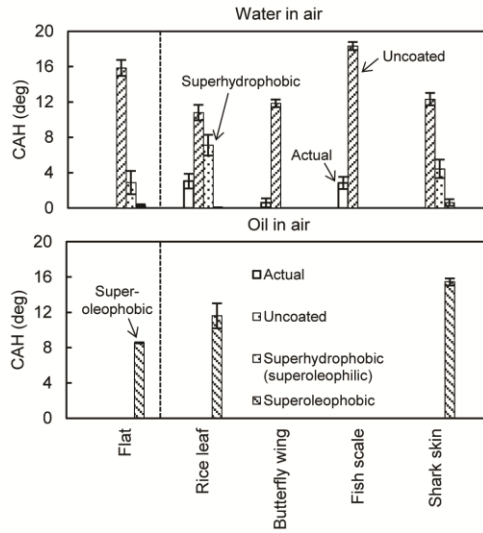
Apparent contact angle (CA)
(actual, replica, and rice leaf inspired samples)



(b)

Figure 65c

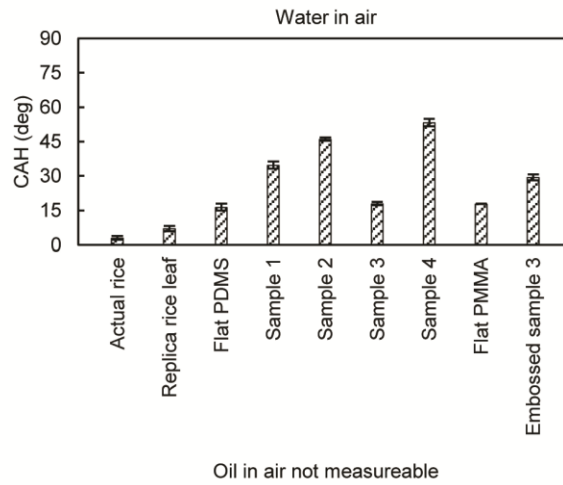
Apparent contact angle hysteresis (CAH)
(actual, replica, and coated samples)



(c)

Figure 65d

Apparent contact angle hysteresis (CAH)
(actual, replica, and rice leaf inspired samples)



(d)

higher contact angle than the uncoated samples, showing the effectiveness of the superhydrophobic coating (Bixler and Bhushan, 2012b). The superhydrophobic coating is also reported oleophilic at the solid-water-oil interface, and the superoleophobic coating is superoleophobic at the solid-air-oil interface (Bixler and Bhushan, 2013d). For the rice leaf inspired samples, Samples 1-4 exhibit hydrophobic contact angles with Sample 3 the highest at 146° and Embossed sample 3 at 101° (Bixler and Bhushan, 2013e). It should be noted that the oil CAH cannot be determined due to the low oil contact angle in air (Bixler and Bhushan, 2013d, 2013e).

When comparing measurements from various samples, there is a noticeable difference between actual and replica samples. Using Eq. 17 and Eq. 18a with experimental data provides results shown in Table 12. A comparison shows that rice leaf and butterfly wing measurements align well with the Cassie-Baxter equation, whereas fish scales and shark skin measurements align well with the Wenzel equation (Bixler and Bhushan, 2012b). This is reportedly due to the different mechanisms at work and how the sample materials and structures differ (Bixler and Bhushan, 2013d). For instance, a low surface energy nanostructured coating was applied to rice leaf urethane replicas in order to mimic actual rice leaves; however the nanostructured morphology differs from actual rice leaves (Bixler and Bhushan, 2012b, 2013a).

4.5.5. Wettability, drag, and antifouling

A comparison of drag results with wettability shows no direct correlation, however high CA coupled with low CAH leads to efficient antifouling. Drag reduction

Table 12: Replica sample CA predictions (Bixler and Bhushan, 2012b).

Sample	Actual			Replica			
	Roughness factor (R_f)	Fractional liquid-air contact area (f_{LA})	Measured CA	CA calculated using Wenzel Eq. 4	CA calculated using Cassie-Baxter Eq. 5	Measured CA (uncoated)	Measured CA (coated)
Rice leaf (<i>Oryza sativa</i>)	3.33	0.85	164**	59	141**	118	155*
Butterfly wing (<i>Blue Morpho didius</i>)	4.41	0.93	161**	48	152**	84	n/a
Fish scales (<i>Oncorhynchus mykiss</i>)	1.61	0.33	58*	76*	99	94*	n/a
Shark skin (<i>Isurus oxyrinchus</i>)	2.14	0.44	n/a	71*	105	98*	158

*indicates Wenzel regime **indicates Cassie-Baxter regime

mechanisms differ for various fluids under investigation with considerations given to liquid repellency, adhesion, and anisotropic flow characteristics. Reportedly drag reduction occurs with superhydrophobic/ oleophobic and superoleophilic surfaces; and antifouling with superhydrophobic/ oleophobic surfaces (Bixler and Bhushan 2012, 2013a, 2013b, 2013c, 2013d, 2013e). In the case of water flow, superhydrophobicity and low adhesion provides the greatest drag reduction (Bixler and Bhushan, 2012b). However in oil flow, the superoleophilic surfaces provide drag reduction via the thin film effect but superoleophobic surfaces perform similarly due to liquid repellency and low adhesion

(Bixler and Bhushan, 2013a). Therefore lower drag is achieved when appropriate wettability is coupled with the appropriate surface morphology, which can lead to anisotropic flow, liquid repellency, low adhesion, control of turbulent vortices, and/or production of the thin oil film.

Bixler and Bhushan (2013d, 2013e) report that high CA and low CAH alone does not always lead to drag reduction or antifouling. It has been shown that superhydrophobic surfaces provide drag reduction (Daniello et al., 2009; Jung and Bhushan, 2010; Bixler and Bhushan, 2013d), however the surface must be relatively smooth for such benefit. For instance, Sample 2 shows a relatively high water contact angle of 137° but also shows a drag increase in water, oil, and air. The tall pillars of Sample 2 are believed to impede fluid flow and the benefit from high contact angle is negated (Bixler and Bhushan, 2013e). For drag reduction, it is important to achieve high CA and low CAH with a relatively smooth surface such as the one employed with the rice leaf replica (Bixler and Bhushan, 2013d). The greatest self-cleaning is shown with the lotus effect samples; where the maximum contaminant removal is reported with Embossed sample 3 and rice leaf replica at 86% and 95%, respectively (Bixler and Bhushan, 2013e). It is believed that anti-biofouling may also improve with lotus effect surfaces (Bixler et al., 2013).

Understanding drag reducing and antifouling mechanisms is possible with water control models for rice leaf, butterfly wing, fish scale, and shark skin (Bixler and Bhushan 2012b, 2013e). As shown with simplified conceptual models in Figure 66, self-cleaning rice leaves and butterfly wings easily repel water, whereas the fish scale and

Water flow control mechanisms leading to low drag and antifouling:
conceptual models of surfaces found in nature

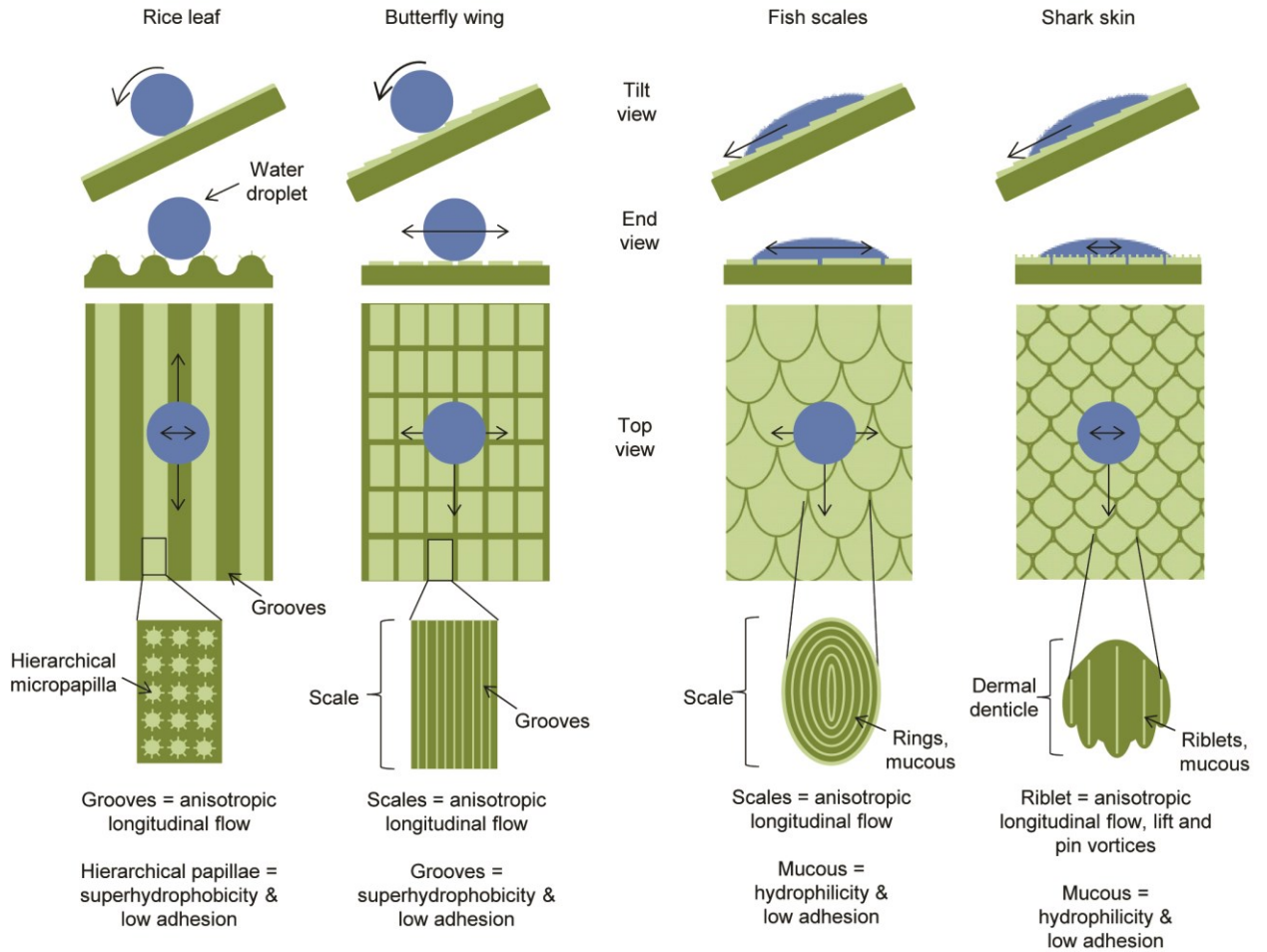


Figure 66: Water droplet control conceptual models of rice leaves, butterfly wings, fish scales, and shark skin (adapted from Bixler and Bhushan, 2012b, 2013d, 2013e). Each example contains mechanisms that are believed to promote low drag, self-cleaning, and antifouling. Arrows indicate the tendencies of fluid flow in transverse and longitudinal directions.

shark skin attract water. Furthermore, the longitudinal grooves, scales, or riblets efficiently direct fluid, which is reported to lower drag. The water droplets sit above the hierarchical surface structures of the rice leaf and butterfly wing, whereas they penetrate the surface structures of fish scales and shark skin. By staying above, the droplet can more easily roll and collect contaminants to improve antifouling efficiency. Mucous found on fish scale and shark skin is believed to act as a lubricant, and further reduce drag with the lower skin friction. This also provides antifouling benefits since the water next to the fish scales and shark skin moves quickly and prevents microorganisms from attaching (Bixler and Bhushan, 2012b).

4.6. Models for low drag and antifouling

In this section, we explain mechanisms behind rice leaf inspired low drag and antifouling surfaces from experimental results involving actual, replica, and rice leaf inspired samples.

4.6.1. Low drag models

It is believed that the combination of anisotropic flow, liquid repellency, and low adhesion are major contributors to drag reduction (Bixler and Bhushan, 2013d, 2013e). The anisotropic flow present with rice leaves and butterfly wings helps to facilitate efficient fluid movement over the surface. This control minimizes movement of fluid molecules in the viscous sublayer and thus reduces the energy losses, which leads to lower drag. A similar effect is also believed to be present with oil flow and superoleophobic surfaces (Bixler and Bhushan, 2013a).

Lowering drag using the rice leaf inspired Sample 3 is demonstrated in Figure 67 with closed channel flow – where hydrophobicity and oleophilicity (thin film effect) are believed to increase slip length (b) and reduce drag (Bixler and Bhushan, 2013e). Reportedly with rice leaf surfaces in oil flow, oil becomes trapped and holds stationary between the micropapillae, and lubricates the solid-liquid interface (Bixler and Bhushan, 2013a). The lubricating effect is believed to increase slip length (b), so therefore the flow velocity increases at the channel wall. A similar effect is expected with the Pitcher plant (*Nepenthes* genus) peristome (Koch and Barthlott, 2009; Bhushan, 2009), which was later demonstrated with the so-called biomimetic slippery liquid infused porous surfaces (Wong et al., 2011).

Using the experimental and modeling information, designing new bioinspired low drag and surfaces is possible with rice leaf inspired models (Bixler and Bhushan 2012b, 2013a, 2013d, 2013e). The rice leaf surface is attractive due to its low drag properties, as well as relatively simple two-dimensional cylindrical pillar geometry. As developed by Bixler and Bhushan (2013e), the basic morphology is shown in Figure 68. Jung and Bhushan (2007) reported that with similar patterns water droplets fully penetrate the area between the pillars when $\delta = H$ (transitioning from Cassie-Baxter to Wenzel regimes) when:

$$(\sqrt{2}P - D)^2 / R \geq H \quad (21)$$

where the known parameters are pitch (P), diameter (D), droplet radius (R), and uniform cylindrical pillar height (H). Eq. 21 provides guidance in developing surfaces to mimic rice leaf geometry with Cassie-Baxter regime.

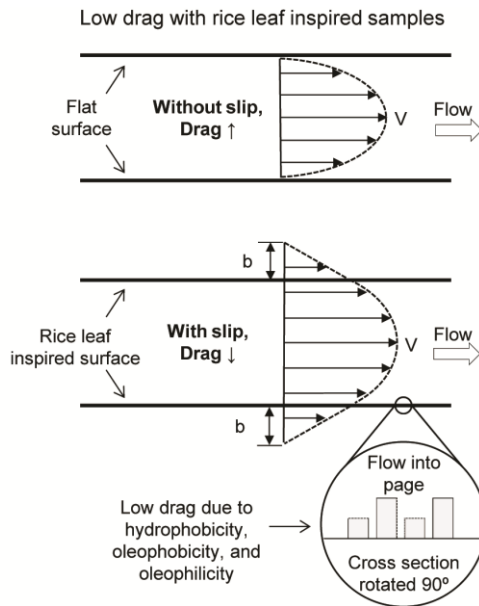


Figure 67: Drag reducing mechanisms with rice leaf inspired samples (adapted from Bixler and Bhushan, 2013d, 2013e). Velocity profiles show that slip length (b) is believed to increase with the rice leaf inspired surfaces. This leads to lower drag, increased flow rate, and improved antifouling. Sample 3 is shown based on the rice and butterfly wing effect with dual height pillars to promote anisotropic flow. It is believed that drag reduction leading to self-cleaning may be achieved by either superhydrophobic/oleophobic or superoleophilic (thin film effect) surfaces.

Anti-inorganic fouling with rice leaf inspired samples

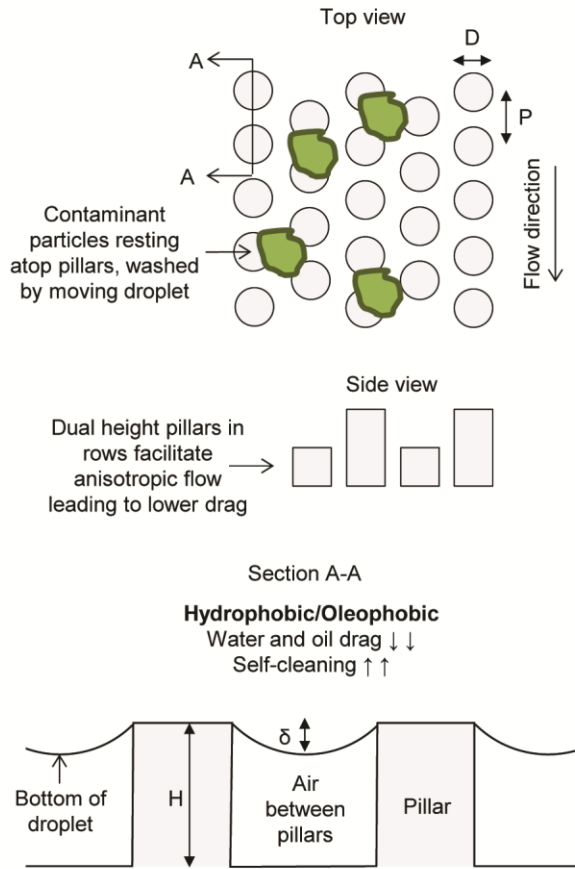


Figure 68: Anti-inorganic fouling mechanisms with rice leaf inspired samples (adapted from Bixler and Bhushan, 2012b, 2013d, 2013e). Model shown utilizes uniformly spaced micro-sized single height pillars in a hexagonal array. Inorganic fouling may be washed away in fluid flow via self-cleaning when coupled with high CA and low CAH.

Bixler and Bhushan (2013e) utilized Eq. 21 to design the new rice leaf inspired surfaces with hexagonal arrays of hierarchical morphologies (Bixler and Bhushan, 2012b, 2013a, 2013d). Shown is the dual height pillar geometry of Sample 3 which is believed to encourage drag reduction, self-cleaning, and antifouling by ensuring liquid repellency, low adhesion, and anisotropic fluid control.

4.6.2. Antifouling models

It is believed that rice leaf inspired surfaces are antifouling against biological and inorganic foulers via self-cleaning and microstructured sharp edged discontinuities, respectively (Bixler et al., 2013). Furthermore, superoleophobic surfaces effectively repel oil contaminants and provide superior anti-smudge properties. Self-cleaning may also be possible with superhydrophilic surfaces, as evident with pitcher plant (Koch and Barthlott, 2009; Bhushan, 2009, 2012; Wong et al., 2011; Nishimoto and Bhushan, 2013). Self-cleaning occurs with the pitcher plant when water uniformly spreads and slides off carrying contaminants (Hunt and Bhushan, 2011; Bhushan, 2012). As far as the samples reported in this paper, the dual-height design of Sample 3 provides superior antifouling properties (Bixler et al., 2013).

As indicated in Figure 69, *E. coli* shaped and sized microorganisms are unable to effectively colonize Sample 3 as well as the flat control sample (Bixler et al., 2013). In many cases, *E. coli* prefer to settle in clusters and around the bases of the pillars, which provide multiple attachment points of contact. It is believed that microorganisms slightly larger than the gap spacing between features are less likely to effectively colonize the surface. Furthermore, it is reported that the sharp edges of the pillars discourage the

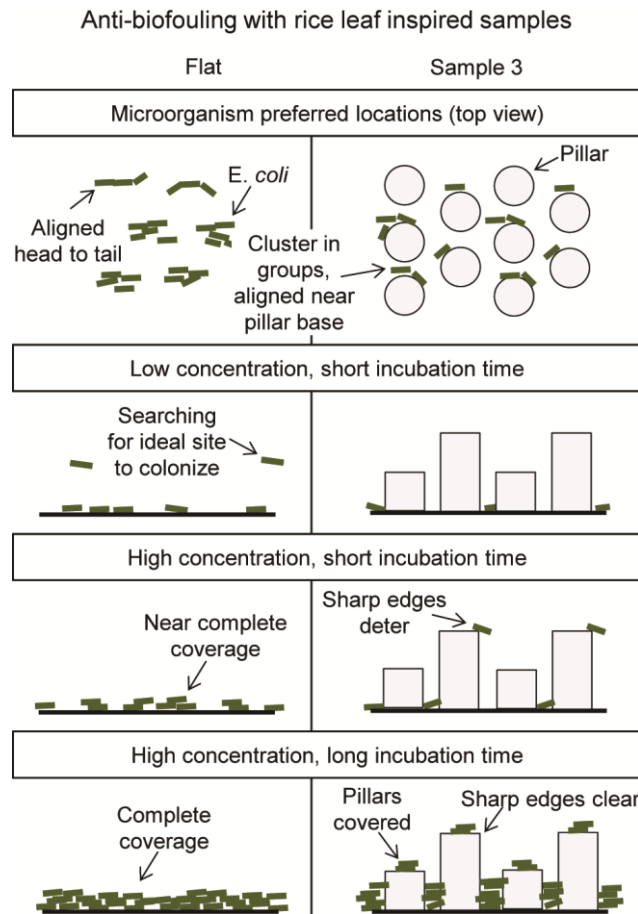


Figure 69: Anti-biofouling mechanisms with rice leaf inspired samples (adapted from Bixler et al., 2013). Shown are conceptual models based on anti-biofouling experiments using *E. coli* with low and high concentrations and short and long incubation times. Microorganisms prefer to cluster in groups and around the base of pillars. Microstructured discontinuities and sharp edges are believed to discourage *E. coli* colonization – where they may expire in the process of searching for an ideal landing site. Similar anti-biofouling mechanisms are expected with microorganisms of various shapes and sizes.

settling and eventual colonization of microorganisms on the surface. *E. coli* are shaped and sized such that the edges provide an inconvenient landing zone for settlement, and thus they continue searching for an ideal location to colonize. It is believed during this process that many *E. coli* expire while searching for a suitable location to permanently attach (Bixler et al., 2013).

Reportedly when *E. coli* concentrations are low and the incubation times are short, only a few *E. coli* are able to colonize the sample surface. However, when the concentrations are high and the incubation times are long, the *E. coli* eventually cover the surface creating a biofilm. Nevertheless, the discontinuities found with the sharp edged micro sized pillars are demonstrated to provide antifouling benefit by delaying colonization (Bixler et al., 2013). The height of the pillars also seems to play a role in antifouling, as shorter pillars found with Sample 1 and 3 were covered with *E. coli* sooner than the taller features with Sample 2 and 4. Nevertheless, such mechanisms are believed to be effective against microorganisms of various shapes and sizes. It is believed that postponing microorganism colonization time could aid in the preventing and spread of infectious diseases. This is true since often surfaces are cleaned periodically and therefore will be less likely to harbor a hazardous biofilm (Bixler et al., 2013).

4.7. Conclusions

When examining the replica and rice leaf inspired samples, the greatest drag reduction occurs in turbulent water flow. I report that the maximum pressure drop reduction is shown with my Embossed sample 3 and rice leaf replica at 23% and 26%,

respectively. In laminar oil flow, a 6% pressure drop reduction is reported using my Embossed sample 3 as compared to 10% with the rice leaf replica. In turbulent air flow, a 12% pressure drop reduction is reported using the Embossed sample 3 as compared to 20% with the rice leaf replica. Additionally, my results indicate that Embossed sample 3 shows similar anti-biofouling performance as Sample 3, at 28% and 29% coverage area reduction, respectively. The greatest anti-inorganic fouling is shown with my lotus effect samples; where the maximum contaminant removal is reported with Embossed sample 3 and rice leaf replica at 86% and 95%, respectively.

Rice leaf inspired samples are believed to provide anisotropic flow, liquid repellency, and low adhesion characteristics – which I present leads to drag reduction and antifouling. Mechanisms are discussed and models provided to help understand the role of surface features in actual, replica, and rice leaf inspired samples. It is believed that drag reduction and antifouling improves with high CA and low CAH, however low CA in oil flow may create a drag reducing thin film effect. I developed a nondimensional pressure drop equation indicating that pressure drop is directly proportional to velocity and nondimensional pressure drop is proportional to the Reynolds number. Furthermore, I demonstrate anti-biofouling with appropriately sized sharp edged discontinuities that discourage the settling and eventual colonization of microorganisms. As reported, *E. coli* are shaped and sized such that the pillar edges provide an inconvenient landing zone – which leads to antifouling. I also demonstrate that anti-inorganic fouling is made possible with lotus effect surfaces, where high contact angle and low contact angle hysteresis are desired.

The reported discoveries are promising for scaled-up production of new low-cost embossed films that may be applied to a variety of curved and flat surfaces. Additional investigations are warranted to further understand drag reduction in real world applications as well as antifouling against a diverse collection of foulers. In conclusion, the outlook of commercially viable low drag and antifouling films is promising for medical, marine, and industrial applications.

CHAPTER 5: CLOSURE

Found throughout living nature is inspiration for innovative engineering solutions. Unique properties of many flora and fauna inspire engineers to create bio-inspired solutions using nature's methods to problem solving. On the micro and nano scale, it is apparent that nature commonly utilizes nano/micro-sized hierarchical structures to survive in harsh environments. This thesis has focused on studying such surfaces in nature with special attention given to low drag and antifouling flora and fauna. Low drag and antifouling properties are desirable for numerous engineering applications in the medical, marine, and industrial applications – which can save time, money, and lives. For example, applications include anti-biofouling medical catheters to reduce the spread of disease, low drag and antifouling surfaces to reduce boat fuel consumption, and anti-inorganic fouling self-cleaning windows.

In this thesis, select samples from nature were thoroughly examined in order to further understand their unique surface structures and properties. I selected samples based on their presumed drag reducing and antifouling potential, with examples from both the ambient and aquatic environments. In order to further understand nature's methods, actual and replica samples were subjected to a series of drag and antifouling experiments. This aided in the understanding of drag reduction in laminar through turbulent flow using a wide range of fluid viscosities (water, oil, and air) as well as antifouling against

biological and inorganic foulers. Shark skin and lotus leaves were initially examined to understand their unique properties and to learn how such properties may be improved. I later determined that other promising surfaces in nature worth studying included rice leaves, butterfly wings, and fish scales.

Samples were thoroughly characterized and conceptual models were developed using various microscopy techniques and laboratory experiments. I collected and present morphology, fluid drag, anti-biofouling, anti-inorganic fouling, contact angle, and contact angle hysteresis experimental results to understand the role of sample geometrical dimensions. Measurements and images are included from light microscope, SEM, and optical profiler to provide qualitative and quantitative information on surface features related to fluid drag and antifouling. Fluid drag is reported with pressure drop measurements from sample lined closed channels as well as with wind tunnel experimentation. Antifouling is reported from anti-biofouling and anti-inorganic fouling experiments – using *E. coli* microorganisms and inorganic contaminant particles

I discovered that rice leaves and butterfly wings exhibit a combination of shark skin (anisotropic flow leading to low drag) and lotus leaf (superhydrophobic and self-cleaning) effects – producing the so-called rice and butterfly wing effect. To further understand this effect, I investigated rice leaves, butterfly wings, fish scales, and shark skin surfaces with experiments using actual, replica, and rice leaf inspired samples. I determined that rice leaves are particularly advantageous due to their superior drag reducing and antifouling properties, as well as their relatively simple morphology. As such, I designed the new rice leaf inspired samples to consist of hierarchical

microstructured pillars and ribs based on the rice leaf morphology. These samples were fabricated using photolithography, soft-lithography, and hot-embossing techniques. To combine effects, nanostructured coatings were applied to select replica samples to produce superhydrophobicity, superoleophilicity, and superoleophobicity. The role of these surface properties for various samples is presented in drag reduction and antifouling models.

This thesis provides guidance in understanding the role of sample geometrical dimensions and surface energy to design low cost options for drag reducing and antifouling surfaces using rice leaf inspired morphologies. More investigation is warranted in studying such surfaces for commercial applications in harsh conditions for durability and effectiveness against various foulers. This may include additional morphologies and embossed sheets subjected to drag and antifouling experimentation. Fouling removal during fluid flow would also be an important parameter to investigate.

BIBLIOGRAPHY

- Abarzua, S., Kacan, S. and Fuchs P. (1999), "Status and Potential of Natural Product Antifoulants," in *Recent Advances in Marine Biotechnology* (eds. Fingerman, M., Nagabhushanam, R. and Thompson, M.F), pp. 37-66, Science Publishers, Enfield, New Hampshire.
- Adiga, S.P., Curtiss, L.A., Elam, J.W., Pellin, M.J., Shih, C.C., Shih, C.M., Lin, S.J., Su, Y.Y., Gittard, S.D., Zhang, J. and Narayan, R.J. (2008), "Nanoporous Materials for Biomedical Devices," *JOM*, March, 26-32
- Allen, R. (ed.) (2010), *Bulletproof Feathers How Science Uses Nature's Secrets to Design Cutting Edge Technology*, Ivy Press, London.
- Amaya, S., Dao, D.V., and Sugiyama, S. (2009), "Study on an Efficient Fabrication Process for PMMA Moveable Microstructures Based on Hot Embossing and Polishing Process," Paper # 978-1-4244-5095-4/09, IEEE, New York.
- Anderson, J.D. (2010), *Fundamentals of Aerodynamics*, 5th Ed., McGraw Hill, New York.
- Anon (1952), *Marine Fouling and its Prevention*, Woods Hole Oceanographic Institute, US Naval Institute, Annapolis, US.
- Anonymous (1999), *Why Is Titanium the Metal of Choice for Medical Applications from Head to Toe?* International Titanium Association, Boulder, Colorado.
- Anonymous (2010), *Sterilization Methods Overview*. Retrieved March 2, 2012, from <http://www.lso-inc.com/sterilization-validation-services/sterilization-methods-overview.html>
- Armellini, D., Reynolds, M.A., Harro, J.M. and Molly, L. (2009), "Biofilm Formation on Natural Teeth and Dental Implants: What is the Difference?" in *The Role of Biofilms in Device-Related Infections* (eds. Shirtliff, M. and Leid, J.G.), pp. 109-122, Springer-Verlag, Berlin.
- Armstrong, R.E., Drapeau, M.D., Loeb, C.A. and Valdes, J.J. (eds.) (2010), *Bio-Inspired Innovation and National Security*, National Defense University Press, Washington, D.C.
- Banerjee, I., Pangule, R.C. and Kane, R.S. (2011), "Antifouling Coatings: Recent Developments in the Design of Surfaces That Prevent Fouling by Proteins, Bacteria, and Marine Organisms," *Adv. Mater.* **23**, 690-718

- Bar-Cohen, Y. (2011), *Biomimetics: Nature Based Innovation*, CRC Press, Boca Raton, Florida.
- Barlow, J.B., Rae, W.H., and Pope, A. (1999), *Low-Speed Wind Tunnel Testing*, 3rd Ed., Wiley-Interscience, New York.
- Barthlott, W. and Neinhuis, C. (1997), "Purity of the sacred lotus, or escape from contamination in biological surfaces," *Planta* **202**, 1-8
- Batchelor, G.K. (1970), *An Introduction to Fluid Dynamics*, Cambridge University Press, Cambridge.
- Baum, C., Simon, F., Meyer, W., Fleischer, L.G., Siebers, D., Kacza, J. and Seeger, J. (2003), "Surface Properties of the Pilot Whale *Globicephala melas*," *Biofouling* **19**, 181–186
- Bechert, D. W., Bruse, M. and Hage, W. (2000a), "Experiments with three-dimensional riblets as an idealized model of shark skin," *Exp. Fluids* **28**, 403–412
- Bechert, D. W., Bruse, M., Hage, W. and Meyer, R. (2000b), "Fluid mechanics of biological surfaces and their technological application," *Naturwissenschaften* **87**, 57–171
- Bechert, D. W., Bruse, M., Hage, W., van der Hoeven, J. G. T. and Hoppe, G. (1997a), "Experiments on drag reducing surfaces and their optimization with an adjustable geometry," *J. Fluid Mech.* **338**, 59–87
- Bechert, D.W., Bruse, M., Hage, W., and Meyer, R. (1997b), "Biological Surfaces and Their Technological Application – Laboratory and Flight Experiments on Drag Reduction and Separation Control," Paper # AIAA-1997-1960, presented at AIAA 28th Fluid Dynamics Conference, Snowmass Village, CO, AIAA, New York.
- Bechert, D.W., Hoppe, G. and Reif, W.E. (1985), "On the Drag Reduction of the Shark Skin," Paper # AIAA-85-0546, presented at AIAA Shear Flow Control Conference, Boulder, CO, AIAA, New York.
- Bechert, D.W., Hoppe, G., van der Hoeven, J.G.T. and Makris, R. (1992), "The Berlin oil channel for drag reduction research," *Exp. in Fluids* **12**, 251-260
- Becker, K. and Wahl, M. (1996), "Behavior patterns as natural antifouling mechanisms of tropical marine crabs," *J. Exp. Mar. Biol. Ecol.* **203**, 245–258
- Bers, A. and Wahl, M. (2004), "The Influence of Natural Surface Microtopographies on Fouling," *Biofouling* **20**, 43–51

- Bhushan, B. (2003), "Adhesion and stiction: Mechanisms, measurement techniques, and methods for reduction," *J. Vac. Sci. Technol.* **21**, 2262-2296
- Bhushan, B. (2009), "Biomimetics: Lessons from Nature – an Overview," *Phil. Trans. R. Soc.* **367**, 1445-1486
- Bhushan, B. (2010), Springer Handbook of Nanotechnology, 3rd Edition, Springer, New York.
- Bhushan, B. (2012), Biomimetics: Bioinspired Hierarchical-Structured Surfaces for Green Science and Technology, Springer-Verlag, Heidelberg, Germany.
- Bhushan, B. and Jung, Y.C. (2011), "Natural and Biomimetic Artificial Surfaces for Superhydrophobicity, Self-Cleaning, Low Adhesion, and Drag Reduction," *Prog. Mater. Sci.* **56**, 1-108
- Bhushan, B., Cichomski, M., Hoque, E., DeRose, J.A., Hoffmann, P. and Mathieu, H.J. (2006a), "Nanotribological characterization of perfluoroalkylphosphonate self-assembled monolayers deposited on aluminum-coated silicon substrates," *Microsyst Technol* **12**, 588–596
- Bhushan, B., Hansford, D. and Lee, K.K. (2006b), "Surface modification of silicon and polydimethylsiloxane surfaces with vapor-phase-deposited ultrathin fluorosilane films for biomedical nanodevices," *J. Vac. Sci. Technol. A* **24**, 1197-1202
- Bhushan, B., Jung, Y.C. and Koch, K. (2009a), "Micro-, Nano- and Hierarchical Structures for Superhydrophobicity, Self-Cleaning and Low Adhesion," *Phil. Trans. R. Soc.* **367**, 1631-1672
- Bhushan, B., Jung, Y.C. and Koch, K. (2009b), "Self-Cleaning Efficiency of Artificial Superhydrophobic Surfaces," *Langmuir*, **25**, 3240-3248
- Bixler, G.D. and Bhushan, B. (2012a), "Biofouling Lessons from Nature," *Phil. Trans. R. Soc. A*, **370**, 2381-2417
- Bixler, G.D. and Bhushan, B. (2012b), "Bioinspired rice leaf and butterfly wing surface structures combining shark skin and lotus effects," *Soft Mat.*, **8**, 11271-11284
- Bixler, G.D. and Bhushan, B. (2013a), "Bioinspired micro/nanostructured surfaces for oil drag reduction in closed channel flow," *Soft Mat.*, **9**, 1620-1635
- Bixler, G.D. and Bhushan, B. (2013b), "Shark skin inspired low-drag microstructured surfaces in closed channel flow," *J. Colloid Interf. Sci.* **393**, 384-396
- Bixler, G.D. and Bhushan, B. (2013c), "Fluid Drag Reduction with Shark-skin Riblet Inspired Microstructured Surfaces," *Adv. Funct. Mater.* **23**, 4507-4528.

- Bixler, G.D. and Bhushan, B. (2013d), "Fluid Drag Reduction and Efficient Self-Cleaning with Rice Leaf and Butterfly Wing Bioinspired Surfaces," *Nanoscale* **5**, 7685-7710.
- Bixler, G.D. and Bhushan, B. (2013e), "Rice- and Butterfly-Wing Effect Inspired Self-Cleaning and Low Drag Micro/nanopatterned Surfaces in Water, Oil, and Air Flow," *Nanoscale*, in press.
- Bixler, G.D. and Bhushan, B. (2013f), "Rice- and Butterfly-Wing Effect Inspired Low Drag and Antifouling Surfaces: A Review," *under review*.
- Bixler, G.D., Theiss, A., Bhushan, B., and Lee, S.C. (2013), "Anti-fouling Properties of Microstructured Surfaces Bio-inspired by Rice Leaves and Butterfly Wings," *under review*.
- Blevins, R.D. (1984), *Applied Fluid Dynamics Handbook*, Van Nostrand-Reinhold, New York.
- Bormashenko, E., Bormashenko, Y., Stein, T., Whyman, G. and Bormashenko, E. (2007), "Why Do Pigeon Feathers Repel Water? Hydrophobicity of Pennae, Cassie-Baxter Wetting Hypothesis and Cassie-Wenzel Capillarity-Induced, Wetting Transition" *J. Colloid Interf. Sci.* **311**, 212-216
- Bott, T.R. (1988a), "Crystallization Fouling – Basic Science and Models," in *Fouling Science and Technology* (eds. Melo, L.F., Bott, T.R. and Bernardo, C.A.), pp. 251-260, Kluwer Academic Publishers, Dordrecht, The Netherlands.
- Bott, T.R. (1988b), "Crystallization of Organic Materials," in *Fouling Science and Technology* (eds. Melo, L.F., Bott, T.R. and Bernardo, C.A.), pp. 275-280, Kluwer Academic Publishers, Dordrecht, The Netherlands.
- Brennan, A.B., Baney, R.H., Carman, M.I., Estes, T.G., Feinberg, A.W., Wilson, L.H. and Schumacher, J.F.. (2010), "Surface Topographies for Non-Toxic Bioadhesion Control," United States Patent no. 7 650 848
- Brostow, W. (2008), "Drag reduction in flow: review of applications, mechanism and prediction," *J. Indust and Eng Chem* **14**, 408-416
- Burger, E.D., Munk, W.R. and Wahl, H.A. (1982), "Flow Increase in the Trans Alaska Pipeline Through Use of a Polymeric Drag-Reducing Additive," *J. Petro Tech*, **34**, 377-386
- Buttner, C.C. and Schulz, U. (2011), "Shark skin inspired riblet structures as aerodynamically optimized high temperature coatings for blades of aeroengines," *Smart Matl. and Struct.* **20**, 1-9

- Callow, M.E. (1986), "A World-Wide Survey of Slime Formation on Anti-Fouling Paints," in *Algal Biofouling* (eds. Evans, L.V. and Hoagland, K.D), pp. 1-20, Elsevier Science Publishers, Amsterdam.
- Callow, M.E. (1999), "The Status and Future of Biocides in Marine Biofouling Prevention," in *Recent Advances in Marine Biotechnology* (eds. Fingerman, M., Nagabhushanam, R. and Thompson, M.F), pp. 109-126, Science Publishers, Enfield, New Hampshire.
- Callow, M.E. and Callow, J.A. (2002), "Marine Biofouling: a Sticky Problem," *Biologist* **49**, 1-5
- Callow, M.E., Pitchers, R.A. and Milne A. (1986), "The Control of Fouling by Non-Biocidal Systems," in *Algal Biofouling* (eds. Evans, L.V. and Hoagland, K.D), pp. 145-158, Elsevier Science Publishers, Amsterdam.
- Camper, A.K. and McFeters, G.A. (2000), "Problems of Biofouling in Drinking Water Systems," in *Industrial Biofouling Detection, Prevention and Control* (eds. Walker, J., Surman, S. and Jass, J.), pp. 15-38, Wiley, New York.
- Cao, L., Jones, A.K., Sikka, V.K., Wu, J. and Gao, D. (2009), "Anti-Icing Superhydrophobic Coatings," *Langmuir* **25**, 12444-12448
- Caram, J.M. and Ahmed, A. (1991), "Effect of Riblets on Turbulence in the Wake of an Airfoil," *AIAA* 29 (11), 1769-1770
- Caram, J.M. and Ahmed, A. (1992), "Development of the Wake of an Airfoil with Riblets," *AIAA* 30 (12), 2817-2818
- Carman, M.L., Estes, T.G., Feinburg, A.W., Schumacher, J.F., Wilkerson, W., Wilson, L.H., Callow, M.E., Callow, J.A. and Brennan, A.B. (2006), "Engineered Antifouling Microtopographies—Correlating Wettability with Cell Attachment," *Biofouling* **22**, 11–21
- Chan, J. and Wong, S. (eds.) (2010), *Biofouling Types, Impact and Anti-Fouling*, Nova Science Publishers, New York
- Charles, C.H., Mostler, K.M, Bartels, L.L. and Mankodi, S.M. (2004), "Comparative Antiplaque and Antigingivitis Effectiveness of an Chlorhexidine and an Essential Oil Mouth Rinse: 6-Month Clinical Trial," *J Clin Periodontal* **31**, 878-884
- Clare, A.S. and Aldred, N. (2009), "Surface Colonization by Marine Organisms and its Impact on Antifouling Research," in *Advances in Marine Antifouling Coatings and Technologies* (eds. Hellio, C. and Yebra, D.), pp. 46-79, CRC Press, Boca Raton, Florida.

- Clarkson, N. (1999), "The Antifouling Potential of Silicone Elastomer Polymers," in *Recent Advances in Marine Biotechnology* (eds. Fingerman, M., Nagabhushanam, R. and Thompson, M.F), pp. 87-108, Science Publishers, Enfield, New Hampshire.
- Collins, M.W. and Brebbia, C.A. (eds.) (2004), *Design and Nature II Comparing Design in Nature with Science and Engineering*, WIT Press, Southampton, UK.
- Cologer, C.P. (1984), "Six Year Interaction of Underwater Cleaning with Copper Based Antifouling Paints on Navy Surface Ships," *Nav. Eng. J.* **96**, 200–208
- Copisarow, M. (1945), "Marine Fouling and its Prevention," *Science* **101**, pp. 406-407
- Costerton, J.W. (ed.) (2008), *Springer Series on Biofilms*, Springer-Verlag, Berlin.
- Coustols, E. (1989), "Behavior of Internal Manipulators: "Riblet" Models in Subsonic and Transonic Flows," Paper # AIAA-89-0963, presented at AIAA Shear Flow Conference, Tempe, AZ, AIAA, New York.
- Coustols, E. and Cousteix, J. (1994), "Performances of Riblets in the Supersonic Regime," *AIAA* 32 (2), 431-433
- Coustols, E. and Schmitt, V. (1990), "Synthesis of Experimental Riblet Studies in Transonic Conditions," in *Turbulence Control by Passive Means* (eds. Coustols, Kluwer, Dordrecht), pp. 123-140, The Netherlands.
- Cristiani, P. (2010), "Electrochemical Technologies for Antifouling Treatments of Cooling Circuits," in *Biofouling Types, Impact and Anti-Fouling* (eds. Chan, J. and Wong, S.), pp. 175-198, Nova Science Publishers, New York.
- Cui, Z. and Wan, Y. (2005), "Biofouling in Membrane Separation Systems," in *Surfaces and Interfaces for Biomaterials* (ed. Vadgama, P.), pp. 493-544, CRC Press, Boca Raton, Florida.
- Cunningham, A.B., Lennox, J.E. and Ross, R.J. (2008), *Biofilms in Industrial Environments*. Retrieved June 27, 2011, from http://biofilmbook.hypertextbookshop.com/public_version/contents/contents.html
- Daniello, R.J., Waterhouse, N.E. and Rothstein, J.P. (2009), "Drag reduction in turbulent flows over superhydrophobic surfaces," *Phys. Fluids* **21**, 085103
- Davenport, J. (1999), "Antifouling Properties of the Dogfish Egg Case and Their Possible Application in Developing Nontoxic Alternatives to Antifouling Paints," in *Recent Advances in Marine Biotechnology* (eds. Fingerman, M., Nagabhushanam, R. and Thompson, M.F), pp. 21-36, Science Publishers, Enfield, New Hampshire.

- Davies, M. (ed.) (2002), *Standard Handbook for Aeronautical and Astronautical Engineers*, McGraw-Hill, New York.
- de Nys, R. and Steinberg, P. (2002), "Linking Marine Biology and Biotechnology," *Curr. Opin. Biotechnol.* **13**, 244–248
- Dean, B. and Bhushan, B. (2010), "Shark-skin Surfaces for Fluid-Drag Reduction in Turbulent Flow: a Review," *Phil. Trans. R. Soc.* **368**, 4775-4806
- Dean, B. and Bhushan, B. (2012), "The effect of riblets in rectangular duct flow," *Appl. Surface Sci.* **258**, 3936-3947
- Denkena, B., Kohler, J. and Wang, B. (2010), "Manufacturing of functional riblet structures by profile grinding," *CIRP J. Manuf. Sci. Tech.* **3**, 14-26
- Deyuan, Z., Yuehao, L., Huawei, C. and Xinggang, J. (2011a), "Exploring Drag-Reducing Grooved Internal Coating For Gas Pipelines," *Pipeline & Gas Journal* March, 59-60
- Deyuan, Z., Yuehao, L., Xiang, L. and Huawei, C. (2011b), "Numerical Simulation and Experimental Study of Drag-Reducing Surface of a Real Shark Skin," *J. of Hydrodynamics* **23**, 204-211
- Dickinson, P.H. and Proudley, G.M. (1991), "Methods of Manufacture and Surface Treatment Using Laser Radiation," United States Patent no. 4 994 639
- Dobretsov, S. (2009), "Expected Effect of Climate Change on Fouling Communities and its Impact on Antifouling Research," in *Advances in Marine Antifouling Coatings and Technologies* (eds. Hellio, C. and Yebra, D.), pp. 222-239, CRC Press, Boca Raton, Florida.
- Donlan, R.M. (2001), "Biofilms and Device-Associated Infections," *Emerg. Infect. Dis.* **7**, 277-281
- Dror, N., Mandel, M., Hazan, Z. and Lavie, G. (2009), "Advances in Microbial Biofilm Prevention on Indwelling Medical Devices with Emphasis on Usage of Acoustic Energy," *Sensors* **9**, 2538-2554
- Dunham, B. (2009), Cool Plasma Packs Heat Against Biofilms. Retrieved June 24, 2011, from http://uscnews.usc.edu/science_technology/cool_plasma_pack_heat_against_biofilms.html
- Ebert, D. and Bhushan, B. (2012a), "Wear-resistant rose petal-effect surfaces with superhydrophobicity and high droplet adhesion using hydrophobic and hydrophilic nanoparticles," *J. Colloid Interf. Sci.* **384**, 182-188

- Ebert, D. and Bhushan, B. (2012b), "Transparent, Superhydrophobic, and Wear-Resistant Coatings on Glass and Polymer Substrates Using SiO₂, ZnO, and ITO Nanoparticles," *Langmuir* **28**, 11391-11399
- Edgar, G. (1997), *Australian Marine Life: the Plants and Animals of Temperate Waters*. Reed Books, Victoria.
- Emmenegger, C.R., Brynda, E., Riedel, T., Sedlakova, Z., Houska, M. and Alles, A.B. (2009), "Interaction of Blood Plasma with Antifouling Surfaces," *Langmuir* **25**, 6328-6333
- Enyutin, G.V., Lashkov, Y.A., and Samoilova, N.V. (1995), "Drag Reduction in Riblet-Lined Pipes," *Fluid Dynamics*, 30 (1), 45-48
- Epstein, N. (1988), "Particulate Fouling of Heat Transfer Surfaces: Mechanisms and Models," in *Fouling Science and Technology* (eds. Melo, L.F., Bott, T.R. and Bernardo, C.A.), pp. 143-164, Kluwer Academic Publishers, Dordrecht, The Netherlands.
- Feng, L., Li, S., Li, Y., Li, H., Zhang, L., Zhai, J., Song, Y., Liu, B., Jiang, L. and Zhu, D. (2002), "Super-Hydrophobic Surfaces: From Natural to Artificial," *Adv. Mater.* **14**, 1857-1860
- Feng, X. and Jiang, L. (2006), "Design and Creation of Superwetting/Antiwetting Surfaces," *Adv. Mater.* **18**, 3063-3078
- Fingerman, M., Nagabhushanam, R. and Thompson, M.F. (eds.) (1999), *Recent Advances in Marine Biotechnology*, Science Publishers, Inc., Enfield, New Hampshire.
- Finlay, J.A., Callow, M.E., Schultz, M.P., Swain, G.W., and Callow, J.A. (2002), "Adhesion Strength of Settled Spores of the Green Alga *Enteromorpha*," *Biofouling* **18**, 251-256
- Fischer, E.C., Castelli, V.J., Rodgers, S.D. and Bleile, H.R. (1984), "Technology for Control of Marine Biofouling – A Review," in *Marine Biodeterioration: An Interdisciplinary Study* (eds. Costlow, J.D. and Tipper, R.C.), pp. 261-300, Naval Institute Press, Annapolis, Maryland.
- Flemming, H.C., Szewzyk, U. and Griebe, T. (eds.) (2000), *Biofilms Investigative Methods and Applications*, Technomic Publishing Co., Lancaster, Pennsylvania.
- Flemming, H.C., Wingender, J., Moritz, R., Borchard, W. and Mayer, C. (1999), "Physio-chemical Properties of Biofilms – A Short Review," in *Biofilms in the Aquatic Environment* (eds. Keevil, C.W., Godfree, A., Holt, D. and Dow, C), pp. 1-12, The Royal Society of Chemistry, Cambridge.

- Fletcher, J.T., Finlay, J.A., Callow, M.E., Callow, J.A., and Ghadiri, M.R. (2007), "A Combinatorial Approach to the Discovery of Biocidal Six-Residue Cyclic, l-a-Peptides Against the Bacteria Methicillin-Resistant *Staphylococcus aureus* (MRSA) and *E. coli* and the Biofouling Algae *Ulva linza* and *Navicula perminuta*," *Chem. Eur. J.* **13**, 4008-4013
- Fox, R.W. and McDonald, A.T. (1998), *Introduction to Fluid Mechanics*, Wiley, New York.
- Gaudet, L. (1989), "Properties of riblets at supersonic speed" *Applied Scientific Research* **46**, 245-254
- Genzer, J. and Efimenko, K. (2006), "Recent developments in superhydrophobic surfaces and their relevance to marine fouling: a review" *Biofouling* **22**, 339-360
- Gillcrist, M. C. and Reidy, L. W. (1989), "Drag measurements on marine vehicles with a riblet surface coating," in *Drag Reduction in Fluid Flows* (eds. Sellin, R. and Moses, R.), pp. 99-106, Ellis Horwood Publishers, Chichester, England.
- Gompertz, K., Bons, J.P., and Gregory, J.W. (2012), "Passive Trip Evaluation Using Infrared Thermography," Paper # AIAA-2012-0678, presented at 50th AIAA Aerospace Sciences Meeting, Nashville, TN, AIAA, New York.
- Goodwyn, P.P., Maezono, Y., Hosoda, N. and Fujisaki, K. (2009), "Waterproof and translucent wings at the same time: problems and solutions in butterflies," *Naturwissenschaften* **96**, 781-787
- Gordon, D.P. and Mawatari, S.F. (1992), *Atlas of Marine-fouling Bryozoa of New Zealand Ports and Harbours*, Miscellaneous Pub, New Zealand Oceanographic Institute.
- Gordon, J.E. (1976), *The new science of strong materials, or why you don't fall through the floor*, 2nd Ed., Pelican-Penguin, London, UK
- Greer, S.P., Iken, K.B., McClintock, J.B. and Amsler, C.D. (2003), "Individual and Coupled Effects of Echinoderm Extracts and Surface Hydrophobicity on Spore Settlement and Germination in the Brown Alga *Hinckesia irregularis*," *Biofouling* **19**, 315-326
- Griebe, T. and Flemming, H.C. (2000), "Rotating Annular Reactors for Controlled Growth of Biofilms," in *Biofilms Investigative Methods and Applications* (eds. Flemming, H.C., Szewzyk, U. and Griebe, T.), pp. 1-22, Technomic Publishing Co, Inc., Lancaster, Pennsylvania.

- Guenther, J. and de Nys, R. (2007), "Surface Microtopographies of *Tropical* Sea Stars: Lack of an Efficient Physical Defense Mechanism Against Fouling," *Biofouling* **23**, 419-429
- Guo, Z. and Liu, W. (2007), "Biomimic from the superhydrophobic plant leaves in nature: Binary structure and unitary structure," *Plant Science* **172**, 1103-1112
- Gunneberger, R. and Hage, W. (2011), "Drag characteristics of longitudinal and transverse riblets at low dimensionless spacings," *Exp. Fluids*, **50**, 363-373
- Hall-Stoodley, L, Costerton, J.W. and Stoodley, P. (2004), "Bacterial Biofilms: from the Natural Environment to Infectious Diseases," *Nature Reviews*. **2**, 95-108
- Han, M., Lim, H.C., Jang, Y.-G., Seung, S.L., and Lee, S.-J. (2003), "Fabrication of a Micro-Riblet Film and Drag Reduction Effects on Curved Objects," Paper # 0-7803-7731-1, presented at 12th International Conference on Solid State Sensors, Actuators and Microsystems, Boston, MA.
- Harder, T. and Yee, L.H. (2009), "Bacterial Adhesion and Marine Fouling," in *Advances in Marine Antifouling Coatings and Technologies* (eds. Hellio, C. and Yebra, D.), pp. 113-131, CRC Press, Boca Raton, Florida.
- Hellio, C. and Yebra, D. (eds.) (2009), *Advances in Marine Antifouling Coatings and Technologies*, CRC Press, Boca Raton, Florida.
- Herzberg, M. and Elimelech, M. (2007), "Biofouling of reverse osmosis membranes: Role of biofilm-enhanced osmotic pressure," *J. of Membrane Science* **295**, 11-20
- Hirt, G. and Thome, M. (2007), "Large area rolling of functional metallic micro structures," *Prod. Eng. Res. Devel.* **1**, 351-356
- Hunt, J. and Bhushan, B. (2011), "Nanoscale biomimetics studies of *Salvinia molesta* for micropattern fabrication," *J. Colloid Interf. Sci.* **363**, 187-192
- Israelachvili, J. N. (1992), *Intermolecular and Surface Forces*, 2nd ed., Academic Press, London.
- Jang, P.S., Benney, D.J. and Gran R.L. (1986), "On the origin of streamwise vortices in a turbulent boundary layer," *J. Fluid Mech.* **169**, 109-123
- Jass, J. and Walker, J.T. (2000), "Biofilms and Biofouling," in *Industrial Biofouling Detection, Prevention and Control* (eds. Walker, J., Surman, S. and Jass, J.), pp. 1-12, Wiley, New York.

- Jones, G. (2009), "The Battle Against Marine Biofouling: a Historical Review," in *Advances in Marine Antifouling Coatings and Technologies* (eds. Hellio, C. and Yebra, D.), pp. 19-45, CRC Press, Boca Raton, Florida.
- Jung, Y.C. and Bhushan, B. (2009), "Wetting Behavior of Water and Oil Droplets in Three-Phase Interfaces for Hydrophobicity/philicity and Oleophobicity/philicity," *Langmuir* **25**, 14165-14173
- Jung, Y. C. and Bhushan, B. (2010), "Biomimetic structures for fluid drag reduction in laminar and turbulent flows," *J. Phys.: Condens. Matter* **22**, 1-9
- Jung, Y.C. and Bhushan, B. (2010), "Biomimetic structures for fluid drag reduction in laminar and turbulent flows," *J. Phys.: Condens. Matter* **22**, 1-9
- Keevil, C.W., Godfree, A., Holt, D. and Dow, C. (eds.) (1999), *Biofilms in the Aquatic Environment*, The Royal Society of Chemistry, Cambridge, UK.
- Kennedy, J.L. (1993), *Oil and gas pipeline fundamentals*, PennWell Books, Tulsa, Oklahoma.
- Kesel, A. and Liedert, R. (2007), "Learning from Nature: Non-Toxic Biofouling Control by Shark Skin Effect," *Comp. Biochem. Physiol. A* **146**, S130
- Ketchum, B.H. (1952), "Factors Influencing the Attachment and Adherence of Fouling Organisms," in *Marine Fouling and Its Prevention*, pp. 30–40, Woods Hole Oceanographic Institution
- Khan, M.S., Rehman, S., Ali, M.A., Sultan, B. and Sultan, S. (2008), "Infection in Orthopedic Implant Surgery, its Risk Factors and Outcomes," *J. Ayub. Med. Coll. Abbottabad* **20**, 23-25
- Kim, S.H., Kwak, S.Y., Sohn, B.H. and Park, T.H. (2003), "Design of TiO₂ nanoparticle self-assembled aromatic polyamide thin-film-composite (TFC) membrane as an approach to solve biofouling problem," *J. of Membrane Science* **211**, 157-165
- Kissinger, P.T. (2005), "Biosensors-a perspective," *Biosens. Bioelectron* **20**, 2512-2516
- Kline, S.J., Reynolds, W.C., Schraub, F.A. and Runstadler, P.W. (1967), "The structure of turbulent boundary layers," *J. Fluid Mech.* **30**, 741–773
- Koch, K. and Barthlott, W. (2009), "Superhydrophobic and Superhydrophilic Plant Surfaces: an Inspiration for Biomimetic Materials," *Phil. Trans. R. Soc.* **367**, 1487–1509
- Koch, K., Bhushan, B. and Barthlott, W. (2009a), "Multifunctional Surface Structures of Plants: An Inspiration for Biomimetics," *Prog. Mater. Sci.* **54**, 137-178

- Koch, K., Bhushan, B., Jung, Y.C., and Barthlott, W. (2009b), "Fabrication of artificial Lotus leaves and significance of hierarchical structure for superhydrophobicity and low adhesion," *Soft Matter* **5**, 1386-1393
- Kricka, L.J., Fortina, P., Panaro, N.J., Wilding, P., Alonso-Amigo, G., and Becker, H. (2002), "Fabrication of plastic microchips by hot embossing," *Lab Chip* **2**, 1-4
- Krieger, K. (2004), "Do pool sharks really swim faster?" *Science* **305**, 636-637
- Kwon, S., Kim, H., Ha, J.W. and Lee, S.Y. (2011), "Prevention of Protein and Polymeric Nanoparticles Adsorption using Perfluoropolyether," *J. Ind. Eng. Chem.* **17**, 259-263
- Lang, A. W., Motta, P., Hidalgo, P. and Westcott, M. (2008), "Bristled shark skin: a microgeometry for boundary layer control," *Bioinspir. Biomim.* **3**, 1-9
- Lebret, K., Thabard, M., and Hellio, C. (2009), "Algae as Marine Fouling Organisms: Adhesion Damage and Prevention," in *Advances in Marine Antifouling Coatings and Technologies* (eds. Hellio, C. and Yebra, D.), pp. 80-112, CRC Press, Boca Raton, Florida.
- Lee, H.J., Willis, C.R. and Stone, C.A. (2011), "Modeling and Preparation of a Superhydrophobic Non-woven Fabric," *J. Mater Sci.* **46**, 3907-3913
- Lee, J.D., Gregorek, G.M., and Korkan, K.D. (1978), "Testing Techniques and Interference Evaluation in the OSU Transonic Airfoil Facility," Paper # AIAA-1978-1118, presented at 11th Fluid and Plasma Dynamics Conference, Seattle, WA, AIAA, New York.
- Lee, K.K., Bhushan, B. and Hansford, D. (2005), "Nanotribological characterization of fluoropolymer thin films for biomedical micro/nanoelectromechanical system applications," *J. Vac. Sci. Technol. A* **23**, 804-810
- Lee, S.J. and Lee, S.H. (2001), "Flow field analysis of a turbulent boundary layer over a riblet surface," *Exp. Fluids* **30**, 153-166
- Lee, W., Jin, M.K., Yoo, W.C. and Less, J.K. (2004), "Nanostructuring of a Polymeric Substrate with Well-Defined Nanometer-Scale Topography and Tailored Surface Wettability," *Langmuir* **20**, 7665-7669
- Lewis, J.A. (2009), "Non-Silicone Biocide-Free Antifouling Solutions," in *Advances in Marine Antifouling Coatings and Technologies* (eds. Hellio, C. and Yebra, D.), pp. 709-724, CRC Press, Boca Raton, Florida.
- Lide, D.R. (ed.) (2009), *CRC Handbook of Chemistry and Physics*, 90th Edition, CRC Press, Boca Raton, Florida.

- Lim, A.L. and Bai, R. (2003), "Membrane fouling and cleaning in microfiltration of activated sludge wastewater," *J. Membrane Sci.* **216**, 279–290
- Lin, L., Cheng, Y.T., and Chiu, C.J. (1998), "Comparative study of hot embossed micro structures fabricated by laboratory and commercial environments," *Microsyst Technol* **4**, 113-116
- Lin, L., Chiu, C.J., Bacher, W., and Heckeke, M. (1996), "Microfabrication Using Silicon Mold Inserts and Hot Embossing," Paper # 0-7803-3596-1/96, presented at 7th International Symposium on Micro Machine and Human Science, IEEE, New York.
- Liu, K. and Jiang, L. (2011), "Bio-inspired designed of multiscale structures for function integration," *Nano Today* **6**, 155-175.
- Liu, K.N., Christodoulou, C., Riccius, O. and Joesph, D.D. (1990), "Drag Reduction in Pipes Lined with Riblets," *AIAA* **28** (10), 1697-1698
- Liu, M., Wang, S., Wei, Z., Song, Y. and Jiang, L. (2009), "Bioinspired Design of a Superoleophobic and Low Adhesive Water/Solid Interface," *Adv. Mater.* **21**, 665-669
- Livio, M. (2002), *The golden ratio: the story of phi, the world's most astonishing number*, Broadway Books, New York.
- LoVetri, K., Gawande, P.V., Yakandawala, N. and Madhyastha S. (2010), "Biofouling and Anti-fouling of Medical Devices," in *Biofouling Types, Impact and Anti-Fouling* (eds. Chan, J. and Wong, S.), pp. 105-128, Nova Science Publishers, New York.
- Lowrey, P. and Harasha, J. (1991), "A preliminary assessment of the feasibility of using riblets in internal flows to conserve energy," *Energy* **16**, 631-642
- Luchini, P., Manzo, F., and Pozzi, A. (1991), "Resistance of a grooved surface to parallel flow and cross-flow," *J. Fluid Mech.* **228**, 87-109
- Ma, H., Bowman, C.N., and Davis, R.H. (2000), "Membrane fouling reduction by backpulsing and surface modification," *J. Membrane Sci* **173**, 191-200
- Maloney, J.M., Uhland, S.A., Polito, B.F., Sheppard Jr, N.F., Pelta, C.M. and Santini Jr, J.T. (2005), "Electrothermally Activated Microchips for Implantable Drug Delivery and Biosensing," *J. Control. Release* **109**, 244-255
- Manov, D.V., Chang, G.C. and Dickey, T.D. (2003), "Methods for Reducing Biofouling of Moored Optical Sensors," *J. Atmos. Ocean Tech.* **21**, 958-968

- Mappes, T., Worgull, M., Hecke, M., and Mohr, J. (2008), "Submicron polymer structures with X-ray lithographic and hot embossing," *Microsyst. Technol.* **14**, 1721-1725
- Marentic, F. J. and Morris, T. L. (1992), "Drag reduction article," United States Patent no. 5 133 516
- Marrie, T.J. and Costerton, J.W. (1984), "Morphology of Bacterial Attachment to Cardiac Pacemaker Leads and Power Packs," *J. Clin. Microbiol.* **19**, 911-914
- Marrie, T.J., Nelligan, J. and Costerton, J.W. (1982), "A Scanning and Transmission Electron Microscopic study of an Infected Endocardial Pacemaker Lead," *Circulation* **66**, 1339-1341
- Martell, M.B., Perot, J.B., and Rothstein, J.P. (2009), "Direct numerical simulations of turbulent flows over drag-reducing ultrahydrophobic surfaces," *J. Fluid Mech.* **620**, 31-41
- Martell, M.B., Rothstein, J.P. and Perot, J.B. (2010), "An analysis of superhydrophobic turbulent drag reduction mechanisms using direct numerical simulation," *Phys. Fluids* **22**, 065102
- Martínez-Palou, R., Mosqueira, M., Zapata-Rendón, B., Mar-Juárez, E., Bernal-Huicochea, C., Clavel-López, J. and Aburto, J. (2011), "Transportation of heavy and extra-heavy crude oil by pipeline: A review," *J or Petro Sci and Eng*, **75**, 274-282
- Mathur, A., Roy, S.S., Tweedie, M., Mukhopadhyay, S., Mitra, S.K., and McLaughlin, J.A. (2009), "Characterization of PMMA microfluidic channels and devices fabricated by hot embossing and sealed by direct bonding," *Current Appl. Phys.* **9**, 1199-1202.
- Matsunaga, T., Nakayama, T., Wake, H., Takahashi, M., Okochi, M. and Nakamura, N. (1998), "Prevention of Marine Biofouling Using a Conductive Paint Electrode," *Biotechnol. Bioeng.* **59**, 374-378
- Melo, L.F., Bott, T.R. and Bernardo, C.A. (eds.) (1988), *Fouling Science and Technology*, Kluwer Academic Publishers, Dordrecht, The Netherlands.
- Menton, D. 2008 The seeing eye. AnswersMagazine.com. July-Sept., pp. 76-79
- Meuler, A.J., Smith, J.D., Varanasi, K.K., Mabry, J.M., McKinley, G.H., Cohen, R.E. (2010), "Relationships between Water Wettability and Ice Adhesion," *ACS Appl. Mat. Interf.* **2**, 3100-3110
- Meyer, W. and Seegers, U. (2004), "A preliminary approach to epidermal antimicrobial defense in the Delphinidae," *Mar Biol.* **144**: 841-844

- Millar, M. (2005), "Microbial Biofilms and Clinical Implants," in *Surfaces and Interfaces for Biomaterials* (ed. Vadgama, P.), pp. 619-631, CRC Press, Boca Raton, Florida.
- Mizuno, J., Harada, T., Glinsner, T., Ishizuka, M., Edura, T., Tsutsui, K., Ishida, H., Shoji, S., and Wada, Y. (2004), "Fabrications of Micro-Channel Device by Hot emboss and Direct bonding of PMMA," proceedings IEEE ICMENS (Banff, Canada, 25-27 Aug), 26-29
- Monroe, D. (2007), "Looking for Chinks in the Armor of Bacterial Biofilms," *PLoS Biol* **5**, 2458-2461
- Montali, A. (2006), "Antibacterial Coating Systems," *Injury* **37**, S81-S86
- Morton, G. (2000), "Problems of Biofilms in Industrial Waters and Processes," in *Industrial Biofouling Detection, Prevention and Control* (eds. Walker, J., Surman, S. and Jass, J.), pp. 79-102, Wiley, New York.
- Munson, B., Young, D. and Okiishi, T. (2005), *Fundamentals of Fluid Mechanics*, 5th Ed., Wiley, New York.
- Narasimhan, J. and Papautsky, I. (2004), "Polymer embossing tools for rapid prototyping of plastic microfluidic devices," *J. Micromech. Microeng.* **14**, 96-103
- Nebot, E., Casanueva, J.F., Solera, R., Pendon, C., Taracido, L.J., Casanueva-Robles, T. and Lopez-Galindo C. (2010), "Marine Biofouling in Heat Exchangers," in *Biofouling Types, Impact and Anti-Fouling* (eds. Chan, J. and Wong, S.), pp. 65-104, Nova Science Publishers, New York.
- Neinhuis, C. and Barthlott, W. (1997), "Characterization and Distribution of Water-repellent, Self-cleaning Plant Surfaces," *Annals of Botany* **79**, 667-677
- Neumann, D. and Dinkelacker, A. (1991), "Drag measurements on V-grooved surfaces on a body of revolution in axial flow," *App Sci Res*, **48**, 105-114
- Newman, J.D. and Turner, A.P.F. (2005), "Home blood glucose biosensors: a commercial perspective," *Biosens. Bioelectron* **20**, 2435-2453
- Nishimoto, S. and Bhushan, B. (2013), "Bioinspired self-cleaning surfaces with superhydrophobicity, superoleophobicity, and superhydrophilicity," *RSC Adv.* **3**, 671-690
- Nitschke, P. (1983), "Experimental investigation of the turbulent flow in smooth and longitudinal grooved pipes," Max-Planck Institute for Stromungsforschung, Gottingen, West Germany.

- Nosonovsky, M. and Bhushan, B. (2008), *Multiscale Dissipative Mechanisms and Hierarchical Surfaces*, Springer, New York.
- Nosonovsky, M. and Bhushan, B. (2009), "Multiscale Effects and Capillary Interactions in Functional Biomimetic Surfaces for Energy Conversion and Green Engineering," *Phil. Trans. R. Soc.* **367**, 1511-1539
- O'May, G.A., Jacobsen, S.M., Stickler, D.J., Mobley, H.T.L. and Shirtliff, M.E. (2009), "Complicated Urinary Tract Infections due to Catheters," in *The Role of Biofilms in Device-Related Infections* (eds. Shirtliff, M. and Leid, J.G.), pp. 123-164, Springer-Verlag, Berlin.
- O'Toole, J.C., Cruz, R.T. and Seiber, J.N. (1979), "Epicuticular Wax and Cuticular Resistance in Rice," *Physiol. Plant* **47**, 239-244
- Oeffner, J. and Lauder, G.V. (2012), "The hydrodynamic function of shark skin and two biomimetic applications," *J. Exp. Biology* **215**, 785-795
- Okochi, M., Yokokawa, H., Lim, T.K., Taguchi, T., Takahashi, H., Yokouchi, H., Kaiho, T., Sakuma, A. and Matsunaga, T. (2005), "Disinfection of Microorganisms by Use of Electrochemically Regenerated Periodate," *App Environ Microbiol* **71**, 6410-6413
- Olsen, S., Pedersen, L., Laursen, M., Kiil, S. and Dam-Johansen, K. (2007), "Enzyme-based antifouling coatings: a review," *Biofouling* **23**, 369-383
- Ou, J., Perot, B. and Rothstein, J.P. (2004), "Laminar drag reduction in microchannels using ultrahydrophobic surfaces," *Phys. Fluids* **16**, 4635-4643
- Pangarkar, B.L., Sane, M.G. and Guddad, M. (2011), "Reverse Osmosis and Membrane Distillation for Desalination of Groundwater: A Review," *ISRN Materials Science*, Volume 2011, Article ID 523124
- Parini, M.R. and Pitt, W.G. (2006), "Dynamic removal of oral biofilms by bubbles," *Coll. Surf. B* **52**, pp. 39-46
- Pasmore, M. and Marion, K. (2009), "Biofilms in Hemodialysis," in *The Role of Biofilms in Device-Related Infections* (eds. Shirtliff, M. and Leid, J.G.), pp. 167-192, Springer-Verlag, Berlin.
- Posamentier, A.S. and Lehmann, I. (2007), *The fabulous Fibonacci numbers*, Prometheus Books, New York.
- Pritchard, A.M. (1988), "Deposition of Hardness Salts," in *Fouling Science and Technology* (eds. Melo, L.F., Bott, T.R. and Bernardo, C.A.), pp. 261-274, Kluwer Academic Publishers, Dordrecht, The Netherlands.

- Railkin, A.I. (2004), *Marine Biofouling Colonization Processes and Defenses*, CRC Press, Boca Raton, Florida.
- Ralston, E. and Swain, G. (2009), "Bioinspiration – the Solution for Biofouling Control?" *Bioinsp. Biomim.* **4**, 1-9
- Ramasamy, M.S. and Murugan, A. (2007), "Fouling Deterrent Chemical Defense in Three Muricid Gastropod Egg Masses from the Southeast Coast of India," *Biofouling* **23**, 259–265
- Rao, D., Webb, J.S. and Kjelleberg, S. (2005), "Competitive Interactions in Mixed-Species Biofilms Containing the Marine Bacterium *Pseudoalteromonas tunicata*," *Appl. Environ. Microbiol* **71**, 1729-1736
- Rao, D., Webb, J.S. and Kjelleberg, S. (2006), "Microbial Colonization and Competition on the Marine Alga *Ulva australis*," *Appl. Environ. Microbiol* **72**, 5547-5555
- Ray, D.L. (ed.) (1959), *Marine Boring and Fouling Organisms*, University of Washington Press, Seattle.
- Reidy, L.W. and Anderson, G.W. (1988), "Drag Reduction for External and Internal Boundary Layers Using Riblets and Polymers," Paper # AIAA-1988-0138, presented at 26th AIAA Aerospace Sciences Meeting, Reno, NV, AIAA, New York.
- Reif, W. (1985), *Squamation and ecology of sharks*. Courier Forschungsinstitut Senckenberg, Frankfurt, Germany, 78, 1-255
- Reis, R.L. and Weiner, S. (eds.) (2004), *Learning from Nature How to Design New ImplanTable Biomaterials*, Kluwer Academic Publishers, Norwell, MA.
- Richardson, D.S. (1984), "Biofouling in Freshwater Cooling Systems," in *Biotechnology in the Marine Sciences* (eds. Colwell, R.R, Sinskey, A.J. and Pariser, E.R), pp. 243-248, Wiley, New York.
- Ridgway, H.F., Kelly, A., Justice, C. and Olson, B.H. (1982), "Microbial Fouling of Reverse-Osmosis Membranes Used in Advanced Wastewater Treatment Technology: Chemical, Bacteriological, and Ultrastructural Analyses," *App Environ Microbiol* **45**, 1066-1084
- Rohr, J.J., Andersen, G.W., Reidy, L.W. and Hendricks, E.W. (1992), "A comparison of the drag-reducing benefits of riblets in internal and external flows," *Exp. in Fluids*, **13**, 361-368
- Roos, N., Luxbacher, T., Glinsner, T., Pfeiffer, K., Schulz, H., and Scheer, H.C. (2001), "Nanoimprinting Lithography with a Commercial 4 Inch Bond System for Hot Embossing," *Proc. SPIE*, 4343, 427-435

- Saliterman, S.S. (2006), *Fundamentals of BioMEMS and Medical Microdevices*, SPIE, Washington.
- Sareen, A., Deters, R.W., Henry, S.P. and Selig, M.S. (2011), "Drag Reduction Using Riblet Film Applied to Airfoils for Wind Turbines," Paper # AIAA-2011-558, presented at 49th AIAA Aerospace Sciences Meeting, Orlando, FL, AIAA, New York.
- Sato, O., Kubo, S. and Gu, Z.Z. (2009), "Structural Color Films with Lotus Effects, Superhydrophilicity, and Tunable Stop-Bands," *Acc. Chem. Res.* **42**, 1-10
- Scardino, A.J. (2009), "Surface Modification Approaches to Control Marine Biofouling," in *Advances in Marine Antifouling Coatings and Technologies* (eds. Hellio, C. and Yebra, D.), pp. 664-692, CRC Press, Boca Raton, Florida.
- Scardino, A.J., Guenther, J. and de Nys, R. (2008), "Attachment Point Theory Revisited: the Fouling Response to a Microtextured Matrix," *Biofouling* **24**, 45 – 53
- Schulz, M.J., Shanov, V.N. and Yun, Y. (eds.) (2009), *Nanomedicine Design of Particles, Sensors, Motors, Implants, Robots, and Devices*, Artech House, Boston.
- Schumacher, J.F., Aldred, N., Callow, M.E., Finlay, J.A., Callow, J.A., Clare, A.S. and Brennan, A.B. (2007a), "Species-Specific Engineered Antifouling Topographies: Correlations between the Settlement of Algal Zoospores and Barnacle Cyprids," *Biofouling* **23**, 307- 317
- Schumacher, J.F., Carman, M.L., Estes, T.G., Feinberg, A.W., Wilson, L.H., Callow, M.E., Callow, J.A., Finlay, J.A., and Brennan, A.B. (2007b), "Engineered antifouling Microtopographies – effect of feature size, geometry, and roughness on settlement of zoospore of the green alga *Ulva*," *Biofouling* **23**, 55-62
- Sharma, N., Charles, C.H., Lynch, M.C., Qaqish, J., McGuire, J.A., Galustians, J.G. and Kumar, L.D. (2004), "Adjunctive Benefit of an Essential Oil-Containing Mouth Rinse in Reducing Plaque and Gingivitis in Patients Who Brush and Floss Regularly," *J American Dental Assoc* **135**, 496-504
- Sharma, S., Popat, K.C. and Desai, T.A. (2007), "Design and Biological Applications of Nanostructured Poly(Ethylene Glycol) Films," in *Nanotechnology in Biology and Medicine Methods, Devices, and Applications* (ed. Vo-Dinh, T.), pp. 39-1, CRC Press, Boca Raton, Florida.
- Sheng, X., Ting, Y.P. and Pehkonen, S.O. (2010), "Force Measurements of Bacterial Adhesion to Metals Using Cell Probe in Atomic Force Microscopy," in *Biofouling Types, Impact and Anti-Fouling* (eds. Chan, J. and Wong, S.), pp. 129-154, Nova Science Publishers, New York.

- Shirtliff, M. and Leid, J.G. (eds.) (2009), *The Role of Biofilms in Device-Related Infections*, Springer-Verlag, Berlin.
- Simoes, M., Simoes, L.C. and Vieira, M.J. (2010), "A Review of Current and Emergent Biofilm Control Strategies," *LWT – Food Science and Technology* **43**, 573-583
- Smeltzer, M.S., Nelson, C.L. and Evans, R.P. (2009), "Biofilms and Aseptic Loosening," in *The Role of Biofilms in Device-Related Infections* (eds. Shirtliff, M. and Leid, J.G.), pp. 57-74, Springer-Verlag, Berlin.
- Somerscales, E.F.C. and Knudsen, J.G. (eds.) (1981), *Fouling of Heat Transfer Equipment*, Hemisphere Publishing Corporation, Washington.
- Staples, M., Daniel, K., Cima, M.J. and Langer, R. (2006), "Application of Micro- and Nano-Electromechanical Devices to Drug Delivery," *Pharm. Res.-Dordr.* **23**, 847-863
- Stoodley, P., Sauer, K., Davies, D.G. and Costerton, J.W. (2002), "Biofilms as Complex Differentiated Communities," *Annu. Rev. Microbiol.*, **56**, 187–209
- Subaschandar, N., Kumar, R., and Sundaram, S. (1999), "Drag Reduction Due to Riblets on a GAW(2) Airfoil," *J. of Aircraft*, **36** (5), 890-892
- Sun, T., Feng, L., Gao, X. and Jiang, L. (2005), "Bioinspired Surfaces with Special Wettability," *Acc. Chem. Res.* **38**, 644-652
- Sundaram, S., Viswanath, P.R., and Rudrakumar, S. (1996), "Viscous Drag Reduction Using Riblets on NACA 0012 Airfoil to Moderate Incidence," *AIAA* 34 (14), 676-682
- Thomas, J.G., Corum, L. and Miller, K. (2009), "Biofilms and Ventilation," in *The Role of Biofilms in Device-Related Infections* (eds. Shirtliff, M. and Leid, J.G.), pp. 75-106, Springer-Verlag, Berlin.
- Trinidad, A., Ibanez, A., Gomez, D., Garcia-Berrocal, J.R. and Ramierz-Camacho, R. (2010), "Application of Environmental Scanning Electron Microscopy for Study of Biofilms in Medical Devices," *Microscopy: Science, Technology, Applications and Education*, 1, 204-210
- Unknown (ed.) (2007), *Pilot's Encyclopedia of Aeronautical Knowledge*, United States Federal Aviation Administration, Skyhorse, New York.
- Vadgama, P. (ed) (2005), *Surfaces and Interfaces for Biomaterials*, CRC Press, Boca Raton, Florida.

- Vajda, S. (1989), *Fibonacci & Lucas numbers, and the golden section: theory and applications*, Halsted Press, New York.
- Valdes, E.R. (2010), "Bio-inspired Materials and Operations," in *Bio-Inspired Innovation and National Security* (eds. Armstrong, R.E., Drapeau, M.D., Loeb, C.A. and Valdes, J.J.), pp. 139-156, NDU Press, Washington, DC.
- Velten, T., Bauerfeld, F., Schuck, H., Scherbaum, S., Landesberger, C., and Bock, K. (2010), "Roll-to-Roll Hot Embossing of Microstructures," Paper # 978-2-35500-011-9, presented at DTIP, Seville, Spain, EDA Publishing.
- Venkatesan, R. and Murthy, P.S. (2008), "Macrofouling Control in Power Plants", in *Springer Series on Biofilms* (ed. Costerton, J.W.), pp. 265-290, Springer-Verlag, Berlin.
- Viswanath, P. R. (1999), "Riblets on Airfoil and Wings: A Review," Paper # AIAA-99-3402, presented at the AIAA 30th Fluid Dynamics Conference, Norfolk, VA, AIAA, New York.
- Viswanath, P. R. and Mukund, R. (1995), "Turbulent Drag Reduction Using Riblets on a Supercritical Airfoil at Transonic Speeds," *AIAA* 33 (5), 945-947
- Viswanath, P.R. (2002), "Aircraft viscous drag reduction using riblets," *Prog Aerospace Sci*, **38**, 571-600
- Vladkova, T. (2007), "Surface Engineering for Non-Toxic Biofouling Control," *J. Univ. Chem. Technol. Metallurgy* 43, 239-256
- Vladkova, T. (2008), "Surface Modification Approach to Control Biofouling", in *Springer Series on Biofilms* (ed. Costerton, J.W.), pp. 135-162, Springer-Verlag, Berlin.
- Vleugels, I.R. (2006), "Multi-Functional Coating Solution," Euprofile, Public Service Review: European Union 18, 1-2
- Vo-Dinh, T. (ed.) (2007), *Nanotechnology in Biology and Medicine*, CRC Press, Boca Raton, Florida.
- Wagner, T., Neinhuis, C. and Barthlott, W. (1996), "Wettability and Contaminability of Insect Wings as a Function of Their Surface Sculptures," *Acta Zoologica* **77**, 213-225
- Walker, J., Surman, S. and Jass, J. (eds.) (2000), *Industrial Biofouling Detection, Prevention and Control*, Wiley, New York.

- Walsh, M.J. (1990a), "Effect of Detailed Surface Geometry on Riblet Drag Reduction Performance," *J. Aircraft*, **27** (6), 572-573
- Walsh, M. J. (1990b), "Riblets. Viscous Drag Reduction in Boundary Layers," *Progr. in Astronaut. and Aeronaut.*, **123**, 203-261
- Walsh, M. J. and Lindemann, A. M. (1984), "Optimization and application of riblets for turbulent drag reduction," Paper # AIAA-84-0347, presented at AIAA 22nd Aerospace Sciences Meeting, Reno, NV, AIAA, New York.
- Walsh, M.J. (1982), "Turbulent Boundary Layer Drag Reduction using Riblets," Paper # AIAA-1982-0169, presented at AIAA 20th Aerospace Sciences Meeting, Orlando FL, AIAA, New York.
- Walsh, M.J. and Lindemann, A.M. (1984), "Optimization and application of riblets for turbulent drag reduction," Paper # AIAA-1984-0347, presented at AIAA 22nd Aerospace Sciences Meeting, Reno, NV, AIAA, New York.
- Walters, L.J., Smith, C.M. and Hadfield, M.G. (2003), "Recruitment of Sessile Marine Invertebrates on Hawaiian Macrophytes: do Pre-Settlement or Post-Settlement Processes Keep Plants Free from Fouling?" *Bull. Mar. Sci.* **72**, 813-883
- Wenzel, R.N., (1936), "Resistance of solid surfaces to wetting by water," *Indust. Eng. Chem.* **28**, 988-994
- Wetzel, K.K. and Farokhi, S. (1996), "Interaction of Riblets and Vortex Generators on an Airfoil," Paper # AIAA-1996-2428-CP, presented at the AIAA 14th Applied Aerodynamics Conference, New Orleans, LA, AIAA, New York.
- White, F. (2006), *Viscous Fluid Flow*, 3rd ed., McGraw Hill, New York.
- Wilkins, E.M. (2005), *Clinical Practice of the Dental Hygienist*, Lippincott Williams and Wilkins, Philadelphia.
- Wilkinson, S. P. and Lazos, B. S. (1988), "Direct drag and hot-wire measurements on thin-element riblet arrays," in *Turbulence Management and Relaminarisation* (eds. Liepman, H.W. and Narasimha, R.), pp. 121-131, Springer-Verlag, Berlin.
- Wilkinson, S. P., Anders, J. B., Lazos, B. S. and Bushnell, D. M. (1988), "Turbulent drag reduction research at NASA Langley: progress and plans," *Inter. J. Heat Fluid Flow* **9**, 266-277
- Wilkinson, S.P. (1983), "Influence of wall permeability on turbulent boundary-layer properties," Paper #AIAA-1983-0294, presented at the 21st Aerospace Sciences Meeting of the American Institute of Aeronautics and Astronautics, Reno, NV, AIAA, New York.

- Willemsen, P. (2005), "Biofouling in European Aquaculture: is there an easy solution," TNO Industrial Technology.
- Wisniewski, N., Moussy, F. and Reichert, W.M. (2000), "Characterization of Implantable Biosensors Membrane Biofouling," *Fresenius J. Anal. Chem.* **366**, 611-621
- Wong, T.-S., Kang, S.H., Tang, S.K.Y., Smythe, E.J., Hatton, B.D., Grinthal, A. and Aizenberg, J. (2011), "Bioinspired self-repairing slippery surfaces with pressure-stable omniphobicity," *Nature*, **477**, 443-447
- Yeh, P.Y., Kizhakkedathu, J.N., Madden, J.D. and Chiao, M. (2007), "Electric Field and Vibration-Assisted Nanomolecule Desorption and Anti-Biofouling for Biosensor Applications," *Coll. Surf. B* **59**, 67-73
- Yen, J. (2010), "Marine Dynamics," in *Bulletproof Feathers How Science Uses Nature's Secrets to Design Cutting-Edge Technology* (ed. Allen, R.), pp. 22-43, University of Chicago Press, Chicago.
- Zheng, Y., Gao, X. and Jiang, L. (2007), "Directional adhesion of superhydrophobic butterfly wings," *Soft Matter* **3**, 178-182
- Zodrow, K., Brunet, L., Mahendra, S., Li, D. and Zhang, A. (2009), "Polysulfone ultrafiltration membranes impregnated with silver nanoparticles show improved biofouling resistance and virus removal," *Water Research* **43**, 715-723